Formation and Transformation of Colloidal Metal Halide Nanoparticles

by

Jakob C Dahl

A dissertation submitted in partial satisfaction of the

requirements for the degree of

Doctor of Philosophy

in

Chemistry

in the

Graduate Division

of the

University of California, Berkeley

Committee in charge:

Professor Armand Paul Alivisatos, Chair
Professor Peidong Yang
Professor Mark Asta

Spring 2022

Formation and Transformation of Colloidal Metal Halide Nanoparticles

Abstract

Formation and Transformation of Colloidal Metal Halide Nanoparticles

by

Jakob C Dahl

Doctor of Philosophy in Chemistry

University of California, Berkeley

Professor Armand Paul Alivisatos, Chair

Colloidal nanocrystals are miniscule pieces (< 100 nm or $\sim 1/1000$th the width of a human hair) of solid materials suspended in a liquid. Semiconductor nanocrystals have controllable optical properties like color, which make them appealing for use in displays, LEDs, solar cells and many other devices that rely on the interaction of matter with light or electricity. The color and other optical properties are related to the size and composition of the crystals, which makes control over these properties crucial to any application.

Creating these crystals is often more of an art than a science, with large differences in results arising between chemicals sourced from different suppliers, laboratories, practitioners and any (even slight) changes in the process of making them. The work in this thesis is part of a broader scientific movement aimed at a more scientific understanding and rational control of the synthesis process. To keep the nanocrystals small and stable requires the use of surfactants or ligands, which are chemicals that can interact both with a charged or polar environment such as the nanocrystal and a non-polar environment such as the surrounding medium. The metal halide nanocrystals we focus on here are particularly sensitive to these ligands and the surrounding medium, as they are more similar in nature to salt, whereas most other materials used to make nanocrystals are more similar to rocks. As a result, changing the environment around the nanocrystals can transform the type, shape or composition of the crystal. The studies herein investigate the formation of metal halide nanocrystals, how transformations between them occur and how both processes are interrelated.

The rapid development in precision and scale of machine learning (ML) methods capable of predictions based on large sets of data has roused the interest of scientists across many disciplines. Concurrently, improvements in the automation of chemical synthesis and characterization methods now allow for the generation of data on hundreds to thousands of reactions necessary to use such data science methods. Due to the complexity of chemical synthesis in general, and nanocrystal synthesis in particular, using ML to predict the outcomes of reactions is an attractive proposition. This thesis introduces methods from machine learning and

data science to the synthesis of nanocrystals, and connects them to more physical models of this process.

In this thesis, Chapter 1 outlines the important concepts related to nanocrystals, their properties, characterization methods and reactions. We then briefly introduce current trends of using machine learning and data science to understand synthesis. In Chapter 2, we use high-throughput synthesis experiments coupled to automated deconvolution of optical absorption spectra to gain an overview of the reaction landscape around one well-studied metal halide nanocrystal material, $CsPbBr_3$. In Chapter 3, we investigate in more detail the formation and transformation processes of one material we found of central importance in the overview, the atomically thin nanosheets of OLA_2PbBr_4 using *in-situ* absorption spectroscopy and joint fits of spectral and kinetic models, as well as more traditional kinetic analysis where appropriate. Further analysis of precursor reactions is provided in Chapter 4. We then examine synthesis and properties of a family of cesium silver metal halide double perovskites in Chapter 5. Finally in Chapter 6, we discuss the implications of this work on different scientific fields.

To my family and QinQin, for love; to my friends and community, for support; to books, for giving me refuge in realms magical at times when science was not.

Contents

List of Figures

List of Tables

Acknowledgments

First, I would like to thank my advisors, Prof. Paul Alivisatos and Dr. Emory Chan, for letting me join their labs, mentoring me and giving me advice, feedback and the independence to pursue the projects I cared about. Thanks also to Negest Williams, for making sure I got paid and helping me manage all the administrative details of my work.

I would like to thank all my collaborators - these projects would not have been possible without you. Dr. Yehonadav Bekenstein - thanks for making space for me in the double perovskite project, being my mentor and going through the scientific process together with me. Prof. Wendy Gu and Dr. Thomas Bischof for offering additional mentorship in my first year. Dr. Wojciech Osowiecki and Dr. Joseph Swabeck for helping me understand and use equipment and supporting me on the first project I did on my own. To Xingzhi Wang and Samuel Gleason - thanks for bearing with me while I tried to become a mentor through copious trials and errors, continuing to work with me anyway and building up our little machine learning subgroup together. Thanks also to my undergraduate mentees - Tasneem Khan, Xiao Huang and Prachi Khandekhar - it was a great learning experience on my part, I hope you got something out of it, too! Dr. Samuel Niblett for working through kinetics simulations with me and not getting too exasperated by the project dragging on forever, and Prof. David Limmer for encouraging and advising us. Dr. Yao Cai, Dr. Matthias Loipersberger and Dr. Yeongsu Cho for doing some tricky DFT calculations when I needed them. Prof. Mark Asta and Prof. Peidong Yang for being very generous with their resources collaborating with me and providing interesting discussion (and agreeing to serve on my committee). Prof. Eran Rabani for helping me work through mathy models of 2D nanosheet spectra (mathy for me, at least). Dr. Ye Zhang and Dr. Jianmei Huang for helping out with measurements. Prof. Kristin Persson, Prof. Gerbrand Ceder, Dr. Anubhav Jain and Dr. Carolyn Sutter-Fella for inviting me and the Alivisatos and Chan Labs into the data-driven synthesis science grant and especially Kristin for supporting me in my future endeavors. Emma Vargo, Dr. Katherine Evans and Prof. Ting Xu for working with Tasneem and me on the block-copolymer prediction project. Ilana Porter, Stefano Toso and Dr. Dmitry Baranov, Ethan Curling, Caitlin McCandler, Dr. Zhuolei Zhang and Dr. Artiom Skripka - thanks for including me in your projects - it has been a pleasure working with you. Dr. Justin Ondry for teaching me to use the TEM, Jason Calvin for working the ITC for me - and both for working together on the GURP project. Dr. Karen Bustillo for helping me with STEM-EDS measurements and interpretation. Dr. Hasan Celik and Dr. Alicia Lund for helping me with NMR measurements. Dr. Kathleen Durkin, Dr. Wei Feinstein and Edison Lam for help with setting up computation.

Thanks also to the scientific community in Berkeley and beyond, especially the Alivisatos and Chan groups, and many others - all the people who were open to discussions of all things nanocrystal and machine learning with me - Dr. Assaf Ben-Moshe, Dr. Ayelet Teitelboim, Dr. Brent Kosher, Dr. Arunima Balan, Dr. Matthew Hauwiller, Prof. Carissa Eisler, Dr. Chris Chen, Prof. Jennifer Listgarten, Dr. Aditi Krishnapriyan, Dr. Vida Jamali, Dr. Amirali Aghazadeh, Dr. Zhi Li, Dr. Shaul Aloni, Dr. Ivan Moreno-Hernandez, Dr.

Katherine Requejo-Roque, Dr. Sean Lubner, Philip Nega, Priscilla Pieters, Michelle Crook, Dr. David Nenon, Dr. Myungwhan Oh, Dr. Mingee Cho, Dr. David Litt, Emma and Conrad Stansbury, QinQin Yu and many, many others. The Hallatschek group for always being welcoming and including me in their social activities. Dr. Quinten Akkerman, Prof. Dmitry Talapin, Prof. Lilac Amirav, Prof. Lilo Pozzo, Prof. Jonathan Owen and Prof. Joshua Schrier for making me feel welcome in the broader nanocrystal and materials machine learning community.

And of course - to all of the people who helped me get to Berkeley to begin with, starting with my parents - who, while not scientists, still managed to instill great curiosity of the world around us in me. Thanks to QinQin Yu for being my partner in life, and her parents, Prof. Lixin Ma and Prof. Ping Yu for being kind and supportive. My siblings, for bearing with me when I was nerding out. Many great teachers at the secondary schools I attended in Germany - particularly Dr. Ingo Schnell, who encouraged my early forays into chemistry. Thanks to all the people who helped in my undergraduate education at MIT - for teaching me, providing very generous financial aid and being a great community. In particular, Prof. Yogesh Surendranath and Prof. Troy van Voorhis for letting me join their labs as well as Dr. Joseph Falcone and Dr. Michael Mavros for mentoring me. Prof. JoAnne Stubbe for being a great academic advisor and letting me take all kinds of classes. All the people who helped the two of us in our Kepler Tech Lab project in Rwanda - Kepler and all the helpful staff and students, as well as our great student teaching team around Alphonse Habyarimana, the PKG center and Dr. Allison Hynd for funding, Dr. Pedro Reynolds-Ceullar and D-lab for training and NuVu for testing.

Finally for funding my research, I thank the National Science Foundation Graduate Research Fellowship program for their grants under DGE 1752814 and the the Kavli NanoScience Institute, University of California, Berkeley for their Philomathia Graduate Student Fellowship. Work at the Molecular Foundry was supported by the Office of Science, Office of Basic Energy Sciences, of the U.S. Department of Energy under Contract No. DE-AC02-05CH11231. Other work reported here was supported by the U.S. Department of Energy, Office of Science, Office of Basic Energy Sciences, Materials Sciences and Engineering Division, under Contract No. DE-AC02-05-CH11231 within the Physical Chemistry of Inorganic Nanostructures Program (KC3103), the Inorganic/Organic Nanocomposites Program (KC3104) and the Data Science for Data-Driven Synthesis Science Program (KCD2S2). Computational resources were provided by the U.S. Department of Energy, Office of Science, Office of Basic Energy Sciences, Materials Sciences and Engineering Division under Contract No. DE-AC02-05-CH11231 within the Materials Project program (KC23MP), the Lawrencium computational cluster resource provided by the IT Division at the Lawrence Berkeley National Laboratory with funding by the Director, Office of Science, Office of Basic Energy Sciences, of the U.S. Department of Energy under Contract No. DE-AC02-05CH11231 and the Molecular Graphics Facility in the Chemistry Department at UC Berkeley with funding by the National Institutes of Health under NIH S10OD023532. Instruments in CoC-NMR are supported in part by NIH S10OD024998.

Chapter 1

Nanocrystal Properties, Reactions and Machine Learning

1.1 Overview

This work connects research from nanoscience, physical synthetic chemistry, materials science, machine learning and physical modeling. As such, it is impossible to give a comprehensive overview of all the relevant fields. Instead, this introduction aims to briefly introduce the relevant portions utilized here, and provides references we have found helpful in understanding these topics.

1.2 Colloidal Semiconductor Nanocrystals and their Properties

Nanocrystals are any crystalline material with at least one dimension below 100 nm in size. Colloidal nanocrystals in particular are materials suspended in solution, usually through the action of surfactants. Nanocrystals have been used for centuries - some medieval stained glass windows contain nanoscale particles of gold and silver that impart particularly brilliant red colors. A first scientific description of a nanocrystal synthesis for "gold [...] in exceedingly fine particles" was given by Faraday in 1857.[1] However, characterization methods at that time made it difficult to investigate nanocrystals in more detail. Nanoscale imaging techniques, especially the electron microscope, renewed scientific development in the area starting in the 1950s, with seminal work by Turkevich et al.[2] on the formation of gold nanocrystals demonstrating non-linear processes and understanding size distributions. The discovery of the unique optical properties in semiconductor nanocrystals was driven by colloidal experiments performed by Louis Brus and coworkers,[3] solid state experiments by Ekimov et al.[4] and underlying theory developed by Alexander Efros.[5] Briefly, making a semiconductor nanocrystal smaller will increase the energy of absorption and emission energies, leading to an experimentally observed blue-shift. This change in energy, termed quantum confinement, can be explained qualitatively through a simple particle in a box model. Solutions to Schrödinger's wave equation for a particle confined to a box become successively higher in energy as the box becomes smaller. The theory is applicable to semiconductor nanocrystals because absorbing light and thus raising an electron from the valence band to the conduction band creates an exciton - a quasi-particle arising from the attraction between the excited electron and the electron hole it leaves behind - which can be described as such a particle in a confined environment. These size-dependent optical properties are key to current applications in displays, where meeting or exceeding color standards makes visuals appear more lifelike.[6] Being able to estimate the size of a nanocrystal based on its optical properties will also be key to understanding some of the later measurements and analysis in this thesis.

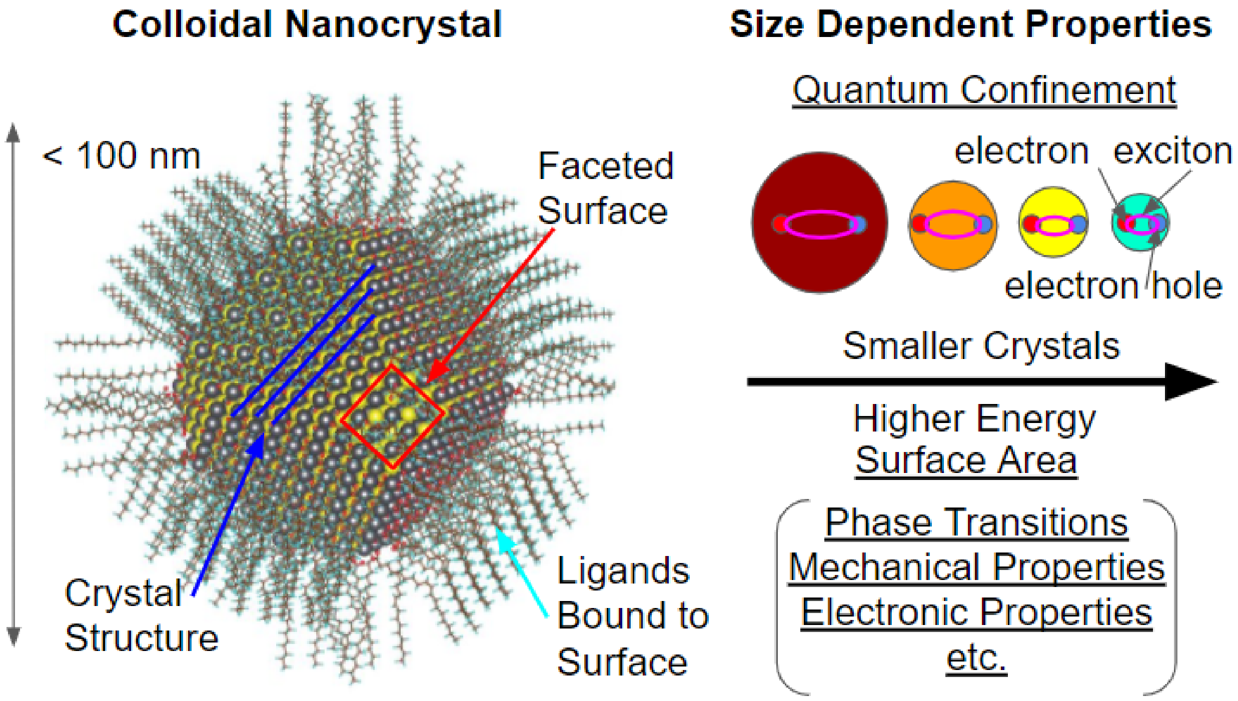

Figure 1.1: *Nanocrystal Properties*

Another key aspect of nanocrystals is their high surface area relative to the volume they occupy. This has led to a number of other applications in catalysis[7] and sensing.[8] Due to the high ratio of surface area to volume, the structure and chemistry of the surface play a key role in determining the reactions of nanocrystals, from nucleation to growth, transformation or catalysis. As with other crystals, the surface composition corresponds to a facet, or cut, along a crystallographic direction. In addition, colloidal nanocrystals have ligands bound to their surface. While we know experimentally that the binding of ligands to complexes in solution and to the surfaces of nanocrystals has profound impacts on their formation, none of the currently existing quantitative nanocrystal synthesis models described in 1.5 actually include ligands as explicit chemical agents, and are thus not able to capture any of the changes in faceting or growth type that ligands typically induce.

Finally, it is important to note that all colloidal nanocrystals exist as ensembles, i.e. a large number of particles. Due to the size-dependent nature of their properties, making sure that particles are similar in size and shape is crucial to a good synthesis. The relative size distribution, i.e. the standard deviation of observed sizes divided by the average size is the main measure of quality here. This can vary a lot depending on the synthesis technique used and the material formed, but for somewhat isotropic shapes, a size distribution of less than 5% is considered nearly monodisperse,[9] and distributions of less than 20% are still useful in many contexts.

1.3 Nanocrystal Characterization Techniques

Next, we will briefly introduce the basic characterization techniques used to characterize nanocrystals in this thesis: absorption and photoluminescence spectroscopy, transmission electron microscopy and x-ray diffraction.

Absorption spectroscopy is a measure of how much light is absorbed by a substance - usually by transferring an electron from a lower, ground level state to a higher energy excited state. We perform this measurement mainly using a liquid solution of nanocrystals. With an equal probability of absorption for each particle, the amount of light passing through such a solution should decay exponentially with increasing length and concentration. The resulting relation of the logarithm of absorption forms the equation known as Beer's law. Performing this measurement across different wavelengths of light then yields a characteristic absorption spectrum of a material. Based on the size-dependant optical properties of nanocrystals, absorption spectroscopy can be used not only to measure the concentration and type of nanocrystals, but also determine which size may be present in solution.[3] Due to the rich information and fast and efficient measurements, it is an indispensable tool for high-throughput investigations of nanocrystals, though the analysis can be challenging due to the overlap of multiple spectra. In this thesis, we develop data-driven analysis techniques to gain understanding of nanocrystals primarily from their absorption spectra.

The flip side of absorption, photoluminescence, is the light emitted by a material when the electrons excited to a higher energy level by light decay back down again to an unoccupied lower energy level. Measuring how much light is emitted at different wavelengths yields a photoluminescence emission spectrum (PL), whereas observing how much light is being emitted while changing the wavelength at which the material is excited gives a photoluminescence excitation spectrum (PLE), which in the most simple case should overlap directly with the absorption spectrum.

Next to the concentration of emitting particles, another factor affecting this measurement is the efficiency at which particles with higher energy levels emit light to decay down to the ground state instead of using other processes, such as releasing this energy as heat. A measure of the efficiency, the ratio of the number of photons emitted divided by the number of photons absorbed, known as the photoluminescent quantum yield (PLQY) is thus a central measure of quality for semiconductor nanocrystals. While a large part of nanoparticle synthesis optimization efforts is spent optimizing the PLQY,[10] this work focuses on more fundamental explanation of the nanocrystal synthesis, though we will report and discuss quantum yields when measured.

As a nanoscale characterization technique, transmission electron microscopy is indispensable.[11] The basic technique relies on accelerating electrons released into a vacuum through applying an electric field with a high voltage, usually on the order of 100 - 200 kV. Using magnets, the beam of electrons can be focused onto a sample in a manner analogous to a light microscope, and expanded again to a viewing area, in which the electrons strike a material that emits visible light when exposed to electrons, which allows detection of the resulting image with a camera. Due to the wave-particle duality of matter and the small mass of electrons, the electron waves have a small wavelength of less than 10 pm, which enables focus to very small areas and resolution of image features as small as the size of an atom. This makes it such a powerful technique for understanding nanoscale materials, as we can simultaneously see a picture of the nanocrystals to determine their size and shape of the crystals as well as gain potential information on their structure and crystallographic facets exposed on the surface. Because of the interactions of electrons with matter, which excite high energy X-ray transitions that are unique to each element, electron microscopy can also be used to understand the elemental composition of a sample by analyzing spectra of the reflected or transmitted beams.

X-ray diffraction (XRD) uses this characteristic X-ray emission to generate X-rays of a single wavelength by sending a beam of electrons onto a target made of a single element, which is copper or molybdenum in our case. After filtering and collimating the X-rays into a single beam, they are then directed to a sample. X-rays are reflected by core electrons of atoms, and in a crystalline material, these reflections occur at regularly spaced intervals, or crystallographic planes. At any particular angle, if the distance traveled between X-rays reflected from adjacent positions is equal to an integer multiple of half the wavelength, they will constructively interfere, satisfying the Laue condition and leading to the Bragg equation. Deviating from this angle reduces the intensity of this reflection. This angle dependent intensity pattern is characteristic of a particular crystal structure, and can in principle be used to directly identify the arrangement of all atoms in a crystal. In this work, we will mainly use powder XRD, in which crystal orientation is not controlled and only one set of angles is measured, leading to less definitive, possibly overlapping patterns that are used more as a fingerprint to match with previously determined patterns than as a way to determine the crystal structure from the measurement alone. In addition, for nanosized crystals, this reduction in intensity is less sharp, as there are only tens or hundreds of atoms in a reflecting array and thus a small deviation in angle will cause less destructive interference. Through the Debye-Scherrer equation, it is possible to estimate crystallite sizes based on the width of observed peaks in an XRD pattern. A great tutorial on how to prepare and analyze

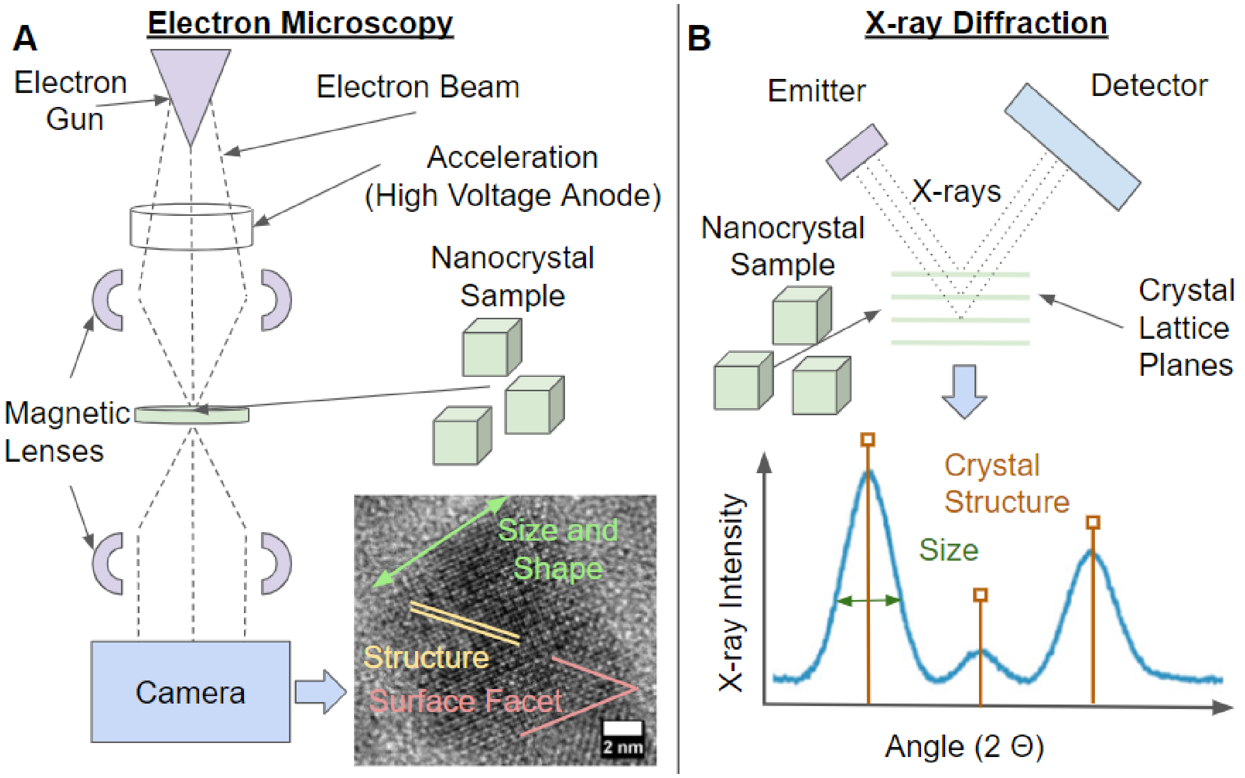

Figure 1.2: *Principles of Nanocrystal Characterization with TEM (A) and XRD (B)*

powder x-ray diffraction of nanocrystals was written recently by Holder et al..[12]

1.4 Colloidal Nanocrystal Synthesis Techniques

The most common synthesis technique for colloidal nanocrystals uses a sudden mixing of two or more chemicals required for the formation of these crystals, often termed "hot-injection", as this is accomplished by rapidly adding a solution containing some of the components to a hot solution containing the remaining components. This sudden mixing causes crystals to form, or nucleate, in solution. Once crystals have formed, they can increase in size by adding material from solution (growth), physically connecting to other crystals (attachment), or exchange material with other crystals (ripening). Without outside intervention, these processes continue indefinitely, resulting in the growth of large crystals. To solve this problem, synthesis of nanocrystals in solution will usually include ligands to stabilize the species in solution and prevent aggregation. While this type of synthesis is easy to set up and allows a variety of chemicals to be used, it is difficult to scale to industrial synthesis and can be strongly influenced by fluid transfer during mixing.

Instead of initiating the nanocrystal formation reaction through the mixing of two reagents, it is also possible to heat the prepared mixture to a temperature at which the reaction will occur. This "heat-up" synthesis is simpler, as there is no requirement to add chemicals to a solution at high temperature. Control over the reaction comes entirely through the control of the temperature - at some temperature, the activation barrier for precursors to decompose, or for nanocrystals to nucleate is reached, with the reaction proceeding from there. Naturally, this comes with its own challenges - variables such as the rate at which the reaction is heated that are not important in a hot-injection synthesis are now major controlling factors.

Once initial nanoparticles have been formed, it is possible to continue growing more material on them. In general, this process of heterogeneous nucleation, i.e. forming nuclei on existing material, is more efficient and controllable than the homogeneous nucleation required to create nanocrystals. There are a variety of different methods with different names using this basic idea with slight variations, such as seeded growth,[13] shell growth and self-limiting reactions such as c-ALD or SILAR. While these reactions are of paramount importance for established semiconductor quantum dots or metal nanoparticles, heterogeneous nucleation is not well-studied in the case of metal halide nanocrystals, and we will not be working with this technique here.

In some cases, nanocluster reactions can become self-limiting without creating a two-step process, forming clusters with a defined number of atoms. Creating these clusters generally requires an even higher degree of control than forming nanoparticles. The number of atoms in these clusters have such a defined number so that they can be enclosed by low-index, stable surface facets, without adatoms or holes. These "magic sized clusters" (MSCs) have been found in the synthesis of many different types of nanoparticles, and can even be used as precursors in a heat-up type reaction.[14]

For all of the methods described above, problems with experimental reproducibility are the Achilles heel of nanoparticle synthesis. Even going back to Faraday, a note on the preparation cautioned practitioners to be meticulous about cleaning, stating "A glass supposed to be clean, and even a new bottle, is quite able to change the character of a given gold fluid".[1]

In the recent nanoparticle literature, some very popular protocols were found to be strongly influenced by minute impurities in some of the reagents - to the point where different bottles from the same chemical supplier would produce different results. For instance, trioctylphosphine oxide, a frequently used solvent for CdSe nanoparticle synthesis,[9] contains impurities of phosphonic acids without which the synthesis does not proceed as planned.[15] Minute impurities of iodide in a commonly used surfactant, cetyltrimethylammonium bromide can suppress the formation of gold nanorods[16]. For the metal halide nanocrystals studied here, water is a very strong binding agent, and even small inclusions can substantially alter the reaction outcome.[17]. Choosing a synthesis protocol that appears stable to these inclusions is important for generating a reasonable understanding of the overall reaction outcome.

1.5 Colloidal Nanocrystal Synthesis Models

Next, we briefly review the most important models used to describe formation of nanocrystals. All of these models have been applied at various times to explain aspects of nanocrystal formation, though they operate at different limits and may not predict the stable existence of nanosized crystals in solution at all. Figuring out which model is most applicable to a certain situation is not a trivial matter and has been subject to recent contention within the scientific community.[18–21]

Classical crystal nucleation theory is an equilibrium model, based broadly on the assumption that bonds on the surface of a crystal are less energetically favourable than bonds in the interior. As surface grows with the square of the radius and volume grows with the cube of the radius, the energy of a crystallite will first increase due to formation of the unfavourable surface, then decrease as more of the energetically favourable interior forms. The peak of this energy is the critical nucleus size, as nuclei smaller than this size have a thermodynamic driving force to shrink, whereas larger crystals have a thermodynamic driving force to continue growing indefinitely. Thermodynamic fluctuations across this critical nucleus size then drive the appearance of crystals in solution. Based on classical nucleation theory, nanocrystals should not be stable in solution - while this theory is thus often referenced and is the basis upon which most other theories have been built, it cannot be applied to predict the nucleation or growth of nanocrystals without further modification.

A further result of this theory concerns the exchange of mass between crystals of different sizes in solution. If such an exchange of mass is allowed, it is energetically favourable for a smaller crystal to transfer mass to a larger crystal. Given not just two crystals, but a distribution of crystals of different size in solution, larger crystals should become larger and smaller crystals smaller, giving rise to a wider distribution of sizes. This Ostwald ripening process of observing an increase in size as well as widening in size dispersion of crystals, can be experimentally observed in a large number of systems, including in nanocrystals. While Ostwald ripening can become dominant during nanocrystal reactions, it is only a growth model and thus cannot describe the full nanocrystal nucleation and growth process.

On a semi-quantitative, explanatory level, the LaMer model is the model of choice for most nanocrystal synthesis practitioners.[22,23] The fundamental proposition of this model is that to create nanosize crystals, one must create a burst of nuclei at the same point in time, depleting the components or monomers in solution and thus kinetically trapping nanoparticles at small sizes. Most commonly, two monomer concentration limits for crystal formation are assumed: a saturation limit, i.e. a limiting concentration above which crystal growth occurs and a higher supersaturation limit, which leads to nucleation when surpassed. Quickly releasing monomers into solution leads to concentrations briefly surpassing the nucleation threshold and nucleation of particles, which decreases the monomer concentration back below the supersaturation threshold, keeping nucleation near-instantaneous. Monomer concentrations above the saturation limit now allow for slow, continuous growth of the crystals. While LaMer and Dinegar formulated a mathematical treatment of this model, the graphical depiction of this process is perhaps the most widely known qualitative description of nanocrystal formation.

A modified version of classical nucleation theory that incorporates some of the elements of LaMer's work along with simulation of a continuum of nanocrystal sizes was developed initially by Sugimoto et al.[24] and further refined by others in the past two decades. In essence, by assuming that during burst nucleation the rate of monomers entering solution and the rate of crystal nucleation and growth are identical, it is possible to set up and solve a simplified differential equation for the rate of nucleation and growth as a function of the supersaturation concentration. Further modifications are based on the realization that this assumption only holds for the time of maximum supersaturation,[25] and include more balanced models capable of reproducing experimentally observed nanoparticle size distributions.[26]

A simplistic model of nanocrystal nucleation and growth that fits neatly into the structure of chemical kinetics was developed by Watzky and Finke for metal nanocrystal growth in the 1990s.[27] It requires only two rate constants, one for nucleation of nanocrystals through a bimolecular reaction of two monomers in solution and further an autocatalytic growth rate for a reaction between the nanocrystal and additional monomers. This model can be fit to the disappearance of precursor in solution, or the appearance of nanocrystalline material, and often describes the resulting sigmoidal curves quite well. In contrast to the LaMer model, this fit usually leads to descriptions of slow, continuous nucleation coupled to fast, autocatalytic growth. While the overall concentrations of reagents and products can be well described by this model, estimating nanocrystal sizes is more difficult. Without further modification, the Finke-Watzky model will always predict a population of nanocrystals monotonously decaying in number with increasing size, as larger crystals contain more monomers and will thus grow quickly, while new small crystals are continuously added to the population. This contrasts with the nearly gaussian distributions of nanocrystal size observed under well-optimized synthesis conditions. Recent work modifying this model with a second, slower growth rate for larger nanocrystals can reproduce experimental size distributions, though the size at which this growth rate is arbitrarily imposed will greatly influence the size predicted as an outcome.[28]

In the limit that nanocrystal nucleation and growth are both faster than the generation of the monomers required for these processes, this precursor decomposition process turns into the major controlling factor of the synthesis.[29,30] Owen and co-workers have pioneered much of the work in this area, leading to libraries of precursors with different reactivity that is partly predicted by classical physical organic chemistry concepts such as Hammett parameters.[31] By tuning this effect, the speed at which precursors are released can be controlled, which in turn controls the number of nuclei, the period of time over which nucleation is distributed as well as the growth rate of the nanocrystals.

In a model recently developed by the Norris and coworkers, facet-limited growth is directly addressed.[32] This directly builds on the finding that many nanocrystals are well faceted, with faces generally defined by crystallographic orientation, and that completing a facet is thermodynamically favourable. If nucleation of a new facet is the rate limiting step, then growth of the crystal can be modeled as a series of facet growth steps. If, just as in classical nucleation theory, there is a critical nucleus size for a facet, an adlayer below that size is subject to thermodynamic fluctuations, whereas a adlayer larger than this size will grow to cover the entire facet. This has the potential to lead to a growth instability: If one facet is significantly thinner than the others, such that the critical adlayer nucleus is smaller than the facet on one of the facets, this will result in much faster growth of the thin facets. Based on previously reported values for surface tension, line tension and bulk energy, a thermodynamic model of this facet growth was developed, and applied to nanoplatelet growth, as well as to growth of magic sized clusters. We will develop a similar model in chapter 3 for 2D perovskite nanosheets that we refine purely based on experimental data.

Finally we note here some models which have been used mostly on a qualitative level, usually to rationalize the formation of anisotropic nanostructures such as rods or plates in a homogeneous solution.[33] Some previous research has suggested that nanocrystals may form through the use of the surfactants used as ligands as soft templates. Without the nanocrystals, ligands readily form nanoscale structures such as round micelles, bilayers or other shapes. In analogy to the use of polymer or other organic molecular structures as templates to form mesoporous materials, these shapes could serve as a template to induce certain forms such as gold nanorods. Another frequently used idea concerns the binding of ligands or other synthesis elements to different facets. If certain facets of the crystal have particles bound with more strength than others, they will be less available for reactions and thus grow more slowly.

1.6 Properties specific to metal halide nanocrystals

Most semiconductor nanocrystals are made of moderately hard materials with strong bonds, such as CdSe or InP. Metal halide nanocrystals are an exception in this regard - the ionic nature of their bonds results in a much softer material that rearranges easily and undergoes reactions readily at room temperature. Three important aspects are changed significantly: degradation, transformation and crystal annealing.

Degradation processes in metal halide nanocrystals often result in the dissolution of the crystalline structure. Alcohols,[34] amines,[35] thiols and other organosulfur compounds[36] and phosphonic acids[37] readily dissolve lead halide perovskites and other metal halide nanostructures - even solvation with less strongly binding groups such as amides (dimethylformamide) or esters ($\gamma-$butyrolactone) is possible and has been used to create metal halide precursor inks.[38] The ease of these degradation processes remains a major problem to the industrial application of lead halide perovskites in particular.[39]

Chemical transformation of nanocrystals has been observed in many different materials, including the harder II-VI and III-V semiconductors. However, it is usually only a transformation of one part of the lattice, i.e. through cation exchange - generally with the assumption that this is mainly driven by cation vacancy diffusion and that the anion lattice remains stable.[40] In metal halide nanocrystals, both the anion and the cation lattice are labile, and so both anion[41,42] and cation exchange can be observed. However, due to the lability of both lattices, it is possible to also change the phase of the material completely.[35,43,44] These unusual nanocrystal transformations are also implicated in the formation of some metal halide materials, adding additional complexity to an already difficult system.[45]

Crystal annealing is an important process to enable the formation of perfect single crystals. While reaching a nanocrystalline size can make it easier for a crystal to anneal, the bond strength can still remain extremely important. For this reason, high quality II-VI semiconductors need to be synthesized at high temperatures.[10] The even stronger bonds of III-V semiconductors sometimes require temperatures above what can be reached with organic solvents.[46] Metal halide nanocrystals have much weaker bonds - crystal annealing appears to occur at or close to room temperature. This plays a crucial role in the formation of high quality, highly luminescent crystals of lead halide perovskites at low temperatures.

Specifically for the lead halide perovskites, another important aspect to the creation of highly luminescent crystals is what is called the defect-tolerant electronic structure.[47,48] This arises from a difference in the orbitals that form the highest occupied state (HOMO or the top of the valence band) and the lowest unoccupied state (LUMO or bottom of the conduction band). In most semiconductors, these are the bonding (HOMO) and anti-bonding (LUMO) orbitals between the two elements. As a result, any missing bonds (non-bonding) will lead to energy levels between the bonding and antibonding states that will disrupt the process of absorbing and emitting photons. In the lead halide perovskites, both the HOMO and the LUMO are composed of antibonding orbitals. Missing bonds will only subtly shift the electronic states - these electronic states will still influence the overall efficiency, but not as severely.[37]

Lastly, we consider surface bonding. For metal halide nanocrystals, the most common binding motifs and ligands are either an interaction between a positively charged ligand (usually oleylammonium or another protonated amine) and a negatively charged surface rich in halide anions, or binding of a negatively charged ligand (usually oleate, though many other acid anions may bind similarly) to a positively charged surface rich in metal cations.[49] For the lead halide perovskites in particular, the binding of oleylammonium can occur in vacant cesium sites on the surface in a highly coordinated fashion.[50] This strong bond to oleylammonium can even lead to the formation of layered 2-D perovskite materials[51] - a macroscale, version of the colloidal 2-D nanoplates we will investigate in Chapter 3.

1.7 General Introduction to Machine Learning

Machine learning or artificial intelligence is an old field, dating back to the advent of computers. Machine learning in its most general form means enabling a computer to become better at a task by being exposed to some form of knowledge. The basic process is asking a computer to predict what will happen in a system - and supplying it with data and some model that could predict what is happening. The computer then fits the model to the data, and for any useful learning process, the computer should make increasingly accurate predictions as the number of data points used in the fit are increased. In a very general sense, fitting a straight line to a number of points using a computer is a form of machine learning that most scientists will have performed before.

Modern machine learning takes advantage of large datasets and complex statistical models to try and make predictions of complicated systems. Increased computational power and more general models have catapulted this area from a minor subfield in computer science to a general tool with applications across all science and engineering disciplines. Fundamentally, the ability to predict outcomes is central to all STEM disciplines, so general purpose prediction algorithms have enormous appeal. For an excellent practical overview of modern machine learning practices, we highly recommend Andrew Ng's introductory online course on machine learning,[52] as well as the documentation of the scikit-learn package.[53]

Machine learning prediction algorithms are usually defined first by the type of task they are to perform. Briefly, there is a division of prediction tasks into classification tasks in which the desired outcome is a class or quality - such as image recognition of a cat or a dog - and regression tasks in which the desired outcome is a quantity, such as the price of a house. Further, there are supervised tasks in which there are external sources which can give a correct answer - the correct label, or the correct number - and unsupervised tasks in which the correct answer is not given and correlations or clusters of the data should be found. Finally, there are tasks in which there are multiple outputs (i.e. predicting the number of cats and the number of dogs in an image).

A second division is given by the type of algorithm. Linear regression models can still be used in a modern machine learning context, though usually in a multi-variate fashion and using regularization terms to limit the number of variables used for the prediction. Non-linear algebraic relations can sometimes be added in by including polynomial or other algebraic features of the outputs. Decision trees can be used for a wide variety of tasks, especially in an ensemble where multiple trees are used together to predict the output, such as a random forest algorithm. Support vector machines and kernel ridge regressions utilize distance metrics between points to predict outcomes and have also been used widely in chemistry. While there are many other model types, perhaps the most widely used in general are neural networks - i.e. layered, individually simple computational models which transmit predictions in parallel and in series to each other in ways reminiscent of neurons in a brain. Finally, there are a number of approaches using graph theory that can be utilized to predict outputs. For chemistry, perhaps the most relevant of these are molecular graph approaches - i.e. models that conceive of molecules as a collection of nodes (atoms) with connections (bonds).[54]

One of the pitfalls of machine learning is overfitting, i.e. the use of so many variables in a model that each datapoint is uniquely identified and no trend or correlation is learned. To ensure this does not occur, machine learning practitioners routinely divide their data into a training set that is used to fit the algorithm, and a test set that is utilized to test whether the algorithm is truly predictive. Only the results of the test set are relevant to the evaluation of whether the machine learning algorithm succeeded at its task. In addition, some algorithms may need to be tuned to the problem by changing what is called hyperparameters, i.e. the number of variables being fitted or the value of regularization penalties. In some models, especially deep learning models, the number of these hyperparameters can be large enough to store information in itself, so that iterating between training and testing set while optimizing these parameters can lead to information transfer about the contents of the testing set. Thus, a good practitioner will also utilize a separate validation set - i.e. section out part of the training set that is used not to train parameters directly, but to optimize the hyperparameters. To further ensure that the hyperparameters are useful for the entire training set and not only to predict that specific validation set, it is useful to use cross-validation, which means iterating which parts of the training set are used to train parameters vs. hyperparameters and finding those hyperparameters that are most useful over the entire training set.

An important application for machine learning, especially in synthesis is not simply the prediction of outcomes,[55,56] but the use of those predictions to generate new experimental conditions and reevaluation of the model after said experiments have been performed. This type of feedback loop is termed active learning. In principle, any model could be used in such a feedback loop. However, the method by which experiments are chosen - termed the aquisition function - is usually dependent not only on the predicted outcome of the model, but also in the predicted uncertainty of the model outcome. Ensemble models that natively incorporate some uncertainty by combining multiple prediction algorithms or functions can quickly be incorporated into such a scheme (i.e. random forests, gaussian processes etc.). Alternatively, bayesian statistics can be used to estimate model certainty, or a separate model can be trained to predict the uncertainty of the first model. Given the model uncertainty, it is then possible to explore possible parameter space to create a more accurate model by choosing experiments with the highest uncertainty or to exploit the given knowledge to optimize some performance metric by choosing experiments that are most likely to give the best results. Together with automated synthesis techniques, active learning has the potential to change the way experiments are chosen and performed.[57]

1.8 Machine Learning in Synthesis Science

Modeling has long had a distinct place in synthesis science. Linear, or at least analytic,[58] models of reaction kinetics or reaction rates as a function of temperature, concentrations or chemical substituents are part of the standard repertoire that chemists use to investigate how reactions happen and are considered foundational for the the general subfield of physical synthetic or physical organic chemistry. However, many reactions do not yield neat, analytically solvable models. Connections between different reactions quickly yield thorny differential equations and non-linear processes - especially in nanoparticle synthesis.

As a result, synthesis science is one of the areas in chemistry facing the most prediction uncertainty - which is a prime opportunity for machine learning methods. There is, however, one important caveat: Many of the most successful machine learning techniques, especially deep learning and the use of neural networks, require tens or hundreds of thousands of data points. Chemical synthesis is laborious, and generating more than a thousand data points can be a serious chore. This limits the types of algorithms that can be successfully employed.[59]

Nevertheless, there has been a lot of attention in this field over the last few years. In the field of organic chemistry, the Doyle,[55] Asparu-Guzik,[60] Denmark,[61] and Cronin[62] groups have taken much of the early initiative in this area, utilizing a variety of algorithms to predict reaction outcomes from chemical inputs, particularly in organic chemistry. The Schrier[56] and Ceder[63] groups have pioneered similar work in materials synthesis. For nanocrystals, the Sargent[64], Buonassissi[65] and Cronin[66] groups have started working in this area.

Given the difficulty of performing and analyzing the many experiments required to train machine learning models, there is a concurrent effort to aquire large datasets. Three distinct methods are useful to consider here. First, many laboratories have studied a system over years and may have amassed a large data volume that only needs to be transcribed to be useful for machine learning applications.[56] Second, fields that have been studied for some time often have rich literature - which can be extracted either manually or using machine learning techniques for natural language processing.[62] Finally, robotic liquid handling[67] and microfluidic setups allow high-throughput synthesis campaigns with thousands of experiments. All of these efforts are complemented by ways to streamline data reporting and create relevant databases, such as the dark reactions project,[56] ESCALATE,[68] the materials project[69] and the open reaction database[70].

Active learning regimes that attempt to optimize some important property or explore a system are an active area of research. In the general materials synthesis fields, much of this work has been pioneered by groups around Maruyama and Takeuchi. For nanocrystals, researchers around Buonassissi[65] and Cronin[66] have been able to predict and tune spectra of metal nanoparticles through utilizing active learning in connection with robotic synthesis infrastructure. Tuning the emission spectra of lead halide perovskite nanocrystals has also been achieved using flow systems and machine learning by the deMello[71] and Abolhassani groups.

In general, all of this previous work has tried to simplify chemical reactions for the use of machine learning in one of two ways: either turning it into a single variable quantitative (regression) task, such as predicting catalysis efficiency or optimizing the absorption ratio of two peaks, or transforming it into a qualitative task (classification), predicting reaction outcomes. In reality, these two tasks are two sides of the same coin: there are multiple possible products of chemical reactions, each of which may be measured at a variable concentration - which would turn the problem into a more complex, multioutput regression task.

1.9 Scientific Machine Learning

To gain more scientific insight from the large volume of data used for machine learning, there is a movement to incorporate more scientifically interpretable models. There is movement from two sides: on one hand, machine learning models are being interrogated for possible scientific insight.[56,61] On the other, physical models are being given more flexibility and parameters than might traditionally be done.[72] Overall, the goal of this type of research is to create algorithms that would both give scientific insight and are flexible enough to handle and accurately predict large volumes of data.

In cases in which there is thermodynamic control, much work on this area has focused on mapping phase boundaries. This can be done by utilizing general purpose algorithms to predict where good boundaries lie, or by integrating the results with theoretical calculations of formation energy and chemical potential.

Systems under kinetic control depend not on the formation energy of each chemical, but rather on the activation energy between each pair of reagents. If only one activation energy matters, as in the enantiodetermining step of catalytic reactions, this becomes a relatively straightforward task. For systems with multiple parameters, the scientific prediction of outputs requires modeling of the kinetics by finding solutions to differential equations - a task that must be repeated anew for each initial condition queried. While this is expensive, the computational cost of calculating differential equations has also decreased significantly. Current work on utilizing physics-informed neural networks to create general purpose solutions for differential equations, especially for problems including simulation of chemical reactions.

Overall, there is clearly room for growth in the area of scientific machine learning, and all of the introduced topics here remain areas of active research. Ideal models cannot clearly be identified - and may indeed be system specific. Work in this thesis attempts to utilize machine learning or statistical techniques to learn more about the process of nanocrystal formation. We hope that this recount will be helpful to others embarking on similar journeys.

Chapter 2

Elucidating the Cs-Pb-Br Perovskite Nanocrystal Reaction Network

Reproduced in part with permission from: Dahl, J. C.; Wang, X.; Huang, X.; Chan, E.M. ; Alivisatos, A. P. “Elucidating the weakly-reversible Cs-Pb-Br Perovskite Nanocrystal Reaction Network with High-Throughput Maps and Transformations” *Journal of the American Chemical Society* **2020**, Copyright 2020 American Chemical Society

Advances in automation and data analytics can aid exploration of the complex chemistry of nanoparticles. Lead halide perovskite colloidal nanocrystals provide an interesting proving ground: there are reports of many different phases and transformations, which has made it hard to form a coherent conceptual framework for their controlled formation through traditional methods. In this work, we systematically explore the portion of Cs-Pb-Br synthesis space in which many optically distinguishable species are formed using high-throughput robotic synthesis to understand their formation reactions. We deploy an automated method that allows us to determine the relative amount of absorbance that can be attributed to each species in order to create maps of the synthetic space. These in turn facilitate improved understanding of the interplay between kinetic and thermodynamic factors that underlie which combination of species are likely to be prevalent under a given set of conditions. Based on these maps, we test potential transformation routes between perovskite nanocrystals of different shapes and phases. We find that shape is determined kinetically, but many reactions between different phases show equilibrium behavior. We demonstrate a dynamic equilibrium between complexes, monolayers and nanocrystals of lead bromide, with substantial impact on the reaction outcomes. This allows us to construct a chemical reaction network that qualitatively explains our results as well as previous reports and can serve as a guide for those seeking to prepare a particular composition and shape.

2.1 Introduction

Data science and high-throughput experimentation have enabled rapid exploration in different areas of chemistry such as chemical biology,[73] drug discovery,[74] reaction discovery,[75] reaction optimization[55] and materials discovery.[56,76] Nanocrystal syntheses have additional complexity by adding different dimensionalities[77] to the multicomponent phase diagrams explored in more traditional bulk materials design.[78] Due to this complication, nanocrystal synthesis science has been mostly restricted to single-[77,79] or two-component systems.[14,30,80,81] Lead halide perovskites[51,82,83] are three component systems and have a more complex and rich phase diagram, with nanocrystals of multiple species forming easily,[84–86] and chemical transformations between them accessible at or just above room temperature.[35,44,87] This makes them an ideal system to test whether we can increase our understanding of chemistry in complex nanocrystal phase diagrams by using automated synthesis and analysis methods.

The synthesis of lead halide perovskites can be controlled through a variety of parameters. Generally, such nanocrystals are made by addition of lead, cesium and bromide precursors to an alkane solution containing amine and carboxylate terminated alkyl moieties that act as agents to complex free metal ions or bind to the surfaces of any nanocrystallites.[88] Temperature and relative concentration of each of these species yields a synthetic space of large dimensionality. Prior studies established many interesting features of this space. Temperature can be used to tune the size of $CsPbBr_3$ nanocubes[88] and the thickness of $CsPbBr_3$ nanoplatelets.[89] While amine-free synthesis have been reported,[90] in the vast majority of synthesis in which amines are present they strongly influence the outcome. Amine chain length,[91] concentration[92] and protonation[92] are reported to control the formation of plates vis-a-vis cubes, their thickness as well as formation of the Cs_4PbBr_6 phase.[92] Secondary amines restrict the reaction entirely towards cubes.[93] Using ligand-assisted reprecipitation, cubes, plates, rods and spheres can all be made with variations in the chain length of the surfactant carboxylic acids and amines.[94] Further analysis suggested that it is ratios of lead to amine[95,96] and Cs to ammonium[92,97] that control the system rather than an absolute concentration of amine. In this work, we further explore how these and other factors interact with each other and build chemical understanding about why they matter.

The chemical transformations in this nanocrystal system are additional essential features of this system not usually observed for nanocrystals. Of particular importance is the reversible nature observed in the transformation between $CsPbBr_3$ and Cs_4PbBr_6.[44] The transformation from $CsPbBr_3$ to Cs_4PbBr_6 is accomplished through addition of oleylamine[35] and can be strongly accelerated by adding thiols[35] or thiocyanate,[98] switching from a process that takes seconds in an isotropic regime to taking hours or days in a more gentle layer-by-layer fashion depending on the chemical strength of the etchant solution.[98] The reverse transformation from Cs_4PbBr_6 to $CsPbBr_3$ can be induced by adding oleic acid or heat[44], solubilized $PbBr_2$,[84] or removing CsBr.[43] Additionally, a Br-deficient environment appears to lead to the formation of $CsPbBr_3$ through CsBr and Cs_4PbBr_6 intermediates,[99] suggesting that bromine might also induce transformation from Cs_4PbBr_6

to $CsPbBr_3$. Other transformations have also been observed: In a polar/nonpolar solvent mixture, $CsPbBr_3$ was shown to slowly transform to $CsPb_2Br_5$ after addition of dimethyldodecylammonium bromide.[87] These transformations are not confined to the Cs-Pb-Br phase space. In the $CH_3NH_3PbX_3$ system, lead halide nanocrystals can be transformed into the perovskite material,[100,101] likely through intercalation reactions that are similar to those found in bulk.[100] Reversible transformation to metal-depleted species with amines was also observed with lead-free double perovskites nanocrystals.[102](see Chapter 5 We expand on these transformations and use them as qualitative measures to test which reactions are allowed, reversible or prohibited.

Integrating these diverse results into a cohesive picture has been difficult. Experimental work attempting to map out and integrate the synthesis has been limited, usually dealing with individual slices through the multidimensional synthesis landscape, such as the transition from synthesizing Cs_4PbBr_6 to $CsPbBr_3$,[96] or the formation of platelets of different sizes and cubes.[95] The first succeeded in directly mapping a small portion of a synthesis phase diagram, with the second using a machine learning model to give an approximation. The number of syntheses performed inherently limits the reliability and density of the maps produced – automated synthesis and analysis protocols can help gain better information. Previous studies display a single outcome dimension such as the ratio of Cs_4PbBr_6 to $CsPbBr_3$,[96] or average layer thickness of nanoplates,[95] or size of nanocubes,[92] which is useful to isolate a particular effect. Finding a way to display and reason with the multidimensional nature of this system is crucial to developing further and more coherent understanding.

This work explores the rich phase space of cesium lead bromide nanocrystal synthesis through factorial sets of 2337 synthesis experiments performed on a synthesis robot. An automated algorithm provides a deconvolution of absorption spectra into nine optically distinct species, from which we construct a detailed, multidimensional map of the synthetic space. We then traverse synthetic space: we test 149 transformations of the observed species upon addition of additional reagents. We observe an equilibrium of nanocrystalline, atomic layer and molecular lead halide phases which can serve as intermediates for the formation of different ternary cesium lead halide phases and geometries. This aids us in constructing a chemical reaction network that connects the synthesis and transformation reactions, explains the observation of multiple synthetic pathways, weakly reversible behavior and apparent nonlinearity close to transition points. Finally, we discuss a range of observations from previous reports and find that our model has strong qualitative explanatory power, including over properties not initially considered. Our combination of high-throughput experimentation and quantitative analysis allows us to gain an overview of the reaction space, qualitatively analyze the transformations within this space, and build a more complete chemical understanding in the form of a chemical reaction network not apparent through either method alone.

2.2 Results and Discussion

To construct a chemical reaction network, we first need to characterize and confirm the identity of the 9 different reaction products we observe. We then examine an example of transitions between species to see how different variables change the synthesis outcome. To gain a better overview of reaction space, we want to explore the synthesis in an high-throughput fashion, which we accelerate by building an automated deconvolution algorithm which transforms absorption spectra into fractions of different species. Based on the deconvolution, we build a map of synthesis space as a function of Cs, Pb and OLA concentrations. From the map, we can gain insight into the possible reactions occurring during formation and transformation of nanocrystals. We then test these transformation reactions, which helps us determine which of the possible reaction pathways are valid and leads us to the chemical reaction network we describe. Finally, we consider the implications of our model and show that it has significant qualitative explanatory power over previously reported results.

Species Observed in CsPbBr Synthesis Space

We synthesized cesium lead bromide and lead bromide species using a modified version of the method reported by Imran et al.[103] By varying reagent concentrations, we observed formation of nine species that could be differentiated based on their UV-Vis absorption spectra, and made reference samples to characterize and confirm their identity by UV-Vis absorption, X-ray diffraction and transmission electron microscopy (TEM) (Figure 2.1). High resolution TEM images A.1.1 of $Cs_xPb_yBr_z$ show lattice d-spacings of Cs_4PbBr_6, $CsPb_2Br_5$, $PbBr_2$ and $CsPbBr_3$ nanocubes. For 2, 3 and 4 ML nanoplatelets, stacking distances of the nanoplatelets can be measured, which were found to be roughly in range with those calculated from XRD patterns. No useful HR-TEM images for 1 ML nanoplatelets were obtained due to instrumental limitations and the instability of the sample under electron beams.

$CsPbBr_3$ nanocubes,[88] nanoplatelets between 1 and 4 lead bromide layers[97,104] and Cs_4PbBr_6[84] have been thoroughly described elsewhere and our results match literature properties.

We will describe the properties of $CsPb_2Br_5$, $PbBr_2$ nanocrystals and molecular lead halide species here in more detail, as we have found ambiguities in the literature regarding their characteristics. XRD patterns of $CsPb_2Br_5$ nanocrystals match well with the bulk diffraction pattern[105] (2.1C3). These nanocrystals usually have a clearly observable absorption peak around 320 nm, with onsets starting at 350 nm (2.1 B3). This matches data from reflectance spectra of bulk crystals.[105] While we observe photoluminescence from these species (See Figure A.1.3), it is similar to that of $CsPbBr_3$ species and could easily arise due to small impurities of perovskite cubes or plates in the sample, as has been indicated for the Cs_4PbBr_6 phase.[106] $PbBr_2$ nanocrystals, as determined by XRD (2.1C2), have a variable absorption onset, occurring between 345 and 370 nm with peaks or shoulders between 330 and 350 nm ((2.1B2)). This is close to the reflectance spectrum observed for $PbBr_2$

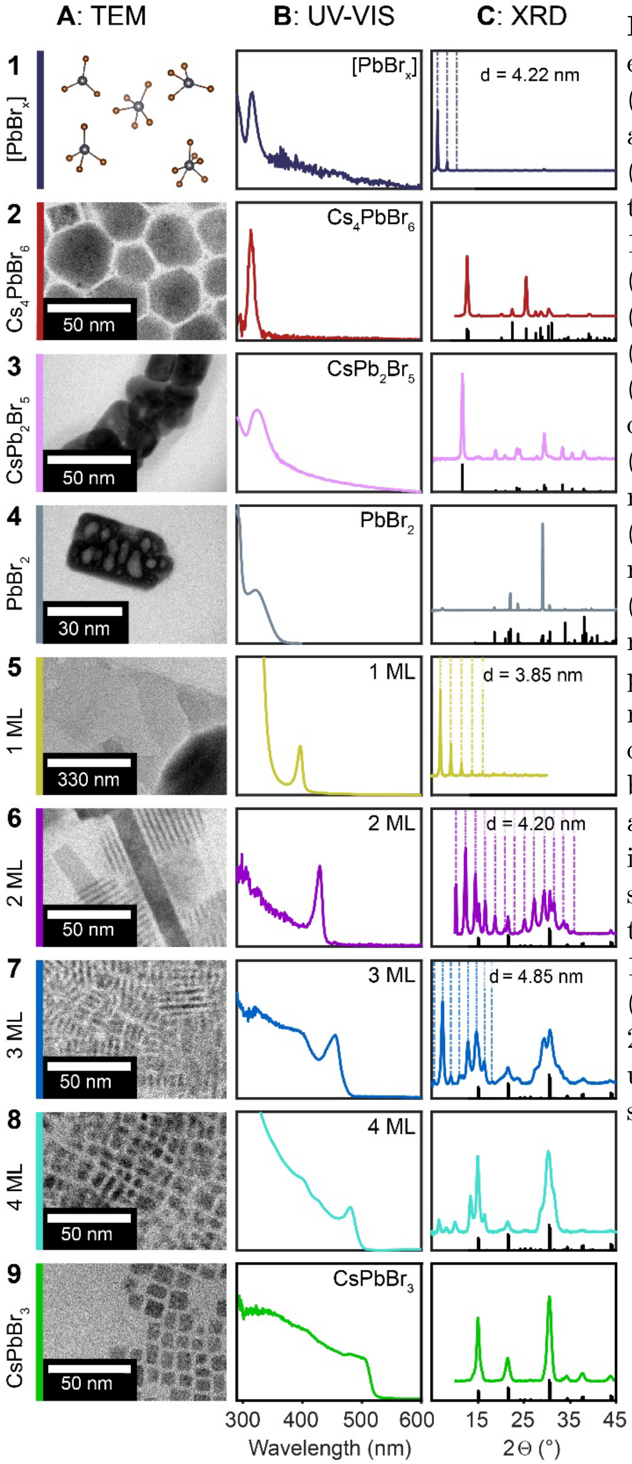

Figure 2.1: Transmission electron microscopy images (A), absorption spectra (B), and powder X-ray diffraction (C) of the nine species synthesized in this work: (row 1) $[PbBr_x]^{+2-x}$ complexes, (2) Cs_4PbBr_6 nanocrystals, (3) $CsPb_2Br_5$ nanocrystals, (3) $PbBr_2$ nanocrystals, (5) OLA_2PbBr_4 nanosheets or 1 monolayer plates (1 ML), (6) $OLA_2CsPb_2Br_7$ nanoplatelets or 2 layer plates (2 ML), (7) $OLA_2Cs_2Pb_3Br_{10}$ nanoplatelets or 3 layer plates (3 ML), (8) $OLA_2Cs_3Pb_4Br_{13}$ nanoplatelets or 4 layer plates (4 ML), (9) $CsPbBr_3$ nanocubes. Vertical axes of (B) and (C) are in arbitrary units and represent absorbance and scattering intensity, respectively. Black sticks in (C) correspond to ICSD reference patterns 162158 (Cs_4PbBr_6), 254290, ($CsPb_2Br_5$), 202134 ($PbBr_2$), 243735 ($CsPbBr_3$). We were unable to image $[PbBr_x]^{+2-x}$ species under TEM (1 A).

in bulk,[107] and would suggest that nanocrystals observed ((2.1A2)) do not display strong quantum or dielectric confinement, unlike smaller structures others have prepared.[100,101]

Lead halide complex species can be made by employing a high molar ratio of OLA to Pb-OA of 10:1 and no Cs-OA. We observe an absorption peak at 313 nm in dodecane (2.1B1). The Emission spectrum shows a peak at 450 nm and a FWHM of 30 nm – this may be a fluorescence signal from the species itself (see Figure A.1.3). Some of this signal may also be present in the $PbBr_2$ sample. If dried, the lead halide species appears to assemble into a layered species, as determined by the characteristic stacking patterns (2.1C2). In previous publications, a lead halide species was reported as $[PbBr_3]$- with an absorption peak around 320 nm in polar solvents.[108] The peak we observe in non-polar solvents overlaps almost exactly with the peak of Cs_4PbBr_6, which may lead to confusion of the two species. To distinguish the two spectra, it is necessary to consider the line shape of the two peaks: Cs_4PbBr_6 has a sharper peak with a FWHM of 10 nm centered around 315 nm, with an onset only starting at 340 nm, while the lead halide complex has broader peak with a FWHM of 15 nm centered on 313 nm and an onset starting around 350 nm. Further research is needed to prove and characterize the presence of any particular complex in apolar solvents. Until such research is performed, we believe it is more appropriate to use the terms $[PbBr_x]$ or lead bromide complexes when discussing these species. (A.1.2). Further investigation the topic of lead halide complexes in more detail is discussed in Chapter 4.

We can confirm the identity of nanocrystalline species through X-ray diffraction patterns, further corroborate these patterns with high-resolution TEM (Figure A.1.1) and provide a match with their optical absorbance spectra. Given that we observe and differentiate nine species that can be made in this synthesis, we show next how we can go about using this information to understand transitions between different areas of synthetic space.

Transitions Between 2 and 3 Monolayer Nanoplates

A useful example is the transition from 2 to 3 monolayer (ML) platelets 2.2. The synthesis outcomes can be observed by the characteristic peaks in optical density at 431 nm (2 ML) and 455 nm (3 ML). Increasing the concentrations of lead oleate and cesium oleate in the synthesis solution will drive a transition from the creation of 2 to 3 layer platelets in this reaction, which can be deduced from the increase in optical density of the peak at 455 nm and decrease of the peak at 431 nm upon increasing reagent concentration. Oleylamine has the opposite effect: increasing concentration leads to higher 2 ML peaks and decreasing concentration leads first to higher 3 ML peaks and then a decrease in the 3 ML peak with a corresponding increase of a 4 ML peak at 473 nm. What is unexpected is the abruptness of this transition: starting at the lower lead and cesium regime or at higher oleylamine regimes, several reactions produce almost no discernible 3 ML peak. There is a sudden change to conditions producing mostly 3 ML plates, leading to a complete reversal of majority products by the variation of only 10-20 % in the amount of oleylamine and lead, or 50% in the amount of cesium. We also observe that the synthesis becomes more variable close to these transition points (2.3), with some reactions at ostensibly the same conditions producing more 2-layer plates and

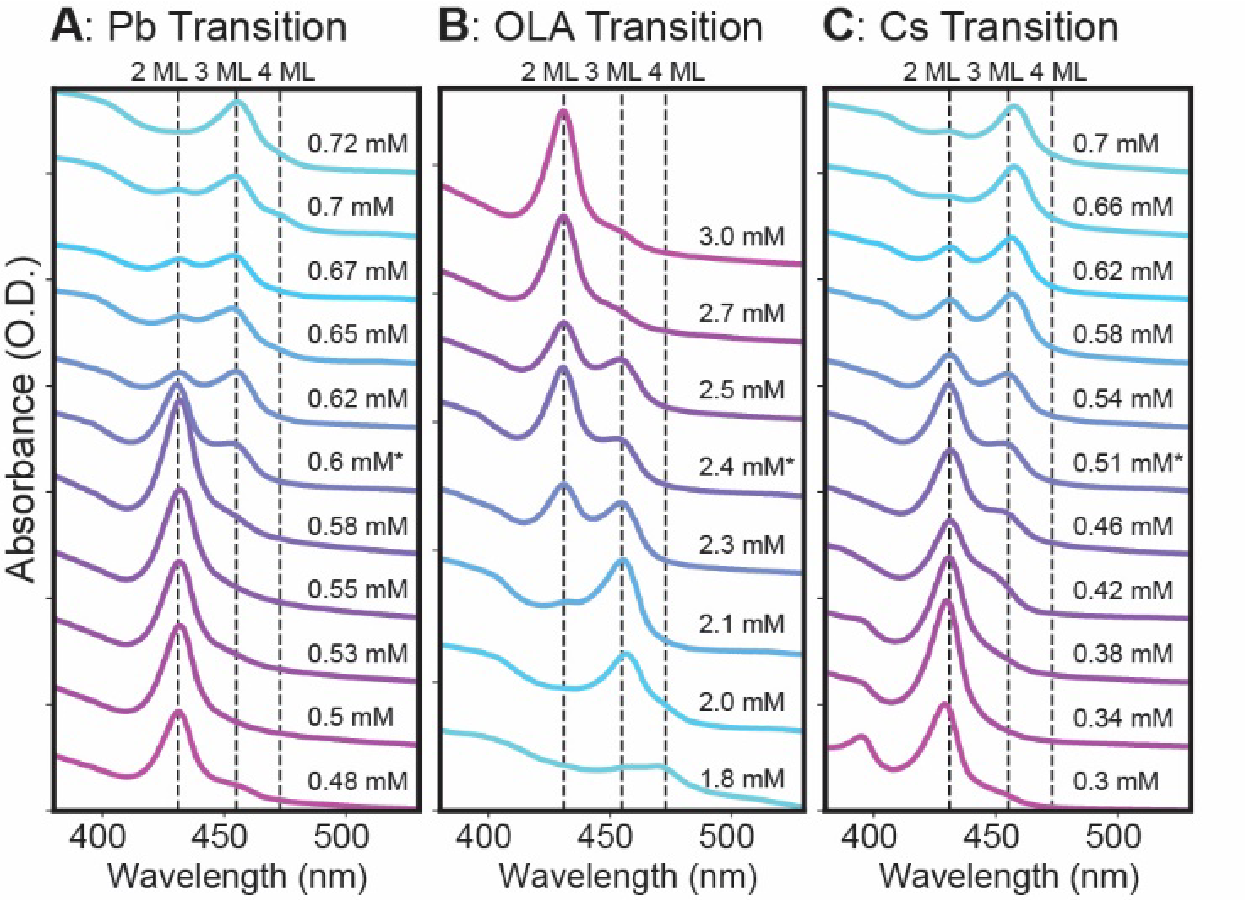

Figure 2.2: Absorption spectra of as-synthesized solutions of 2 ML and 3 ML nanoplatelets describing a transition point at a Pb-OA concentration ([Pb]) of 0.6 mM, oleylamine concentration ([OLA]) of 2.4 mM, Cs-OA concentration ([Cs]) of 0.51 mM, depending on changes in A) Pb-OA concentration ([OLA] = 2.4 mM, [Cs] = 0.51 mM) B) oleylamine concentration ([Pb] = 0.6 mM, [Cs] = 0.51 mM) and C) Cs-OA concentration ([Pb] = 0.6 mM, [OLA] = 2.4 mM)

other reactions forming mostly 3 layer plates. If this system is non-linear, minute variations in the synthesis conditions due to small errors in addition, dilution or temperature control would strongly influence a reaction close to a critical point and lead to large experimentally observed errors. Reactions performed at conditions that are further from a critical point would be more reproducible. Any effort to create useful maps of the synthetic space must grapple with the shape of this terrain, with areas of relative stability bounded by regions of abrupt change and high variability.

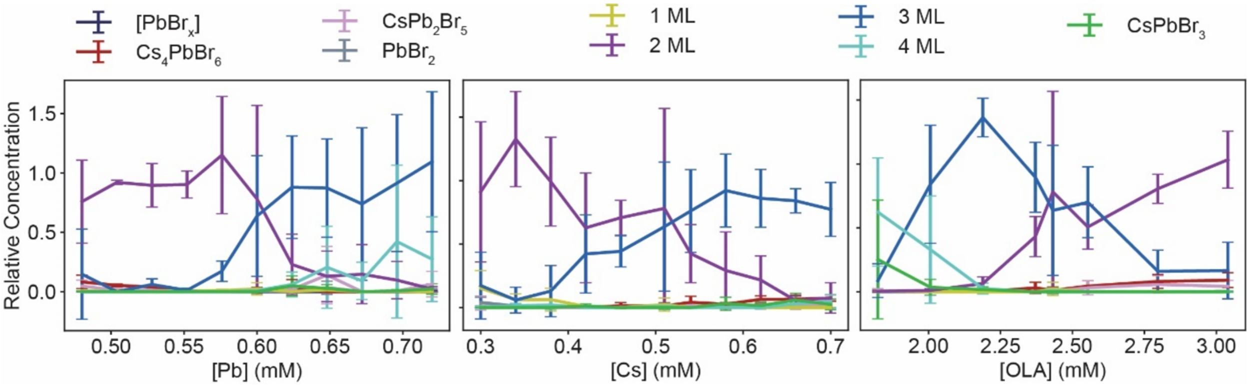

Figure 2.3: Spectral purity / relative concentrations vs amounts of reagents added for reactions crossing close to the transition point shown in 2.2(0.51 mM Cs, 0.6 mM Pb and 2.4 mM OLA). Error bars are the standard deviation of reactions performed in triplicate on the same plate. While all colors are shown, only 2 ML (purple), 3 ML (blue) and 4 ML (turquoise) have major contributions).

Spectral Deconvolution

To systematically investigate the synthetic parameters that result in the formation of the 9 different species, we used our high-throughput workflow to synthesize 2337 samples and measure their absorption spectra. For this large number of reactions, it was crucial to develop an automated method that allowed us to consistently determine the type and approximate amount of each chemical species in the synthesis reaction from absorbance spectra 2.4. Our method treats each measured spectrum as a linear combination of reference spectra for each species (2.4C). We used a least absolute shrinkage and selection operator (LASSO[109,110]) constrained to positive values to add penalties for relying on too many of the reference spectra to fit a measured spectrum, which gave consistent results and restricted the spectra chosen to the majority species in a sample (2.4 D).

As can be seen in Figure A.1.3, the nanoplatelets and nanocubes have similar emission features as those shown in previous reports.[88,104] The one exception is the second sample for 2 ML plates, in which a second peak arises which looks spectrally very similar to the one for the 3 ML plates. This is likely due to a small contamination of 3 ML plates in the sample, which is not unlikely given the long red tail in the absorption (Figure 2.2 C). However, it does

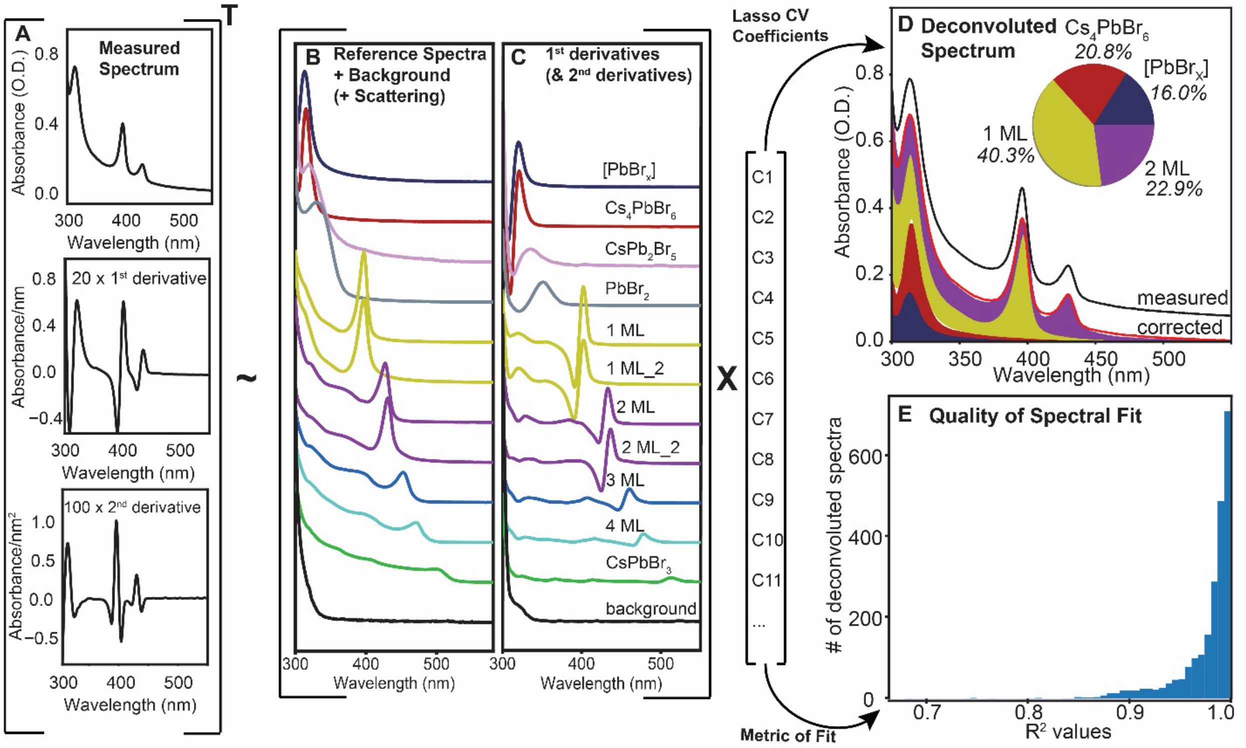

Figure 2.4: Vector representation of the spectral deconvolution process. An experimentally measured spectrum and its first and second derivatives (A) are deconvoluted using a LASSO algorithm into a linear combination of 11 reference spectra (B) and their derivatives (C). Deconvoluted example spectrum (D), showing fractional contributions of [$PbBr_x$], Cs_4PbBr_6, 1 and 2 ML. (E) Distribution of R2 values for the fits of the 2337 spectra measured for this work.

illustrate one advantage that absorption spectra have over emission spectra for assigning sample identity: due to inner filter effects and different emission efficiencies, this sample would seem like a 50-50 mixture of 2 and 3 ML plates based on emission data, whereas based on absorption it is clear that an overwhelming majority of the sample is composed of 2 ML plates. Fitting values only to the absorption spectra resulted in assignment of species which had no matching peaks in the measured spectrum, and frequently overestimated the amount of $CsPbBr_3$ and larger platelets. Using the first and second derivatives of the absorbance as additional features increased the sensitivity to peak position. The linear combination of reference spectra fit the measured spectra well, with an average R^2 value of 0.976; over 80 % of the spectra have an R^2 value above 0.95 (Figure 2.4 E). Based on error simulations for this method, we estimate that the fractions of species calculated based on absorbance should be accurate to within 2-3 % of the measured value (2.13), unless the fraction itself is below 5 % (see 2.4 for a discussion of simulated and experimental errors). Deconvolution of spectra containing simulated 4 ML and $CsPbBr_3$ absorption exhibited higher errors, with significant underestimates once the fraction of 4 ML or $CsPbBr_3$ was lower than 10 % A.1.5 This error is significantly smaller than the average experimentally measured variation of 10-25 % absolute error in the measured fractions for repeated nanocrystal synthesis under the same experimental conditions. Larger experimental variations are observed at for a small number of individual points A.1.7. Overall, this high-throughput spectral deconvolution allows us to consistently and reproducibly determine the relative amount of the species produced by a synthesis.

High-Throughput Synthesis Map

Having established a method to quantify the distribution of species produced by Cs-Pb-Br nanocrystal reactions, we mapped the formation of those species over a range of Cs-OA, Pb-OA, and OLA concentrations in order to gain a holistic view of synthetic space. Other maps of other variables can be found in section 3 of the SI. We performed synthesis experiments in a factorial expansion across 9 concentrations of cesium precursor (0.0-0.8 mM, in steps of 0.1 mM), 9 concentrations of lead precursor (0.13 to 1.24 mM, 0.12 mM steps) and 6 concentrations of oleylamine (1.2, 1.8, 2.4, 3.0, 3.6 and 4.9 mM) for a total of 486 reactions. Reactions (500 µL) were performed at 30° C, with a concentration of 4.8 mM oleic acid and 12.2 mM benzoyl bromide added to each solution. We construct the synthesis map in 2.5 from the resulting absorption spectra (as an example, see 2.9 using spectral deconvolution to determine the fraction of each species at each reaction condition (2.10). Colors correspond to different products, while contour levels (50 %, 70 % and 90 %) indicate levels of purity by spectral analysis. To determine the new insight we can extract from this high-throughput dataset, we first consider a broad overview of the map. All nine species shown in Figure 2.1 can be found at some point in this dataset. In fact, we only identified the $PbBr_2$, $[PbBr_x]$ and $CsPb_2Br_5$ species after analyzing spectra that did not fit well during deconvolution. Additionally, the observation of areas of the same color connecting in the map means that similar conditions usually create similar products, which is sensible chemically and supports our assessment that the analysis is accurately detecting the relative amount of different species. This is especially important in cases where the species are spectrally similar, as is the case between lead bromide complexes (dark grey) and Cs_4PbBr_6 (red). The cases in which clear islands appear, such as the 3 ML (blue) island in the 2 ML (purple) cluster in Figure 2.5 D appear correct in their spectral assignment, are caused by single reactions and are most likely experimental outliers. Domains that persist over a range of variations are robustly identified, but the exact positions of boundaries should be treated with robust skepticism. Future studies with greater precision of dispensing and higher map densities are also surely worth pursuing in order to carefully traverse the boundaries between the domains. Our best judgement is that the current experiments provide no evidence for magic numbers, or one island of a composition that is wholly surrounded by another composition. Overall, the map represents a portion of synthetic space containing all species we are analyzing and shows that those species cluster into areas with similar conditions.

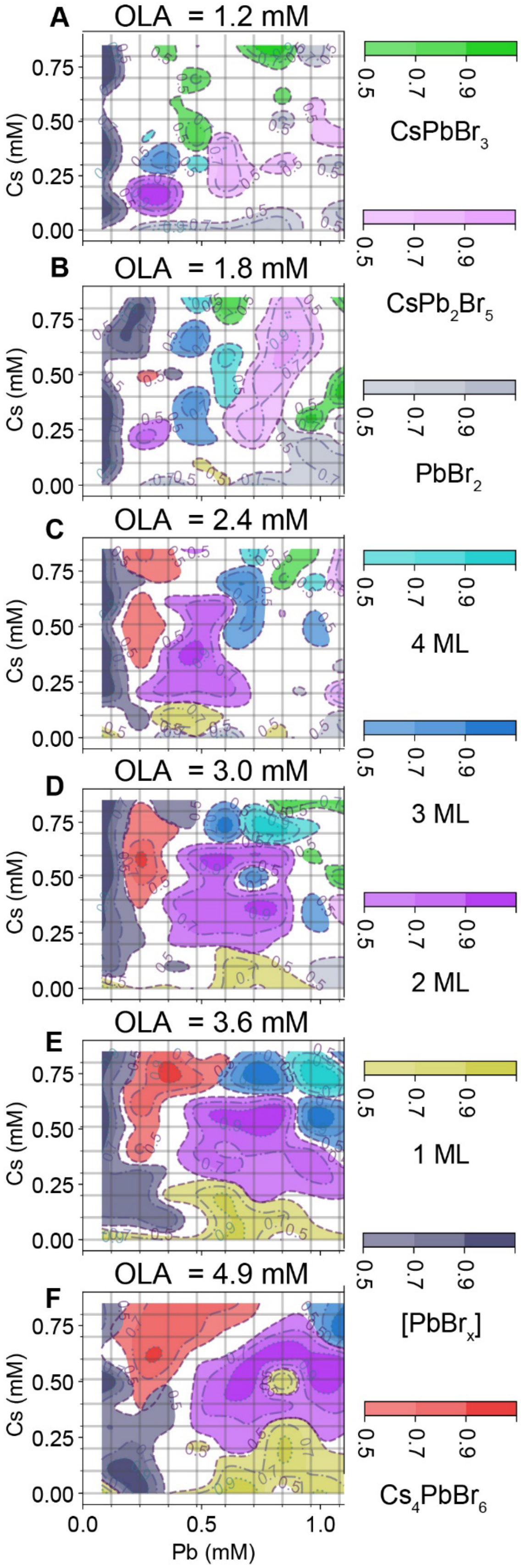

Figure 2.5: Map of majority species and level of spectral purity depending the concentration of cesium and lead at oleylamine concentrations of (A) 1.2 mM, (B) 1.8 mM, (C) 2.4 mM, (D) 3.0 mM, (E) 3.6 mM, and (F) 4.9 mM. Reactions were performed at the intersection of the grid lines; areas between are colored via cubic interpolation of all neighboring data points. Colored regions of the map indicate the majority species (species fraction ¿ 0.5), with contour shading defined by color scales on the right. White denotes no majority species.

Considering Potential Reactions based on Positions in Synthetic Space

. We now consider specific species and their position in synthetic space. We will use this information to learn how Cs, Pb and OLA precursor concentrations tune synthetic pathways and construct hypothesis of reaction pathways to test. The distribution of perovskite species is consistent with previous reports of Pb/OLA[95] ratios or Cs/OLA[92] ratios controlling the reaction outcome. Nanocrystals of lead-rich ($CsPb_2Br_5$) and lead-depleted (Cs_4PbBr_6) phases appear towards the right side (high Pb) and upper side (high Cs) of Figure 2.5, respectively, as would be expected from their stoichiometry. The role of OLA in the formation of Cs_4PbBr_6matches with that previously reported, with higher [OLA] leading to more Cs_4PbBr_6,[92] as does the role of the Cs/Pb ratio.[96] The synthesis of $CsPb_2Br_5$ has not been explored similarly to date. We observe that nanocrystals with $CsPb_2Br_5$ phase form at high [Pb] and low [Cs], which would be expected based on the lead-rich stoichiometry. The formation of $CsPb_2Br_5$ at lower [OLA] is unexpected, however. As there is no obvious incorporation of oleylamine into either Cs_4PbBr_6 or $CsPb_2Br_5$ or clear surface stabilization, this suggests that oleylamine is likely important in the formation processes. We next consider the areas of the map that contain the binary lead bromide species to understand how they fit into this synthetic space. Perhaps the most surprising result of this map is that at the lowest [Pb], there is always lead bromide complex present irrespective of the amount of Cs-OA in solution. With increasing amounts of oleylamine, the region occupied by the lead bromide complex expands to higher lead concentrations, except at high Cs concentrations where the Cs_4PbBr_6 phase will form. Regions containing $PbBr_2$ nanocrystals or OLA_2PbBr_4 nanosheets are confined mainly to the low [Cs] regime, as would be expected for binary lead bromide phases. In general, $PbBr_2$ is the major species at low levels of OLA while the nanosheets dominate at high [OLA]. The concentration of lead plays a role at intermediate [OLA], with higher concentrations of lead leading to formation of more $PbBr_2$. As the binary lead halide species occupy all of the synthetic space at the lowest inorganic component concentrations, it is quite likely that they play key roles in the formation process of all of the ternary compounds, as for the formation of nanocrystals we would need to pass through those areas of low inorganic component concentrations to achieve the higher concentrations required for crystallite nucleation. Considering the concept of passing through lower inorganic component concentrations to reach regions with higher inorganic component concentrations during synthesis, we examine which species are most often found next to each binary lead bromide species. $PbBr_2$ is adjacent to regions containing $CsPb_2Br_5$, and in most regions containing $CsPbBr_3$ at lower Cs concentrations. 1 ML are connected to $PbBr_2$ at higher OLA concentrations or lower Pb concentrations. These single layer plates are in turn almost always adjacent to bilayer plates at higher Cs concentrations. The lead bromide complex is found next to all perovskite phases, the Cs_4PbBr_6 phase and the monolayer plates at lower Pb concentrations, and adjacent to the Cs_4PbBr_6 at lower Cs concentrations. Multiple potential pathways towards product formation now become apparent, depending on whether products form based on direct nucleation from lead halide complexes, from transformation of the other lead halide species or through dissolution and reprecipitation. Moving to the interactions of the ternary phases, the set of 2-, 3- and 4-layer plates and nanocubes are lined up in that order along a series of increasing Cs or Pb values, or decreasing OLA values, which suggests a potential island nucleation mediated layer growth pathway of the plates as in II-VI nanocrystals. Larger plates and nanocubes are adjacent to the $CsPb_2Br_5$ phase at higher Pb values, and sometimes at lower Cs values, which could potentially be explained through transformations of the $CsPb_2Br_5$ and the $CsPbBr_3$ phases. Majority Cs_4PbBr_6 areas appear to be adjacent only to the 2 and 3 ML plates at lower Pb values, though there is some formation of Cs_4PbBr_6 at lower Pb values in areas containing any perovskite. Overall, the synthesis map suggests many possible reactions that we can group into multiple possible pathways towards formation of different products and nanocrystal transformation processes.

Testing Reaction Pathways through Chemical Transformations

While the adjacency of two species in synthetic space can help us construct hypothetical reaction pathways, it is not clear that the chemical transformation between the two species occurs - and if so whether it is reversible or irreversible. This is crucial to determine which of the potential pathways are relevant in nanocrystal transformation and formation reactions. To probe this directly, we used the map to find sets of two points in which the majority species changes by slightly varying the concentration of only one species. We then attempt to transform one of these species into the other by adding Cs-OA, OLA or Pb-OA after the reaction was initiated by halide precursor injection to see which of the possible reactions exist. By examining the reactions which exist, we can also understand which reactions are reversible due to the presence of forward and inverse reactions. Figure 2.6 A and B describe this process by showcasing four examples of chemical transformations. In Figure 2.6A, a solution containing $PbBr_2$ nanocrystals can be transformed into $CsPbBr_3$ by adding Cs-OA, or into a solution containing 1 ML plates by adding OLA. The two transformations have very similar results to the direct synthesis, suggesting that there is a reaction pathway from $PbBr_2$ to these species that is not much different to the formation in the synthesis reaction. In Figure 2.6 B, a solution containing 1 ML plates is transformed into $PbBr_2$ by adding Pb-OA or into a mixture of 2 ML plates by adding Cs-OA. The transformation into lead bromide appears facile, whereas the transformation into the nanoplates appears much more complicated. Compared to the initially synthesized sample, most of the 1 ML plate peak remains in the sample after Cs-OA addition, a small amount of 2 ML plates is formed, and no 3 ML plates appear at all. From this information, we can deduce that there is an equilibrium between $PbBr_2$ and 1 ML, a pathway from $PbBr_2$ to $CsPbBr_3$ and a partial reaction from 1 ML to 2 ML, whereas the reaction from 1 ML to 3 ML does not occur.

We examine the outcome of 149 transformation reactions, focusing on which interactions suggested from the map are real reactions. 2.6 C summarizes the outcomes of all reactions performed, allowing us to constrain possible formation and transformation sequences. For the binary lead bromide species, all forward and inverse transformations are possible through either addition of oleylamine or lead. Presence of forward and inverse reactions implies the

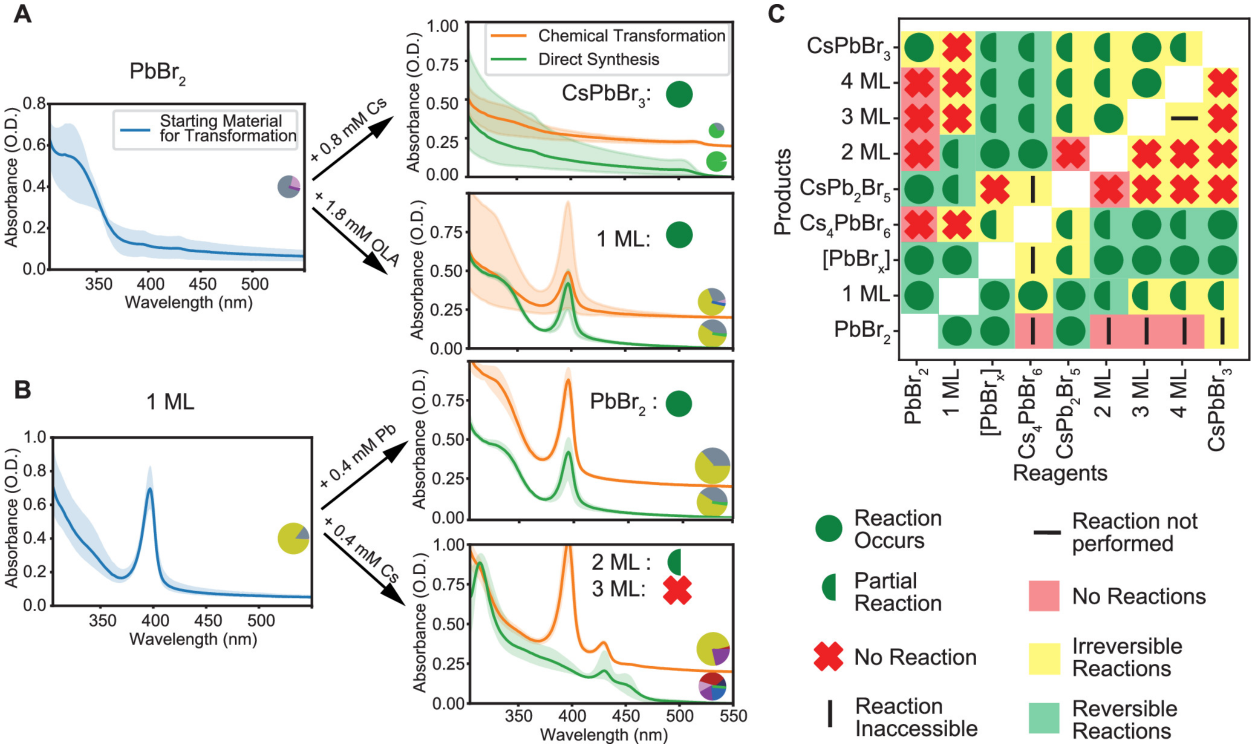

Figure 2.6: Chemical transformations between species in the Cs-Pb-Br reaction network. (A) Successful transformations of $PbBr_2$ nanocrystals (right) into $CsPbBr_3$ (upper left) through addition of 0.8 mM Cs-OA and into 1 ML nanosheets (lower left) through addition of 18 mM oleylamine. (B) Successful transformation of 1 ML (right) into a mixture of 1 ML and $PbBr_2$ nanocrystals through addition of 0.4 mM Pb-OA (upper left) and mixed results from a transformation into a mixture of 2 ML (partially successful) and 3 ML (unsuccessful) through addition of 0.4 mM Cs-OA. (C) Matrix classifying all pairs of transformations by observed outcome. Inaccessible reactions are transformations in which there is no possible single reagent route from the reagent species to the product species in the parameter space given by the map in 2.5. Reversible reactions correspond to both possible reactions being observed, irreversible reactions correspond to one of the two possible reactions observed.

existence of a reversible equilibrium between the lead halide nanocrystal, monolayer and complex species. As we remarked previously, the formation of nanocrystals likely proceeds through at least one of these binary lead halide phases. The equilibrium between the binary lead bromide species provides a platform that enables switching between different potential pathways depending on the synthesis conditions.

We now examine what reactions are possible when moving towards the ternary species by adding Cs-OA. $PbBr_2$ can be transformed to $CsPb_2Br_5$ and to large $CsPbBr_3$ crystals, but not to the 2-4 ML platelets or Cs_4PbBr_6. 1 ML platelets can only be partially transformed to 2 ML platelets, but not to larger platelets, cubes or the other ternary phases. As no cesium is present in the initial solution, it is not possible for 2 ML nuclei with a stoichiometry of $OLA_2CsPb_2Br_7$ to form before Cs injection. This may suggest that the strict limitation to Ostwald ripening growth of 2 D nanoplatelets through island nucleation mediated growth shown for II-VI semiconductors[32,111,112] may be relaxed in the $CsPbBr_3$ system and that growth in the confinement direction may occur, though it is likely to be a rare event. The only species accessible from the lead halide complex through adding Cs is Cs_4PbBr_6 at high OLA concentrations, which is confirmed by chemical transformation as well as an independent study published after this article was posted as a pre-print.[113] If additional lead is administered to a solution containing lead bromide complex in which some Cs is already present, full transformation to Cs_4PbBr_6 and 2 ML plates as well as partial transformation to larger perovskite products is observed. The partial transformation to larger perovskite products is intriguing: instead of forming one or two of the platelet phases as is observed in direct synthesis, adding lead to a solution containing lead bromide complex and cesium induces formation of all the perovskite species (2 ML, 3 ML, 4 ML plates and nanocubes) as well as the single monolayer plate in the same reaction solution. This suggests that the process of forming the nanoplatelets is changed when starting from a solution containing Cs and the lead halide complex, as opposed to a halide free solution. This observation has significant implications for the development of a holistic picture of the synthesis of cesium lead halide nanocrystals, as it suggests that lead bromide complexes are not the most direct intermediates on the way to formation of perovskite species.

Let us finally examine transformations among the ternary species to further elucidate growth and transformation reactions. It is possible to transform a thinner nanoplate into a thicker one or a nanocube by adding lead or cesium, but it is not possible to transform a thick nanoplate into a thin nanoplate. Instead, adding oleylamine to perovskite species results in the formation of lead halide complex, Cs_4PbBr_6 (as reported in a series of previous work[35,44]), and single layer nanosheets. Transformation into $PbBr_2$ or $CsPb_2Br_5$ also appears suppressed. The ubiquitous presence of lead halide complex in reactions in which OLA was added to the solution adds further credence to the dissolution-reprecipitation processes proposed for the transformation between perovskites and other ternary phases.[44,87] The Cs_4PbBr_6 phase appears to react quite similarly to the lead bromide complex concerning the reactions producing the perovskite phases, producing the entire array of perovskite species when lead is added, suggesting the possibility that the two phases may share reaction pathways. However, it does not appear to have a ready transformation towards $PbBr_2$, mainly due to its location on the opposite side of synthetic space.

Chemical Reaction Network

Integrating these observations into a diagram of cesium lead bromide nanoparticle formation leads us to 2.7. In our interpretation, the most important concept is the mutual equilibrium of lead halide species at the top of the diagram, with $PbBr_2$ nanocrystals, single monolayer plates and lead bromide complexes interconverting. This equilibrium is a uniquely determining factor in the reaction because of the different reactions each of the species may take when exposed to cesium: $PbBr_2$ reacts with cesium to form either nanocubes or $CsPb_2Br_5$, whereas the monolayer plate will react to form a 2 layer plate and the molecular complex will form Cs_4PbBr_6. The platelets appear to grow irreversibly one layer at a time, which could be explained both by island nucleation mediated layer growth in the confinement direction as suggested by the transformation of 1 ML to 2 ML plates or nucleation of larger cores and subsequent layer dependent Ostwald ripening as in II-VI nanoplatelets.[111] All phases can be decomposed into lead bromide complex, which can then react to Cs_4PbBr_6 and lead bromide monolayers and nanocrystals, enabling dissolution-reprecipitation processes for all transformations between cesium lead bromide nanocrystals.

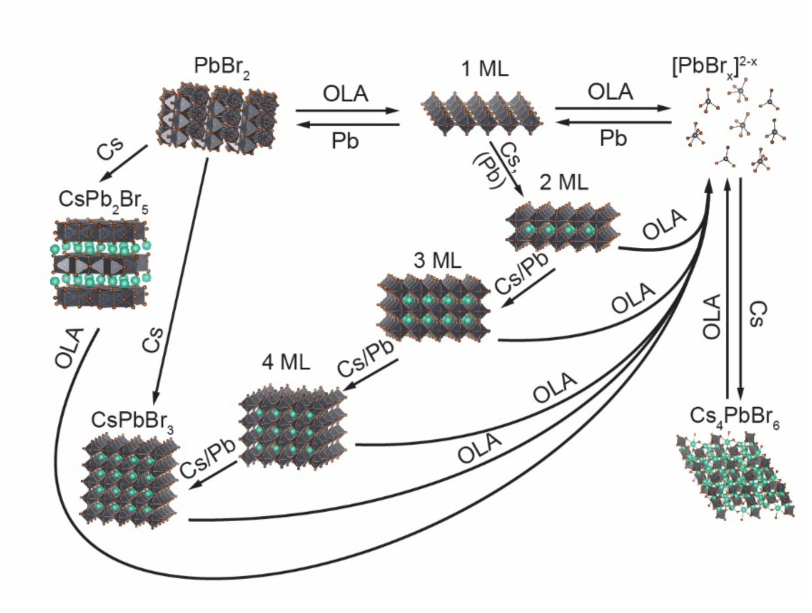

Figure 2.7: Diagram of reactions of $Cs_xPb_yBr_z$ nanocrystals.

Now that we have obtained an overall reaction diagram, let us examine what information we can learn from its structure. The connectivity of the reaction diagram suggests the existence of a multi-component reaction network as the basis of the $CsPbBr_3$ formation reaction. While not all the reactions shown here are reversible, the reaction network allows any species to be converted to any other species if the appropriate path through the network is taken. This property of a network is known as weak reversibility to mathematicians studying chemical reaction network theory.[114] To chemists, weak reversibility may offer an explanation for why certain reactions, such as the transformation of perovskite nanocrystals to Cs_4PbBr_6 or $CsPb_2Br_5$ can sometimes take days even though all crystals can be formed and dissolved rapidly at room temperature. The reactions that take longer must proceed over several intermediates, any of which might only be present in miniscule amounts, thus reducing the overall speed of transformation drastically even if each individual reaction is facile. Another important result of thinking of this synthesis in terms of a reaction network is allowing for non-linear changes in product amounts despite linear variations of the input: Critical points and non-linear transitions from one species to the next frequently arise when multiple reactions are coupled with each other, even if each reaction is linear. This can qualitatively explain the sudden transitions between chemical species, such as in the perovskite nanoplatelets. It also explains why it is usually quite easy to create 2 and 3 layer species in a phase-pure manner, while larger species are often found in mixtures. Overall, the reaction network structure provides concepts that help explain some of the peculiar chemical properties observed in this nanocrystal system, such as reversible ligand-induced phase transformation and critical points in the production of several products.

Integration with previous Results

We now consider the effect of the chemical reaction network on $CsPbBr_3$ synthesis. There are two formation pathways of $CsPbBr_3$ species, and they are modulated through an equilibrium of the intermediate lead bromide species. We discuss previously reported nanocrystal synthesis results to provide further context and to test the explanatory power of the chemical model developed. Due to the presence of lead, bromide and oleylammonium ions in solution, syntheses derived from the method of Protesescu et al.[88] may be considered a transformation from different binary lead halide species in solution to ternary phases upon addition of Cs. Our reaction network can explain the results of temperature control in this method, which induces formation of thin nanoplates at 90 °C,[104] thicker nanoplates at 130 °C, small nanocubes at 160 °C[88] and larger nanocrystals at 200 °C. We see similar effects shifting the areas where plates and cubes are formed at lower temperatures and with the different synthetic method we employ (Figure A.1.4). The transition from platelets to cubes is easy to explain in terms of relative amounts of $PbBr_2$ and OLA_2PbBr_4 in equilibrium leading to different reaction pathways and products. However, if there is truly a dynamic equilibrium between these two species, it should also influence the crystallite size, which is likely to influence the size of species after transformation. If conditions strongly favor one side of the equilibrium, crystals of that species are unlikely to ever dissolve fully and as a result, particle sizes are likely to be larger. In a balanced dynamic equilibrium state, we would expect rapid formation and dissolution of crystals of both species, leading to overall smaller crystallite sizes.

We consider here spectra of 1 ML and $PbBr_2$ species as evidence of the size dependence of those species on the concentration of oleylamine as proposed in the equilibrium argument. 1 ML plates synthesized at low Pb values have very strong quantum confinement in one dimension and only show a slight blueshift in the absorption peak at low concentrations of oleylamine (from 397 nm in the other samples to 395 nm at 1.8 mM and 392 at 1.2 mM, see Figure 2.8). $PbBr_2$ nanocrystals synthesized at high Pb values have a less defined absorption feature, but larger and more gradual shifts in their spectra, ranging almost 20 nm from the

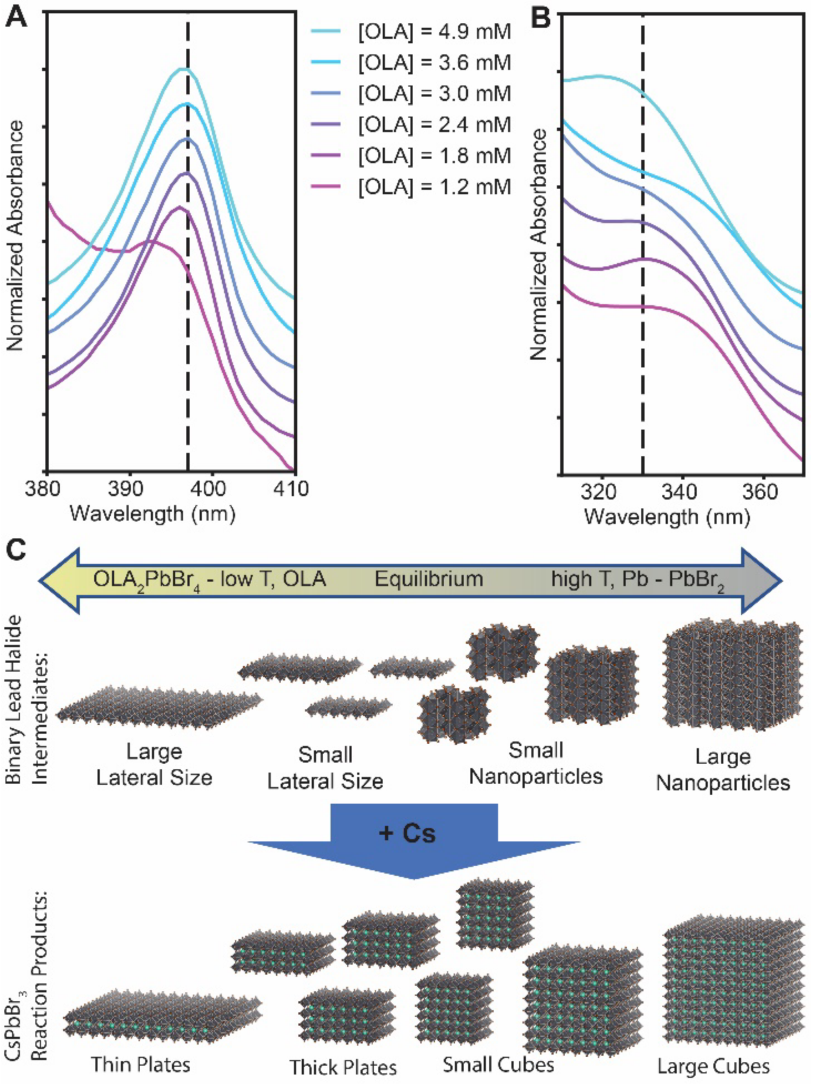

Figure 2.8: A) Spectra of OLA_2PbBr_4 nanosheets (1 ML plates) at varying concentrations of oleylamine. [Cs] = 0, [Pb] = 0.13 mM, [Br] =12.9 mM, [OA] = 5.4 mM. B) Spectra of $PbBr_2$ nanocrystals at varying concentrations of oleylamine. [Cs] = 0, [Pb] = 0.92 mM, [Br] =12.9 mM, [OA] = 9.2 mM. C) Scheme showing the proposed effect of the equilibrium between OLA_2PbBr_4 nanosheets and $PbBr_2$ nanocrystals on the size and shape of reaction intermediates and on perovskite nanoplates and cubes.

shoulder at 340 nm for an oleylamine concentration of 1.2 mM to the shoulder appearing around 320 nm for an oleylamine concentration of 4.9 mM.

The two lead halide species have different pathways towards perovskite species formation. 1 ML plates can substitute the native oleylammonium for Cs, which would then allow layer growth. The reverse surface substitution of oleylammonium for Cs perovskite species has been observed to strongly control the ligand environment.[37,50] $PbBr_2$ can convert to $CH_3NH_3PbBr_3$ through intercalation of CH3NH3+ ions and a subsequent phase change,[100,101] so we assume here that the transformation from $PbBr_2$ to $CsPbBr_3$ occurs through a similar mechanism. The size of precursor or reaction intermediate should also influence the size of species post transformation. For monolayer lead bromide, a larger crystal size means a larger lateral size, since without cesium, this layered compound is confined in one dimension. Research examining the growth of CdSe nanoplatelets[32] suggests that under conditions of layer-by-layer growth on an anisotropic nanocrystal, a larger lateral size would decrease growth in the confinement dimension. Large 1 ML nanosheets will likely grow into thin plates, whereas smaller nanosheets have a lower island nucleation barrier. Mixtures will predominantly occur between small cubes and thick plates with smaller lateral sizes. For $PbBr_2$, smaller crystal sizes before Cs intercalation would lead to smaller perovskite cubes, and larger crystals would lead to larger cubes.

Research from Almeida et al.[92] provides further evidence for the previous argument of larger lead bromide size under conditions favoring the lead bromide species, based on the observation of $PbBr_2$ precipitation at high temperatures. This is also observed in inverse temperature crystallization experiments in more polar solvents, though the intermediates at play are likely somewhat different due to coordination of solvent molecules. In nanocrystal systems, this precipitation can be suppressed by adding more oleylamine and oleic acid, as would be predicted by the equilibrium argument. In addition, co-formation of nanoplatelets at lower temperatures is often observed, which is easy to explain by the presence and reaction of two binary lead halide species through separate pathways at those temperatures. The acid base equilibrium described can also easily be incorporated into this analysis. Changing the ratio of oleylammonium to oleylamine changes the behaviour of the system because it is the oleylammonium species which is bound to and stabilizes the monolayer plates. Larger amounts of oleylammonium result in more growth of platelets instead of cubes. The type of amine ligand used can also provide some insight into this mechanism. As implied by the stoichiometry of the lead bromide monolayer, two amines per unit cell are required for the formation. If shorter, straighter chains of amines are used, achieving this packing is easier, so nanoplatelet formation is increased, while longer or more disordered amines decrease nanoplatelet formation.[91,95] Secondary amines which do not fit into the monolayer formula unit will completely suppress the formation of nanoplatelets, leading to highly monodisperse cubes.[93] The authors of that paper indeed suggest that there should be several pathways towards perovskite nanocrystal formation, as we prove here. In addition, dialkylamines appear to also suppress the transformation into Cs_4PbBr_6. All of these observations can be readily explained by the formation of only $PbBr_2$ nanocrystals as intermediates in this reaction. If the monolayer and lead bromide complex are almost entirely suppressed, the $PbBr_2$

size is determined exclusively by reaction kinetics and the supersaturation would be quite high, leading to a sudden burst nucleation and monodisperse cubes. Virtually no lead would leave the surface of the nanocrystals as a lead halide complex after synthesis, suppressing both Ostwald ripening and the transformation to Cs_4PbBr_6. To create phase and shape pure $CsPbBr_3$ nanocubes, the reaction with secondary amines is more effective precisely because it suppresses all the other pathways in this synthesis. However, it is not possible to perform this synthesis with the Cs injection technique reported by Protesescu et al.,[88] as the suppression of the equilibria means that solid $PbBr_2$ precursor will not dissolve into the other, more soluble lead halide species, as was also shown by Imran et al.[93] We thus find that our reaction diagram model has significant qualitative explanatory power and can connect to and help explain results observed with different synthetic methods, different precursors and different surfactants. Let us now examine some of the previous work examining kinetics and intermediates of portions of this process. One of the first proposed intermediates in this process was the formation of Pb0 seeds which could then act as nucleation sites for further attachment.[115] We believe that the particles seen may have been $PbBr_2$ nanocrystals, which we are able to observe through absorption, X-ray diffraction and electron microscopy and are also able to transform them into $CsPbBr_3$, but not into perovskite nanoplates. Similar phase transformation experiments from binary lead halide nanocrystals have been successfully demonstrated for methylammonium lead bromide and iodide.[100,101] We agree with the assessment that the two-dimensional OLA_2PbBr_4 phase plays a key role in the formation of platelets, as suggested by Imran et al.[93] and demonstrated here. through suppression of the platelet pathway with secondary amines. This pathway is determined by kinetics, especially if the benzoyl bromide synthesis route is taken, as shown by the irreversibility of the platelet growth reaction. While we were not able to track the formation of CsBr during the formation of nanocrystals to corroborate evidence from Wen et al. of a $CsPbBr_3$ formation path that advances through CsBr and Cs_4PbBr_6[99,108] this path can be incorporated into our model through the transformation of CsBr to Cs_4PbBr_6, both of which can then act as Cs reservoirs in the reaction pathways that we demonstrated, which might help explain the range of different sizes of perovskite species produced by slow, continuous nucleation of perovskite species upon addition of lead oleate to lead halide complex or Cs_4PbBr_6. This last argument may help stress the point that this reaction diagram is only complete in the Cs-Pb-Br system with respect to reactions we can observe – other reactions may play a role and could help expand this diagram further in the future, or adapt it for use in other lead halide perovskite systems. We thus show that the model we have built allows us to transfer knowledge from our synthesis study to other methods as well as explaining additional properties such as size control that were initially not examined, demonstrating the qualitative explanatory power of our results. We believe that expanding the knowledge of dynamic processes in this complicated nanocrystal system provides a new frontier for increasing and refining our understanding of nanocrystal formation and transformation reactions.

2.3 Conclusion

We use quantitative and qualitative analysis of high-throughput synthesis data to determine a cohesive chemical reaction network for lead halide and cesium lead halide nanocrystals. This is accomplished through combining factorial exploration of synthesis space and an automated method for deconvoluting absorption spectra to create maps and transformations. We find that this nanocrystal reaction network is weakly reversible, which helps explain the equilibria observed between nanocrystal species of different phases. The reaction is largely determined by an equilibrium between lead bromide nanocrystals, monolayers, and complexes. We examine previously published experiments through the lens of our model and find that our reaction network has substantial qualitative explanatory power. This work can offer a cohesive understanding of the formation and transformation reactions of cesium lead halide nanocrystals. Furthermore, our combination of quantitative mapping and qualitative transformation experiments allows us to gain a holistic view of the reaction that is helpful for developing understanding. The work presented here also suggests that further combinations of high throughput tools with data science approaches can be productive in deciphering reaction networks that govern the synthesis of nanomaterials. We believe this approach could be transferred to other complex chemical systems where an interplay of kinetic and thermodynamic factors complicates the outcomes.

Since the publication of this work and the associated dataset, there has been significant exchange with other scientists, leading to multiple collaborations. Based on the high-quality 2 ML plates produced here, a collaboration with the Manna group at the Italian Institute for Technology using X-Ray diffraction peaks as an interferometry method showed that the assemblies of 2 ML plates formed during drop-casting approach single-crystal quality.[116] Using emission data from the high-throughput dataset, the Bekenstein group has investigated the changes in Stokes-shift as a function of perovskite nanoplate size and found that while the Stokes shift increases with increasing perovskite nanocube quantum confinement, the Stokes shift will decrease with increasing 1D confinement, i.e. decreasing plate thickness, of perovskite nanoplatelets. Ongoing work in the Alivisatos group with Ethan Curling uses relative quantum yield data extracted from the dataset to probe the changes in quantum yield as a function of bromide concentration across multiple perovskite products. Initial work with the Sutter-Fella group demonstrated that the deconvolution algorithm could be utilized successfully to determine the ratios of different species from *in-situ* absorption data of thin-film double perovskite processing. Finally, the dataset was utilized twice in a research class teaching first-year undergraduates how to gain scientific insights from large datasets in nanoscale materials chemistry.[117]

2.4 Experimental

Synthesis

Materials

Cesium acetate (99%), hexane (mixed isomers, 98 %) and ethyl acetate ($\geq$ 99.5 %) were purchased from Fisher Scientific. Lead(II) acetate trihydrate ($\geq$ 99.5 %), benzoyl bromide (97 %), oleic acid (technical grade, 90 %), oleylamine (technical grade, 70 %) and dodecane (99 %) were purchased from Sigma-Aldrich. All chemicals were obtained from commercial suppliers and used without further purification.

Cesium and Lead Oleate solutions

Solutions of cesium (I) oleate (Cs-OA) and lead (II) oleate (Pb-OA) were prepared similar to a previous report.[118] 192 mg (1 mmol) of cesium acetate were placed into a 4 mL glass vial with stir bar, and 1 mL of Oleic Acid was added. For lead oleate solutions, 379 mg (1 mmol) lead acetate were placed into a 4 mL glass vial with stir bar, and 1.5 mL of Oleic Acid was added. The mixtures were stirred for 3 hours at 100 °C on a hot plate and used without further purification. Mixtures were briefly reheated before synthesis to ensure full mixing of precursors.

Manual Synthesis of phase-pure cesium lead bromide species

In Collaboration with Xingzhi Wang and Xiao Huang

Manual synthesis of phase-pure cesium lead bromide species was carried out using reaction conditions as noted in 2.1, in a method derived from the synthesis reported by Imran et al..[103] In each reaction, all reagents except benzoyl bromide were dissolved in the solvent and stirred. Benzoyl bromide was then injected to the solution to start the reaction - either pure, or as a 1.1 mM solution in hexane, as noted. To make the reactions easier to purify, reaction solvent was changed from dodecane to hexanes except where otherwise noted, and concentrations of all reagents were increased by about a factor of 10 from similar high-throughput synthesis.

Purification of phase-pure cesium lead bromide species

In Collaboration with Xingzhi Wang and Xiao Huang

$PbBr_x$ Reaction mixture was reacted for about 2 min to form a cloudy suspension. Solid products were collected by centrifugation (10 g, 2 min) and resuspended in 1 mL dodecane. Cs_4PbBr_6 Reaction mixture was reacted for about 1 min. To collect products, 1 mL ethyl acetate was added to form a cloudy suspension. Solid products were collected by centrifugation (10 g, 2 min) and resuspended in 1 mL hexanes. $PbBr_2$ Reaction mixture was reacted for about 15 minutes to form a slightly cloudy suspension.Supernatant was collected by centrifugation (10 g, 10 min). To collect solid products, 5 mL ethyl acetate was added to supernatant to from cloudy mixture. The mixture was centrifuged (10 g, 10 min) to collect precipitate. To resuspend product, 3 mL of 53 mM OA in hexane was added. Supernatant was collected by centrifugation (8 g, 5 min) and resuspension. $CsPb_2Br_5$ Reaction mixture was reacted for about 5 min to form a cloudy suspension. Solid products were collected by centrifugation (7.5 g, 1 min) and resuspended in 1 mL hexanes to form a cloudy sus-

Species	Temperature	Solvent	OLA (mM)	OA (mM)	Cs-OA (mM)	Pb-OA (mM)	Total OA (mM)	Benzoyl Br (µL)
$PbBr_x$	RT	dodecane	4.9	4.8	0	0.27	9.2	12 (1.1 mM)
Cs_4PbBr_6	100 °C	dodecane	91	80	80	20	429	10
$PbBr_2$	RT	hexanes	21	7.5	0	6.7	112	15
$CsPb_2Br_5$	RT	hexanes	1.8	4.8	0.50	0.93	11	12 (1.1 mM)
1 ML	RT	hexanes	18	22	0	6.7	112	15
2 ML	100 °C	dodecane	182	80	10	20	207	10
3 ML	RT	hexanes	30	48	5.0	8	102	120 (1.1 mM)
4 ML	RT	hexanes	30	48	7.0	11	121	120 (1.1 mM)
$CsPbBr_3$	RT	hexanes	18	48	6.0	6.7	99	120 (1.1 mM)

Table 2.1: Reaction conditions for phase pure species observed in high-throughput synthesis in Figure 2.1

pension. 1 ML nanoplatelets Reaction mixture was reacted for about 2 minutes to form a cloudy suspension. Solid products were collected by centrifugation (10 g, 10 min). To resuspend product, 3 mL of 100 mM OA and 46 mM OLA in hexane was added. The mixture was sonicated for 30 minutes, then centrifuged (10 g 10 min) to collect supernatant. 2 ML nanoplatelets Reaction mixture was reacted for about 1 min. To collect products, 1 mL ethyl acetate was added to form a cloudy suspension. Solid products were collected by centrifugation (10 g, 2 min) and resuspended in 1 mL hexanes. 3 ML nanoplatelets Reaction mixture was reacted for about 2 min. Solid side products were removed by centrifugation (10 g, 2 min). Solvent was depleted by N2 flow until a cloudy suspension was formed, to which about 1 mL ethyl acetate was added. Solid products were collected by centrifugation (10 g, 2 min) and resuspend in 1 mL hexanes. The resulting solution was centrifuged (7.5 g, 1 min) to remove side products. 4 ML nanoplatelets Reaction mixture was reacted for about 2 min. Solid side products were removed by centrifugation (10 g, 2 min). Solvent was depleted by N2 flow until a cloudy suspension was formed, to which about 1 mL ethyl acetate was added. Solid products were collected by centrifugation (10 g, 2 min) and resuspend in 1 mL hexanes. The resulting solution was diluted 10x in ethyl acetate. Side products were then removed by centrifugation (10 g, 2 min). $CsPbBr_3$ nanocubes Reaction mixture was reacted for about 2 min. Solid side products were removed by centrifugation (10 g, 2 min). Solvent was depleted by N2 flow until a cloudy suspension was formed, to which about 1 mL ethyl acetate was added. Solid products were collected by centrifugation (10 g, 2 min) and resuspend in 1 mL hexanes. The resulting solution was centrifuged (7.5 g, 1 min) to remove side products.

High-Throughput Synthesis

For high-throughput synthesis, dodecane solutions of cesium oleate (200 x diluted from a Cs-OA stock solution), lead oleate (200 x diluted from a Pb-OA stock solution), benzoyl bromide (80 x diluted - except where noted otherwise), oleylamine (100 x diluted) and oleic acid (80 x diluted) were freshly prepared for every run. Dodecane was chosen as a solvent because of its high boiling point to prevent evaporation during the reaction and observation, as well as its high optical transparency. Using a Hamilton NIMBUS4 Microlab liquid handling robot, dodecane, oleylamine, lead oleate, oleic acid and cesium oleate solutions were added in varying proportions to a 96 well plate equipped with single-use 1 mL glass vials. The entire plate was heated to the reaction temperature while shaking at 300 rpm and kept at the reaction temperature for 800 s. Under continued shaking, benzoyl bromide solution was added to each vial, for a final reaction volume of 500 µL. This addition sequence was typically performed within 600 s. The plate was kept at the reaction temperature and shaken for another 600 s after the addition.

High-Throughput Postsynthetic Transformations

The addition sequence for post synthetic transformation reactions starts in the same fashion as the other high-throughput experiments. After waiting for 600 s upon addition of benzoyl bromide, varying amounts of cesium oleate, lead oleate or oleylamine solution were added while shaking, up to a final reaction volume of 500 µL. Upon addition of the post-synthetic reagents, the reaction plate was shaken for another 600 s before transferal to the microplate for absorption measurements. For every post-synthetic reaction, six vials were prepared with the initial amount of reagents, and three vials were prepared with the final amount of reagents. In three of the six first vials, the difference between initial and final reagent amounts was added after the addition of benzoyl bromide solution, the other three were kept as a reference for the starting material.

Characterization

Absorption Spectroscopy

In Collaboration with Xingzhi Wang and Xiao Huang

UV-Vis absorption spectra of the cesium lead bromide species were recorded using a Shimadzu UV-3600 double beam spectrometer. Samples were prepared by diluting stock solutions of samples by a factor of 50 in hexanes. For each measurement, a blank spectrum was subtracted from the signal as background.

Photoluminescence Spectroscopy

In Collaboration with Xingzhi Wang

Photoluminescence emission and excitation spectra of $CsPbBr_3$ cubes, 4 ML and 3 ML nanoplatelets were recorded by an Edinburgh FLS 980 Spectrometer. The sample preparation procedures were the same as those for UV-Vis absorption spectrometry.

Powder X-ray diffraction (PXRD)

In Collaboration with Xingzhi Wang and Xiao Huang

XRD patterns of NCs were acquired using a Bruker D2 Phaser X-ray diffractometer equipped with a Cu Kα of 1.5445 Åwavelength. Samples were prepared by drop-casting 100 µL stock solutions of NCs onto a silicon substrate. Samples were dried under air flow prior to measurements.

Transmission electron microscopy (TEM)

In Collaboration with Xingzhi Wang and Xiao Huang

TEM images of the cesium lead bromide species were acquired using a FEI Tecnai T20 transmission electron microscope equipped with a Gatan RIO16IS camera and a LaB6 filament. All images were recorded under 200 kV accelerating voltage. Samples were prepared by dropcasting about 10 µL 1000 x diluted stock solutions onto a carbon support with 400 copper mesh. Samples were dried under ambient conditions prior to imaging. High-resolution TEM images were taken under identical conditions.

High-throughput absorption and emission spectra

From a 96-well plate reaction, 30 µL of each 500 µL final reaction solution were removed, diluted with 270 µL dodecane and placed into a 96-well Hellma quartz microreader plate. A Biotek Synergy 4 microplate reader was used to evaluate the reaction solutions. An automatic calibration was carried out before each plate was measured, then absorption spectra were recorded from 250 to 700 nm in 1 nm increments with a single reading per data point, while emission spectra were recorded from 400 to 550 nm in 1 nm increments with an excitation wavelength of 330 nm, with a detector sensitivity of 70 and a single reading per data point.

Data Analysis

Spectral Processing

Spectra and reagent amounts were loaded into a pandas dataframe.[119] Spectra that had low absorbance at 250 nm (¡ 2.5 O.D.) were uniformly discarded, as low absorption in this region indicated a lack of benzoyl bromide addition, except for solutions created with low concentration Br stock solutions. Absorption spectra for references 2.4 B were chosen based on their visual similarity to spectra of phase-pure compounds synthesized by hand (Figure 2.1), and a single power scattering line (with the power constrained between -4 and 0) was fitted to the 550-700 nm region using the $curve_fit$ algorithm and subtracted from the spectrum. Reference spectra of perovskite species were normalized to the optical density at 310 nm, and other materials were scaled to the same order of magnitude. We expect the absorption cross section at this wavelength to be mainly dominated by a transition between Pb s and p orbitals under the influence of a bromide coordination environment which should be roughly similar for all of the materials examined here. In addition, one spectrum of background absorption from a vial containing no discernible products as well as scattering lines corresponding to different negative integer power dependencies on the wavelength were added to the references to emulate multiple scattering length scales from the Rayleigh to Mie limits.

Spectral Deconvolution

First and second derivatives of every spectrum with respect to wavelength were calculated after smoothing using a Savitzky-Golay filter[120] as implemented in scipy[121] with a window length of 21 data points and a 4th order polynomial. As the numerical values of the derivatives are smaller than the values of the absorption, the first derivative was weighted 20 times higher and the second derivative was weighted 100 times higher than the original spectrum to yield numerically similar and uniformly increased numbers. A cross-validating LASSO algorithm, LassoCV[53] was used to find the coefficients of best cross-validated fit of the collection of reference spectra and their associated derivatives to every single spectrum and its associated derivatives 2.4(A), assigning a penalty value for using reference spectra based on cross validation. These coefficients correspond approximately to the concentration of the respective reference species in the reaction solution, up to a constant extinction coefficient. Fractions of coefficients as well as an R^2 parameter of fit, the final penalty value and the number of iterations were extracted for every spectrum.

Map Construction Example

For our main map 2.5, we wanted to show the raw absorption data and showcase how the data analysis process in going from measured absorption data to map proceeded. In 2.9, we show all 81 spectra that go into a single panel of the map (a single concentration of oleylamine). The spectra are split into 9 stacked plots by the amount of lead added to each reaction, with 9 spectra in each stacked plot ordered based on the amount of Cs in the reaction. In addition, next to each spectrum is shown the deconvolution of the absorption based on our algorithm, in a pie chart, like the one shown in 2.4. In these pie charts, the fraction of the pie chart corresponds to the species of the given color, while the size of the pie chart corresponds to the total amount of spectrally observed species in the mixture.

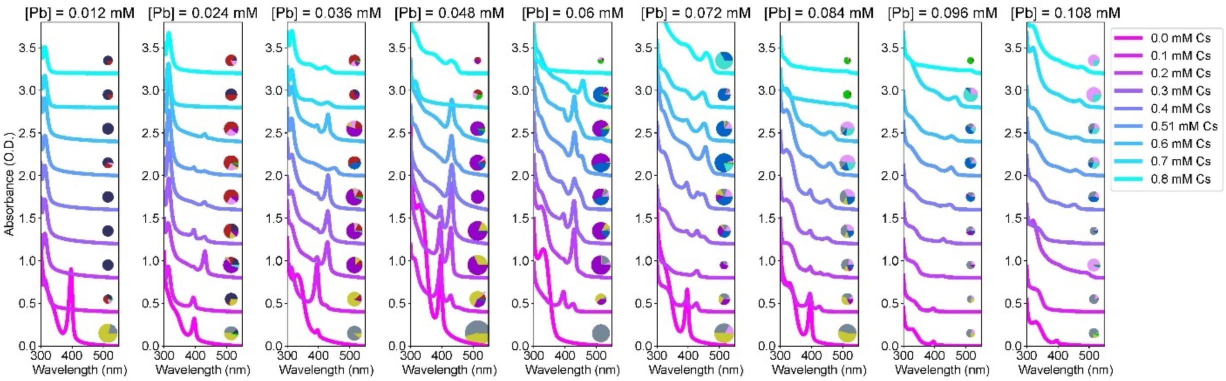

Figure 2.9: Absorption spectra and deconvolution of a factorial set of 9*9 synthesis experiments at an oleylamine concentration of 2.4 mM.

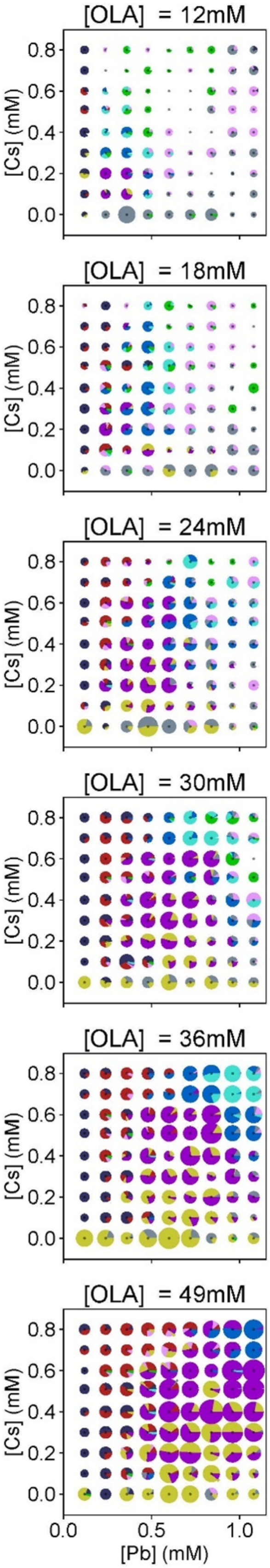

Figure 2.10: Arrays of pie charts showing the fractions and amounts of different chemical species in the synthesis solution, arrayed by their synthesis conditions for a OLA/Cs/Pb factorial experiment. Color Code: Green for $CsPbBr_3$ nanocubes; Pink for $CsPb_2Br_5$ nanocrystals; Grey for $PbBr_2$ nanocrystals; Cyan for 4-layer plates (4 ML); Blue for 3-layer plates (3 ML); Purple for 2-layer plates (2 ML); Yellow for OLA2PbBr4 nanosheets (monolayers); Dark Grey for Lead halide complex [$PbBr_x$]; Red for Cs_4PbBr_6 nanocrystals. [Br] = 12.72 mM, OA = 4.8 mM + adjustments for solubility of lead and cesium precursors

The next step towards the map in Figure 2.5 is to remove the spectra and reduce the information to the array of pie charts, with the position on the x-y plane showing the concentrations of lead and cesium in the synthesis and the pie chart colors and size showing the result of the synthesis in Figure 2.10. There are 6 subplots corresponding to the amount of oleylamine in the synthesis – these correspond to the 6 panels of the map. This displays an enormous wealth of information, showing the amount of 9 species as well as their synthesis conditions for all 486 points individually. However, this amount of information is perhaps a bit much for a casual glance, which is why we further reduced the complexity to the color and purity of the majority species in the map, with radial basis function interpolation between points to create the appearance of spatial extent.

Transformation Matrix Construction Example

We synthesized both the starting and ending points of a potential transformation reaction directly and performed the chemical transformation by preparing another vial by adding the amounts of reagents needed for the starting point, adding the halide precursor and then adding the reagent necessary to bring the vial to the same concentration as the ending point. Performing the chemical transformation in the synthesis solution enables us to directly probe the viability of nanocrystal transformation reactions, as we can look at transformations and compare them to the directly synthesized solution at the same exact concentrations. If both reactions between two species are possible, there is likely an equilibrium connecting the two.

To speed up the exploration of transformations, a single starting material was created as a reference for multiple transformations, creating a cluster of related transformations. In the following figures 2.11, we show an example of the raw data, including ranges of the absorption values in repeated experiments as well as the deconvoluted result of the distribution of different species.

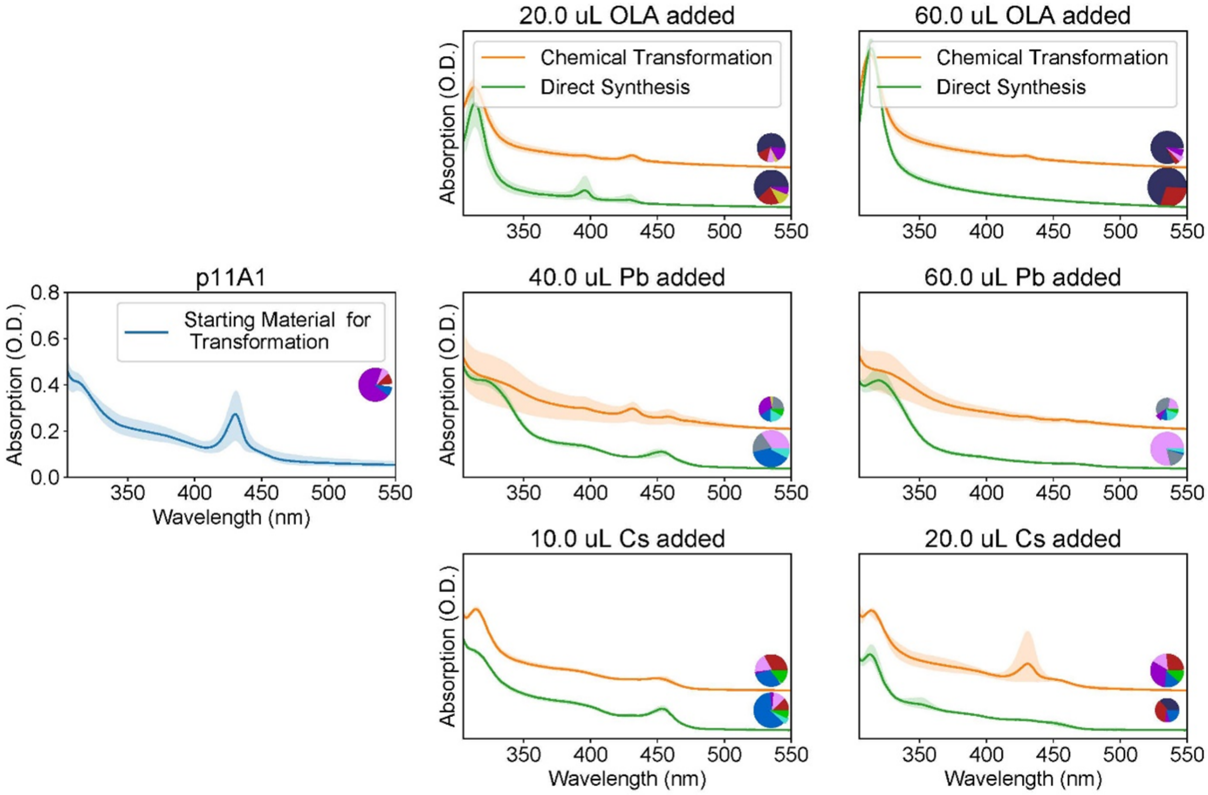

Figure 2.11: Attempted transformations of 2 ML plates into 3 ML plates (successful) 4 ML plates (partially successful), $CsPb_2Br_5$ (unsuccessful) and $[PbBr_x]$ (successful)

In the following example 2.12, we have sorted all the transformation reactions by their majority species of the starting material reference, and then sorted within those groups by the majority species of the direct synthesis reference. For all reactions, we display the pie chart denoting the composition of species for the starting material, transformation and direct synthesis. The reactions are displayed along a series of octagons, with the inner (blue) octagon showing the starting material, the middle (orange) octagon showing the chemical transformation and the outer (green) octagon showing the direct synthesis. If a major side product is expected and formed, or an unexpected reaction product is formed, we also consider it in our analysis of which transformations are allowed.

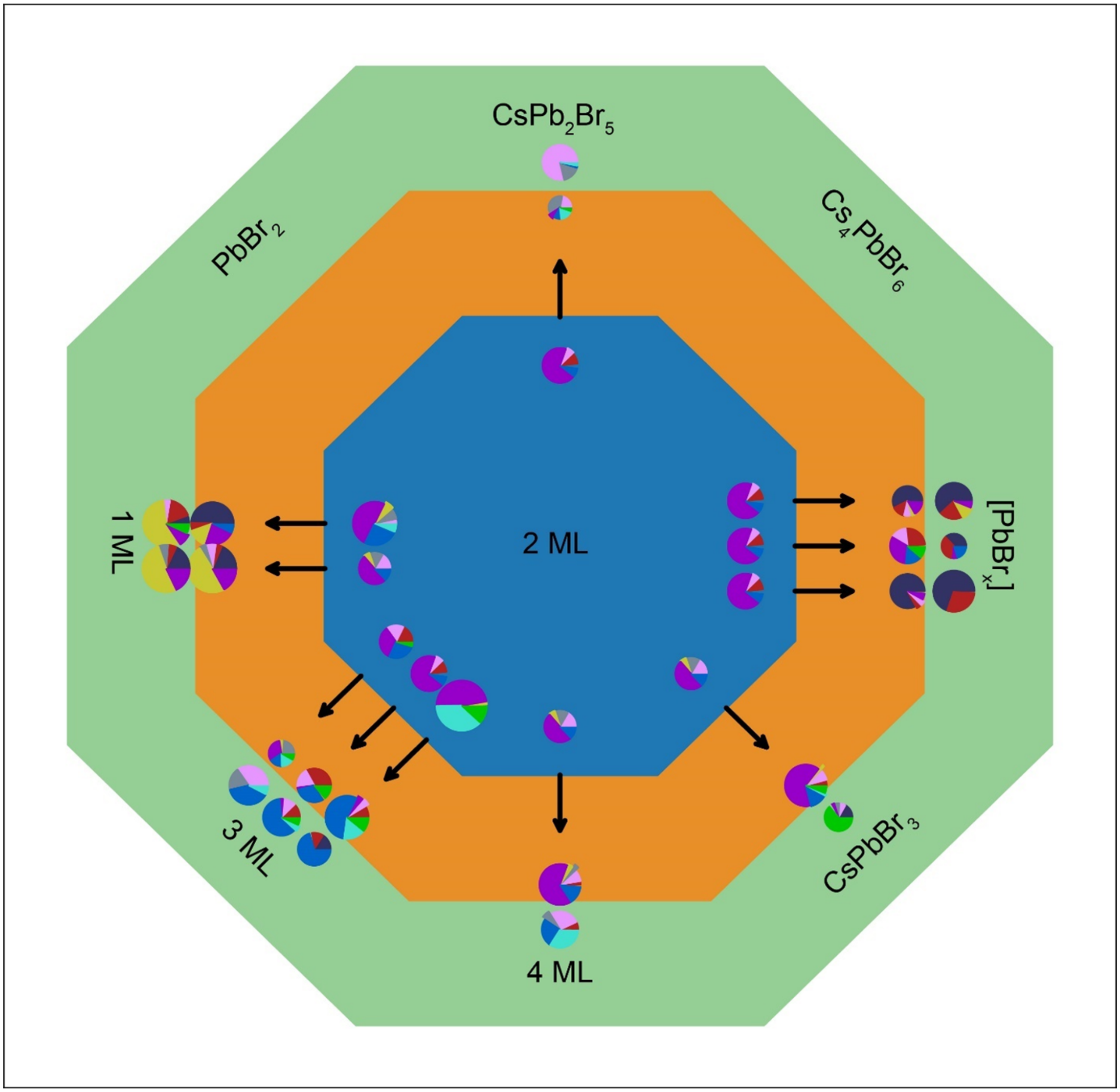

Figure 2.12: Chemical transformations (orange octagon) starting from 2 ML plates (blue octagon) going towards other species (sides of the green octagon). Transformations to [$PbBr_x$] are successful, whereas the transformation towards Cs_4PbBr_6 is partially successful. There is no direct reaction towards $PbBr_2$, and the reaction towards $CsPb_2Br_5$ appears mostly suppressed. 1 ML and 3 ML plates can form successfully. Reaction towards 4 ML and $CsPbBr_3$ are partially successful, resulting in an incomplete reaction and some co-formation of 3 ML plates.

Error Analysis

Next to obvious experimental errors such as failed injections which could be rejected in a straightforward manner due to their much lower absorbance in the UV, there are more subtle errors that may influence the dataset. In this section, we simulate the errors we would expect to observe due to the spectral deconvolution as well as report measures of the experimental standard deviations from duplicated experiments.

Errors due to the Spectral Deconvolution Algorithm

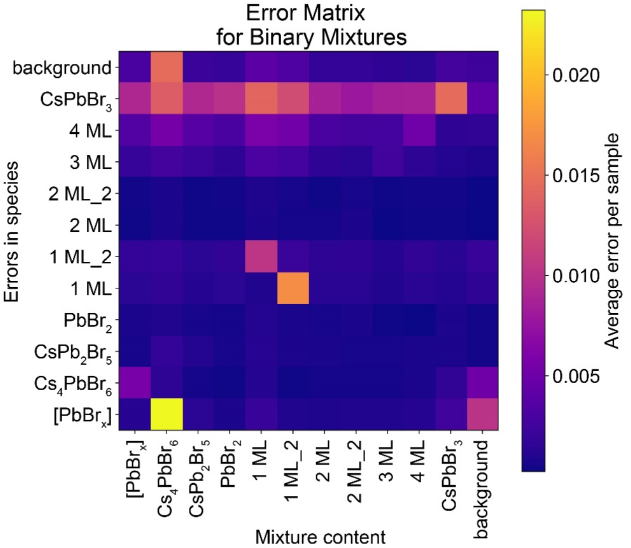

Figure 2.13: Error Matrix for simulated binary mixtures of all reference spectra

To estimate the errors of the deconvolution, we simulated binary mixtures of all possible combinations of reference spectra. For each combination, a logarithmic distribution of 19 points between 0.01 x and 0.99 x was chosen, which allowed better sensitivity close to unity and close to 0. We used the deconvolution algorithm to analyze the simulated spectra. This allowed us to compare the deconvolution of the algorithm with the true values we used to construct the spectra. For every spectrum, we calculated the outer product of the deconvoluted species values with the true values and calculated the absolute difference of this matrix from the outer product of the true values to return an error matrix for that sample. In this error matrix, the y axis denotes deviations from the true values in a certain species, and the x axis denotes the mixture of another species in which those deviations occurred, while color shows the magnitude of the error. All error matrices for the simulated dataset were added and each entry divided by the number of samples in that entry (12*19 for each diagonal entry and 19 for each off-diagonal entry) to give an average deviation per sample. We find that the average errors in spectral deconvolution are less than 2 % of the species fraction, as in Figure 2.13.

To gain a better overview of each individual mixture, we plotted the real fraction of each species against the calculated fraction (see Figure A.1.5). Ideally, this would be a straight line, as shown by the blue line in each plot. There are some outliers for $CsPbBr_3$ and 4 ML platelets in the range of 5-10 %. All the deviations are under the line, pointing to a consistent underestimation of these species. As we are applying a penalty on the coefficients in the fitting in order to more consistently eliminate confusing minority contributions and avoid overfitting, it is not surprising to see an underestimation at low true values.

Errors from Experimental Sources

To estimate experimental errors, we selected all entries that were identical with respect to the values of temperature and addition concentrations in the dataset. This was performed both for the mapping/transition type experiments and for the transformation type experiments. For each species in each type of experiment, we plot a histogram of the standard deviations and calculate the average and median standard deviation. For the experimental standard deviations, we find overall average errors in the fractions to be in the range of 2 – 10 % depending on the species, both for mapping and transformation experiments, as shown in Figure A.1.6.

However, this averaging over all duplicated fractions includes fractions in which a species does not have a significant presence, which we arbitrarily define here as a fraction of less than 5 %. Only counting those experiments for each species in which there is a fraction larger than 5 % allows us to more accurately estimate how large the errors are of the fractions observed in an experiment, which are more on the order of 10 - 25 % , as shown in Figure A.1.7.

There are a significant number of outliers at higher errors, signifying that occasional experiments may produce completely different results if repeated. This is the most likely explanation for the “islands” (i.e. regions containing only 1 data point that are surrounded by regions containing a different species) found in some of the maps. We created an approximation of an experimental confusion matrix by going through each of the sets of duplicates, and finding the outer product of the difference and the average of each duplicate, adding these matrices together for all duplicates and then dividing by the sum of all autocorrelations between the averages of duplicates to normalize for the amount of products found overall. This way of showcasing the most common experimental confusions is shown in Figure 2.14, which allows us to observe, for instance, that conditions that produce $CsPbBr_3$ nanocubes could also lead to formation of $[PbBr_x]$, Cs_4PbBr_6 or 3 and 4 ML plates, but never 1 or 2 ML plates, and only small amounts of $PbBr_2$ or $CsPb_2Br_5$.

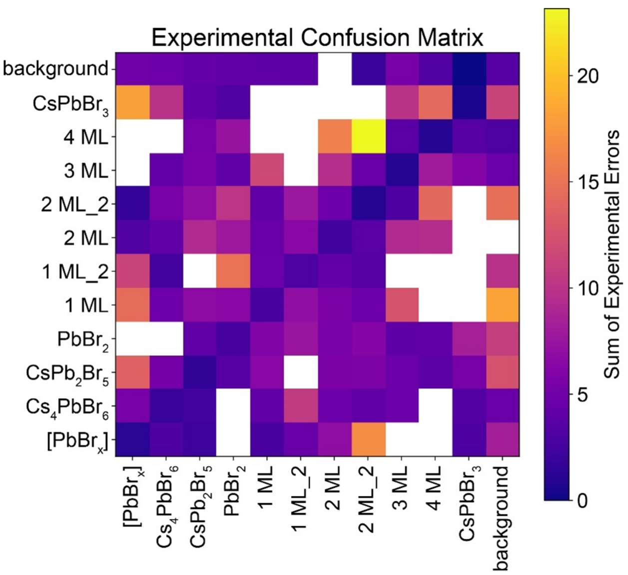

Figure 2.14: Experimental Confusion Matrix. Showing the sum of experimental errors normalized by the amount of overlap between two species. White regions have no substantial overlap.

At this point, we do not know the causes of these errors; they may be due to human error in preparing stock solutions, hidden variables such as changes in humidity and room temperature or other measures not considered here. It is likely that the non-linear nature of the experiments further exacerbates these errors; indeed, we find that in transition experiments, errors appear to become larger close to transition points (see Figure 2.3).

Chapter 3

Scientific Machine Learning of 2D Perovskite Nanosheet Formation

In collaboration with Dr. Samuel Niblett and Prof. David Limmer at UC Berkeley, Prof. Eran Rabani at UC Berkeley, Dr. Yeongsu Cho from the Berkelbach group at Columbia, Ye Zhang from the Yang group at UC Berkeley and Xingzhi Wang from the Alivisatos group at UC Berkeley

3.1 Introduction

Machine learning methods make it possible to predict outcomes of complex chemical systems,[55,61,62] including nanocrystal synthesis.[64,95] Much recent work has focused on predicting reaction outcomes given experimental inputs, essentially treating the synthesis process as a black box. However, while it is difficult to understand synthesis, some fundamental properties are widely understood. Most importantly, synthesis involves a kinetic process,[30,58,80] i.e. we need information about the behaviour of a reaction in time for deeper understanding. For reactions in which we know that they are thermodynamically determined, it may be reasonable to ignore these kinetic effects. In reactions where this is not certain, time series data is of crucial importance for understanding the reaction. While work on time-series prediction utilizing machine learning techniques exists, this has so far not been applied to chemical synthesis.

Physically modeling the kinetics of reactions has long had a distinct place in synthesis science. Linear, or at least analytic,[58] models of reaction kinetics or reaction rates as a function of temperature, concentrations or chemical substituents are part of the standard repertoire that chemists use to investigate how reactions happen. However, many reactions do not yield neat, analytically solvable models. Connections between different reactions yield stiff differential equations and non-linear processes - especially in nanoparticle synthesis.[26,45] Ideally, time series modeling utilizing machine learning would connect to physical models in such a way that we gain models that are fast to evaluate and that allow us to determine physical parameters such as rate constants and explore mechanisms.

There is movement from both sides: on one hand, machine learning models are being interrogated for possible scientific insight.[56] On the other, physical models are being given more flexibility and parameters than might traditionally be done.[122] Systems under kinetic control depend not on the formation energy of each chemical, but rather on the activation energy between each pair of reagents. If only one activation energy matters, as in the enantiodetermining step of catalytic reactions, this becomes a relatively straightforward task that can be predicted with linear regression.[123] For systems with multiple important rates, the scientific prediction of outputs requires modeling of the kinetics by finding numerical solutions to differential equations - a task that must be repeated anew for each initial condition queried. While this is expensive, the computational cost of calculating differential equations has also decreased significantly. The Scientific Machine Learning project uses fast numerical solution of differential equations to model complex behaviour in a physically understandable way across multiple domains.[124]

As an interesting system to investigate, we choose to examine the formation of two dimensional perovskite nanosheets. This material sits at the intersection of the highly active fields of two-dimensional materials[125–127] and perovskite nanostructures.[85,128] Two dimensional materials capture the imagination of scientists across disciplinary boundaries with their unusual strength, optical, electronic and spintronic properties.[126,127] Potential applications in catalysis,[129] sensing,[130] electronics[131] and ultralight materials showcase the broad possibilities given by these materials. Two-dimensional halide Van-der-Waals structures have also been studied extensively.[51] These structures display strong quantum confinement, exciton binding energies and directional transport, as is the case for other 2D materials.

Understanding the formation mechanisms of these structures remains a challenge, especially since most procedures require growth in a thin-film environment which is difficult to probe in-situ.[132–134] Especially the early stages of the reaction remain mostly unexplored. By utilizing colloidal synthesis techniques, we can achieve much higher concentrations of early stage nuclei that we can directly visualize, and obtain high quality time series data through absorption spectroscopy. In addition, the blue-shift of the 2D exciton peak due to lateral quantum confinement allows us to probe the size of the nanoflakes during early growth. Combining both time and concentration information is crucial to creating a useful model of the growth of these materials.

In addition to potential interest for the 2D materials community, this research connects directly to the synthesis science of nanocrystals, and perovskite nanocrystals in particular.[135,136] Synthesis science of perovskite nanocrystals has been obstructed by the absence of kinetic data with good time resolution.[136] By cooling the reaction down close to room temperature and using stopped flow spectroscopy, we can gather an abundance of absorption spectra resolving the appearance of species early in the formation process. In previous research, we and others have shown that binary lead halides can transform into the ternary perovskite nanocrystal species.[43–45,137,138] In particular, the formation route of ternary lead halides appears to be controlled by an equilibrium between solution complexes, 2D perovskite nanosheets and lead bromide nanocrystals (see Chapter 2). This equilibrium explained previous synthesis control strategies and we investigate the dynamics of these reactions further here.

Models of nanocrystal synthesis have been developed continuously since early work by Turkevich[2] and LaMer[22]. More modern models[21] include purely chemical versions such as the Finke-Watzky formalism[27], models utilizing thermodynamic ideas from classical nucleation theory and LaMer's work pioneered by Sugimoto et al.[24] as well as applications of nucleation theory to facet-limited growth developed recently by the Norris group.[32] We develop our own models explicitly for two dimensional nanosheet growth that fit into a chemical formalism while testing different types of growth laws and allowing us to track size distributions over time.

In this work, we probe the synthesis of colloidal, single layer 2D perovskites using in-situ stopped flow absorption spectroscopy, which yields time series of spectral information at millisecond resolution. Next to discussing qualitative results, we employ traditional kinetic analysis to understand a lead bromide chemical exfoliation mechanism by which nanosheets form. Finally, we construct a model of the spectral absorption as a function of size as well as a model of the kinetic behaviour of nanosheet nucleation and growth. Through combination of these two models, we enable prediction of the entire stopped flow time series. By fitting this model to experimental data and evaluating extrapolative cross-validation prediction accuracy, we can determine physical parameters of the system and the most realistic reaction mechanism.

3.2 Results and discussion

Characterization of Nanoscale Exfoliation

Lead halide nanocrystals transform into $\mathrm{OLA_2PbX_4}$ when exposed to oleylamine. This can be observed from optical absorption spectroscopy by the appearance of a sharp exciton peak at 397 nm (Figure 3.1 A) and the smoothing of the lead bromide shoulder at 330 nm. Additionally, this product shows characteristic repeating X-ray diffraction peaks of stacked monolayers, unlike the lead bromide nanocrystals (Figure 3.1 B). The transformation into 2D perovskite material from a lead halide crystal has been observed before, both in the solid state and in colloidal solution, though no clear proof of the 2-dimensional nature of the resulting product was offered. We demonstrate that the product formed by transforming colloidal lead bromide nanocrystals is indeed an atomically thin $\mathrm{OLA_2PbBr_4}$ nanosheet through atomic force microscopy imaging (Figure 3.1). Sheets formed in this manner are much larger than the initial nanocrystals they were formed from, as evident from transmission electron microscopy. This could happen through two different processes: Either dissolution of the nanocrystals and reprecipitation and growth into large sheets, or exfoliation of nanosheets from the nanocrystals and subsequent Ostwald ripening.

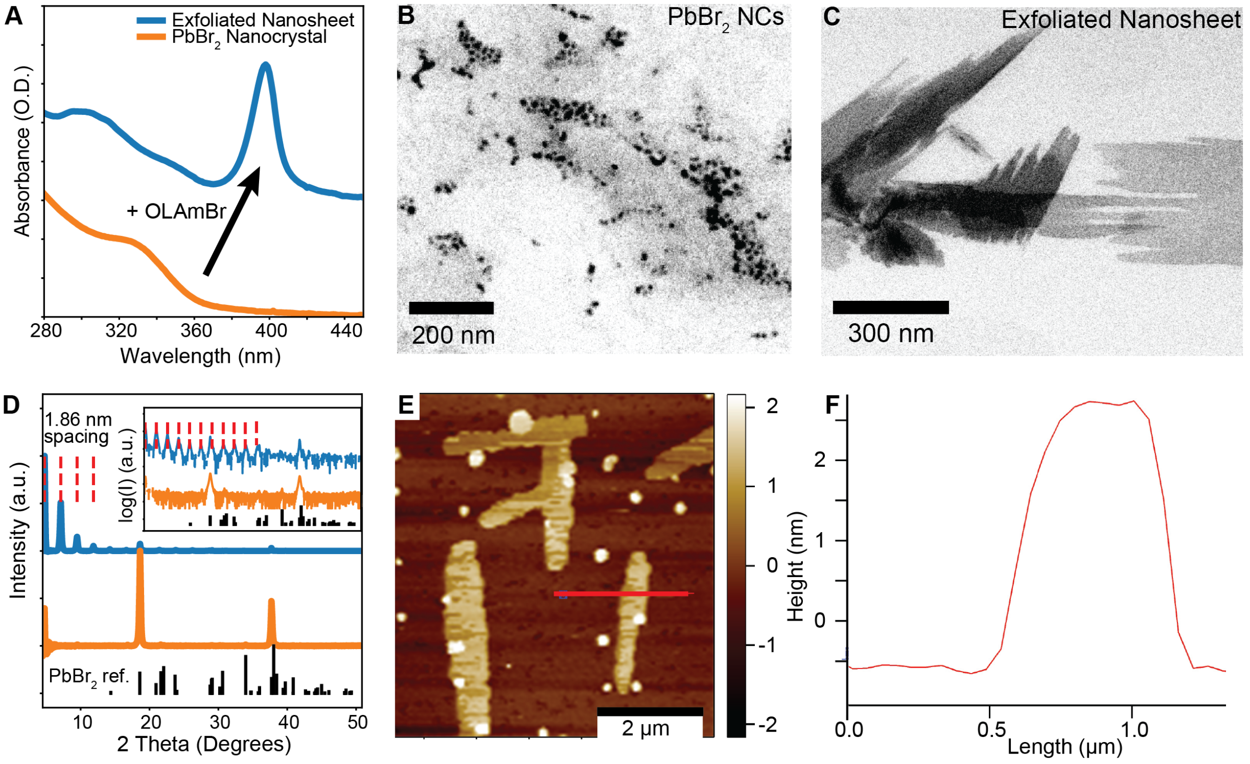

Figure 3.1: *Characterization of Exfoliation Process* A) UV-VIS Absorption Spectra of $PbBr_2$ nanocrystal solution before and after treatment with oleylammonium bromide to form OLA_2PbBr_4 nanosheets B) TEM image of $PbBr_2$ nanocrystals. C) TEM image of OLA_2PbBr_4 nanosheets generated from $PbBr_2$ nanocrystals through exfoliation. D) X-ray diffraction pattern of $PbBr_2$ nanocrystals before and after exfoliation to OLA_2PbBr_4 nanosheets. E) AFM image of OLA_2PbBr_4 nanosheets. F) Cross-section of OLA_2PbBr_4 nanosheets showing single layer height of 3 nm

In-Situ Studies of Exfoliation and Synthesis

To determine which of these processes occurs, and whether this process is relevant to the synthesis of 2D perovskite nanosheets, we utilized stopped flow studies. For the transformation, $PbBr_2$ nanocrystal solutions were mixed with oleylammonium bromide solutions prepared through reaction of benzoyl bromide with oleylamine. On a qualitative level, what is most apparent is that the characteristic 2D perovskite exciton peak appears immediately above 390 nm, with hardly any observable blue-shift at shorter time scales (Figure 3.2 A), regardless of the initial conditions chosen (Figure A.2.1). This implies that the nanosheets do not undergo dissolution and renucleation during this transformation process because they do not form small nanosheets - instead, entire layers of the lead bromide nanocrystals are formed at once, which suggests a chemical exfoliation mechanism (Figure 3.2 B).

For the synthesis, solutions containing lead oleate, oleylamine and oleic acid were mixed with benzoyl bromide solutions. As in previous work, there is a transition from producing

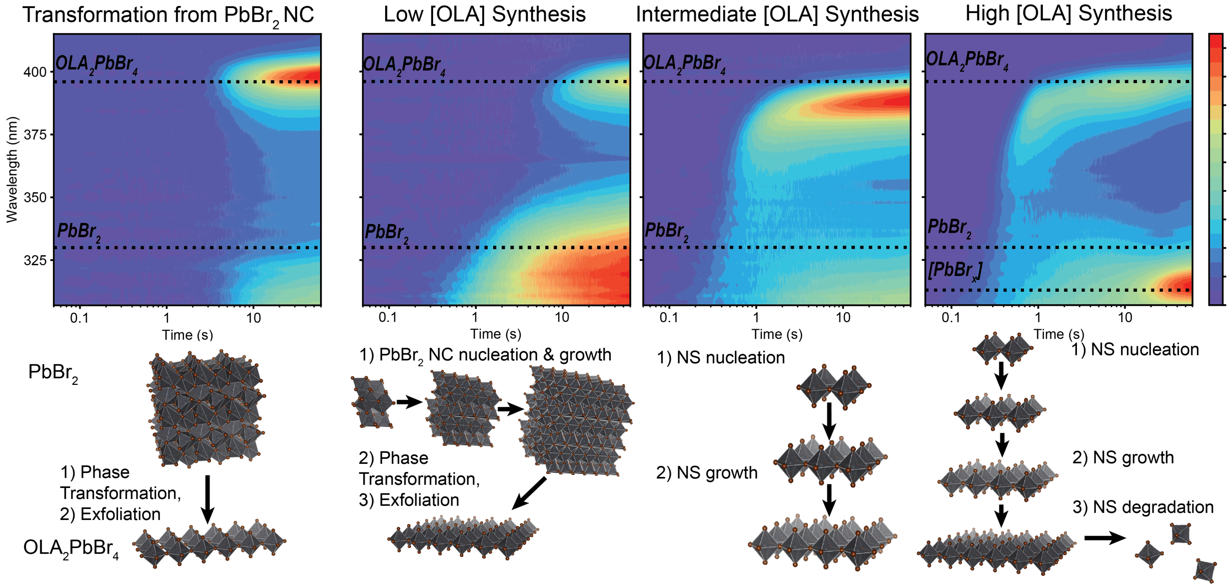

Figure 3.2: *Qualitative Observations in Stopped Flow of OLA_2PbBr_4 Synthesis* A - D Stopped flow absorption maps of OLA_2PbBr_4 nanosheets formed through A) Transformation from $PbBr_2$ nanocrystals. B) Synthesis at low OLA concentrations. C) Synthesis at intermediate OLA concentrations. D) Synthesis at high OLA concentrations. E-H Cartoons of proposed formation processes at conditions related to E) Transformation (A), F) Low [OLA] synthesis (B), G) Intermediate [OLA] synthesis (C), H) High [OLA] Synthesis

mainly $PbBr_2$ nanocrystals at low ratios of OLA to Pb precursors to mainly producing 2 D perovskites (1 ML or OLA_2 $PbBr_4$) at higher ratios. At low OLA/Pb ratios formation of $PbBr_2$ nanocrystals occurs before the formation of OLA_2 $PbBr_4$ perovskite, which displays a similarly small blue-shift to the direct transformation from $PbBr_2$ nanocrystals. This suggests that the transformation pathway is relevant in nanoparticle synthesis if $PbBr_2$ nanocrystals are formed. Conversely, at high OLA to Pb ratios there is a large observed blue-shift of the excitonic peak early on in the synthesis (around 50 nm or 200 meV) and no formation of $PbBr_2$ nanocrystals, suggesting de-novo formation of perovskite nanosheets. These qualitative observations imply that there are two mechanisms by which 2 D perovskites may be formed in colloidal solution: either through a transformation process from $PbBr_2$ nanocrystals (Figure 3.2 E, F), or via a direct nucleation and growth pathway (Figure 3.2 G, H). We have also observed that there appear to be intermediate processes, i.e. transformation from very small $PbBr_2$ nanocrystals at OLA/Pb ratios between those shown in Figure 3.2 B and C (Figure A.2.2).

Kinetic Analysis of Activation Energy of 2 D Perovskite formation via $PbBr_2$ nanocrystals

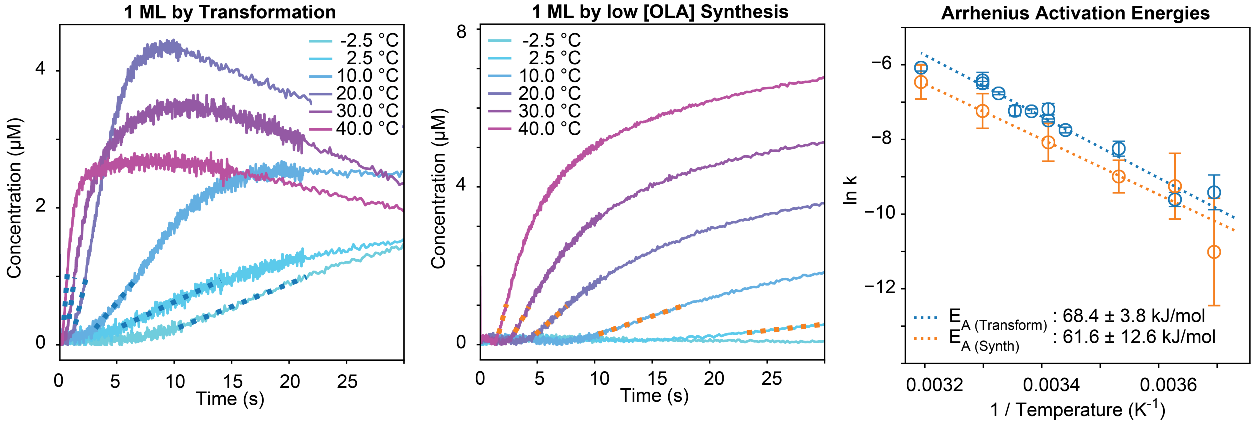

Figure 3.3: *Activation Energy of Transformation* A) Kinetic traces of OLA_2PbBr_4 concentrations at different temperatures. B) Kinetic traces of OLA_2PbBr_4 concentrations in a low OLA concentration synthesis at different temperatures. C) Arrhenius plot of initial kinetic rates extracted from A and B showing activation energies.

In addition to a qualitative analysis of the species observed in the stopped flow measurements, we also attempted to analyze the rate of appearance of OLA_2 $PbBr_4$ at early times. This was possible for any stopped flow measurement in which we did not observe significant blue-shifts (i.e. which follow the transformation pathway), as the deconvolution algorithm used to determine the concentration of OLA_2PbBr_4 uses this peak to assign species identity. We successfully extracted linear fits for this initial time for both the direct transformation (Figure 3.3A) as well as the synthesis at low OLA/Pb ratios (Figure 3.3B) at a variety of temperatures. A standard Arrhenius plot of the logarithm of kinetic rates versus inverse temperature (Figure 3.3C) demonstrates that the activation energies for both the direct transformation and the low OLA/Pb ratio synthesis cannot be distinguished within standard error. This is another piece of evidence that both reactions occur via the same mechanism.

Defining a combined physical model to determine nucleation and growth models of 2 D perovskite nanosheets

By utilizing kinetic models based on different mechanistic possibilities and critically evaluating their ability to fit and predict data, we can infer information about the nanocrystal formation process that we cannot observe directly. As we could not use conventional kinetic analysis approaches to understand the de-novo nucleation and growth of 2D perovskite nanosheets, we developed a combined spectral and kinetic model. Unlike for the transformation from $PbBr_2$, in which the exciton of the nanoplatelet does not experience confinement, we were not able to perform a kinetic analysis for any stopped flow measurement in which there were substantial blues-shifts of the exciton peak (i.e. which proceed via a direct nucleation pathway). Performing this analysis requires deconvolution of small sheets growing in lateral size and shifting their exciton into the observed absorption peak and large platelets with no such shift growing in mass. The spectral model in particular presented some challenges as we were unable to quantify lateral sizes at which exciton confinement proves relevant, as well as the associated changes to the exciton extinction coefficient. To overcome this problem, we created a model of the spectrum and coupled it to a kinetic model of the reaction, which allowed us to directly simulate the spectral data from stopped flow absorption measurements.

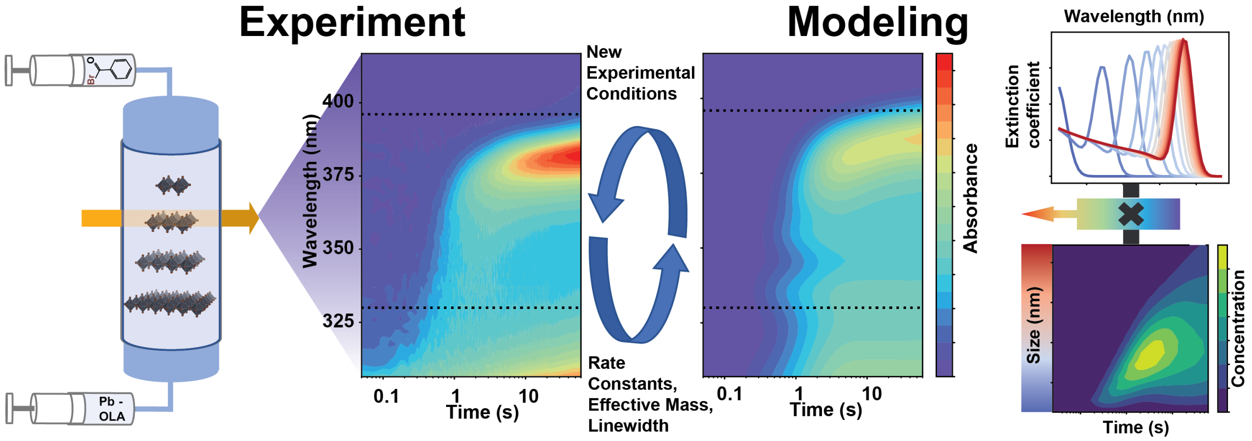

Figure 3.4: *Overview of Combined Model*

Effective Mass Model

In collaboration with Dr. Yeongsu Cho, Berkelbach group, Columbia University and Prof. Eran Rabani, UC Berkeley

To enable a reasonable estimate of the excitonic energy as a function of size, we calculated the optical gaps and bandgaps of a series of square nanoplates. Based on previous observations, electrons and holes have similar effective masses. The band gap without exciton binding, E_{Gap}, should thus be modeled as dependent on the mass of the hole and the electron separately:

$$E_{Gap} = E_{Gap,bulk} + E_{con,e} + E_{con,h} \tag{3.1}$$

Where $E_{Gap,bulk}$ is the bulk band gap, $E_{con,e}$ and $E_{con,e}$ are the confinement energies of the electron and hole, respectively. Using a particle in a 2D box model leads to the following equation:

$$E_{Gap} = E_{Gap,bulk} + \frac{\hbar^2\pi^2}{4m_{e*}L^2} + \frac{\hbar^2\pi^2}{4m_{h*}L^2} \tag{3.2}$$

Where $\hbar$ is the reduced Planck's constant, m_{e*} and m_{h*} are the effective electron and hole masses and L is the side length of the confined species. The observed optical gap, $E_{Exciton}$ with exciton binding energy should be modeled with the effective mass of the exciton, i.e. the combined mass of electron and hole, i.e.

$$E_{Exciton} = E_{Gap,bulk} - E_{Exc_bind,bulk} + \frac{\hbar^2\pi^2}{4(m_{e*} + m_{h*})L^2} \tag{3.3}$$

Where $E_{Exc_bind,bulk}$ is the bulk exciton binding energy. A classical effective mass models with a $\frac{1}{L^2}$ dependence was unable to capture the resulting trends in size. However, a model using a $\frac{1}{L}$ dependence was able to capture the calculated results of both optical gaps and bandgaps well using the effective mass, bulk exciton gap and bulk exciton binding energy as fitting parameter to fit both datasets simultaneously, with $m_{e*} \approx m_{h*}$ as suggested by previous measurements (see Figure 3.5). Such a $\frac{1}{L}$ dependence has been suggested before for effective mass models of confined semiconductor nanocrystals. This leads to the following, final equations:

$$E_{Gap} = E_{Gap,bulk} + 2\frac{\hbar^2\pi^2}{4m_{e*}L} \tag{3.4}$$

$$E_{Exciton}(L) = E_{Gap,bulk} - E_{Exc_bind,bulk} + \frac{\hbar^2\pi^2}{8m_{e*}L} \tag{3.5}$$

The effective mass of $\approx 0.17e_m$ fit based on this equation was found to be in good agreement with previous calculations and measurements that suggest an effective mass of $\approx 0.1e_m$. In addition, experimental measurements of $E_{Exciton}$ on micron scale single layer $(C_4H_9NH_3)_2PbBr_4$ crystals show a peak emission energy in line with the fit optical bandgap of 408 nm.

Spectral Model

In collaboration with Prof. Eran Rabani, UC Berkeley

Next, we modified a model from .. et al. to allow estimation of the excitonic peak extinction coefficients and peak widths as a function of lateral plate size. The original model estimated peak width as

$$Width_{Exciton}(L) \sim \frac{\delta E_{Exciton}(L)}{\delta L}\frac{1}{\sigma_L} \tag{3.6}$$

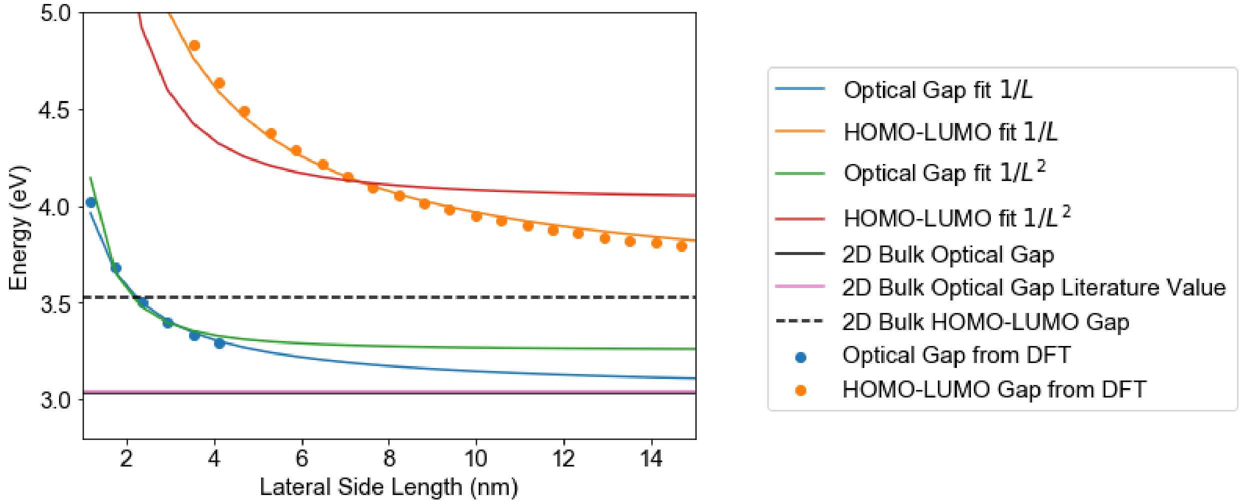

Figure 3.5: *Effective Mass Model* Joint fits to optical and bandgap values calculated from DFT based on the effective mass model in equations 3.4 and 3.5, showing a $\frac{1}{L}$ and $\frac{1}{L^2}$ dependence. Fit values for the chosen $\frac{1}{L}$ dependence : $m_{e*} = m_{h*} = 0.17e_m$, $E_{Gap,bulk} = 3.52eV$, $E_{Exc_{b}ind,bulk} = 0.49eV$

$$Ext_{Exciton}(L) \sim \frac{1}{E_{Exciton}(L)} \frac{1}{Width_{Exciton}(L)} \tag{3.7}$$

where $E(L)$ is the energy as a function of size, L is the size and σ_L is the size distribution. Most crucially, we substitute our expression for the effective mass and add constant bulk exciton linewidths and extinction coefficients, since the bulk material is a 2D material with strong exciton binding energy. In addition, based on our spacing of individual plates as integer side lengths with differences in size of ΔL, we approximate $\sigma_L \approx \frac{\Delta L}{L}$

$$Width_{Exciton}(L) = A\frac{\hbar^2\pi^2}{8m_{e*}L^2} + B \tag{3.8}$$

$$Ext_{Exciton}(L) = C\frac{16m_{e*}^2L^2}{\hbar^4\pi^4\Delta L} + D \tag{3.9}$$

We model the excitonic peak as a gaussian, with the center given by the effective mass model, and the exciton extinction coefficient and peak width determined by the above equations. To this gaussian, we add a power law for wavelengths lower than the peak, describing the distribution of states above the bandgap. Experimental spectra can be described sufficiently by this model. On all of the free parameters involved in the spectral model, we imposed limits based on spectra of large OLA_2 $PbBr_4$ nanosheets in solution, coupled with ICP measurements of Pb concentrations.

Kinetic Model

In collaboration with Dr. Samuel Niblett and Prof. David Limmer, UC Berkeley
Similar to Riedinger et al.,[32] we use the assumption that nucleation of facets (or in this purely 2D case, edges) is the rate determining step to simplify the resulting simulation. Using this assumption, all nanosheets grow and shrink laterally using the same set of equations. We created multiple models based on different mechanistic possibilities.

1. One or two monomer units could be involved in the nucleation of new edges.
2. Attachment and detachment could be based on the number of edge atoms in a plate (4N - 4), or it could be identical for every plate size.
3. Detachment might or might not involve ligands.

This gives rise to the following differential equation for each $Plate_{N\times N}$, in which possible choices have been italicized:

$$\begin{aligned}\frac{d[Plate_{N\times N}]}{dt} &= k_{attach} \times [Plate_{(N-1)\times(N-1)}][Monomer]\textit{[Monomer](4(N-1) - 4)} \\ &- k_{attach} \times [Plate_{N\times N}][Monomer]\textit{[Monomer](4N - 4)} \\ &- k_{detach} \times [Plate_{N\times N}]\textit{(4N - 4) [Ligand]} \\ &+ k_{detach} \times [Plate_{(N+1)\times(N+1)}]\textit{(4(N+1) - 4) [Ligand]}\end{aligned} \tag{3.10}$$

For the *de-novo* nucleation of 2D - nanosheets, i.e. the formation of $Plate_{2\times2}$ with 4 monomer units, we additionally consider two nucleation reactions:

$$M_3 + Monomer \longrightarrow Plate_{2\times2} \tag{3.11}$$

$$M_2 + M_2 \longrightarrow Plate_{2\times2} \tag{3.12}$$

In the first law, the potential intermediate M_3 composed of 3 monomer units could also be made in two different ways:

$$M_2 + Monomer \longrightarrow M_3 \tag{3.13}$$

$$3Monomer \longrightarrow M_3 \tag{3.14}$$

with M_2 always formed through a reaction of two Monomer units. Including the possibility of ligand involvement in the $Plate_{2\times2}$ denuclation reaction and with factorial expansion of each choice, we consider here $3_{Nuc}\times2_{Denuc,Ligand}\times2_{Attach,Monomer}\times2_{Attach,Edge}\times2_{Detach,Ligand}\times 2_{Detach,Edge} = 96$ different reaction possibilities. Adding in solution reactions such as the decomposition of benzoyl bromide and formation of lead halide complexes (see Chapter 4), we set up full kinetic models for each of these possibilities. Utilizing a modified Runge-Kutta method implemented in fortran, we were able to numerically solve the differential equations within reasonable parameter regimes and produce time traces of different concentrations as well as particle size distributions varying through time.

Optimization Process

By multiplying the concentration of each plate at each point in time calculated with the kinetic model with the extinction coefficient of each plate, we can effectively simulate the stopped flow measurement at conditions in which only the 2D perovskite nanosheet forms. We constructed a loss function by adding the χ^2 loss of the entire stopped flow experiment to the χ^2 loss of peak position and height, with a penalty for solutions that did not produce nanosheets or timed out after 20 s. Using a differential evolution algorithm, we determined the rate constants of the kinetic model and the optical constants in the spectral model within physically reasonable bounds for each of the 96 potential mechanisms.

Through an extrapolative cross-validation and testing, we utilized 3 out of 9 stopped flow experiments to fit the data, and examined the predictive ability of the resulting models on the other experiments, including a test set of two additional experiments, one of which had a value of bromide precursor 3 times higher than any other experiment. This allowed reasonable comparison of the models across experimental conditions with different benzoyl bromide, oleylamine and lead oleate concentrations. Such an extrapolative cross-validation procedure would not be useful in a traditional machine learning context, where extrapolation is frequently not possible and model training is relatively cheap. In our case, training the models requires significant computational expense, and the physical nature of the models makes extrapolative predictions useful.

Analysis of combined model results

On a qualitative level, the models were able to reproduce important features of the spectra, such as the general shape of the peak wavelength evolution. Important features such as the observed blueshift of peak wavelengths at short timescales and general shape of the peaks could be observed in simulated stopped flow experiments. Quantitatively, the models show some correlation with the overall spectral values, though with generally relatively low R^2 (≤ 0.4) and high χ^2 (≥ 64 values for cross validation and test sets that suggest there is still some portion of the physics which is not captured appropriately. Further optimization of the simulations is required to improve models and may allow determination of a preferential mechanism.

The ability of models to fit the data had different sensitivity to different parameters. This parameter sensitivity was similar even with models utilizing different rate laws. Many parameters, such as most solution rates did not change the final results even when varied over a wide parameter regime, as long as they did not fall below a certain critical value. This indicates that these reactions are fast compared to the rate determining step in the model. Unsurprisingly, plate and layer nucleation rates and denucleation rates significantly affect how well the simulation fits the data. There appears to be a correlation between plate and layer nucleation, i.e. reasonable fits could be obtained by increasing or decreasing both rate constants while keeping the ratio between them constant. Layer dissolution did not appear

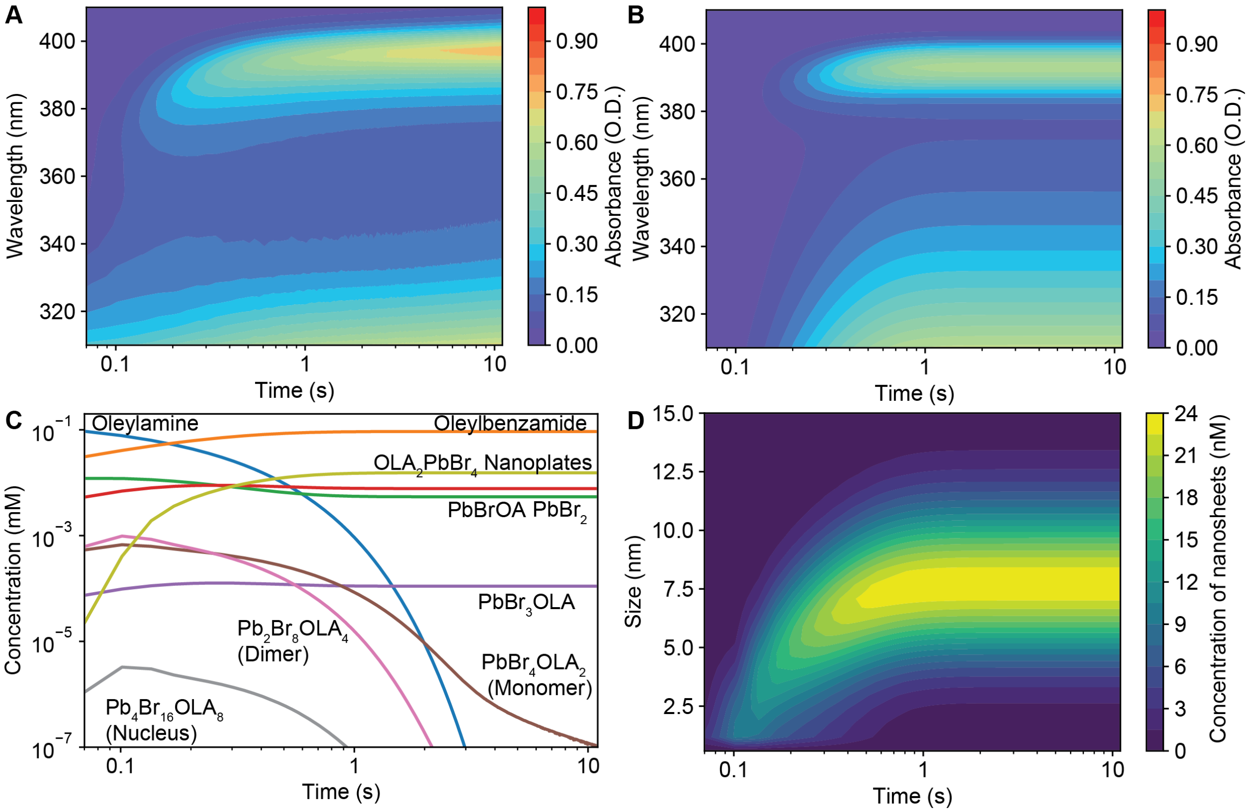

Figure 3.6: *Extrapolation from Optimized Combined Model* A) True stopped flow results for extrapolation at high bromide concentrations. B) Simulated stopped flow results at identical conditions. C) Time traces of concentrations of simulation in B) D) Particle size distribution as a function of time in simulation in B)

to correlate with either plate or layer nucleation. We did not observe a strong sensitivity to the optical parameters, except for the overall extinction coefficient.

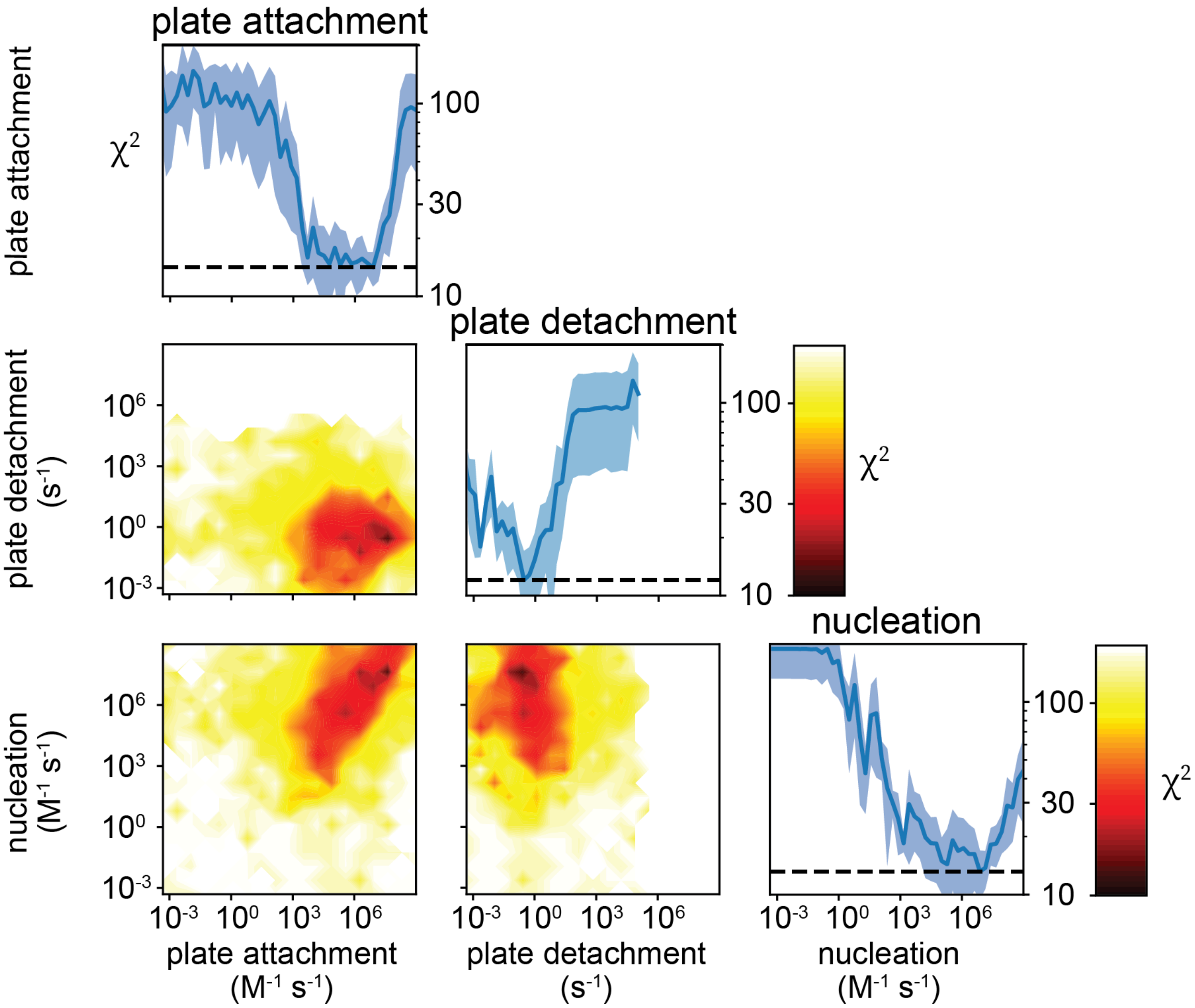

Figure 3.7: *Parameter Determination*

3.3 Conclusion

Overall, we have obtained in-situ optical data of a 2D perovskite nanosheet synthesis with high time resolution. We demonstrate that there are two formation pathways for this nanoscale species, chemical exfoliation and direct nucleation, which can be controlled through the ratio of oleylamine to lead in the synthesis. Observation of transformation reactions from synthesized $PbBr_2$ nanocrystals with oleylammonium bromide have similar activation energies as synthesis occuring through chemical exfoliation. We have complemented traditional kinetic analysis techniques by further developed a scientific machine learning model, a physically interpretable model including a spectral and a kinetic component that can be fit directly to observed stopped-flow data and allows extrapolative prediction of experiments with conditions differing significantly from the training dataset. By evaluating the quality of extrapolative prediction of a combinatorial set of kinetic models with different rate laws, we can attempt to predict the mechanism by which 2D perovskite nanosheets are formed. This framework fits neatly into the gap between traditional physical modeling and machine learning and could be useful for understanding and predicting synthesis problems more generally.

3.4 Methods

Synthesis

Chemicals and Materials

Dodecane (>99.0%), lead acetate ($PbCH_3COO$, >97.0%), oleylamine (OLA) ≥99.0%), oleic acid (OA) ≥99.0%) and benzoyl bromide ≥99.0%) were purchased from Sigma Aldrich. Hexane (mixed isomers, 98 %) was purchased from Fischer Scientific. All materials were used as received.

Synthesis and Transformation of lead bromide nanocrystals

Lead Acetate was dissolved in oleic acid, and stock solutions of lead oleate solution was prepared as in Chapter 2. Lead bromide nanocrystals were synthesized by mixing 60 µL lead oleate solution with 60 µL oleic acid and 20 µL oleylamine in a 4 mL vial containing 2 mL of hexanes and a stirbar. At room temperature, 9 µL of benzoyl bromide were added to the mixture, then the solution was stirred for 10 minutes. An equal amount of isopropanol was added to the solution to induce precipitation, then the mixture was centrifuged at 5,000 rpm. The resulting pellet was redispersed in hexanes.

Characterization

Powder X-ray diffraction (PXRD) patterns of NCs were acquired using a Bruker D2 Phaser X-ray diffractometer equipped with a Cu Kα of 1.5445 Åwavelength. Samples were prepared by drop-casting 100 µL stock solutions of NCs onto a silicon substrate. Samples were dried under air flow prior to measurements.

Transmission electron microscopy (TEM)

Transmission electron microscopy images of the cesium lead bromide species were acquired using a FEI Tecnai T20 transmission electron microscope equipped with a Gatan RIO16IS camera and a LaB6 filament. All images were recorded under 200 kV accelerating voltage. Samples were prepared by dropcasting about 10 µL 1000 x diluted stock solutions onto a carbon support with 400 copper mesh. Samples were dried under ambient conditions prior to imaging.

Atomic Force Microscopy Imaging

Measurements performed by Ye Zhang, Yang group, UC Berkeley

Nanoplate samples were dropcast onto a silicon chip and dried under ambient conditions. The thickness of the nanoplates was measured using Atomic Force Microscope (MFP-3D Asylum Research, Oxford Instruments) equipped with an acoustic isolation chamber (AEK 2002) and a silicon tip (AC240TS-R3, Asylum Research, Oxford Instruments). The measurements were performed in AC (or tapping) mode and at a low scan rate of 0.2 Hz with a resolution of 256-by-256 pixels.

Pb ICP of nanocrystal solutions

Measurements performed by Xingzhi Wang

Inductively coupled plasma (ICP) spectroscopy was used to measure the concentrations of Pb in transformed nanoplatelet samples. To prepare a sample for ICP, 300 µL stock solution containing colloidal NPLs was dried under constant air flow. The sample was then further dried in vacuum at 90 °C for 2 h. The dried sample was digested in 1.2 mL of a 5:1 (v:v) mixture of 70% nitric acid and 30% hydrogen peroxide to break down all organic ligands and nanostructures. After at least 12 h of digestion, 1 mL of digested sample was diluted to 10 mL in deionized water, with anaddition of 100 µL 1000 ppm Ni standard solution in 2% nitric acid as an internal standard. For each batch of samples, a sample containing only the mixture of nitric acid and hydrogen peroxide was included as a blank sample to rule out potential contaminations during sample preparation.

A Perkin Elmer 5300 DV optical emission ICP with auto sampler was used to perform all the measurements. Calibration curves were constructed using a series of Pb standard solutions obtained by diluting a 1000 ppm Pb standard solution in 2% nitric acid, and a blank standard solution was made using only 2% nitric acid. To each standard solution, 100 µL aforementioned Ni standard solution was added as an internal standard. A calibration curve was constructed each time prior to the measurement of the samples for each batch of samples. To ensure the accuracy of the measurements, each measurement was performed twice in a row, and a measurement was accepted only if its measured intensity of Ni was within 10% of that measured in the blank standard solution.

DFT and GW calculations of perovskite nanosheets

Performed by Dr. Yeongsu Cho The OLA_2PbBr_4 nanosheet is simulated by modifying a tight-binding GW-BSE method described previously and summarized below.[139] A nanosheet is modeled as a square sheet of n×n $PbBr_4$ units with additional Bromides on the boundary. Each $PbBr_4$ unit is assumed to have a cubic, centrosymmetric structure to avoid complexities arising from a broken symmetry such as the Rashba effect. The $PbBr_4$ sheet is sandwiched by layers of organic cations, methylammonium, and suspended in vacuum. Since the frontier orbitals of a nanosheet are primarily comprised of $PbBr_4$,[140] a tight-binding model is constructed in the basis of the Pb 6s and 6p spin-orbitals and the Br 4s and 4p spin-orbitals. The tight-binding parameters are determined by a single fully relativistic DFT calculation with MAPbBr3 approximated as CsPbBr3[141] to impose a perfect cubic symmetry. The DFT was performed with PBEsol exchange-correlation functional[142] and plane augmented wave pseudopotential using Quantum Espresso,[143] followed by the parameter extraction using Wannier90.[144] The non-collinear DFT calculation ensures the tight-binding parameters to incorporate the spin-orbit coupling. Next, we apply the GW approximation by adding a constant self-energy Σ_μ for each atomic orbital μ to the diagonal elements of the tight-binding Hamiltonian. The total approximate GW Hamiltonian is

$$H^{GW}_{\mu\nu} = H^{DFT}_{\mu\nu} + H^{SOC}_{\mu\nu} + \Sigma_\nu \delta_{\mu\nu} \tag{3.15}$$

for atomic orbital μ and ν. Solving $H^{GW}_{h\nu}$ gives the energy ϵ_m and the wave function $C_{\mu m}$ of a molecular orbital m. The tight-binding representation allows to build a Hamiltonian of a nanoparticle with an arbitrary shape, effectively capturing the carrier confinement effect. The self-energies Σ_μ and a rigid scissor shift of the conduction band Σ_{CB} are optimized to best reproduce the ab initio GW band structure of MAPbBr3.[145] There is another type of self-energy arising from the heterogeneous dielectric environment. A charge in a nanosheet has an additional electrostatic self-energy compared to a charge in a uniform bulk material with a dielectric constant ϵ_{PbBr_3}. The shift in the self-energy of an atomic orbital μ whose atom is at the height z_μ is given by

$$\delta\Sigma(z_\mu) = \frac{1}{2} \lim_{\rho \to 0} [(\rho, z_1 = z_2 = z\mu) - 1/(\epsilon_{PbBr_3} \rho)] \tag{3.16}$$

where $W(\rho, z_1, z_2)$ is the screened Coulomb interaction between two charges placed on the planes at z_1 and z_2 and separated by the in-plane coordinate ρ. W is calculated by solving the classical electrostatic problem, assuming the $PbBr_4$ slab and the sandwiching layers of MA are infinite in lateral dimension and have a uniform dielectric constant ϵ_{PbBr_3} and ϵ_{MA}, respectively. The solution is obtained in a closed form via the electrostatic transfer matrix method.[146] For each state, we correct the eigenvalues via the perturbation theory with an expectation value

$$E_{a/i} = \epsilon_{a/i} + \delta\Sigma_{a/i} = \epsilon_{a/i} \pm \sum_{\mu} |C_{\mu,a/i}|^2 \delta\Sigma(z_\mu) \tag{3.17}$$

where a is a virtual orbital and i is an occupied orbital. The optical gap is obtained by solving the Bethe Salpeter equation in the Tamm-Dancoff approximation based on the GW self-energy.[147] The eigenvalue equation for the excitation energy E_X and the wave function A^X_{ia} of an exciton X is given by

$$E_X A_{ia}^X = (E_a - E_i) A_{ia}^X - \sum_{ia} (aa|W|ii) A_{ia}^X \tag{3.18}$$

The two-electron integral associated with the screened Coulomb interaction is evaluated with the zero differential overlap as

$$(aa|W|ii) = \sum_{\mu\nu} C_{\mu a}^{\star} C_{\mu a} C_{\nu i}^{\star} C_{\nu i} W_{\mu\nu} \tag{3.19}$$

where the two-electron integral on the atomic orbital basis is

$$W_{\mu\nu} = \begin{cases} W(\mid \rho_\mu - \rho_\nu \mid, z_\mu, z_\nu) & \text{if } \mu \text{ and } \nu \text{ are on different atoms} \\ (\mu\mu \mid \nu\nu) & \text{if } \mu \text{ and } \nu \text{ are on the same atom} \end{cases} \tag{3.20}$$

Assuming charges on the same atom do not experience the dielectric screening, $(\mu\mu \mid \nu\nu)$ is calculated exactly with the bare Coulomb interaction $1/\rho$, using def2-TZVP basis.

ε_{PbBr_4}	7.5[148]
ε_{MA}	2.1[149]
$\Sigma_{Pb,s}$	0.066 eV
$\Sigma_{Pb,p}$	3.7 eV
$\Sigma_{Br,s}$	7.8 eV
$\Sigma_{Br,p\perp}$	-4.4 eV
$\Sigma_{Br,p\parallel}$	2.3 eV
Σ_{CB}	0.19 eV

Table 3.1: Parameters for the tight-binding GW-BSE calculation of 2D perovskite nanosheets

Stopped Flow Experiments

All stopped flow experiments were performed on an Applied Photophysics SX 20 stopped flow spectrophotometer using a silicon photodiode array with 256 measurement points spaced at equal distance between 190 and 735 nm. The stopped flow chambers were stored under ethanol, then filled with toluene and emptied three times, then filled with dodecane and emptied three times before measurement. Spectral aquisition times (usually $\sim$ 25 ms) and instrument gain were optimized with Dodecane as a solvent to minimize aquisition times while maximizing spectral sensitivity and avoiding detector overflow. A background of dodecane was subtracted internally. Spectra were recorded over 1000 points, usually for 60 seconds and for no longer than 3600 seconds. The syringes and stopped flow chamber were periodically flushed with Ethanol to remove any accidentally deposited material in the measurement chamber, and the same setup procedure was repeated after flushing.

Stock solutions of Br, OLA, OA, Cs-OA and Pb-OA were prepared as as in Chapter 2, but diluted to 8.5, 3.0, 3.2, 1.0 and 0.66 mM in dodecane, respectively. All stock solutions were added to the syringes used for loading the stopped flow chambers with volumes varying between 10 - 100 uL and mixed with 2 mL dodecane. For synthesis experiments, OLA, OA, and Pb-OA solutions were placed in one syringe and Br solutions were placed in the other syringe. For the transformation experiments, a stock solution of lead bromide nanocrystals was prepared at around 1.0 O.D. at 330 nm and placed in the first syringe, while OLA and Br solutions were mixed in the second syringe. Each experiment was performed at least in triplicate for a duration of 60 seconds.

The spectral data was opened in a pandas dataframe, 3 nm were added to the wavelength values to match known peak positions, then a background region from 696 - 735 nm was subtracted from every spectrum to account for oscillatory electronic noise from the detector. The second spectral measurement value in a series was subtracted from all spectra to reduce noise between measurements from residue in the sample chamber. Absorption peaks were fit to the left (lower energy) half of the peak with a gaussian function using peak height, position and width as free parameters in the region of 350 to 410 nm. Fits with a coefficient of determination $R^2 \leq 0.8$ were discarded, as were any peaks with absorbance values lower than 20 mOD. For fitting purposes, absorbance values of all spectra, peak heights and peak positions were averaged between the repeated measurements at the same conditions, and the standard deviations were used as a measure of the experimental error σ to calculate χ^2 statistics used in the fit procedure.

Kinetic Modeling

In collaboration with Dr. Samuel Niblett and Prof. David Limmer, UC Berkeley; Code and description mainly provided by Dr. Samuel Niblett

Concentration profiles were simulated using a simple kinetic model based on multivariate differential rate equations. We separately computed the time-evolution of solution-phase species concentrations and of the plate size distribution (PSD) for a population of nanoplates.

The solution-phase reactions represented the decomposition of benzoyl bromide and subsequent reactions to form a variety of lead halide complexes. Each species was represented using a single concentration, $C_X(t)$, i.e. the liquid was assumed to be well mixed in space. The time derivative of these concentrations took the standard chemical form

$$\frac{dC_X}{dt} = \sum_{i}^{N_r} \nu_X^{(i)} \prod_{j}^{n_r^{(i)}} C_j(t)^{-\epsilon_j^{(i)}}. \tag{3.21}$$

Here, i indexes the liquid-state reactions (of which there are N_r in total), j indexes the $n_r^{(i)}$ reagents of reaction i, $\epsilon_j^{(i)}$ is the reaction order with respect to species j, and $\nu_j^{(i)}$ is the stoichiometric coefficient indicating how many moles of j are consumed or produced by one mole of reaction i. Typically, $\epsilon_j^{(i)} = -\nu_j^{(i)}$ for reagents and 0 otherwise, but this relationship was not required by the model. We required that $\nu_j^{(i)}$ be integer-valued, but not $\epsilon_j^{(i)}$.

Plate growth kinetics were similarly described by a parallel set of differential equations. The key assumptions were taken from Riedinger *et al.*[32] who used simple expressions for the surface, edge and volume energies of a nanoplate to argue that the rate-determining step for nucleation on a thin facet is the formation of a spanning island across that facet. Subsequent expansion of this island to cover the entire facet is thermodynamically favourable and essentially barrierless, allowing calculation of a single activation energy to increase the plate side length by one unit cell. We expect similar energetic considerations to apply in our system and hence have assumed stepwise lateral growth of plates, but due to the differences in chemistry we have not assumed that the same rate laws will pertain as in the Riedinger model.

We write the nanoplate side length as $L = nV^{1/3}$, where V is the volume of a crystalline unit cell and n is an integer indicating the number of cells in a side. For simplicity, we assume that nanoplates are always square prisms, so that each plate geometry is uniquely specified by its plate thickness m and a single L. In the present study we consider chemical compositions without Cs, which are necessary to form three-dimensional nanocrystals, so m is restricted to 1. The PSD for these monolayer plates is denoted $P(n;t)$, being the concentration (in inverse volume units) of plates with n unit cells per side.

Plates are generated from "monomer" units (a designated solution-phase species corresponding roughly to free $PbBr_4$ unit cells) that may aggregate into plate nuclei with $n = 2$ through the following series of elementary steps. We considered three possibilites:

$$A) \quad 2M \longrightarrow M_2, \tag{3.22}$$

$$M_2 + M \longrightarrow M_3, \tag{3.23}$$

$$M_3 + M \longrightarrow P_{2\times 2}. \tag{3.24}$$

$$B) \quad 3M \longrightarrow M_3, \tag{3.25}$$

$$M_3 + M \longrightarrow P_{2\times 2}. \tag{3.26}$$

And

$$C) \quad 2M \longrightarrow M_2, \tag{3.27}$$

$$M_2 + M_2 \longrightarrow P_{2\times 2}. \tag{3.28}$$

In each case, M represents a monomer and P a plate nucleus. These nuclei may then grow or shrink by a layer at a time (increasing or decreasing n respectively). Several rate laws for these processes were considered, captured by the following equation of motion:

$$\frac{\partial P(n;t)}{\partial t} = k_{ad} C_M(t)^{\epsilon_M} \left[P(n-1;t)N(n-1) - P(n;t)N(n)\right] + k_{de} \left[P(n+1;t)N(n+1) - P(n;t)N(n)\right] [OL \tag{3.29}$$

Here C_M is the concentration of monomers and k_{ad} and k_{de} are rate constants for nucleation and desorption of layers on the thin facets, respectively. Mass conservation is enforced by balancing all changes to the PSD with an opposite change in C_M.

The rate-law coefficients $\epsilon_M = 1$ or 2 and $\epsilon_L = 0$ or 1, allowing some flexibility in the mechanism represented by the model. Similarly, the function $N(n) = 1$ or $4n - 4$ controls whether plate growth and shrinking mechanisms are proportional to the number of available edge sites for nucleation, or simply to the total number of plates. Together, different choices of ϵ_M, ϵ_L, $N(n)$ and the nucleation process give 96 possible mechanisms, all of which were examined for their ability to reproduce the experimental data.

To produce a time-dependent concentration profile and PSD, the differential equations 3.21 and 3.29 are simultaneously integrated in discrete time using a 1st order Runge-Kutta integrator with an adaptive timestep controlled by a 2nd-order error estimate. The error at each timestep is approximated as the difference between the new concentrations $C_j(t + dt)$ predicted by the first- and second-order integration schemes. If the maximum estimated error (across all species and plate sizes) exceeds 10^{-8} concentration units, the last timestep is abandoned and $\mathrm{d}t$ reduced by 10%. If the error is smaller than the tolerance, the step is accepted and $\mathrm{d}t$ increased by 10%. Typically $\mathrm{d}t$ is initially small and grows rapidly as the reaction approaches completion and the concentrations level off.

Even with the adaptive timestep, we found that the timestep was often sufficiently large that the plate growth "overshot" the available supply of monomers, causing C_M or some $P(n)$ values to go negative. To avoid this, if a negative concentration was detected we abandoned the current timestep and reduced $\mathrm{d}t$ by half. This simple approach was sufficient to eliminate the problem of spurious negative concentrations and permit stable, efficient solution of the above equations of motion.

Chapter 4

Investigation into Lead Bromide Nanocrystal Precursor Chemistry

In collaboration with Jason Calvin and Dr. Matthias Loipersberger from the Head-Gordon group at UC Berkeley

4.1 Introduction

Connecting reactions occurring in solution with the formation of nanocrystals is fundamental to understanding the overall synthesis process.[14,30,80,150] This intersection of organometallic, inorganic and materials chemistry remains an active area of research for many different nanocrystals.[31] Most importantly, if the rate of reactions in solution is slower than nanocrystal nucleation or growth, the precursors have a profound impact on the dynamic of nanocrystal formation.

As metal nanoparticles are generally formed by reducing metal ions in solution, this work has been driven primarily by consideration of the driving force of the reducing agents in solution.[150] For semiconductor nanoparticles, one fundamental difference from studies on metal nanoparticles is that there are generally two components that are incorporated into the nanocrystal, a metal ion such as Cadmium, Indium or Lead and a main group anion such as sulfur, selenium or phosphorous.[29] In typical CdSe synthesis, elemental selenium is dissolved with an organic phosphine. The resulting phosphine selenide should be considered the active species in the nanocrystal reaction.

To form a monomer that could eventually grow into a nucleus, there first needs to be an association between the two elements. Early work by Owen et al.[30] showed that the decomposition of the phosphine selenide species as had a rate proportional to the concentration of cadmium phosphonate and phosphine selenide, which supported the idea of the formation of a cadmium-selenide complex prior to formation of the monomer, and then a slow decomposition of this complex. Identical rates measured both from the decomposition of the precursor with NMR and the formation of nanocrystal by absorption spectroscopy demonstrate the control of the reaction rate by the precursor conversion. Lowering the electron density at the phosphorous by adding aromatic substituents had the expected effect of lowering the reaction rate. Building off of these observations, organic precursor libraries with controlled decomposition rates were developed, which could be used to tune the formation rate of nanocrystals across several orders of magnitude.[31]

For the lead halide perovskites, systematic investigations have been difficult and produced somewhat disparate results. In part, this may be because all reactions involved are incredibly fast compared to II-VI or III-V nanocrystal synthesis. In addition, lead halide complexes are complicated - the number of halides binding to each lead atom is not well defined. Using X-ray absorption spectroscopy, Sharenko et al. found that lead iodide complexes in dimethylformamide at most synthetically relevant conditions were best explained as hexacoordinated species, though it is unclear whether this was a single lead center or whether there may have been cluster complexes.[151] Multiple such lead iodide cluster complexes with different solvent and counterion inclusions have been isolated, though the lability of the lead halide bond always raises the possibility that different species may exist in solution compared to the solid state.[152–155]

From our previous work on the Reaction Network of perovskite nanocrystals in Chapter 2, it is likely that there is a lead halide complex with an absorption peak at ∼ 313 nm and an emission centered aroun ∼ 450 nm in non-polar solution. Previously, lead bromide complexes absorbing in this wavelength region have been identified as $[PbBr_3^-]$ due to their spectral similarity to species complexes observed (optically) in acetonitrile[156] and their chemical behavior in dimethyl formamide.[108] However, spectra of complexes can shift due to different solvent and coordination environments, as can be seen for shifts between complex inclusion in crystal lattices,[157] solvation in acetonitrile,[156] propylene carbonate,[158] reverse micelles[159] and water.[160] These convoluted optical responses are likely exacerbated by the complicated chemistry of these species: $PbBr_x$ complexes with x ranging from 1 to 7 have been described in water,[160] and polynuclear complexes were found in propylene carbonate.[158] So far, lead bromide complexes in non-polar solutions have only been probed using optical measurements, and only complexation numbers up to 3 bromides per lead have been seriously considered. In addition, the lead bromide complexes were started from dissolution of lead bromide crystals and assumed a starting complex of $[PbBr_2]$.[108,156]

In this work, we will give a perspective on the precursor chemistry involved in the synthesis of $CsPbBr_3$ nanocrystals and related species as discussed in 2 and in 3. We determine rate constants and rate laws of benzoyl bromide decomposition, as well as the equilibrium constants of oleylamine and oleic acid. Further, we discuss the formation of lead bromide complexes derived from our own titration and theoretical results within the context of previous literature results. Finally, we show that large cluster complexes that match expected spectral peaks of magic sized nanosheet clusters exist in solution and can be observed as transient intermediates on the route to multiple perovskite species.

4.2 Results

Equilibrium Constant of Oleylamine and Oleic Acid

Previous research has already described the existence of an acid base equilibrium as well as potential effects of this equilibrium on the synthesis.[92] We repeat these experiments, determining additional data points at higher oleic acid concentration. Through the known linear relationship between chemical peak shift and ratio of fractions of reactions that are fast on the NMR timescale, we can determine the fit of different equilibrium models to the observed data. A simple protonation model with $Keq \sim 15$ and $\Delta G_r^0 = -6.7kJ/mol$ is fully sufficient to describe the data observed here. This equilibrium constant is 3 orders of magnitude lower than expected by comparing pK_a values of the two species - likely due in large part to the reduced stabilization of charged ions in the apolar environment compared to an aqueous system. As shown from the gaussian process surrogate model trained on the experimental data in Figure 4.1, while higher equilibrium constants can also fit the data present, they are significantly less likely and require chemical shift values of oleylammonium to be lower than those measured in solution. These higher equilibrium constants would also not be able to explain the variation in chemical shift observed with temperature. From temperature variation, we can fit $\Delta H_r^0 = -24kJ/mol$ and $\Delta S_r^0 = -60J/(molK)$. An exothermic reaction is reasonable for an acid-base equilibrium, and the decrease in entropy is also reasonable based on the predicted closer association of the charged species in non-polar solution. Fits using homoconjugation of acid-base species with additional equivalents of oleylamine did not yield discernible improvements in the quality of fit - while we cannot exclude this possibility, we find it unlikely to have a significant effect on the equilibrium in dilute solutions.

Reaction of Benzoyl Bromide

Benzoyl bromide and oleylamine react to form oleylbenzamide at room temperature, as confirmed through mass spectrometry and NMR. Benzoyl bromide has a distinctive double peak absorption feature at 295 nm and 282 nm, which shifts to 277 and 270 nm in oleylbenzamide. Reactions with oleic acid were not observed to occur within one minute at 30 °C, though it is likely that they would occur at higher synthesis temperatures. Tracking the decay of the absorption peak at 295 nm allowed us to utilize stopped flow spectroscopy to determine kinetic rates. Rate laws are first order with regards to the concentration of oleylamine and benzoyl bromide, as would be expected from this reaction. A rate constant of around 3 $\mathrm{mM^{-1}\ s^{-1}}$ was measured at 30 °C. Adding oleic acid reduced this rate constant to around 2 $\mathrm{mM^{-1}\ s^{-1}}$, and this value did not substantially change with different ratios of oleic acid to oleylamine. While we would expect the rate of benzyl bromide decomposition to decrease, since protonated amines cannot be utilized for the nucleophilic attacks required for the formation of oleylbenzamide, the fact that there is only a slight decrease suggests that the oleic acid / oleylamine equilibrium is fast enough to not change the rate substantially.

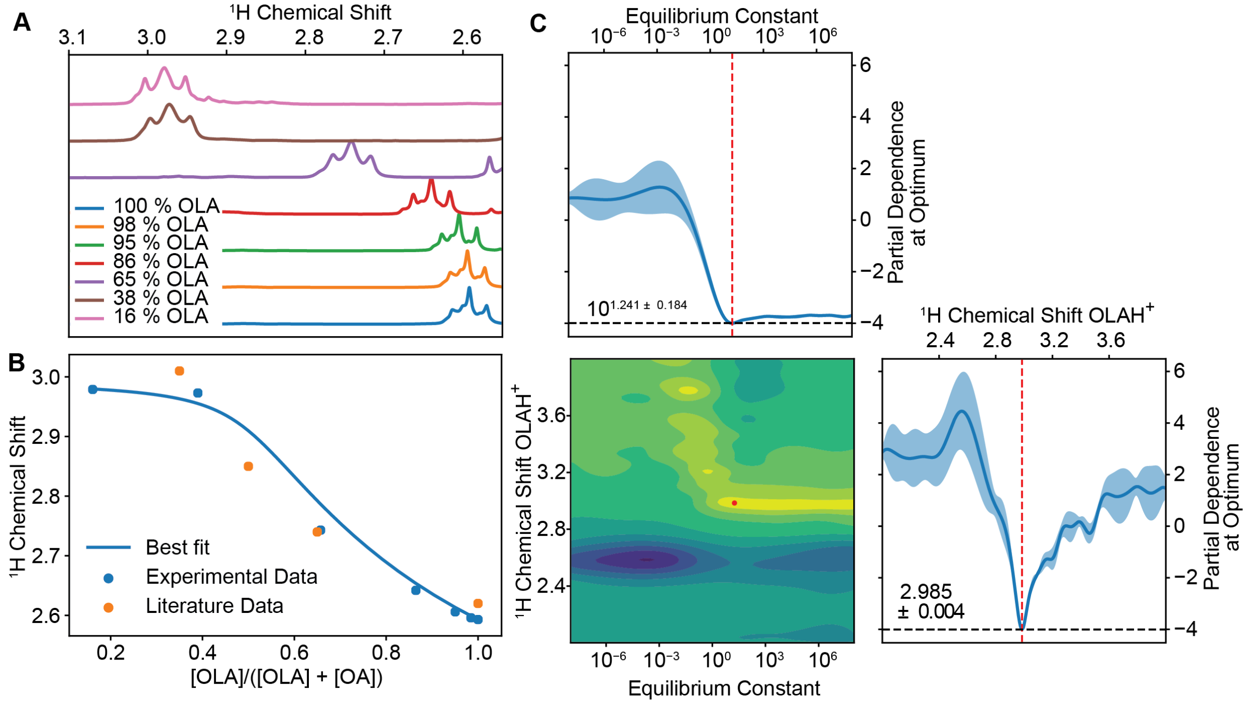

Figure 4.1: *Equilibrium of Oleic Acid and Oleylamine* A) NMR Spectra showing the triplet peak of $NH_2CH_2^\star - R$ at different OLA/OA compositions. B) Equilibrium Equation fit to the NMR shift of the center of the triplet peak in A), including also data from Almeida et al.[92] C) Gaussian Process Surrogate function showing optimal equilibrium constants and oleylammonium $NH_3^+CH_2^\star - R$ ^{1}H Chemical Shift for the fit in B) D) Plot of natural logarithm of calculated equilibrium constant based on fitted $NH_3^+CH_2^\star - R$ ^{1}H Chemical Shift against inverse Temperature showing enthalpy and entropy fit to data reported by Almeida et al.[92]

We thus find the rate equation under the influence of oleic acid to be:

$$\frac{d[BnzBr]}{dt}|_{OA} = 1.8 \pm 0.4mM^{-1}s^{-1}[BnzBr][OLA] \tag{4.1}$$

The use of benzoyl bromide as a precursor for hot injection methods has shown particular promise in reliably forming high quality metal halide nanocrystals.[103] Using Cs injection leads to less reliable synthesis, potentially due to the presence of nanostructures prior to injection as discussed in 2. Different organohalide reagents are starting to be utilized[99,161,162], though the faceting and reaction dynamics may be quite different when compared to traditional synthesis. As we will discuss in chapter 5, trimethylsilyl bromide can also be used for formation of monodisperse perovskite and double perovskite nanocrystals, but the low boiling point makes this a challenging precursor to control at higher temperatures. We have also utilized acyl halides such as 2-ethyl-hexanoyl chloride, appear to provide a greater driv-

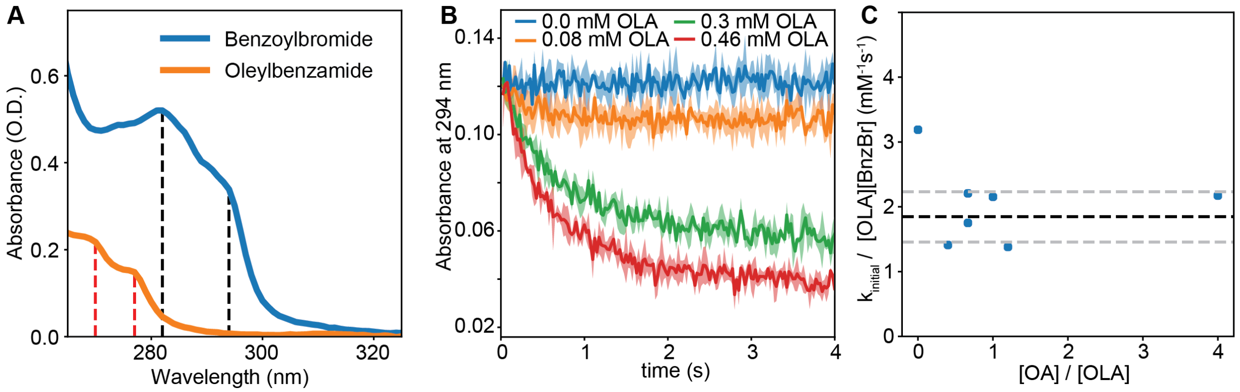

Figure 4.2: *Benzoyl Bromide Degradation* A) Spectra of benzoyl Bromide and Oleylbenzamide, at a nominal concentration of 0.5 mM B) Stopped flow data of changes to the the absorbance at 294 nm with time. C) Calculated rate constant as a function of OA/OLA ratio

ing force and have been crucial to the synthesis of high quality antimony-containing double perovskites. In principle, acyl halides and other organohalide compounds may provide a platform for synthesis modulation of perovskite nanocrystals in a fashion analogous to the thiourea compounds developed for II-VI nanocrystals.[31,163]

Lead Bromide Complexes - Observations

In collaboration with Jason Calvin and Dr. Matthias Loipersberger

By titrating lead oleate - oleylamine solutions with oleylammonium bromide, we were able to gain insight into the complexation equilibrium of the lead bromide complexes starting from a lead species with no bromide complexation. First, we observe the changes in UV-VIS absorption spectroscopy. Prior to titration, a lead oleate complex shows an absorption peak at around 250 nm. Addition of oleylammonium bromide generated *in-situ* gradually causes a red-shift, with the addition of six equivalents of bromide leading to a peak at 295-300 nm. Further addition of bromide then leads to the formation of the previously identified species with the characteristic absorption peak at around 313 nm, which saturates at around 30 bromide equivalents. A high oleylamine to lead ratio was required in order to prevent formation of species with absorption features above 313 nm A.3.1.

From isothermal titration calorimetry (ITC), we can gain a sense of reaction progress by measuring directly the reaction enthalpy. There is a strong exothermic signal during the initial addition of oleylammonium bromide, reaching up to 30 kJ per mole oleylammonium bromide added. This signal is reduced quickly upon further addition of oleylammonium bromide to approximately 5 kJ/mol at six equivalents of bromide, and then decays down close to baseline at the end of the titration (around 28 bromide equivalents). Isothermal titration calorimetry in principle allows the determination of the heats of reaction, as well

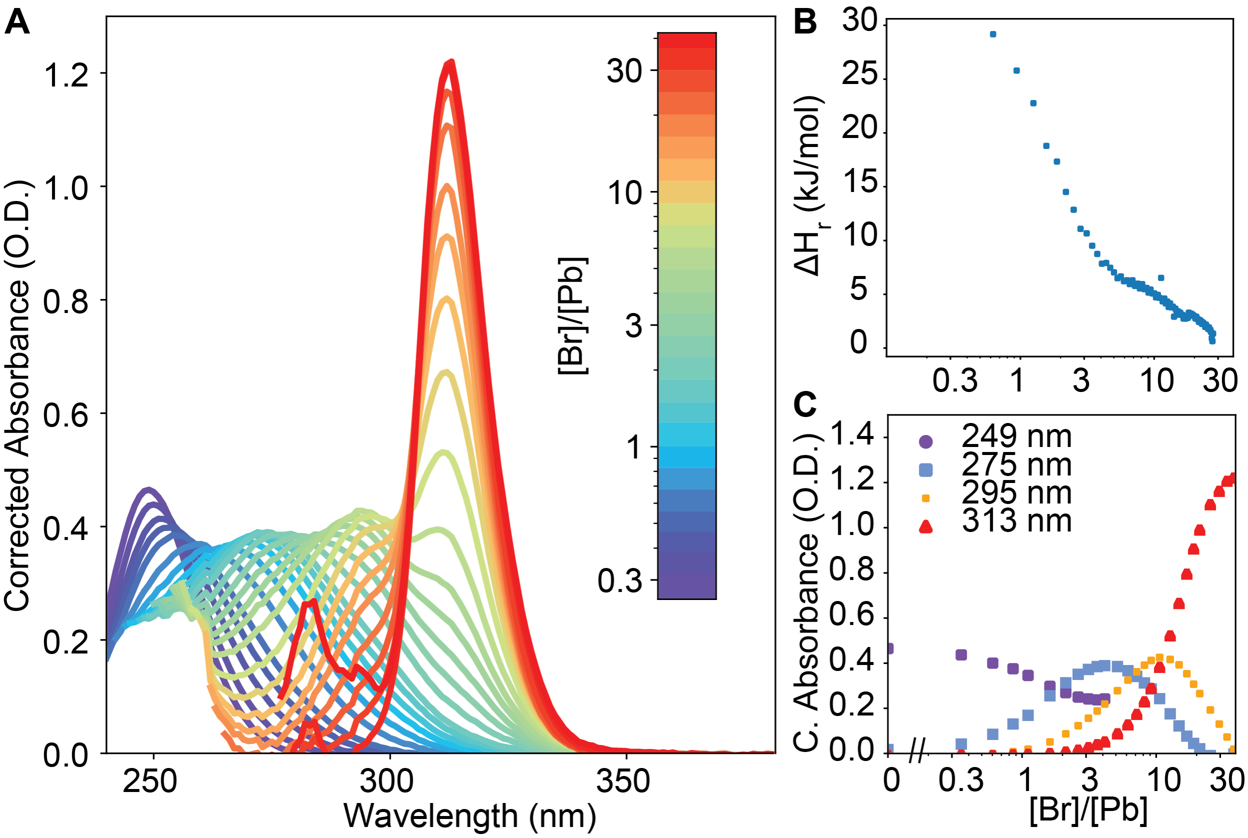

Figure 4.3: *Titration Data* A) Background corrected UV-VIS Absorption Spectra of bromide titration into lead oleate B) Reaction enthalpy measured by isothermal titration calorimetry of bromide titration into lead oleate. C) Change of the Absorbance of several peaks observed in panel A) as a function of bromide equivalents added

as equilibrium constants and the number of additions to a complex, in carefully controlled environments. However, reactions must be well separated to be able to perform this analysis properly. Due to the overlap of multiple reactions, the ITC data shown here can not be interpreted as showing a particular type of reaction. What is clear, though is that there is a qualitative difference between the reactions occurring within the first 6 equivalents of oleylammonium bromide and the reactions occuring thereafter, corresponding to the formation of the species with the 313 nm peak in the optical spectrum.

Using DFT calculations, we can gain additional insight into the reaction. We set up a manifold of different possible lead complexes coordinated by amine, carboxylate and bromide groups, with ammonium groups present as counterions in a non-polar dielectric medium with $\varepsilon_{rel} = 2$. For each PbBrx combination, we identify the complex with the lowest Gibbs formation energy. We observe that lead complexes binding up to two amine groups are

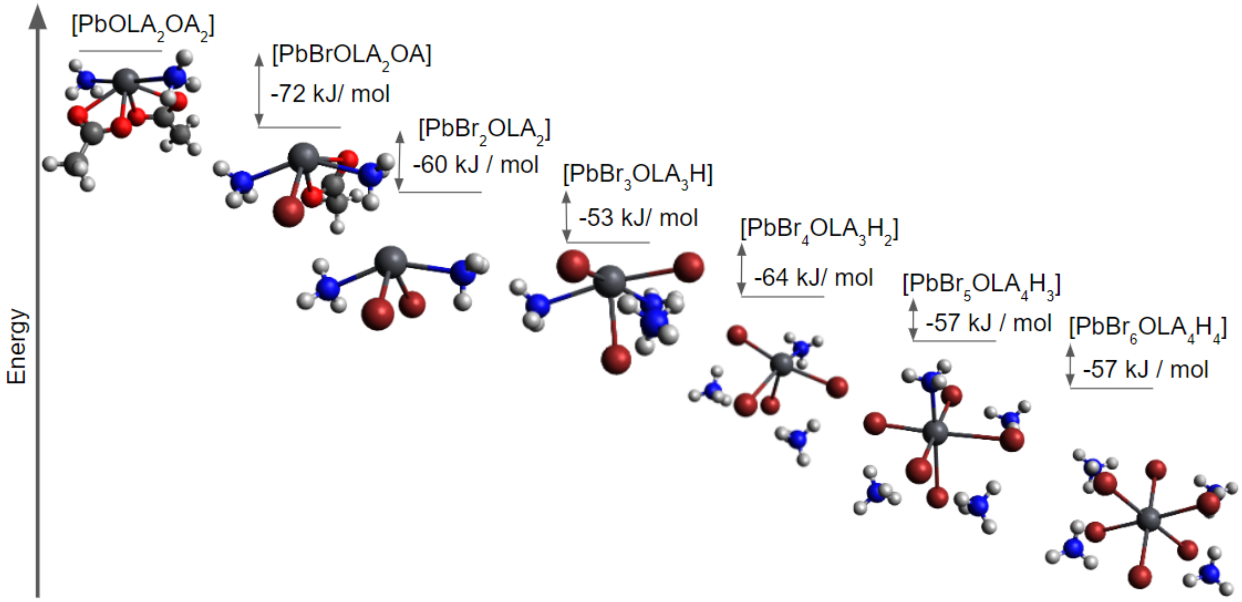

Figure 4.4: *DFT Structures and Energies of Lead Bromide Complexes*

stabilized by 12 - 24 kJ/mol relative to complexes without binding amine groups, and binding more than two amine groups appears generally to destabilize the complex, regardless of coordination number. Complexes with coordination numbers above 6 frequently decompose during geometry relaxation, so we do not consider them here. By using ammonium bromide as an uncharged addition agent, we can then analyze the Gibbs energy of reaction for each bromide addition. This energy is quite negative for each addition up to $PbBr_6^{4-}$, at around 50 - 70 kJ/mol per additional bromide added. This suggests that equilibria of lead binding more bromide counterions are highly favourable beyond 3 bromide ions - which is reasonable from hard-soft acid base theory, in which lead and bromide ions are well matched. The favourable binding also matches experimental observations in aqueous solution measuring bromide ion concentrations, which report $PbBr_7^{5-}$ as the complex at high bromide concentrations. We also note that forming dimers appears generally favourable as well, in line with previous observations of multinuclear complexes. A structurally interesting note: complexes appear to transition from a see-saw geometry with 0-2 bromides to a square pyramidal geometry with 3 and 4 binding bromides to the octahedral coordination found in the solid state lead bromide compounds we study with 5 and 6 bromide ions bound. This suggests that while both oxygen atoms in the acetate binding groups are within binding range of the atom, the acetate group as a whole only occupies a single binding site of the lead complex, as opposed to binding in a bidentate μ_2 fashion.

Lead Bromide Complexes - Analysis

Using the optical absorption data as a starting point, we tested the following model equilibria with different binding bromide binding dynamics:

2Br : $Pb^{2+} + 2Br^- \overset{K_1}{\rightleftharpoons} PbBr^+ + Br^- \overset{K_2}{\rightleftharpoons} PbBr_2$

3Br : $Pb^{2+} + 3Br^- \overset{K_1}{\rightleftharpoons} PbBr^+ + 2Br^- \overset{K_2}{\rightleftharpoons} PbBr_2 + Br^- \overset{K_3}{\rightleftharpoons} PbBr_3^-$

4Br : $Pb^{2+} + 4Br^- \overset{K_1}{\rightleftharpoons} PbBr^+ + 3Br^- \overset{K_2}{\rightleftharpoons} PbBr_2 + 2Br^- \overset{K_3}{\rightleftharpoons} PbBr_3^- + Br^- \overset{K_4}{\rightleftharpoons} PbBr_4^{-2}$

5Br : $Pb^{2+} + 5Br^- \overset{K_1}{\rightleftharpoons} PbBr^+ + 4Br^- \overset{K_2}{\rightleftharpoons} PbBr_2 + 3Br^- \overset{K_3}{\rightleftharpoons} PbBr_3^- + 2Br^- \overset{K_4}{\rightleftharpoons} PbBr_4^{-2} + Br^- \overset{K_5}{\rightleftharpoons} PbBr_5^{-3}$

6Br : $Pb^{2+} + 6Br^- \overset{K_1}{\rightleftharpoons} PbBr^+ + 5Br^- \overset{K_2}{\rightleftharpoons} PbBr_2 + 4Br^- \overset{K_3}{\rightleftharpoons} PbBr_3^- + 3Br^- \overset{K_4}{\rightleftharpoons} PbBr_4^{-2} + 2Br^- \overset{K_5}{\rightleftharpoons} PbBr_5^{-3} + Br^- \overset{K_6}{\rightleftharpoons} PbBr_6^{-4}$

7Br : $Pb^{2+} + 7Br^- \overset{K_1}{\rightleftharpoons} PbBr^+ + 6Br^- \overset{K_2}{\rightleftharpoons} PbBr_2 + 5Br^- \overset{K_3}{\rightleftharpoons} PbBr_3^- + 4Br^- \overset{K_4}{\rightleftharpoons} PbBr_4^{-2} + 3Br^- \overset{K_5}{\rightleftharpoons} PbBr_5^{-3} + 2Br^- \overset{K_6}{\rightleftharpoons} PbBr_6^{-4} + Br^- \overset{K_6}{\rightleftharpoons} PbBr_7^{-5}$

3Br-Dimer : $2Pb^{2+} + 7Br^- \overset{K_1}{\rightleftharpoons} 2PbBr^+ + 5Br^- \overset{K_2}{\rightleftharpoons} 2PbBr_2 + 3Br^- \overset{K_3}{\rightleftharpoons} 2PbBr_3^- + Br^- \overset{K_D}{\rightleftharpoons} Pb_2Br_7^{-3}$

4Br-Dimer : $2Pb^{2+} + 9Br^- \overset{K_1}{\rightleftharpoons} 2PbBr^+ + 7Br^- \overset{K_2}{\rightleftharpoons} 2PbBr_2 + 5Br^- \overset{K_3}{\rightleftharpoons} 2PbBr_3^- + 3Br^- \overset{K_4}{\rightleftharpoons} 2PbBr_4^{-2} + Br^- \overset{K_D}{\rightleftharpoons} Pb_2Br_9^{-5}$

5Br-Dimer : $2Pb^{2+} + 11Br^- \overset{K_1}{\rightleftharpoons} 2PbBr^+ + 9Br^- \overset{K_2}{\rightleftharpoons} 2PbBr_2 + 7Br^- \overset{K_3}{\rightleftharpoons} 2PbBr_3^- + 5Br^- \overset{K_4}{\rightleftharpoons} 2PbBr_4^{-2} + 3Br^- \overset{K_5}{\rightleftharpoons} 2PbBr_5^{-3} + Br^- \overset{K_D}{\rightleftharpoons} Pb_2Br_{11}^{-7}$

As single wavelength / single variable linear methods cannot be applied to any of these equilbria, we created a computational method that allowed the fitting of spectra over multiple equilibrium variables. For each model, we optimized the equilibrium constants by simulating the distribution of complexes under a given equilibrium law, fitting the spectra of each species either through linear interpolation and iterative subtraction of defined spectra or through linear regression of each wavelength, and finally determining the resulting overall fit to the titration data. While linear regression is traditionally used for problems like this, we have found that fits using iterative linear decomposition of spectra resulted in more realistic predicted spectra of the different lead bromide species and lower overall residuals.

One clear result from this analysis is that an equilibrium with 4 lead species (i.e. identification of the 313 nm peak with $\mathrm{PbBr_3^-}$) is not sufficient to fit the overall titration data. Equilibria going to $\mathrm{PbBr_5^{3-}}$ or $\mathrm{PbBr_6^{4-}}$, or including potential polynuclear species are required to accurately represent the data. Our best result was obtained from a model including complexes coordinating up to 5 bromide ions, though we cannot for certain exclude the possibility that models of 6 bromide ions or 5 bromide ions and dimer formation are applicable. We note also that based on the extinction spectra of all models, all estimated extinction coefficients for the 313 nm peak are significantly higher than those for the other lead bromide complexes. This suggests that there is a significant change to the electronic structure, more so than would be expected upon addition of another bromide ion. Proposing a multinuclear species as the basis for the absorption peak at 313 nm thus appears reasonable.

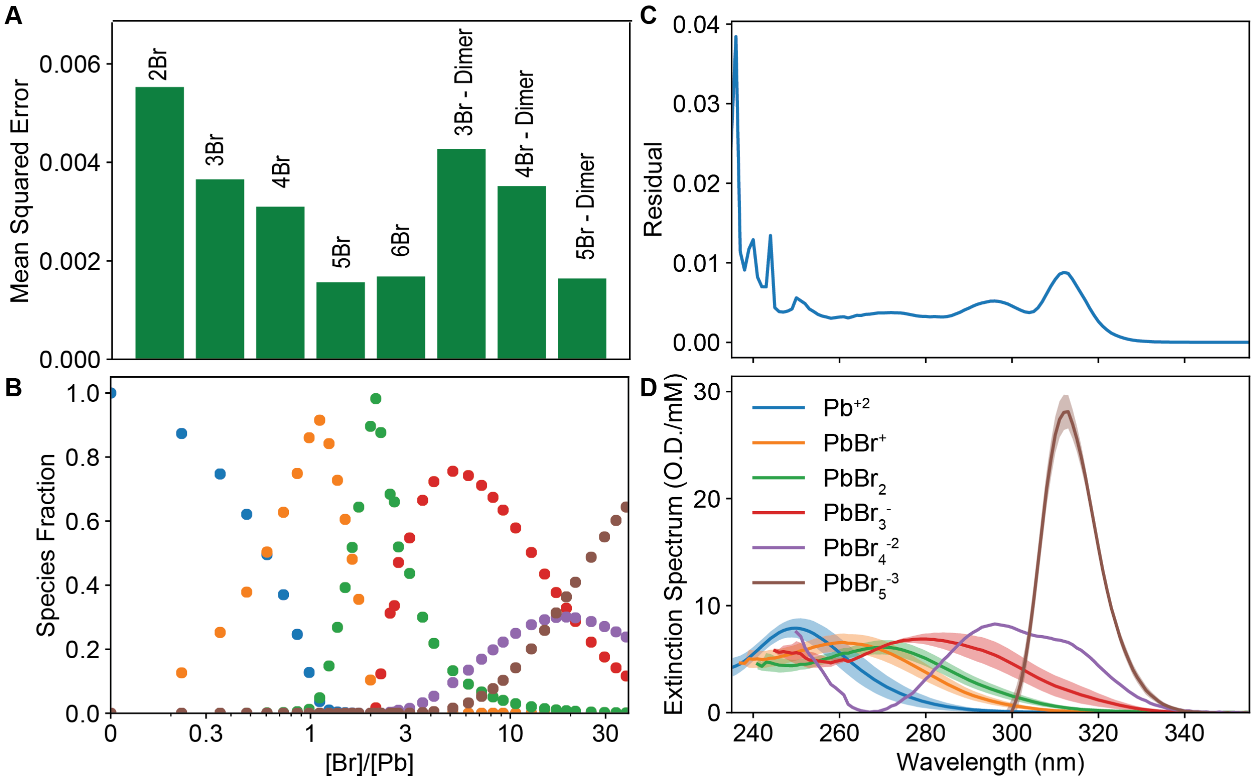

Figure 4.5: *Analysis of PbBr*$_x$ *Complex Titration Data* A: Mean squared error for different models tested B) Simulated concentrations of species from the best performing model in (A), 5Br, at points at which the measurements were conducted C) Residual error of each wavelength for 5Br model D) Calculated Extinction Spectra for the different species in the 5Br model

Effect of Bromide Concentrations on Reaction Extent

Using high-throughput synthesis routines established in chapter 2, we further probed the synthesis of lead bromide at varied concentrations of oleylamine and bromide. This factorial search showed that the three main binary lead halide products previously identified,

$PbBr_2$ nanocrystals, 2-D OLA_2PbBr_4 nanosheets and the lead bromide complex are the main products of this reaction at bromide to lead ratios above 6 - except in cases in which there is an excess of bromide to oleylamine, in which case nanocrystals or not observed. Below the ratio 6:1 ratio of bromide to lead other products appear. Using the previously developed deconvolution algorithm and manually adding new reference spectra until the collection of spectra is well described, these products can be grouped into species with three distinct absorption features: 1) species with rising absorption band starting at around 310-330 nm 2) species with a broad peak around 360 nm. 3) species with a sharp peak around 345 nm. The first looks visually similar to the products in the lead oleate titration and is likely lead bromide complexes with a single lead atom, though we cannot perform our optical previous optical analysis to figure out which coordination number is most likely due to noise in the spectrum below 300 nm. At low OLA : Pb ratios, this products are adjacent to $PbBr_2$ nanocrystals at a Br : Pb ratio of around 2, as would be expected stoichiometrically. Surprisingly, the transition to OLA_2PbBr_4 can also occur at this stoichiometry at slightly higher OLA:Pb ratios - this is likely a result of the chemical exfoliation investigated in Chapter 3. At higher OLA : Pb ratios, the second species is inserted between the 2 D perovskite nanosheet and the first species. The point at which 1 ML, and the species 2 form then shifts gradually to a Pb : Br ratio of 4 : 1. Species 3 occurs primarily between the 313 nm product and the lead bromide complexes, at a Pb:Br ratio above 4:1. Based on the results of the titration experiments, it appears unlikely that products 2 and 3 are complexes with a single lead atom. With the effective mass model in Chapter 3, the species at 345 and 365 nm may be assigned to a 3x3 or 4x4 nm plate, respectively. We will use the terms 3x3 and 4x4 magic sized cluster (MSC) from now on, though this is very much a provisional assignment based on the observed data. While magic sized clusters usually have very sharp peaks, we believe that the lability of lead halide species may cause them to experience subtle differences in coordination environment, which could easily lead to shifts in the spectra, and thus a peak that can change in width and position.

Magic sized nanosheet intermediates

We were able to observe the formation of 3x3 and 4x4 MSCs using stopped flow absorption spectroscopy (Figure 4.7. Both of these species appear at 0.5 - 1 s after a species with an absorption edge starting around 340 nm is formed, which is most likely $PbBr_3$ or $PbBr_4$ based on our titration analysis. We further observed that species with 345 and 365 nm absorption features occur during the formation of different products. Most obviously, the formation of single layer nanosheets through direct nucleation will generally form a species with an absorption spectrum at 370 nm. This species is longer lived at higher olelyamine concentrations and lower temperatures, where a rather sudden transition to larger species can be observed. A species with an absorption peak at 345 nm is clearly present in synthesis of 2 and 3 layer thick nanoplatelets as well as in some synthesis of nanocubes. There appears to be a transition to a species with a peak around 370 to 380 nm, which then shifts in wavelength continuously until the final product is reached. The central position of very

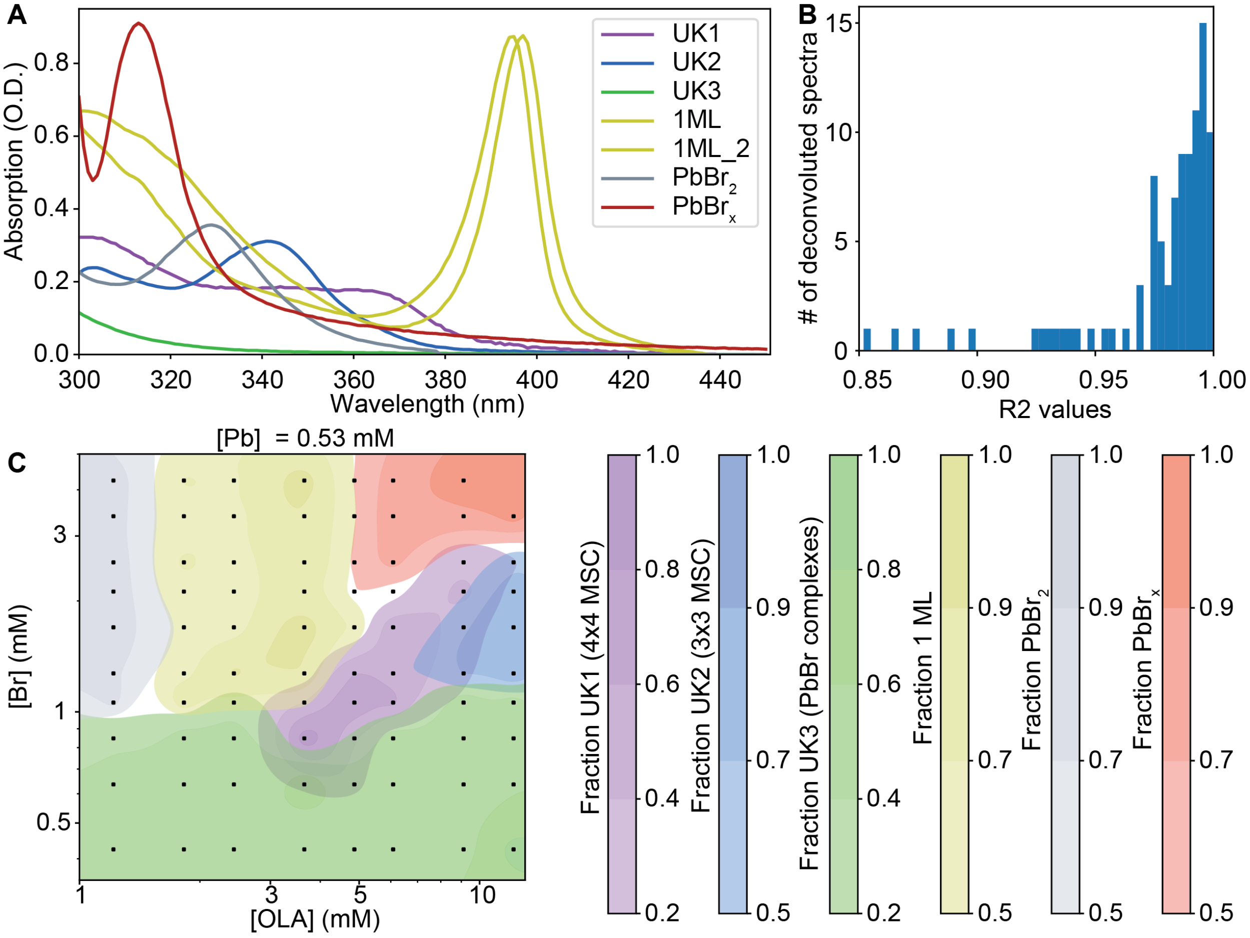

Figure 4.6: *High Throughput Synthesis at low Br : Pb ratios* A) Spectra used to analyze the synthesis B) R^2 values of high-throughput spectra C) Map of product distribution as a function of bromide and oleylamine concentration

small nanosheets in the synthesis of diverse nanoplate and nanoparticle products matches well with previous theory developed for CdSe nanoplatelet formation.[32,111,112] However, while we have occasionally observed kinetics that are in line with Ostwald ripening between thin and thick nanosheets (Figure A.3.2), our observations suggest that in most cases the formation of nanosheets of the final observed thickness or even a transition to an isotropic shape occurs rapidly while the nanosheets are still small in lateral extent.

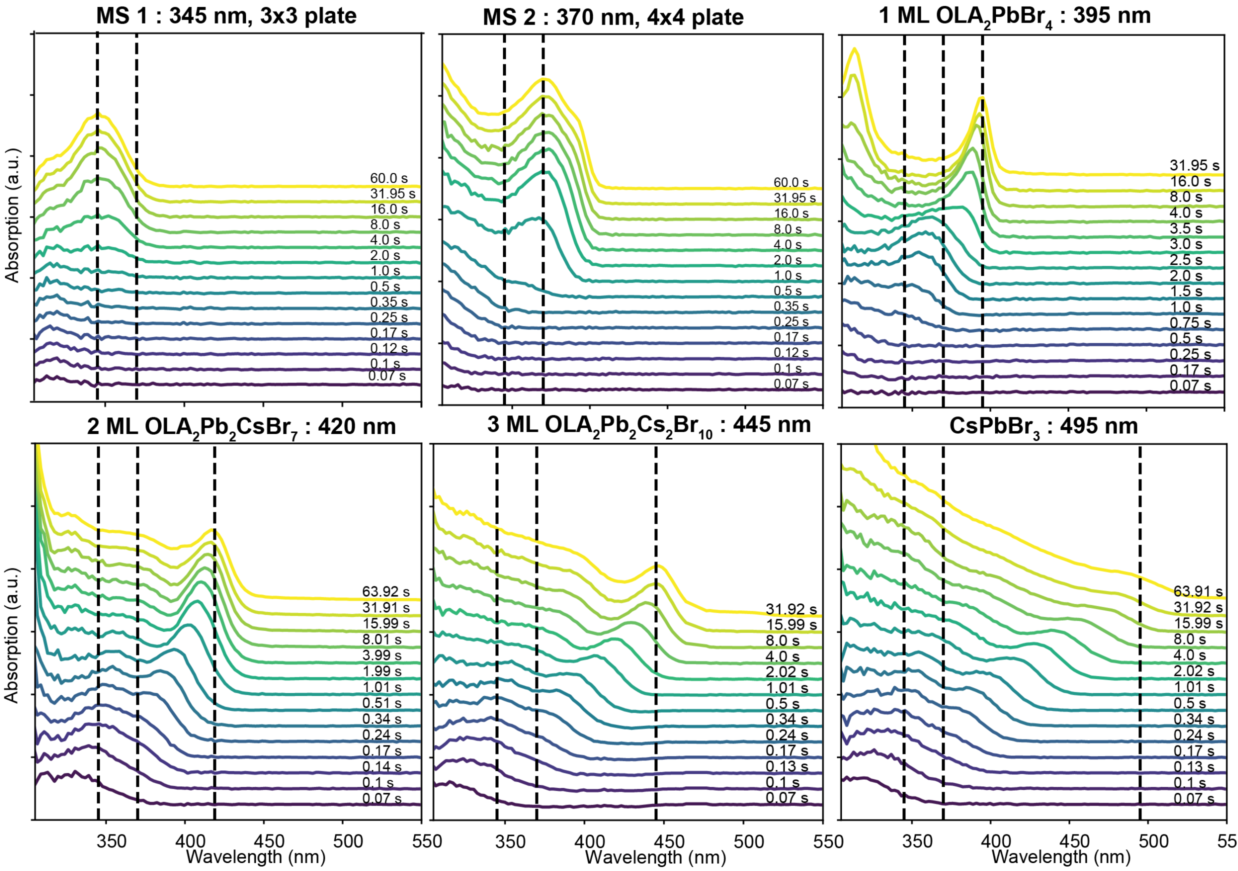

Figure 4.7: *Kinetic Data with potential Magic Sized Cluster Intermediates*

4.3 Conclusion and Outlook

In this work, we have investigated the precursor chemistry and early reaction kinetics of lead bromide species, including cesium lead bromide perovskites. We determine equilibrium constants for the oleylamine / oleic acid equilibrium based on NMR measurements as well as for lead bromide complexation based on optical and calorimetry measurements. Further, we determine the rate constant of decomposition for benzoyl bromide. We show that current models of lead bromide complexation in non-polar solvents must be expanded to include higher-coordinating and multinuclear lead bromide species to accurately describe existing data, which is further supported by DFT calculations. The extent of bromide excess over lead leads to important changes in the final lead bromide nanoparticle products observed as well, with observation of species that may correspond to 3x3 and 4x4 magic sized clusters. We also observe similarly absorbing species in synthesis of single layer lead bromide nanosheets and in perovskite nanocubes as well as 2 and 3 atomic layer thin nanoplatelets.

This work also points out possible synthetic targets, such as the species absorbing at 313, 345 and 365 nm that could be used in order to confirm the chemical identity and structure we propose here, or suggest changes to the model. We also suggest further development in the area of halide precursors, which could be expanded and tuned to change the reaction dynamics. Overall, we develop insight into the cascade of reactions important for perovskite nanocrystal formation. Understanding the basic solution chemistry involved in forming these complex nanocrystals will be crucial to more rational control over metal halide nanocrystal synthesis and their properties.

4.4 Experimental

Nuclear Magnetic Resonance Spectroscopy

In a 1 mL NMR tube, 15 µL of oleylamine were added to 500 µL of Toluene. ^{1}H NMR measurements were performed on a 400 MHz Bruker AVB Spectrometer. After each measurement, more oleic acid was titrated into the mixture, and the measurement repeated.

UV-VIS Titration of Lead Oleate

Lead oleate was prepared as described in chapter 2. 3 µL of lead oleate solution, 40 µL oleylamine and 20 µL oleic acid were added to 4 mL of hexane. 300 µL of this solution were diluted into 2 mL in a quartz glass cuvette for a final lead concentration of 0.065 mM. A benzoyl bromide titration solution was prepared by mixing 3 µL of benzoyl bromide with 2 mL of hexane for a final solution concentration of 12.6 mM, or 0.084 Pb equivalents of bromide per µL. This solution was added stepwise to the solution of lead oleate - oleylamine, and absorption measurements were taken between every addition. The reaction was close to instantaneous. A reference sample including the same amount of oleylamine and oleic acid, but no lead oleate was titrated with the same benzoyl bromide solution to measure and subtract the absorbance of organic oleylbenzamide generated during the reaction. Oleylamine and oleic acid were subtracted from all measurements based on the absorption of the reference prior to titration. A linear exctinction value of oleylbenzamide was calculated from titration of the reference solution (see Figure 4.8), and the calculated absorbance was subtracted from the titrated lead bromide solution. Absorbance values over 1.5 O.D. in raw data measurements were excluded from analysis.

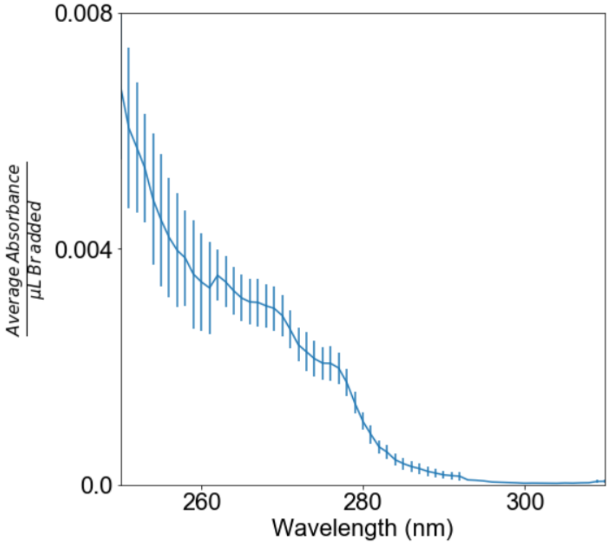

Figure 4.8: *Extionction Spectrum of Oleylbenzamide*

Isothermal Titration Calorimetry of Lead Oleate

Measurements Performed by Jason Calvin

Pre-reacted benzoyl bromide solution was prepared by mixing 66 µL OLA with 33 µL OA in 10 mL dodecane and adding 13.7 µL benzoyl bromide and briefly shaking the solution for a final content of 10 mM bromide, 20 mM OLA and 10.4 mM OA. Lead Oleate solution was added by mixing 3 µL lead oleate solution in OLA (0.66 M Pb content) with 66µL OLA and 30 µL OA in 10 mL dodecane for a final content of 0.2 mM lead, 20 mM OLA and 10.4 mM OA. All measurements were performed using a TA Instruments Nano isothermal titration calorimeter (ITC). For measurement, 1.198 ± 0.006 mL of sample solution was placed in the sample cell (effective volume of 965 ± 5 µL) and 1.198 ± 0.006 mL dodecane was placed in the reference cell with the reference needle. The syringe was loaded with 250 µL of pre-reacted benzoyl-bromide solution in dodecane. The temperature was maintained at 25 °C through the titration. After stirring was initiated at 250 rpm, the samples were allowed to equilibrate until the differential heating slope was $\leq$ 0.1 µW/h and the standard deviation in the differential heating was $\leq$ 0.01 µW over a period of lasting $\sim$ 40 min. After equilibration, an initial baseline was taken for 2400 s, and then 2.2 ± 0.2 µL of titrant solution was injected per injection. Between each injection the solution was stirred for 2400 s to allow the system to return to equilibrium. Integration of titration peaks calculates the heat of reaction. The standard error in the heat of injection is 23 µJ and was determined by injecting water into water. Background subtractions were performed by injecting the ligand solution into a dodecane solution containing equivalent concentrations of oleylamine and oleic acid (20 mM OLA and 10.4 mM OA) in an identical manner to the sample measurements and subtracting the integrated heat from the sample measurements.

DFT Calculations of Lead Halide Complexes

Calculations performed by Dr. Matthias Loipersberger Density functional theory (DFT) calculations for free energies were performed with the Q-Chem package[164](version 5.3.0) using the B3LYP functional[165–167] with a mixed basis for the optimization and frequency calculations (def2-SVP basis for C,H,O, def2-SVPD for N and Br, def2-TZVP basis set for Pb).[168,169]. In addition and the def2-ecp was used for Pb throughout.[170] Gibbs free energies of formation (ΔG^0_f) were used to compute Gibbs free energies of reaction ΔG^0_r. Solvation energies were approximated by performing single-point calculations applying the implicit SMD[171] solvent model (using dodecane) with the larger def2-TZVPPD basis for all elements as implemented in Q-Chem.[164] A combinatorial set of possible charge neutral lead complexes with amine, carboxylate and ammonium ligation with coordination numbers up to 6 was evaluated for each PbBr_x complex, with x being all integers from 0 to 6, assuming a formal +2 charge of lead. Reaction energies were calulated with respect to charge neutral amine, ammonium bromide and ammonium acetate species in solution. The reaction energies of complexes with a number of bromides was evaluated with regard to the complex with the minimum number of ligands for charge balance. The structures of complexes with the most negative Gibbs free energy of reaction compared to the minimal complex are displayed in Figure 4.4, and the reaction energies of ammonium bromide addition (and ligand displacement, where applicable) were calculated between successive complexes.

Analysis of Titration Measurements

All absorption spectra in which there was no absorbance above 340 nm was used in the analysis, background subtracted and selected as described above. This data was fit directly to equilibrium constants. First, the chosen equilibrium constants and the titration conditions were used to calculate substance concentrations using chempys equilibrium system solver.[172]. Based on these calculated concentrations, for each species we determined the points where only that species and species with a lower coordination number are occuring at fractions above 5%. The extinction spectra were then calculated by iteratively finding, for each species, the points at which no other absorbance should be present, then taking the average of the absorbance values divided by the concentration values at each wavelength, and then subtracting the reference spectra from the rest of the dataset. We constructed a loss function based on the logarithm of the mean-square error of fit to the combined spectra and the average variance in absorbance values of the extinction spectra, combined with a penalty for negative absorption values in the extinction spectra. In cases where it was not possible to determine the spectra, a high value was returned. This function was optimized with respect to the equilibrium constants using active learning with a gradient boosting regression tree surrogate function as implemented in scikit-optimize with bounds between 10^{-2} and $10^{1}0$, 250 function calls with expected improvement as the acquisition function.

Stopped Flow Experiments

All stopped flow experiments were performed on an Applied Photophysics SX 20 stopped flow spectrophotometer using a photodiode array with 25 ms integration time for 1000 time points. The stopped flow chambers were stored under ethanol, then filled with toluene and emptied three times, then filled with dodecane and emptied three times before measurement. Stock solutions of Br, OLA, OA, Cs-OA and Pb-OA were prepared as in Chapter 2, but diluted to 8.5 or 0.85, 3.0, 3.2, 1.0 and 0.66 mM in dodecane, respectively. All stock solutions were added to the syringes used for loading the stopped flow chambers with volumes varying between 10 - 100 uL and mixed with dodecane to a final volume of 2 mL. For synthesis experiments, OLA, OA, Cs-OA and Pb-OA solutions were placed in one syringe and Br solutions were placed in the other syringe. Each experiment was performed at least in triplicate for a duration of 60 seconds.

High-Throughput Synthesis and Optical Analysis

For high-throughput synthesis, dodecane solutions of lead oleate (200 x diluted from a Pb-OA stock solution), benzoyl bromide (800 x diluted), oleylamine (100 x diluted) and oleic acid (80 x diluted) were freshly prepared. Using a Hamilton NIMBUS4 Microlab liquid handling robot, dodecane, oleylamine, lead oleate, oleic acid and cesium oleate solutions were added in varying proportions to a 96 well plate equipped with single-use 1 mL glass vials. The entire plate was heated to the reaction temperature while shaking at 300 rpm and kept at the reaction temperature for 800 s. Under continued shaking, benzoyl bromide solution was added to each vial, for a final reaction volume of 500 µL. This addition sequence was typically performed within 600 s. The plate was kept at the reaction temperature and shaken for another 600 s after the addition. 30 µL of each 500 µL final reaction solution were removed, diluted with 270 µL dodecane and placed into a 96-well Hellma quartz microreader plate. A Biotek Synergy 4 microplate reader was used to evaluate the reaction solutions. An automatic calibration was carried out before each plate was measured, then absorption spectra were recorded from 200 to 500 nm in 1 nm increments with a single reading per data point, while emission spectra were recorded from 350 - 500 nm in 1 nm increments with an excitation wavelength of 315 nm, a detector sensitivity of 70 and a single reading per data point.

Chapter 5

Synthesis and Characterization of a Family of Cesium Silver Main-Group Metal Halide Double Perovskites

Adapted in part with permission from:

Bekenstein, Y.; Dahl, J. C.; Huang, J.; Osowiecki, W.T.; Swabeck, J.K.; Chan, E.M.; Yang, P.; Alivisatos, A. P. "The Making and Breaking of Lead-Free Double Perovskite Nanocrystals of Cesium Silver–Bismuth Halide Compositions" *Nanoletters* **2018**, Copyright 2018 American Chemical Society

and

Dahl, J.C.; Osowiecki, W.T.; Cai, Y.; Swabeck, J.K.; Bekenstein, Y.; Asta, M.; Chan, E.M. ; Alivisatos, A.P. "Probing the Stability and Band Gaps of $Cs_2AgInCl_6$ and $Cs_2AgSbCl_6$ Lead-Free Double Perovskite Nanocrystals" *Chemistry of Materials* **2019**, Copyright 2019 American Chemical Society

5.1 Introduction

Metal halide nanocrystals[85,128] are a class of material for which it is possible to create and explore a wide variety of compositions. The prototypical lead system is well studied because of the attractive optoelectronic properties, which include high photoluminescence (PL) quantum yield[88,98] and high tolerance to defects.[47,48] Recent synthetic advances have demonstrated the ability to precisely control the size,[88] shape,[104,173] cation[174,175] and anion[41,42,176] compositions of the nanocrystals to fine tune the respective band gaps and optical properties. Following the surprising observations of good photovoltaic conversion efficiency, potential applications for lead halide perovskites have expanded to include color-tunable light emitting devices, optically pumped low threshold lasers, and efficient photodetectors.[177–179]. In practice, the viability and use of lead halide perovskites in large scale manufacturing is currently limited by two main concerns: the toxicity of lead and the materials' low stability to common operating conditions such as moisture and heat.[39,180]

To circumvent this problem, stable and lead free perovskite systems are a current focus of research in new materials chemistry.[89,102,181,182] Exploration of these systems, and their relative stabilities, offers rich opportunities for learning more about the chemical and physical principles that influence material properties and stability in metal halides. The investigation of these questions is all of the more timely, since the practical application of lead halide perovskite nanocrystals is severely limited by their long-term instability[183] and regulations restricting the use of lead in devices.[184] Identifying environmentally stable, synthetically accessible metal halide nanocrystals that avoid the use of lead while retaining the physical properties of lead halide perovskite archetypes might allow the realization of the many proof-of-concept solar and device applications in development.[185]

Several groups of related materials that substitute lead with other metals have been explored in the recent literature.[186–188] In principle, 3rd- or 4th-row p-block metal halides should have similar electronic structures, due to a potential defect tolerant band structure arising from the Fermi level lying between two antibonding orbitals (mostly composed of metal ns2 and np0) and strong spin-orbit coupling.[189] Tin halide and germanium halide perovskites are the closest structural and electronic analogs to lead halide perovskites and are predicted to demonstrate efficient absorption and emission as well as defect tolerance;[189] Unfortunately, these materials are even less stable to light, heat, and moisture than lead halide perovskites.[137,190–192] $Cs_3M_2X_9$ (M = Sb, Bi) and Cs_2MX_6[193] (M = Sn, Pb, Te) structures are ternary metal halide structures that can accommodate p-block metals, and several interesting examples, including Cs_2SnI_6,[51,194,195] $Cs_3Bi_2I_9$,[196,197] and $Cs_3Bi_2I_9$,[197,198] have been synthesized successfully both in bulk and at the nanoscale. The lower level of structural connectivity of the metal halide octahedra in these structure types reduces conductivity and exciton radii, which may limit their utility in electrical devices. Cs_2AgMX_6 (M = Bi, Sb, In) is a promising structure for lead-free halide perovskites since the metal halide octahedra are connected across all three dimensions.[186] This 3D connectivity may explain why photovoltaic devices made from these materials have exhibited some of the highest power conversion efficiencies reported for lead-free halide materials despite the indirect nature of their band gaps.[197,198]

Besides Cs_2AgBiX_6, two other silver-containing double perovskite crystal structures have recently been reported in bulk: $Cs_2AgSbCl_6$ and $Cs_2AgInCl_6$.[199–201] Although neither of these materials is well suited for photovoltaic applications due to their large band gaps, they may have applications in optoelectronic technologies such as the low-noise UV photodetectors recently demonstrated for $Cs_2AgInCl_6$.[202] Here, we report the successful synthesis of $Cs_2AgSbCl_6$ and $Cs_2AgInCl_6$ nanocrystals and investigate their structure, absorption, and emission properties.

Concerning the understanding of stability, most work has been predicated on the idea that the Goldschmidt tolerance factor[203] can be used as a first guide to predict not only whether a material will form but also what the stability will be. In recent publications, both thermodynamic measurements[180] and more extensive theoretical calculations or literature comparisons[204,205] support the idea that the intrinsic stability of these halide systems does indeed correlate well with the Goldschmidt tolerance factor. However, this does not take into account the relative propensity to decompose according to specific pathways. When a perovskite decomposition product consists of metal–ligand complexes or other molecular species with varied bonding arrangements, the stability of those products can also vary widely across a series of metals, and it is the net reaction thermodynamics that is most relevant. The instability of many members of this class of compounds in the presence of water is of particular practical concern. Even slight exposure to humidity is sufficient to decompose materials such as $CsPbI_3$.[34] Many reports include discussions of stability by documenting X-ray diffraction (XRD) data after a period of storage[200] or immersion of the material in water, ethanol, or another solvent.[34,206] In this work, we develop an assay based on an amine degradation reaction observed previously in $CsPbBr_3$ nanocrystals[35,44] to quantitatively evaluate the stability of $Cs_2AgBiCl_6$, $Cs_2AgSbCl_6$ and $Cs_2AgInCl_6$ nanocrystals relative to $CsPbCl_3$.

5.2 Results and Discussion

Synthesis

To synthesize double perovskite nanocrystals nanocrystals, we use an injection of acyl halides[103] or silyl halides[181] into a solution of metal acetate precursors, rather than adding cesium oleate to a solution of metal halides.[88] Briefly, in an open vial under atmospheric conditions, metal acetates are added to a solution of xylene, oleic acid, and oleylamine, heated to 100 °C, then an acyl halide or silyl halide is injected (see Figure 5.1). This substitutes the water- and air-sensitive antimony(III) chloride or bismuth(III)halide with the more stable acetates as a precursor and provides more tunability over the reaction by enabling the change of type or concentration of halide precursor. In addition, due to the high reactivity of the acyl halides and silyl halides with water, it is possible that some of the increased reproducibility of this synthesis under atmospheric conditions is due to scavenging of residual water from the reaction during halide precursor decomposition. Adding a solution of (aqueous) hydrochloric acid yielded good results for $Cs_2AgBiCl_6$, but not for bromide compositions or the other main group metal.

The ionic nature of the metathesis reaction dictates the rapid nucleation and growth kinetics of the resulting nanocrystals. As a result, the reaction time plays almost no role in determining the resulting NC sizes, and most of the reaction is completed after 40 s, analogous to the reaction time of colloidal lead halide nanocrystals. Longer growth times lead to only small increases in size. The reaction reaches completion after less than 1 min, and nanocrystals are separated from the reaction solution through centrifugation and redispersion. To showcase the broad utility of this synthesis, we also make $CsPbCl_3$ using the same method, which show similar properties as previously reported nanocrystals.

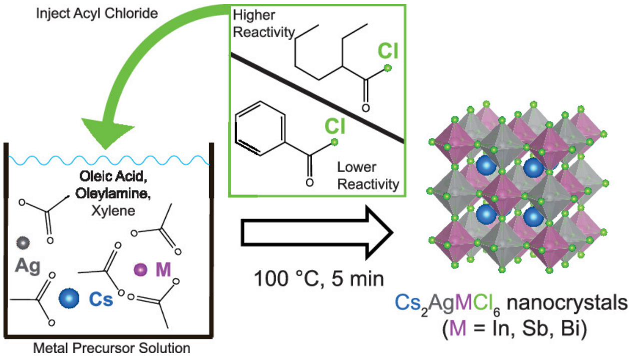

Figure 5.1: Reaction scheme for the synthesis of double perovskite nanocrystals. A solution of metal acetates (cesium, silver and indium, antimony or bismuth) in non-polar solvent with oleic acid and oleylamine is heated to 100 °C, then a halide precursor is injected to form nanocrystals of the corresponding Cs_2AgMX_6 (M = In, Sb, Bi,X = Cl,Br) double perovskite.

For the synthesis of $Cs_2AgSbCl_6$, the control afforded by acyl halide injection is crucial: the addition of an equimolar amount of benzoyl chloride or trimethylsilyl chloride leads to the formation of lamellar structures or stacks of small plates, whereas two equivalents produce a mixture of nanoplatelets and nanocubes; when a more reactive precursor, 2-ethylhexanoyl chloride, is added instead, nanocubes form (Figure A.4.9). This behavior bears some resemblance to the influence of the temperature on the synthesis of $CsPbBr_3$ nanocrystals, with similar lamellar structures found at very low temperatures, which then transition to plates and cubes as the temperature rises.[104] It is possible that the decomposition kinetics of the acyl halide precursor could control the shape of the crystal through a growth instability arising from the competition of nucleation islands on facets of different size, similar to recent reports on the formation of CdSe nanoplatelets.[32] Slower kinetics may allow the formation of plates or even lamellar structures when the difference in activation barrier to form a new layer on a smaller crystal facet instead of a larger crystal facet is a significant part of the overall energetic process; faster kinetics may overwhelm this difference in activation energy, causing isotropic shapes at higher temperatures, higher concentrations of the halide species or with a more reactive halide precursor.

Structural Characterization

In collaboration with Dr. Yehonadav Bekenstein In transmission electron microscopy (TEM) images, we observe cubic nanocrystals with edges approximately 10 nm in length and a size dispersion of about 15%. Reactions forming $Cs_2AgBiCl_6$ with hydrochloric acid form smaller nanocubes with approximately 5 nm side length There is close agreement between sizes determined by TEM (Figure A.4.2) and from Scherrer analysis of X-ray diffraction (XRD) patterns (Figure A.4.3) for $Cs_2AgInCl_6$, $Cs_2AgBiCl_6$ and $Cs_2AgBiBr_6$ crystals (Figure A.4.3) and for $Cs_2AgSbCl_6$ crystals with AgCl impurity synthesized under similar conditions as the $Cs_2AgInCl_6$ crystals. $Cs_2AgSbCl_6$ nanocrystals synthesized in a phase pure manner were larger and less monodisperse (See Figure 5.2.

$Cs_2AgBiBr_6$, $Cs_2AgBiCl_6$, $Cs_2AgInCl_6$ and $Cs_2AgSbCl_6$ nanocrystals appear to exhibit only the elpasolite or double perovskite $F_{m3\bar{m}}$ structure in powder X-ray diffraction measurements of nanocrystal thin films, as determined by comparing the peak positions to the bulk

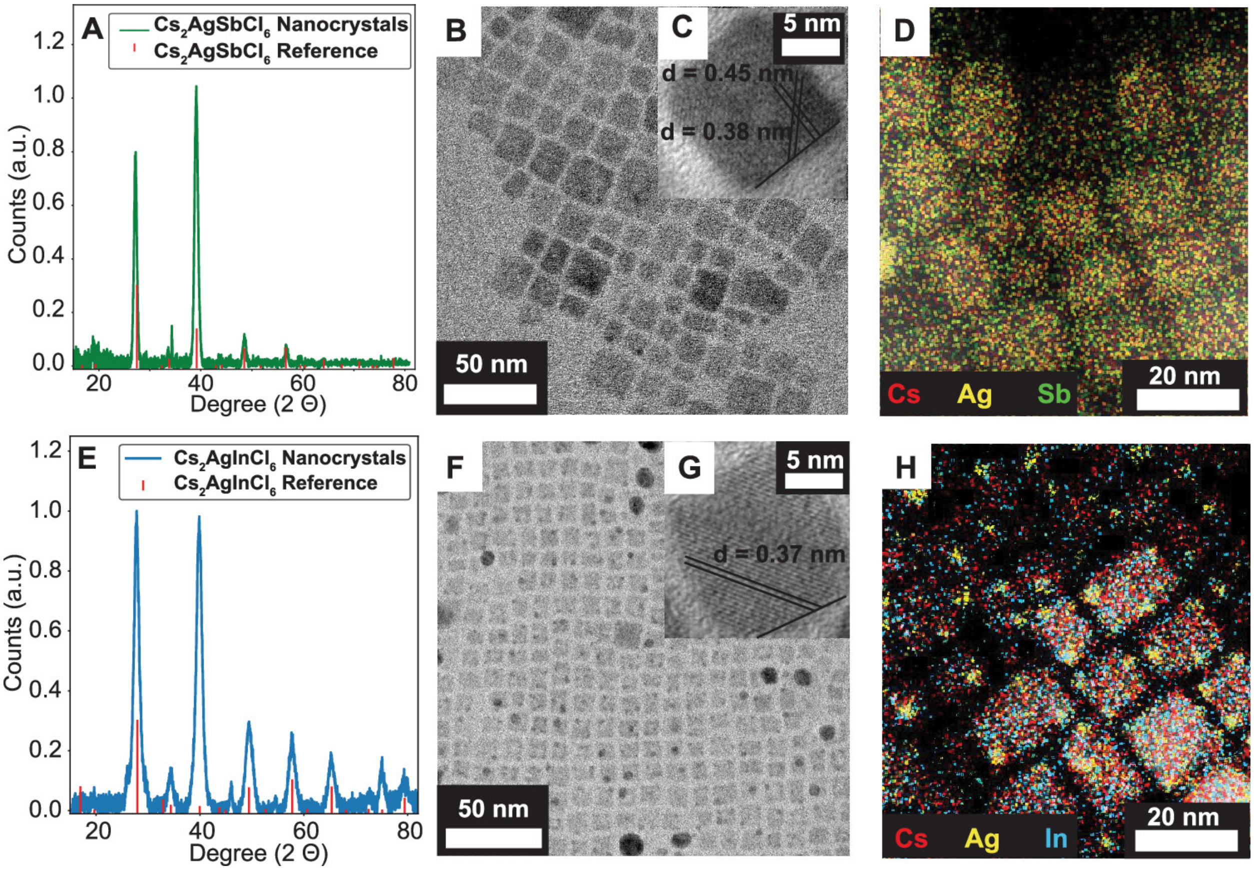

Figure 5.2: *Structural Characterization of* $Cs_2AgSbCl_6$ *and* $Cs_2AgInCl_6$. (A) XRD pattern of nanocrystals measured with a Co source ($\lambda_{K\alpha}$ = 1.7789Å) with references COD 1546185 ($Cs_2AgSbCl_6$), (B) TEM image showing cubic nanocrystals, (C) high-resolution transmission electron microscopy (HR-TEM) image of a nanocube on a [100] zone axis showing 0.45 nm ($\langle 200 \rangle$) lattice planes parallel to the edge of the cube and 0.38 nm ($\langle 220 \rangle$) planes diagonal to the edge of the cube, and (D) STEM–EDS map of $Cs_2AgSbCl_6$ showing co-localization of cations. (E) XRD pattern of nanocrystals measured with a Co source ($\lambda_{K\alpha} = 1.7789$Å) with reference COD 1546186 ($Cs_2AgInCl_6$). (F) TEM image showing cubic nanocrystals. (G) HR-TEM image of a nanocube on a [100] zone axis showing 0.37 nm ($\langle 220 \rangle$) lattice planes diagonal to the edge of the cube and (H) STEM–EDS map of $Cs_2AgInCl_6$ showing co-localization of cations as well as silver spots.

$F_{m3\bar{m}}$m phases (Figure 5.2). Orientation effects appear to change the relative peak intensities in the nanocrystal thin films we measure compared to the bulk phase. Under some synthesis conditions, we observe AgCl impurities, which can be removed following synthesis through careful centrifugation and redissolution of the nanocrystals in the case of $Cs_2AgInCl_6$ but not for $Cs_2AgSbCl_6$. We eliminated impurities in $Cs_2AgSbCl_6$ by changing the ratio of M(III) to Ag(I) precursor (Figure A.4.1). Due to the negligible optical response in the region important for $Cs_2AgSbCl_6$, we can measure the properties of $Cs_2AgSbCl_6$ nanocrystals without interference in a mixed sample of AgCl and $Cs_2AgSbCl_6$ nanocrystals (see SI for a more thorough discussion of the AgCl impurity).

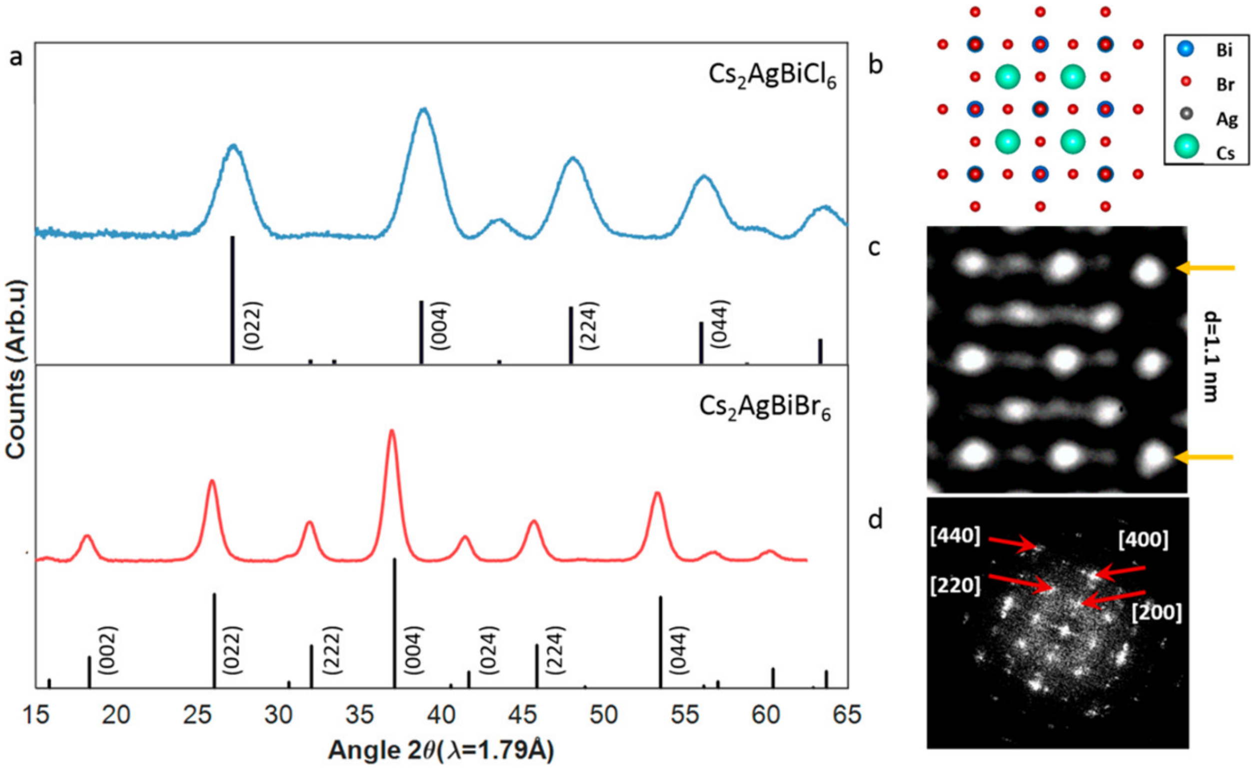

Figure 5.3: *Structural Characterization of $Cs_2AgBiBr_6$ and $Cs_2AgBiCl_6$* (a) XRD patterns of $Cs_2AgBiBr_6$ (red) and $Cs_2AgBiCl_6$ (blue) NCs compared to the reported pattern. (b) Model of an extended unit cell of $Cs_2AgBiBr_6$, viewed down the 100 zone axis. (c) HRTEM of a unit cell depicting a contrast difference between columns with Bi/Ag and Cs compared to those with only halides. The (001) lattice spacing is measured to be 1.1 nm. (d) FFT analysis of lattice fringes from a few oriented NCs demonstrates the cubic nature of this crystal structure on the nanoscale

Single NC high-resolution transmission electron microscopy (HRTEM) studies show similar lattice spacing of 5.5 Åfor $Cs_2AgBiBr_6$; these studies also confirm the crystals are bounded by [200] surfaces. In most cases, this zone axis is closely aligned with the TEM optical axis due to the cubic morphology of the crystals. These properties simplify structural studies at the atomic level. For example, three types of atomic columns exist parallel to the ⟨200⟩ axis: Br columns, Cs columns, and mixed Ag,Bi,Br columns. Indeed, the HRTEM demonstrated columns of different contrast similar to those depicted in the cartoon. High-resolution TEM images of $Cs_2AgInCl_6$ nanocrystals display a lattice spacing of 3.7 Åcorresponding to a ⟨220⟩ plane. For $Cs_2AgSbCl_6$ nanocrystals, we observe 3.8 and 4.5 Ålattice spacings that correspond well to ⟨220⟩ and ⟨200⟩ planes. The correspondence of the lattice spacings throughout the crystal to high-reflectivity, low-index planes supports the claim that these nanocrystals are phase pure and single crystalline. The orientation of these planes relative to the edges further suggests that the cubes are terminated by [200] facets, similar to reports on lead halide perovskites

Silver Halide Impurities

In many of the synthesis used, an impurity of AgCl was found. The AgCl phase is present as a second phase of nanocrystals, as determined by XRD Scherrer Radii ($\sim$ 15 nm) and TEM images where it can be seen as large round spheres (Figure A.4.4). AgCl appears to form at a molar ratio to $Cs_2AgSbCl_6$ of approximately 1:1, as determined by the excess of Ag over Sb in the EDS analysis of large-scale images (Figure A.4.6).AgCl has a direct bandgap of 3.25 eV and an indirect bandgap of 5.15 eV,[207] as well as an exciton radius of 1.5 nm.[208] In a Tauc analysis for $Cs_2AgInCl_6$, it would be possible to observe a contribution of AgCl to the bandgap, which we should expect to be strongly indirect and around 3.25 eV due to the negligible quantum confinement at that size of AgCl crystal, but those samples do not show any X-ray diffraction peaks from AgCl and also do not show any bandgap at 3.25 eV. However, for the $Cs_2AgSbCl_6$ band gaps, contributions from any gap significantly above the measured gap around 2.5 eV would not be visible.Purification of AgCl from $Cs_2AgInCl_6$ was accomplished by concentrating the sample by evaporating all but 50 µL of the nanocrystal solution in hexanes with a stream of N2 gas, separating out the precipitate by centrifuging at 14,000 rpm for 10 minutes and redissolving the pellet in $\sim$ 1 mL of hexane. Any insoluble solids were discarded, and this procedure was repeated another time. The $Cs_2AgSbCl_6$ crystals with AgCl impurities were more similar in size ($\sim$ 10 nm) to the other nanocrystals, and were thus used for further analysis on bandgaps, STEM-EDS and degradation, as individual crystals could be confirmed as $Cs_2AgSbCl_6$ phase for STEM-EDS and the optical properties used for bandgaps and degradation were not noticeably different from the pure phase.

Probing Bandgaps

In collaboration with Dr. Yehonadav Bekenstein, Dr. Yao Cai and Dr. Joseph Swabeck There are discrepancies in reports of optical spectra between nanocrystal[181] and bulk measurements[186] which could lead to the interpretation that there is significant quantum confinement in these systems. To the naked eye, the $Cs_2AgBiBr_6$ NC suspension with its distinct yellow color is clearly optically different from the orange-red color of bulk material. Dilute solutions of $Cs_2AgBiBr_6$ NCs have a typical absorption spectrum featuring a sharp absorption peak positioned at $\sim$ 430 nm and a long absorption tail at longer wavelengths, suggesting an indirect transition consistent with the reported bulk properties. A similar functional form with a sharp peak is observed for the Cl compositions, with the peak positioned at 365 nm. A similar discrepancy is also observed in the absorption spectra of nanocrystal solutions for $Cs_2AgInCl_6$ and $Cs_2AgSbCl_6$, which have a rising shoulder from 310 to 290 nm for $Cs_2AgInCl_6$ nanocrystals as reported previously[182] and peaks at 360 and 300 nm for $Cs_2AgSbCl_6$ nanocrystals, which are both significantly removed from the reported bulk band edge.[201] The dual absorption peaks for $Cs_2AgSbCl_6$ nanocrystals are similar to the shape of reflectometry peaks found in bulk samples.[201] A Tauc analysis[209] on absorption spectra of dilute solutions of $Cs_2AgSbCl_6$ and $Cs_2AgInCl_6$ nanocrystals indicates band gaps of 2.83 ± 0.02 and 4.15 ± 0.05 eV, respectively (Figure A.4.7). This is a significant blue-shift from the reported bulk band gaps of 2.5 and 3.5 eV,[201] which at first glance would lead to the conclusion that these double perovskite nanocrystals show significant quantum confinement. A confinement energy as large as 1 eV may occur and was reported for quantum confined perovskite nanoplates.[104,173] However, it is expected to be strongly dependent on the size and dielectric environment confining the exciton.

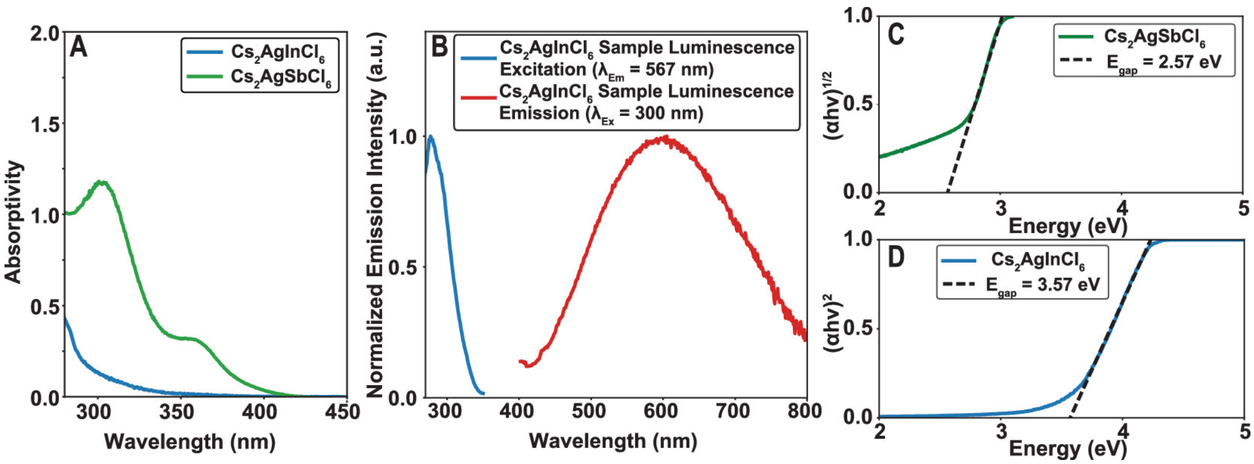

Figure 5.4: *Optical Properties of $Cs_2AgSbCl_6$ and $Cs_2AgInCl_6$ nanocrystals*(A) UV–visible absorption spectra of $Cs_2AgSbCl_6$ and $Cs_2AgInCl_6$ nanocrystals, with peaks centered at 360 and 300 nm for $Cs_2AgSbCl_6$ and no discernible peak for $Cs_2AgInCl_6$. (B) Photoluminescence (PL) and photoluminescence excitation (PLE) spectra of $Cs_2AgInCl_6$ samples. The maximum PL occurs at 550 nm, the maximum PLE at 300 nm. (C) Tauc plot of the absorption spectrum of concentrated $Cs_2AgSbCl_6$ nanocrystals showing an indirect band gap of 2.57 ± 0.05 eV. (D) Tauc plot of absorption spectrum of concentrated $Cs_2AgInCl_6$ nanocrystals showing a direct band gap of 3.57 ± 0.03 eV

We do not observe a corresponding blue-shift of the broad emission of $Cs_2AgInCl_6$ ($\leq$0.1 eV) compared to the emission in bulk. The photoluminescence quantum yield of $Cs_2AgInCl_6$

nanocrystals was measured to be 0.6%, which is within measurement error of the quantum yield reported previously.[182] The excitation spectrum of this emission decays into the background at approximately 350 nm or 3.5 eV. This band edge is 0.7 eV lower than the calculated band gap from absorption measurements but nearly identical to the bulk band gap.[199] Similarly, $Cs_2AgBiBr_6$ exhibits detectable photoluminescence centered around 650 nm, with a full width at half-maximum of $\sim$ 200 nm. The weak and broad emission is further consistent with an indirect transition or trap emission, similar to the emission reported for bulk.[186] While current research suggests that the broad emission may be due to self-trapped excitons[210], exposure to phosphonic acids gradually quenches the emission intensity (see Figure 5.7). As phosphonic acids are known to passivate surface traps in CsPbBr3[37], this could indicate at least some contribution to this luminescence from surface traps. The photoluminescence excitation spectrum coincides with the absorption peak at 430 nm, further verifying that light absorbed at the 430 nm peak is emitted from the nanocrystals, and the excitation measurement counts decay into the background at around the same energy as the reported bulk bandgap.

These different optical measurements do not agree with each other, with absorption spectra suggesting confinement energies of 1.0 eV for $Cs_2AgBiBr_6$ and $Cs_2AgBiCl_6$, 0.7 eV for $Cs_2AgInCl_6$ and 0.3 eV for $Cs_2AgSbCl_6$, whereas emission and excitation spectra of $Cs_2AgInCl_6$ and $Cs_2AgBiBr_6$ suggest less than 0.1 eV of confinement. Turning to density functional theory to investigate which level of confinement one should expect in the different double perovskites, we calculate the effective electron and hole masses and dielectric constants (see Table 5.3). The resulting exciton Bohr radii, 1.02 nm for $Cs_2AgSbCl_6$, 0.90 nm for $Cs_2AgBiCl_6$ and 0.82 nm for $Cs_2AgInCl_6$, are an order of magnitude smaller than the size of the crystals, suggesting that quantum confinement should be minimal for these cesium silver metal halide double perovskites.

To further test this dependence, we intentionally varied the NC synthetic conditions for $Cs_2AgBiBr_6$. We used different precursors, temperatures, and ligands that changed both the size and dielectric environment of the NCs. The position of the absorption did not significantly shift with changes in size, demonstrating that the peak does not in fact originate from a confined exciton. Similarly, confined structures of $Cs_2AgSbCl_6$, do not show a blueshift of either the shoulder at 360 nm or the peak at 300 nm, as would be characteristic for a quantum confined exciton peak.

We propose that these discrepancies arise from differences in measurement technique (transmission vs reflection) and concentration of the sample instead of from the underlying optical response. This hypothesis receives further support from thin film transmission measurements of single-crystalline $Cs_2AgBiBr_6$,[211] which shows very similar optical signals to the dilute nanocrystal solutions. Here, we elaborate on how these discrepancies may arise and different techniques to use to ensure comparability between optical absorption measurements from the nanocrystal and solid-state chemistry fields.

Since the absorption spectra are the only measurements supporting the interpretation of strong quantum confinement, we considered the differences in measurement conditions between bulk and nanocrystal to enable a more confident measurement and analysis of band

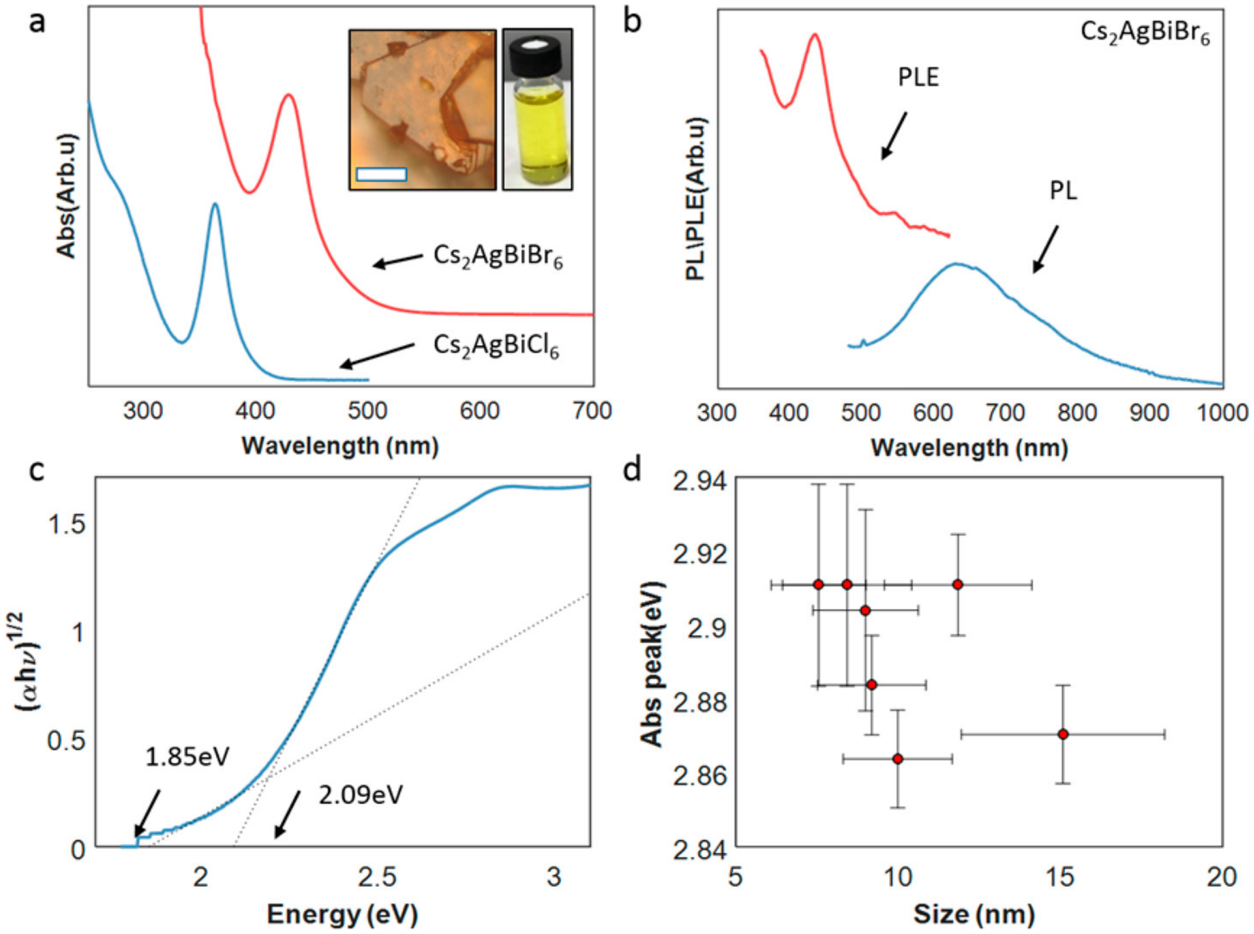

Figure 5.5: *Optical properties of the $Cs_2AgBiBr_6$ NCs.* (a) UV/vis absorption of dilute $Cs_2AgBiBr_6$ (red) and $Cs_2AgBiCl_6$ (blue) NCs suspensions demonstrating the characteristic peaks at 430 and 365 nm, respectively. Inset showing a suspension of $Cs_2AgBiBr_6$ NCs, with distinct yellow color different from the orange-red bulk material. (b) Photoluminescence from excited $Cs_2AgBiBr_6$ NCs (blue) ($\lambda_{exc} = 430nm$), which is similar to photoluminescence described in the literature for bulk crystals. Photoluminescence excitation scan collected at 650 nm (red) traces the absorption peak at 430 nm, but does not decay into the baseline until 550 nm (c) Tauc plot of diffuse absorption measurements of NC films assuming indirect band gap characteristics gives similar measurements of direct (2.09 eV) and indirect (1.85 eV) to that of bulk crystals. (d) Plot of center of absorption peak vs smallest side length of cubes shows no strong dependence of the absorption peak on size, which rules out quantum confinement as a strong contribution to the high energy position of this peak.

gaps in nanocrystals in the cases where there is no emission and excitation data, such as in $Cs_2AgSbCl_6$. Band gaps of bulk materials are commonly calculated from Tauc plots[209] made with data obtained by reflection measurements of pure powders, whereas colloidal nanocrystals are measured in dilute solutions in transmission mode and have historically not been analyzed with Tauc plots. The difference in concentration is large, changing from pure material in bulk to an optically dilute sample for nanocrystals, a range of at least 3 orders of magnitude in the number of unit cells sampled. Preparation of nanocrystal solution samples is usually quite dilute to enable peak analysis of the most strongly absorbing species. As the variation in peak extinction coefficients of transition metal complexes (up to 7 orders of magnitude)[212] exceeds the dynamic range of most absorption spectrometers (0.001–4 absorbance units in the instrument we utilize), it stands to reason that spectra optimized for observing the strongest absorption peaks in nanocrystals may have insufficient signal to accurately measure the absorption at the band edges for weakly absorbing bands. In the case of the cesium silver metal halide double perovskites, the band edge absorption features are indeed expected to be weak since the transitions close to the band edge should be Laporte forbidden for $Cs_2AgInCl_6$ due to the 4d–5 s transition at the band edge[202] and momentum forbidden for the antimony and bismuth double perovskites due to their indirect band gap.[186,201]

To overcome these problems and more accurately measure the absorption at the band edges of $Cs_2AgInCl_6$ and $Cs_2AgSbCl_6$ nanocrystals, we perform Tauc analysis using absorption spectra of nanocrystal solutions that are 300 times more concentrated than those used to observe the absorption maxima. Although these spectra do not provide information on transitions that lie higher in energy due to the noise limit of the detector, this scheme is necessary to obtain precise linear fits of the absorptance spectra at the weakly absorbing band edges. The Tauc analysis of concentrated nanocrystal absorption spectra results in band gaps consistent with those measured for bulk samples,[200,201] with an indirect gap of 2.57 ± 0.05 eV for $Cs_2AgSbCl_6$ and a direct gap of 3.57 ± 0.03 eV for $Cs_2AgInCl_6$. It is possible that for instance the high energy ”band edge” of $Cs_2AgInCl_6$ observed in our dilute samples as well as by others[182] is not due to the inorganic material at all, but rather due to impurities from organic material used in the synthesis, such as residual solvent or impurities in oleylamine (Figure A.4.8). Another possible approach is performing this Tauc analysis on diffuse reflectance measurement of a nanocrystal powder, which we performed for $Cs_2AgBiBr_6$ (Figure 5.5 c). This reflectance measurement shows transitions at 1.85 and 2.09 eV and a bandgap value of 1.97 eV, which is similar to the bulk material.[186]

One possible concern when using concentrated colloidal solutions or nanocrystal powder reflectance measurements for Tauc analysis is that lower-band gap impurities may confound the measurement. However, since the Tauc plot is designed to ignore low probability contributions at lower energies, such as the Urbach tail, it is also insensitive to contamination by lower-band gap impurities, since the slope of any impurity absorptions that are not at their band edge in Tauc plots is significantly different than the slope for the band edge. A good test case is the analysis of $Cs_2AgSbCl_6$: There is a small-band gap impurity of unknown origin in the $Cs_2AgSbCl_6$ spectrum, visible in the deviation of the spectrum from the baseline below the band gap of $Cs_2AgSbCl_6$. Despite the evident impurity, it is possible to assign the slopes to different materials, allowing for an unambiguous identification of the band gap. We confirm that Tauc analysis can be a valuable tool in analyzing energies of band gaps in nanocrystals, if appropriate measurement conditions are chosen. From our optical and theoretical analyses, we further conclude that all of the Cs_2AgMX_6 nanocrystals synthesized here have close to no quantum confinement at the length scale synthesized, are unlikely to exhibit much confinement unless the size is drastically decreased, and that this is likely to be the case for any other silver main-group metal halide double perovskites.

Silver Nanoparticle Decorations and Reductive Degradation

In collaboration with Dr. Yehonadav Bekenstain, Dr. Jianmei Huang and Dr. Wojciech Osowiecki Amines are reducing agents and can produce silver particles in the presence of silver ions. In TEM studies, small circular nanoparticles are frequently observed as higher contrast decorations on the facets or inside the NCs of any double perovskite compositions. Likewise, in the $Cs_2AgInCl_6$ and $Cs_2AgSbCl_6$ materials, we do not observe a significant growth of the nanocrystallites during $\sim$ 5 min 300 pA/nm exposure to the electron beam, though some migration and coalescence do occur.

To further understand this silver degradation pathway of double perovskite nanocrystals NCs, we conducted a STEM-EDS study of NCs with these higher contrast decorations (Figure 5.6a yellow and red areas, respectively). Elemental analysis indicates that these small particles contain almost exclusively silver atoms, suggesting that they are silver nanocrystals (Figure 5.6b, 5.2H). In contrast, the cubic nanocrystals in the background contains stoichiometric amounts of Ag^+ and Bi^{3+}, consistent with their assignment as $Cs_2AgBiBr_6$ material. We also performed high-resolution TEM structural analysis on higher contrast islands still attached to $Cs_2AgBiBr_6$ NCs. These small nanoparticles exhibit a distinct lattice fringe (Figure 5.6c) that does not overlap with those of the background perovskite material. Using selective Fourier filtering (Figure 5.6d–f), we measured a lattice spacing for the higher contrast island of 0.24 nm, which matches the $\langle 111 \rangle$ spacing of metallic silver. The background lattice spacing is 0.4 nm, similar to the double perovskite $\langle 022 \rangle$ spacing. The larger, Ag-depleted nanocrystals undergo a transition from the cubic $F_{m3\bar{m}}$ $Cs_2AgBiBr_6$ to trigonal $p_{3\bar{m}1}$ $Cs_3Bi_2Br_9$ and Cs_3BiBr_6 nanocrystals as confirmed spectroscopically and by XRD (Figure A.4.10 a,b). The overall shape of these byproduct nanocrystals is no longer cubic and more rounded crystals or triangular prisms are observed (Figure A.4.10c,d). The silver degradation products we have observed are summarized in the following reaction equation:

$$3Cs_2AgBiBr6 \longrightarrow Cs_3Bi_2Br_9 + Cs_3BiBr_6 + 3Ag + \frac{3}{2}Br_2 \tag{5.1}$$

which includes the two different ternary $Cs_xBi_yBr_z$ compositions and elemental silver we have observed in optical measurements and in the transmission electron microscope. The oxidation of bromides to bromine is used here for simplification. It is likely that other

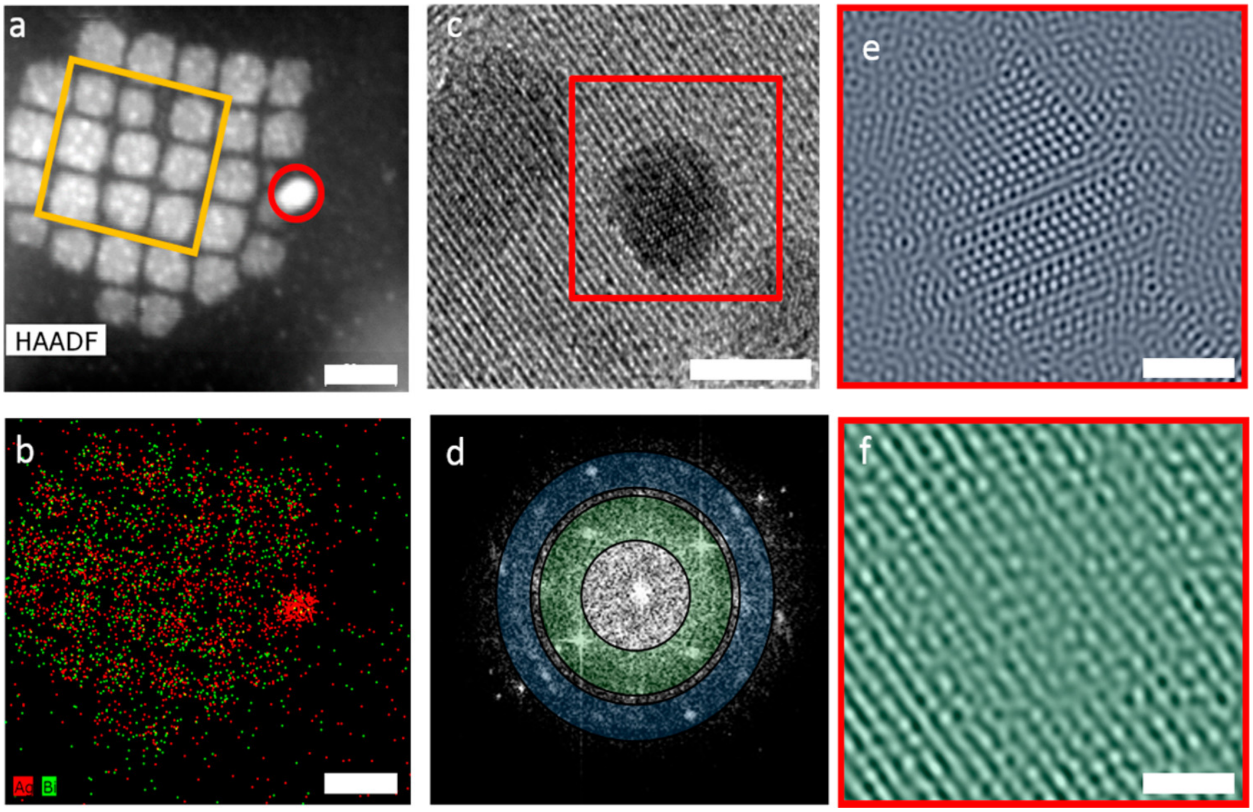

Figure 5.6: (a) HAADF image depicting cubic $Cs_2AgBiBr_6$ NCs and a circular, high-contrast particle. The bright decorations on the cubic NCs are assigned to silver islands. STEM-EDS analysis is used to compare the composition of the yellow frame and red circle areas (Table 1). The scale bar is 20 nm. (b) STEM-EDS images showcasing the uniform distribution of silver and bismuth colocalized in the cubic nanocrystals. The bright circular particle (red) is a silver NC. The scale bar is 20 nm. (c) HRTEM of the decorations on cubic $Cs_2AgBiCl_6$ crystals showing lattice spacing for both the silver nanoparticle and the underlying double perovskite crystal, the scale bar is 2 nm. (d) FFT of the selected area in panel c (red) depicting two different periodicities marked in blue and green. By Fourier filtering the different components, a lattice spacing of (e) 0.24 nm that matches (111) of silver (blue) and (f) 0.4 nm that matched the double perovskites (220) (green) can be clearly separated. The scale bar is 1 nm.

species, such as oleylamine, would be oxidized first. These observations reveal a reductive degradation pathway of Cs_2AgMX_6 NCs in which silver diffusion, reduction, and coalescence are identified as the key source of structural instability. This pathway is likely universal to all silver-containing metal halide nanocrystals, and displays similarities to the photolysis of AgBr used for the development of photographic film.[213]

Stability towards Ligands

Heightened interest in these materials is due to their practical application as future optoelectronic materials. In order to achieve this goal, material stability and point defect formation must be better understood and controlled. Our absorption and emission data strongly suggest that formation of defects and defect states are of importance in these materials. Nanocrystals are a good model system for studying the stability of double perovskite materials because of the ability to combine spectroscopy and observe structural changes with atomic resolution. We first study the stability of $Cs_2AgBiBr_6$ NCs towards reactions with different ligand binding groups by monitoring the NC optical properties. In this experiment, the different ligands were introduced in excess (0.06–3.6% weight/volume) to a colloidal suspension of NCs at room temperature. Thiols and carboxylic acids did not evoke any clear spectral changes, while phosphonic acids suppressed the emission from the nanocrystals but kept the crystal absorption intact. The most important observation in this experiment was with excess primary and tertiary amines, which caused significant spectral changes in the crystals, leading to a disappearance of absorption (and emission) features, which we interpret as complete dissolution of the NCs (see Figure 5.7). This result may suggest a similar surface chemistry for the double perovskite nanocrystals to those of the lead halides in which oleylammonium plays an important role in passivating the halide atoms on the surface,[49] and excess amines degrade the NCs.[35]

We further sought a robust and quantitative measure of perovskite nanocrystal stability, so we utilized the observed degradation with amines to develop a degradation titration assay for $Cs_2AgSbCl_6$, $Cs_2AgInCl_6$, $Cs_2AgBiCl_6$, and $CsPbCl_3$ nanocrystals. Reactions with amines serve as a more reproducible proxy for the stability of perovskite nanocrystals than direct exposure to water, since amines and water are similar in hardness, but amines are miscible with nonpolar colloidal solutions of halide nanocrystals. In the decomposition reaction of $CsPbBr_3$ to Cs_4PbBr_6, it has been proposed that three units of $PbBr_3$ from every four unit cells react with amines to form a complex in solution, leaving behind lead-depleted nanocrystals.[35] For the double perovskites, STEM–EDS analysis of the depleted products after amine degradation reveals trace amounts of Sb, Bi, or In, leaving large aggregates containing Cs, Ag, and Cl (Figures S11–S13). The concentration of double perovskite unit cells converges to a fixed value after being exposed to an excess of amine-containing solutions during the time scale of the reaction. This suggests the possibility that the metal–ligand complexes and other molecular species reach a quasi-equilibrium with the nanocrystals in solution. The degradation process is a complex process on the individual nanocrystal level, and nanocrystals of both double perovskite and perovskite compositions appear to etch, grow,

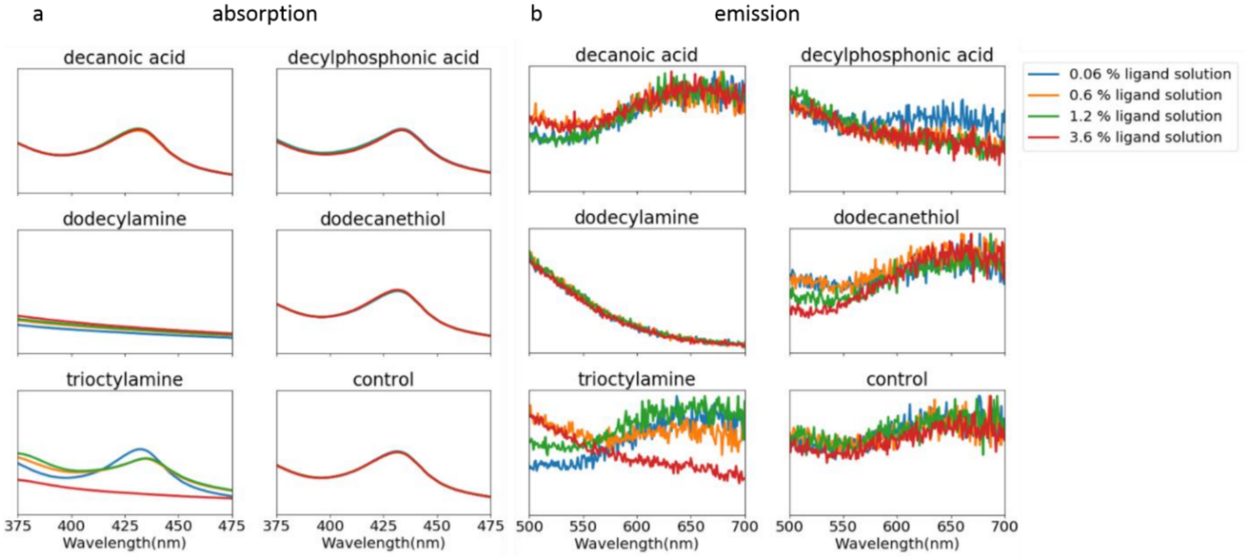

Figure 5.7: Stability of $Cs_2AgBiBr_6$ NCs in various ligand environments with different final ligand concentrations. We tested the decanoic acid, decylphosphonic acid, dodecyl amine, dodecanthiol, trioctylamine, as solutions in toluene, and pure toluene in the control experiment. (a) Depicts absorption measurements, with the 430 nm peak indicating the presence of $Cs_2AgBiBr_6$ NCs while (b) depicts emission, with the emission centered around 650 nm assigned to $Cs_2AgBiBr_6$ NCs

and fuse at the same time (Figure A.4.12). Nevertheless, on the macroscopic level, this process appears reversible, as demonstrated previously for $CsPbBr_3$ nanocrystals through heat or addition of oleic acid.[44] Since we cannot remove amines or nanocrystals from the solution without substantially altering the reaction, we reduce the number of amines available chemically. By protonating the amine by adding oleic acid in excess of that already present as surfactant in the nanocrystal solution, we couple the equilibrium of nanocrystals with amine to an acid-base equilibrium of the amine with oleic acid. This allows us to reverse some of the degradations of double perovskite nanocrystals and suggests reversibility of the nanocrystal degradation reaction at room temperature (Figure A.4.13). We therefore, propose the following reaction with primary amines for all silver main group metal double perovskites (M = Sb, In, Bi)

$$Cs_2AgMX_6 + RNH_2 \rightleftharpoons RNH_2MX_3 + Cs_2AgX_3 \tag{5.2}$$

To measure the degradation behavior of the above reaction, amines are titrated into solutions of nanocrystals in dodecane, and the change in absorption from the original solution is measured. For the materials examined here, $Cs_2AgSbCl_6$ dissolves in the presence of the lowest concentrations of octylamine (0.01–0.1 mM), whereas $Cs_2AgBiCl_6$ dissolves at a higher concentration (∼1 mM) and $Cs_2AgInCl_6$ and $CsPbCl_3$ require still higher concentrations (∼ 10–100 mM). (See Figure 5.8)

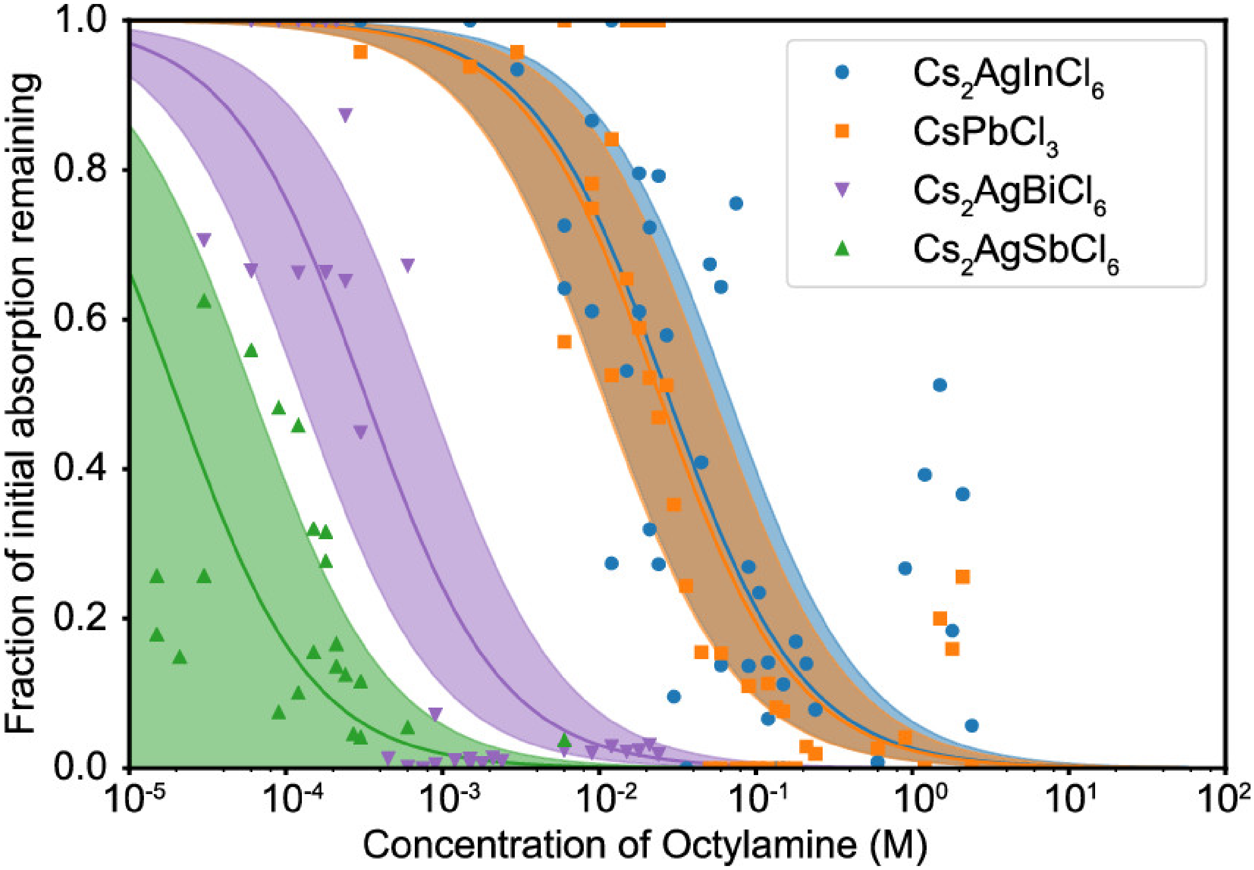

Figure 5.8: *Amine Degradation of Double Perovskite Nanocrystals* Stability analyses of $Cs_2AgSbCl_6$, $Cs_2AgBiCl_6$, $Cs_2AgInCl_6$, and $CsPbCl_3$ nanocrystals. Individual points represent the fraction of initial absorption remaining after 4 h as a function of the different concentrations of octylamine that the nanocrystal solutions were exposed to. The solid lines are fits of the data points to an equilibrium equation 5.3, whereas the shaded regions represent 1 *sigma* confidence intervals for those fits.

These materials can be characterized and compared by the concentration of amine required to degrade a defined fraction of the sample. This point is defined as the 1/e point in our analysis. Based on some of our observations as well as prior publications on $CsPbBr_3$,[44] we postulate that this reaction is in quasi-equilibrium. Under this assumption, we developed a simplified equilibrium model, which we use to fit the data to a model equilibrium constant. The decomposition of several different materials can be well fit with this simplified equilibrium equation, lending additional support to the idea that an equilibrium reaction is occurring. Based on the proposed reaction equation 5.2, we rewrite the equilibrium equation by replacing the concentration of product by the difference between initial and current concentrations of starting material so that the equilibrium constant is expressed entirely by the fraction of starting material remaining and the initial concentration of amines and nanocrystal unit cells

$$K = \frac{X_0 - f_i X_0}{f_i X_0 - L_0(X_0 - f_i X_0)} \tag{5.3}$$

Where K is the equilibrium constant, X_0 is the initial concentration of double perovskite, f_i is the fraction of starting material remaining, and L_0 is the initial concentration of amines. In our experiment, $f_i = \frac{X}{X_0}$ is determined as the fraction of the initial absorption remaining $(\frac{abs}{abs_i})$. The equilibrium equation with one amine binding one metal halide most consistently fits the absorption data, this suggests the $\frac{1}{L_0}$ dependence used in the equation.

The absorption data in the decomposition curves are fit to this equilibrium equation model, and equilibrium constants for each of the nanocrystals are extracted. This equilibrium model is undoubtedly an oversimplification of a complex process involving reactions at different times and length-scales, but it is consistent with the observations and allows us to quantitatively compare the relative stability of these materials. Although the errors on the extracted equilibrium constants are substantial, the differences between the various equilibrium constants are separated by at least one standard error, with exception of the constants of $CsPbCl_3$ and $Cs_2AgInCl_6$, which are close to identical. Using the fitted equilibrium constants, the standard Gibbs free energy of reaction can also be estimated through $\Delta G^0 = -RTlnK$(Table 5.1). The large and negative free energy values agree with the spontaneous occurrence of these reactions in dilute solution at room temperature as well as with the large extracted equilibrium constants.

To verify that the results of the amine titrations are reasonable proxies for real stability differences under atmospheric humidity, we measured the degradation of TEM samples in atmospheric moisture. $Cs_2AgSbCl_6$ placed on a TEM grid degrades into a Sb-depleted phase in a matter of hours, whereas $Cs_2AgInCl_6$ is stable under atmospheric conditions for more than a week (Figure A.4.14). Additionally, the $Cs_2AgSbCl_6$ nanocrystals degrade under standard beam conditions during STEM–EDS measurement (Figure A.4.15), and STEM–EDS measurements of the $Cs_2AgSbCl_6$ nanocrystals exposed to air for more an hour show a significant depletion of Sb content in the crystals, with a corresponding accumulation of amorphous Sb-containing agglomerations outside of the crystals (Figure A.4.16). The difficulty of purifying

AgCl from $Cs_2AgSbCl_6$ might also arise in part from the instability of the parent material, potentially causing some degradations to AgCl during purification.

Compound	$Cs_2AgSbCl_6$	$Cs_2AgBiCl_6$	$Cs_2AgInCl_6$
K_{eq}	5×10^5	3×10^3	40
ΔG^0 (kJ/mol)	-27	-20	-9
1/e point (M OLA)	9×10^{-5}	4×10^{-4}	$4,4 \times 10^{-2}$
Electronegativity (in eV)[214]	2.12	1.88	1.13
Pearson Hardness (in eV)[215]	3.78	3.18	2.75
Standard Formation Energy from the elements/ unit cell (calc, in eV)	-16.5	-17.0	-17.4
Formation energy from most stable precursors/ unit cell (calc, in eV)	-0.04	-0.31	-0.06
Melting Temperature of MCl_3[216] in °C	73.4	234	583
Bond distance ratio in MCl_3	3.4: 2.4	3.2 : 2.5	2.5 : 2.5
Goldschmidt Tolerance Factor	0.94	0.9	0.94
Octahedral Cation/Anion ratio	0.53	0.6	0.54

Table 5.1: Calculated stability parameters and other physical measurements

Based on the quantitative data on the stability of these three compounds, we now consider different factors which could potentially explain the difference in stability between cesium silver chloride double perovskites (see Table 5.1), primarily : (1) The Goldschmidt tolerance factor, (2) the stability of the crystal as measured by crystal formation energies, or (3) the binding affinity of the p-block metals for the amines over chlorides, which should correlate to the hardness of the metal. The Goldschmidt tolerance factor as well as more complicated radius ratio fits that include both the tolerance factor and octahedral radius ratios do not explain the observed trends in stability. Although crystal stability correlated well with the melting point of the binary halides as well as with the standard heats of formation from the elements, the difference in crystal formation energies from the lowest energy starting materials, ΔH_f, which is a more direct measure of the intrinsic crystal stability, did not correlate with the measured stability at all. The Pearson hardness[215] of the elements correlates well with the degradation energy, with Sb, the hardest acid, releasing the most energy during a reaction with the hard amine base and In as the softest acid releasing the least. Metal trichloride melting temperatures also appear to correlate well with the stability. However, other possible measures, such as the hardness of the ions, of the metal halide complexes or solubility might better describe this interaction. To better understand and predict the stability in complex metal halide materials to the wide variety of environmental perturbations, such as humidity, heat, light, electrical current, and others, more experimental and theoretical studies comparing materials in a quantifiable manner are needed. We anticipate that the method presented here could aid in the quantification of the stability of metal halide materials.

5.3 Conclusion

In this section, we demonstrate a colloidal synthesis of nanocrystals of Cs_2AgMX_6 double perovskites using a robust, tunable method of injecting acyl halides under atmospheric conditions and relatively mild temperatures. We identify the type and concentration of the halide precursor as an easily tunable variable that profoundly affects the synthetic outcome. The particles synthesized are crystalline nanocubes of $\sim$ 10 nm edge length terminated with [200] facets and decorated with silver particles. We show that the optical properties remain unchanged from bulk despite the appearance of dilute absorbance spectra and discuss the need to perform concentrated liquid absorption or solid diffuse reflectance measurements for accurate Tauc analysis of nanocrystals. Observation of degradation in different solvent and ligand environments, as well as through decomposition based on silver nanoparticles shows evidence of different degradation pathways. We develop degradation assay using the amine degradation pathway for the nanocrystals and show a decrease in chemical stability from $Cs_2AgInCl_6$ over $Cs_2AgBiCl_6$ to $Cs_2AgSbCl_6$. This ability to quantitatively measure perovskite environmental stability can enhance the understanding of metal halide materials, accelerate the identification of more stable perovskite analogs, and enable the elucidation of design rules for the environmental stability of a broad range of metal halide semiconductor nanocrystals.

5.4 Experimental

Synthesis

Materials

Acetone (99.9%, Fischer Scientific), antimony(III) acetate (99.99%, Aldrich), benzoyl chloride (99%, VWR), bismuth(III) acetate (99.99%, Aldrich), Bromotrimethylsilane (TMS-Br, 97%, Aldrich), cesium Acetate (99.9% Aldrich), cesium standard for ICP (1000 ppm in 2% aqueous nitric acid, Aldrich, TraceCert Lot: BCBK9448V), 2% aqueous nitric acid (Aldrich, 99.999%), 2-ethylhexanoyl chloride (98%, Aldrich), hexanes (mixture of isomers 99.99%, Fischer Scientific), Hydrochloric Acid (HCl, 36.5% w/v in H2O, Fischer Scientific), Indium(III) acetate (99.99%, Aldrich), lead(II) acetate trihydrate (99.99%, Aldrich), octylamine (99%, Aldrich), oleic acid (90%, Aldrich), oleylamine (70%, Aldrich), Toluene (99.9%, Fisher Scientific), silver acetate (99.99%, Aldrich), and m-xylene (99.9%, Fisher Scientific). All chemicals were used as purchased. Bromotrimethylsilane was stored under Argon.

Synthesis of Double Perovskite Nanocrystals In a typical synthesis, 5 mg (0.025 mmol) of cesium acetate, 8 mg (0.05 mmol) of silver acetate, and 0.05 mmol of the main group metal (16 mg indium (III) acetate, 20 mg bismuth (III) acetate, 17 mg antimony (III) acetate) were placed into a 4 mL glass vial with a stir bar. Solvent (Xylene or Toluene) (1 mL), oleic acid (0.25 mL, 0.8 mmol), and oleylamine (0.075 mL, 0.2 mmol) were added, and the vial heated to 100 °C for 10 min in an oil bath. The halide precursor (0.040 mL, 0.3 mmol) was injected quickly. Then, the vials were taken out of the oil bath and left to cool to room temperature. $Cs_2AgSbCl_6$ metal halide and surfactant precursor mixtures that were heated for more than a minute or left stirring under argon at room temperature for a prolonged period of time developed a reddish-brown tint and did not yield nanocrystals. For routine measurements, the nanocrystal reaction mixture was precipitated by centrifugation at 14,000 rpm for 5 min, and the resulting pellet was redispersed in hexanes.

Species	Solvent	OLA (mmol)	OA (mmol)	Cs (mmol)	M (mmol)	Ag (mmol)	Halide (mmol)	Precipitant (mL)
In, Bnzo-Cl	Xylene	0.2	0.8	0.025	0.05	0.05	0.3	None
Sb, Ethexo-Cl	Xylene	0.2	1.3	0.025	0.05	0.02	0.6	None
Bi, TMS-Br	Toluene	0.11	0.11	0.025	0.05	0.02	0.6	Acetone, 2 mL
Bi, HCl	Toluene	0.3	0.3	0.05	0.05	0.06	1.2	Acetone, 4 mL; 2-butanone, 4 mL
Pb, Bnzo-Cl	Xylene	0.2	0.8	0.05	0.05	0.0	0.3	None
Bi, Bnzo-Cl	Xylene	0.2	0.8	0.025	0.05	0.05	0.3	None
Sb (Ag), Ethexo-Cl	Xylene	0.2	0.8	0.025	0.05	0.05	0.3	None
Ag, Bnzo-Cl	Xylene	0.2	0.8	0.0	0.0	0.63	0.75	None

Table 5.2: Reaction conditions for different double perovskites

Reaction Optimization of $Cs_2AgBiBr_6$ Nanocrystals Reaction conditions optimization of $Cs_2AgBiBr_6$ quaternary compounds pose a synthetic challenge due to the large experimental parameter space required for further synthetic optimization. By utilizing high-throughput synthetic techniques that enable fast screening of synthetic parameters, we were able to extend our understanding of the double perovskite NCs. To match the technical requirements of the high-throughput apparatus (lower temperatures, atmospheric conditions) we devised the additional synthetic pathways mentioned above the result in the same nanocrystals. For the reaction optimization, we used a Hamilton Microlab NIMBUS system to dispense liquids, while solids were dispensed by hand. A 24 well reaction plate was set up with 4 mL vials, which were filled with 20 mg bismuth triacetate, 8 mg silver acetate and 2.5, 5, 7.5 and 10 mg cesium acetate. Stock solutions of oleylamine, oleic acid and bromotrimethylsilane in toluene were prepared by adding 2.25 mL oleic acid to 2.25 mL toluene, 2.36 mL oleylamine to 2.14 mL toluene and 0.98 mL bromotrimethylsilane to 1.82

mL toluene. The 24 well reaction plate was set up on the heater/shaker, while the stock solutions were split into 4 equal parts and placed on the reaction deck, along with one 50 mL container of toluene. The NIMBUS robot was programmed to place 16, 31, 62, 125, 250 and 500 µL of the oleylamine and oleic acid stock solutions into the respective containers and fill up the rest of the volume to 1 mL with toluene, creating a full factorial expansion of the ligand and cesium concentration combinations. Then, the heater/shaker was shaken at 500 rpm and heated to 90 °C for 10 minutes, after which 100 µL of TMS-Br solution was added to all the mixtures. The plate was left heating for an additional 30 minutes after injection, then cooled to room temperature. Once the reactions had cooled, heavy particles were precipitated out by centrifugation at 4,000 rpm, after which the supernatant was transferred to Eppendorf tubes, 1 mL acetone was added and the resulting mixture precipitated by centrifugation at 14,000 rpm. This precipitate was suspended in hexane and used in this form. Absorption measurements of the resulting reactions were taken on a Biotek Synergy 2 plate reader. The height of the peak at 430 nm was used as a measure to quantify the amount of double perovskite present in solution.

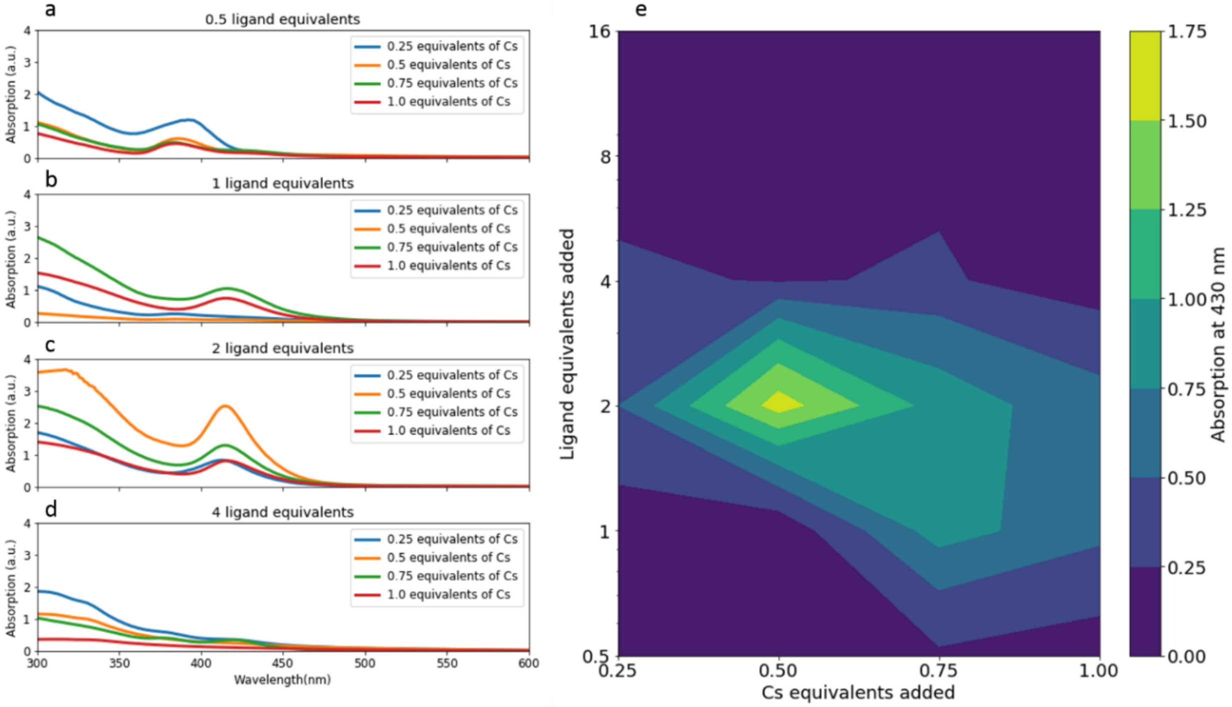

Figure 5.9: *High throughput synthesis optimization.* (a-d) absorption spectra of $Cs_2AgBiBr_6$NCs synthesized with different ratios of ligands and Cs precursor. Bi and Br ratio where kept constant. The peak intensity at 430 nm serves as an indicator for the concentration of NCs produced in the reaction. (e) 2D absorption map (@430nm) shows maximum absorption at 2 Ligand equivalents to 0.5 Cs equivalents

We show the formation of similar high-contrast nanoparticles as observed as side products in our other reactions (Figure A.4.1) and demonstrate that the absorption of AgCl nanocrystals (100 µL as synthesized solution in 3 mL of hexane) is not significant red of 280 nm (Figure A.4.5); We cannot speak to the absorption blue of 280 nm due to the convolution of the absorption of ligand and solvent impurities in the system used for synthesis.

Characterization

Absorption Measurements

For dilute absorption measurements, approximately 10–100 µ L of nanocrystal solution was added to a quartz cuvette containing 3 mL of hexanes and measured in a Shimadzu UV-3600 UV–vis–NIR spectrophotometer. To measure the band edge, the entire concentrated nanocrystal solution was placed in a quartz cuvette and measured in the same spectrophotometer. Then, the absorbance was converted to absorptance, and either the square root (for indirect band gaps in $Cs_2AgSbCl_6$) or the square (for direct band gaps in $Cs_2AgInCl_6$) of this value was plotted against energy. (50) A straight line was fit to the linear part of this function, and the x-axis intercept was reported as the band gap. The errors of the band gap were propagated from the fitting errors in the parameters of the line equation. To ensure that the band edge has been accurately measured, the concentration of nanocrystals was changed by a factor of 2 and a series Tauc plot was generated. If the band gap of two consecutive concentrations converges, as can be seen with the first two and the last two measurements in Figure 5.10, a band edge has been measured. It is, however, still possible that there are several edges with different absorption cross-sections, such as the edge at 4.2 eV. To determine which edge is the correct one, we would suggest validating experimental results with theoretical calculations (such as those of exciton radii) to ensure that the band edge chosen is reasonable.

Photoluminescence Measurements

In collaboration with Dr. Joseph Swabeck

A concentrated nanocrystal solution was placed in a quartz cuvette, and spectral photoluminescence and photoluminescence excitation measurements were taken on an Edinburgh FLS 980 Spectrometer. The photoluminescence quantum yield of $Cs_2AgInCl_6$ was measured at an excitation of 300 nm wavelength in an Edinburgh spectrometer equipped with an integrating sphere. The light out of the integrating sphere was integrated between 480 and 840 nm for emission and between 275 and 325 nm for absorption.

Transmission Electron Microscopy (TEM)

One drop ($\sim$ 10 µL) of dilute nanocrystal solution (prepared for optical measurements, 1:30 dilution) was cast onto a TEM grid (EMS, CF400-Cu). The samples were observed with a 200 kV Tecnai G2 T20 S-TWIN with a Gatan SC200 CCD camera.

X-ray Diffraction

The nanocrystal solution in hexanes was further concentrated by evaporating with a flow of nitrogen. This concentrate was drop-cast onto a low-background substrate, and the X-ray beam focused on the resulting film. Measurements were taken using a GADDS D-8 Series

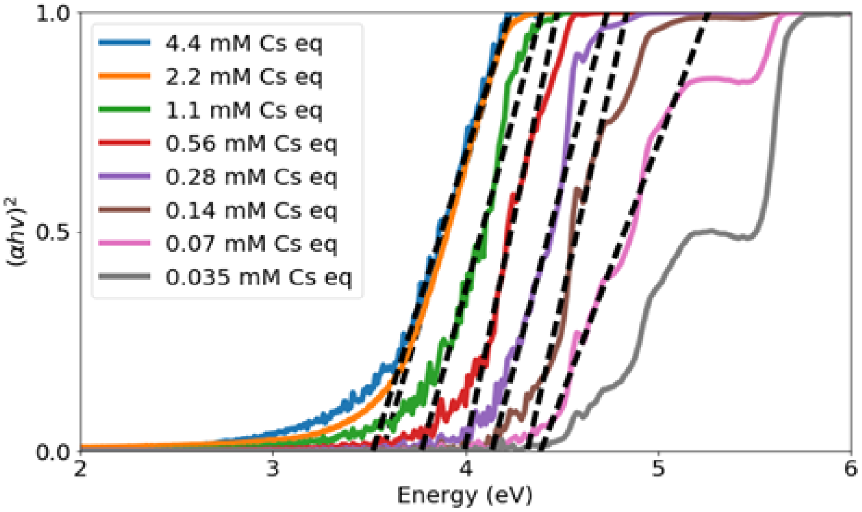

Figure 5.10: *Series of $Cs_2AgInCl_6$ Tauc plots at different concentrations* Concentrations of Cs equivalents are calculated based on molar absorptivities and dilution ratios

1 Diffractometer equipped with a Vantec 500 detector or on a D2 Phaser equipped with a Silicon SSD 160 detector.

Scanning Transmission Electron Microscopy and Energy Dispersive X-ray Spectroscopy (STEM–EDS)

In collaboration with Dr. Wojciech Osowiecki and Dr. Karen Bustillo

A concentrated nanocrystal solution was evaporated with a stream of nitrogen until it became cloudy; then the crystals were precipitated by centrifugation at 4,000 rpm and re-dispersed in hexanes. The centrifugation and re-dispersion were repeated once more, then the solution diluted by about 10x in hexanes. One drop of the solution was drop-cast onto a copper TEM grid (Ted Pella, 01824) that was cleaned with oxygen-plasma right before drop-casting. The instrument was a FEI TitanX operating at 120 kV, using a Fischione high-angle annular dark-field detector with an inner semiangle, β, of 63 mrad. The EDS detector was the FEI Super-X windowless detector with a solid angle of 0.7 radians. Once a larger region of interest was found, it was beam-showered at 235x magnification for 5-10 minutes. The above-mentioned steps of purification from ligands and crosslinking organics on the TEM grid are important to prevent carbon contamination buildup during the measurement. For analysis of the STEM-EDS data, the Bruker Esprit computer program was used. We fit the Cliff-Lorimer factor of the L-edges of Cs, Ag, In, and Sb to the results obtained by using the K-edges of Cs, Ag, In, and Sb during a long exposure at lower magnification. We then subtracted the background spectrum through a group of automatic fits based on a manual selection of regions with no characteristic X-ray peaks and report the composition data calculated by the Bruker Esprit program.

Cs GF-AAS Concentration Measurements

About 1 mL of each nanocrystal stock solution was dried in a vial. High-purity aqueous nitric acid (2%) was added, and the vial sonicated for 20 min. The resulting solutions were weighed and diluted 20,000 times in 2% nitric acid. A 1000 ppm Cs standard solution was diluted 20,000, 50,000, and 200,000 times. These dilutions were used to create a calibration curve, against which the other samples were measured. The solutions had Cs concentrations of 6.194, 6.316, 18.03, and 13.37 ppb for $Cs_2AgSbCl_6$, $Cs_2AgBiCl_6$, $Cs_2AgInCl_6$, and $CsPbCl_{33}$, respectively, and these concentrations were used to calculate the molar absorptivity of the original nanocrystal solutions to keep the concentration approximately the same between the different nanocrystals for comparison in the amine degradation assay (Figure A.4.11).

Amine Degradation Assay

Stock solutions with 1%, 0.1 %, 0.01%, 0.001% and 0.0001 % octylamine in dodecane (v/v) were created through a dilution series. Nanocrystal solutions of 0.3 mM Cs-equivalents concentration were prepared based on the molar absorptivity measured with Cs GF-AAS. 30 µL of this solution was placed into a Helma 96 well quartz plate. 70 µL of dodecane were added and an initial absorption measurement of all the wells was taken in a Biotek Synergy 4 plate reader. 10 - 100 µL of amine stock solution was added to different wells, the wells were topped off with 0 – 90 µL of dodecane for a final well volume of 200 µL, and the absorption measured every 30 minutes for 10 hours. The absorption measurement used for analysis was performed after the absorption had stopped changing (≈ 4 hours). Dodecane was chosen to avoid solvent evaporation during the time frame of the measurement, and octylamine was chosen to enable reasonably fast equilibration of the reaction while also avoiding evaporation of the amine. Degradation processes for all the double perovskite and perovskite nanocrystals can also be observed with other primary amines such as oleylamine, undecylamine or 2-ethylhexylamine and in different non-polar solvents, such as toluene and hexane.

The absorption spectrum at ∼ 4 hours after the addition of amines was fit to a linear combination of the initial absorption spectrum and a scattering function with a generic power law formula $S = a\lambda^b$, where S is the total scattering, λ is the wavelength and a and b are fitting constants This fit was created by linear regression with Python's statsmodels.ole.fit function in the region of 275 - 600 nm for $Cs_2AgInCl_6$, 320 - 600 nm for $Cs_2AgBiCl_6$ and $Cs_2AgSbCl_6$ and 380 – 600 nm for $CsPbCl_3$. The algorithm depicted in Figure 5.11 was the inspiration for further development of the algorithm in Chapter 2. The power of the scattering power law was extracted from the absorption in the region of 450 nm - 600 nm by a linear fit of the decadic logarithm of the absorption to the decadic logarithm of the wavelength, while imposing the physical constraint that the power (fitting constant b) must be between λ^{-4} in a purely Rayleigh scattering, small object limit and independent of wavelength (λ^0) in the large object limit. Modeling the entire peak based off the initial absorption spectrum rather than just modeling the scattering and then using one peak wavelength allowed us to retain much lower rates of error overall, as we calculated the fit of the final spectrum to the initial spectrum over many points instead of just one. (Figure 5.11) The fraction of

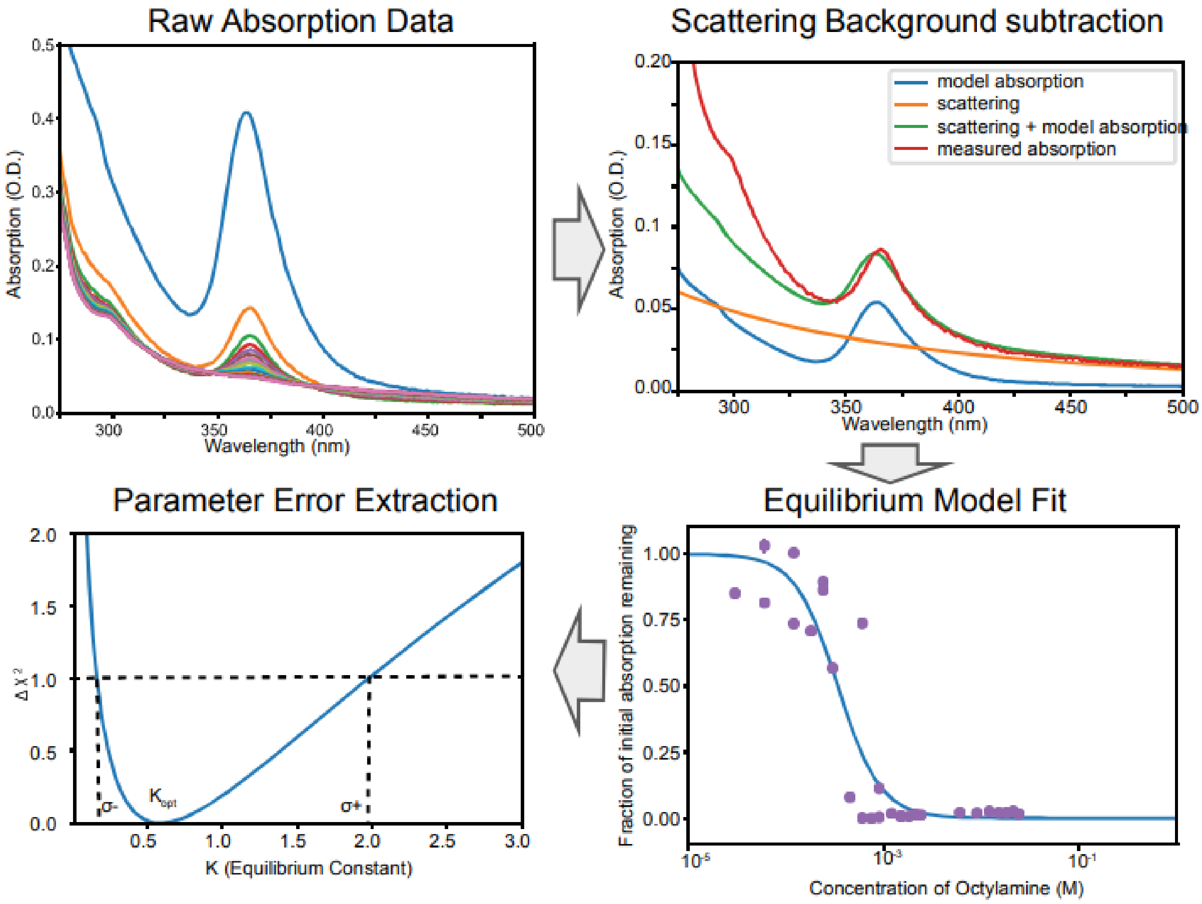

Figure 5.11: *Amine Titration Analysis* Example of decomposition spectra and explanation of data analysis

the initial absorption remaining was chosen as the measure of how much of the nanocrystal material remained undegraded. The linear regression with the initial absorption spectrum provided a quantitative estimate of this fraction. The fraction of remaining absorption was plotted against the concentration of octylamine in solution, and this data was fit using chi^2 minimization to the equation

$$y = \sqrt{\frac{(K - C_0K + x + 1)^2 + 4C_0K - C_0x - 1}{2C_0K}} \tag{5.4}$$

where y is the absorption divided by the initial absorption $\frac{abs}{abs_i}$, K is the equilibrium constant of the transformation, x is the concentration of ligands and C_0 is the initial concentration of double perovskites which was adjusted to 0.035 mM. Parameter errors from this analysis were found by analyzing the difference in chi squared to the minimum chi of this equation with variation of the equilibrium constant; Once this difference reaches 1, the equilibrium constant has reached the bounds of one standard error, which allows us to differentiate between positive and negative bounds of the equilibrium constant.

Theoretical Calculations

Performed by Dr. Yao Cai

All structure relaxations were carried out employing spin-polarized PBE-GGA[217] based density functional theory methods, as implemented in the Vienna ab-initio simulation package (VASP). Gamma-centered 20x20x20 k-point meshes were used for band structure calculations in VASP, employing the Perdew-Burke-Ernzerhof (PBE)5 generalized-gradient approximation (GGA).[218] For the calculations involving molecules, we employ periodic supercells which are carefully tested for energies to be converged (with respect to system size, i.e., to remove artifacts of interactions with periodic images) to within 0.2 meV/atom. The exciton radius (R) was computed within the Wannier–Mott model,[219] using the expression $R = \frac{\epsilon a_{B0}}{m^\star}$, where $m^\star$ is the reduced exciton mass $\frac{1}{m^\star} = \frac{1}{m_e} + \frac{1}{m_h}$, a_{B0} is the Bohr radius, and ε is the dielectric constant of the material. For the dielectric constant, we considered only the contribution from electronic polarization, i.e., taking the high-frequency contribution, assuming $\varepsilon = \varepsilon_{\text{inf}}$. The dielectric constant was calculated by means of density functional perturbation theory, as implemented in Vienna ab initio simulation package (VASP).[218] The average effective mass was calculated using VASP and the methodology implemented in the BoltzTrap code.[220] The PBE-GGA band structure was used as input to BoltzTrap to calculate the conductivity tensor $\frac{\sigma(T,\mu)}{\tau}$, where τ is the constant relaxation time, temperature T set to 300 K, and μ indicates the Fermi level. The average effective mass is calculated as $m = \frac{ne^2\tau}{\sigma}$. The effective mass defined this way is an average of $m(i,k)$ around Fermi level μ, with i the band index, and k the wave vector. Convergence of the effective mass with respect to the density of k-points is carefully tested and the values are found to be converged to within 1% using a 20×20×20 mesh.

compound	$Cs_2AgSbCl_6$	$Cs_2AgBiCl_6$	$Cs_2AgInCl_6$
m_e	0.37	0.38	0.29
m_h	0.49	0.53	0.9
$m^\star$	0.21	0.22	0.22
ϵ_{inf}	4.04	3.74	3.39
E_b (meV)	175	214	260
R(nm)	1.02	0.9	0.82

Table 5.3: Physical parameters calculated based on DFT modeling

Chapter 6

Outlook

6.1 Metal Halide Nanocrystals

The work presented here connects different reactions observed in metal halide nanoparticles into one cohesive picture. We have determined and quantified precursor reactions involved in the synthesis of lead bromide perovskites, discovered potential magic sized cluster intermediates that appear in multiple synthesis pathways, built an overview of cesium lead bromide nanocrystal reactions in general and created and optimized a full physical model of the binary lead bromide (2D perovskite) nanosheet in particular. We show that while synthesis models of other nanocrystals can be applied to metal halide nanocrystal formation reactions under certain conditions, the role that nanocrystal transformation can and does play in the synthesis of lead halide perovskites requires special consideration. We also demonstrate that these transformations are important for metal halide nanocrystals beyond the well-studied lead halide perovskites with the family of silver bismuth, antimony and indium halide nanocrystals we studied.

As mentioned in Chapter 2, the collection of large synthesis and characterization datasets can easily be leveraged for multiple investigations, including understanding factors controlling photoluminescence efficiency and Stokes shift in perovskite nanocrystals, educational applications and synthesis optimization. Based on the workflow we have developed here, we believe it will be possible in future to create models of the entire synthesis process of lead halide perovskites. Future work in understanding perovskite synthesis will require the development of models that integrate nanocrystal formation with phase transformation - keeping track of multiple nanocrystal populations and their size distributions. Many interesting questions remain - the effects of different chemical species of ligands, halides or metals, effects of precursor degradation rates, observing changes in nanocrystal equilibria with temperature or contamination with water, integration of these results with different synthesis protocols and many others. We believe that utilizing the approaches outlined here, it should be possible to integrate this information in a comprehensible manner to ultimately understand and predict how metal halide nanocrystals form and react.

6.2 Nanocrystal Synthesis Science

As new nanocrystalline materials being synthesized move increasingly beyond single component or binary structures, nanocrystal synthesis science will continually increase in complexity. The methods introduced in Chapter 2 could be useful for the exploration of any multinary nanocrystal system with multiple strongly absorbing products - which will include most materials of interest for optoelectronic applications. The model competition in Chapter 3 could be utilized to settle current disagreements on nanocrystal synthesis models - or demonstrate that perhaps synthesis in different nanocrystal systems, or even different portions of the same system, may be best explained by differing models. Explorations of the transitions between models and mechanisms - such as the transition between the chemical exfoliation and the direct nucleation pathway to 2D perovskite nanosheets - promise a rich area for the study of changes in formation mechanisms induced by chemical concentrations or other external driving forces.

We also would like to showcase the utility we derived from absorption spectra. Traditionally, absorption spectra are used for quantitative analysis only in simple cases, such as determining single equilibrium constants with a clear isosbestic point or determining single component formation or degradation reactions in stopped flow measurements. In this work, we have developed multiple algorithms allowing us to work with more complex cases in which many species with overlapping absorption spectra are present in the same solution. To do so requires careful evaluation of possible errors and ideally includes modeling of the underlying physical process, whether kinetic or thermodynamic - or even of the spectra themselves. Based on the ease with which absorption spectra can be obtained, this approach comports well with machine learning and other data driven scientific approaches and could additionally enhance scientific inquiry into nanocrystals in institutions without the resources for complex and expensive equipment such as electron microscopes. The determination of multiple complex solution equilibria from an integrated fit to a series of absorption spectra could also be utilized for work on general equilibria of absorbing species.

6.3 Machine Learning in Synthesis Science

We show here that integrating even simple scientific relationships, such as Lambert-Beer's law of absorption in the deconvolution algorithm in Chapter 2, into machine learning frameworks can create accurate and interpretable data analysis techniques. Further examples are the use of machine learning model selection approaches to validate and select models in Chapter 3 as well as the optimization of a joint spectral-equilibrium model using active machine learning in Chapter 4. The full physical model of stopped-flow absorption spectra can also be considered a type of scientific machine learning, though it is of considerably higher complexity and current training routines require significant computational power. Future work automating the generation of potential models and speeding up computation of chemical kinetics is needed to achieve the goal of inferring complex reaction mechanisms from large data.

Bibliography

[1] M. Faraday. The Bakerian Lecture: Experimental Relations of Gold (and Other Metals) to Light. *Philosophical Transactions of the Royal Society of London*, 147(0):145–181, 1857. ISSN 0261-0523. doi: 10.1098/rstl.1857.0011. URL `http://rstl.royalsocietypublishing.org/cgi/doi/10.1098/rstl.1857.0011`.

[2] John Turkevich, Peter Cooper Stevenson, and James Hillier. A study of the nucleation and growth processes in the synthesis of colloidal gold. *Discussions of the Faraday Society*, 11:55, 1951. ISSN 0366-9033. doi: 10.1039/df9511100055. URL `http://xlink.rsc.org/?DOI=df9511100055`.

[3] R. Rossetti, S. Nakahara, and L. E. Brus. Quantum size effects in the redox potentials, resonance Raman spectra, and electronic spectra of CdS crystallites in aqueous solution. *The Journal of Chemical Physics*, 79(2):1086–1088, jul 1983. ISSN 0021-9606. doi: 10.1063/1.445834. URL `http://aip.scitation.org/doi/10.1063/1.445834`.

[4] A. I. Ekimov and A. A. Onushchenko. Quantum Size Effect in the Optical Spectra of Semiconductor Microcrystals. *Soviet physics. Semiconductors*, 16(7):775–778, 1982. ISSN 00385700.

[5] Alexander L. Efros and Alexei L. Efros. Band to band absorption of the light in semiconductor sphera. *Fiz. Tverd. Tela*, 16(7):1209–1214, 1982.

[6] Yufei Shu, Xing Lin, Haiyan Qin, Zhuang Hu, Yizheng Jin, and Xiaogang Peng. Quantum Dots for Display Applications. *Angewandte Chemie*, 132(50): 22496–22507, dec 2020. ISSN 0044-8249. doi: 10.1002/ange.202004857. URL `https://onlinelibrary.wiley.com/doi/10.1002/ange.202004857`.

[7] Alexis T. Bell. The Impact of Nanoscience on Heterogeneous Catalysis. *Science*, 299 (5613):1688–1691, mar 2003. ISSN 0036-8075. doi: 10.1126/science.1083671. URL `https://www.science.org/doi/10.1126/science.1083671`.

[8] Krishnendu Saha, Sarit S. Agasti, Chaekyu Kim, Xiaoning Li, and Vincent M. Rotello. Gold nanoparticles in chemical and biological sensing. *Chemical Reviews*, 112(5):2739–2779, 2012. ISSN 00092665. doi: 10.1021/cr2001178.

[9] C. B. Murray, D. J. Norris, and M. G. Bawendi. Synthesis and characterization of nearly monodisperse CdE (E = sulfur, selenium, tellurium) semiconductor nanocrystallites. *Journal of the American Chemical Society*, 115(19): 8706–8715, sep 1993. ISSN 0002-7863. doi: 10.1021/ja00072a025. URL `https://pubs.acs.org/doi/abs/10.1021/ja00072a025`.

[10] David A. Hanifi, Noah D. Bronstein, Brent A. Koscher, Zach Nett, Joseph K. Swabeck, Kaori Takano, Adam M. Schwartzberg, Lorenzo Maserati, Koen Vandewal, Yoeri van de Burgt, Alberto Salleo, and A. Paul Alivisatos. Redefining near-unity luminescence in quantum dots with photothermal threshold quantum yield. *Science*, 363 (6432):1199–1202, mar 2019. ISSN 0036-8075. doi: 10.1126/science.aat3803. URL `https://www.sciencemag.org/lookup/doi/10.1126/science.aat3803`.

[11] David J. Smith. Chapter 1. Characterization of Nanomaterials Using Transmission Electron Microscopy. In *Nanocharacterisation*, pages 1–29. Royal Society of Chemistry, 2015. doi: 10.1039/9781782621867-00001. URL `http://ebook.rsc.org/?DOI=10.1039/9781782621867-00001`.

[12] Cameron F. Holder and Raymond E. Schaak. Tutorial on Powder X-ray Diffraction for Characterizing Nanoscale Materials. *ACS Nano*, 13(7):7359–7365, jul 2019. ISSN 1936-0851. doi: 10.1021/acsnano.9b05157. URL `https://pubs.acs.org/doi/10.1021/acsnano.9b05157`.

[13] Marek Grzelczak, Jorge Pérez-Juste, Paul Mulvaney, and Luis M. Liz-Marzán. Shape control in gold nanoparticle synthesis. *Chemical Society Reviews*, 37(9):1783, 2008. ISSN 0306-0012. doi: 10.1039/b711490g. URL `http://xlink.rsc.org/?DOI=b711490g`.

[14] Dylan C. Gary, Maxwell W. Terban, Simon J. L. Billinge, and Brandi M. Cossairt. Two-Step Nucleation and Growth of InP Quantum Dots via Magic-Sized Cluster Intermediates. *Chemistry of Materials*, 27(4):1432–1441, feb 2015. ISSN 0897-4756. doi: 10.1021/acs.chemmater.5b00286. URL `https://pubs.acs.org/doi/10.1021/acs.chemmater.5b00286`.

[15] Fudong Wang, Rui Tang, and William E. Buhro. The Trouble with TOPO; Identification of Adventitious Impurities Beneficial to the Growth of Cadmium Selenide Quantum Dots, Rods, and Wires. *Nano Letters*, 8(10):3521–3524, oct 2008. ISSN 1530-6984. doi: 10.1021/nl801692g. URL `https://pubs.acs.org/doi/10.1021/nl801692g`.

[16] Danielle K. Smith, Nathan R. Miller, and Brian A. Korgel. Iodide in CTAB Prevents Gold Nanorod Formation. *Langmuir*, 25(16):9518–9524, aug 2009. ISSN 0743-7463. doi: 10.1021/la900757s. URL `https://pubs.acs.org/doi/10.1021/la900757s`.

[17] Xiaoyu Zhang, Xue Bai, Hua Wu, Xiangtong Zhang, Chun Sun, Yu Zhang, Wei Zhang, Weitao Zheng, William W. Yu, and Andrey L. Rogach. Water-Assisted Size and Shape

Control of CsPbBr 3 Perovskite Nanocrystals. *Angewandte Chemie International Edition*, 57(13):3337–3342, mar 2018. ISSN 14337851. doi: 10.1002/anie.201710869. URL `https://onlinelibrary.wiley.com/doi/10.1002/anie.201710869`.

[18] James D. Martin. Particle Size Is a Primary Determinant for Sigmoidal Kinetics of Nanoparticle Formation: A "Disproof" of the Finke–Watzky (F-W) Nanoparticle Nucleation and Growth Mechanism. *Chemistry of Materials*, 32(8):3651–3656, apr 2020. ISSN 0897-4756. doi: 10.1021/acs.chemmater.9b02839. URL `https://pubs.acs.org/doi/10.1021/acs.chemmater.9b02839`.

[19] Richard G. Finke, Murielle A. Watzky, and Christopher B. Whitehead. Response to "Particle Size Is a Primary Determinant for Sigmoidal Kinetics of Nanoparticle Formation: A "Disproof" of the Finke–Watzky (F-W) Nanoparticle Nucleation and Growth Mechanism". *Chemistry of Materials*, 32(8):3657–3672, apr 2020. ISSN 0897-4756. doi: 10.1021/acs.chemmater.0c00780. URL `https://pubs.acs.org/doi/10.1021/acs.chemmater.0c00780`.

[20] James D. Martin. Reply to "A Comparison of the Stochastic and Deterministic Approaches in a Nucleation–Growth Type Model of Nanoparticle Formation". *Chemistry of Materials*, 33(13):5437–5445, jul 2021. ISSN 0897-4756. doi: 10.1021/acs.chemmater.1c01690. URL `https://pubs.acs.org/doi/10.1021/acs.chemmater.1c01690`.

[21] Christopher B. Whitehead, Saim Özkar, and Richard G. Finke. LaMer's 1950 model of particle formation: a review and critical analysis of its classical nucleation and fluctuation theory basis, of competing models and mechanisms for phase-changes and particle formation, and then of its application to silver halide, s. *Materials Advances*, 2(1):186–235, 2021. ISSN 2633-5409. doi: 10.1039/D0MA00439A. URL `http://xlink.rsc.org/?DOI=D0MA00439A`.

[22] Victor K. LaMer and Robert H. Dinegar. Theory, Production and Mechanism of Formation of Monodispersed Hydrosols. *Journal of the American Chemical Society*, 72(11):4847–4854, nov 1950. ISSN 0002-7863. doi: 10.1021/ja01167a001. URL `https://pubs.acs.org/doi/abs/10.1021/ja01167a001`.

[23] Christopher B. Whitehead, Saim Özkar, and Richard G. Finke. LaMer's 1950 Model for Particle Formation of Instantaneous Nucleation and Diffusion-Controlled Growth: A Historical Look at the Model's Origins, Assumptions, Equations, and Underlying Sulfur Sol Formation Kinetics Data. *Chemistry of Materials*, 31(18): 7116–7132, sep 2019. ISSN 0897-4756. doi: 10.1021/acs.chemmater.9b01273. URL `https://pubs.acs.org/doi/10.1021/acs.chemmater.9b01273`.

[24] T Sugimoto. Spontaneous nucleation of monodisperse silver halide particles from homogeneous gelatin solution I: silver chloride. *Colloids and*

Surfaces A: Physicochemical and Engineering Aspects, 164(2-3):183–203, may 2000. ISSN 09277757. doi: 10.1016/S0927-7757(99)00366-0. URL `https://linkinghub.elsevier.com/retrieve/pii/S0927775799003660`.

[25] Daniel B. K. Chu, Jonathan S. Owen, and Baron Peters. Nucleation and Growth Kinetics from LaMer Burst Data. *The Journal of Physical Chemistry A*, 121 (40):7511–7517, oct 2017. ISSN 1089-5639. doi: 10.1021/acs.jpca.7b08368. URL `https://pubs.acs.org/doi/10.1021/acs.jpca.7b08368`.

[26] Haoran Yang, Leslie S. Hamachi, Iva Rreza, Wesley Wang, and Emory M. Chan. Design Rules for One-Step Seeded Growth of Nanocrystals: Threading the Needle between Secondary Nucleation and Ripening. *Chemistry of Materials*, 31(11): 4173–4183, jun 2019. ISSN 0897-4756. doi: 10.1021/acs.chemmater.9b00971. URL `https://pubs.acs.org/doi/10.1021/acs.chemmater.9b00971`.

[27] Murielle A. Watzky and Richard G. Finke. Transition Metal Nanocluster Formation Kinetic and Mechanistic Studies. A New Mechanism When Hydrogen Is the Reductant: Slow, Continuous Nucleation and Fast Autocatalytic Surface Growth. *Journal of the American Chemical Society*, 119(43):10382–10400, oct 1997. ISSN 0002-7863. doi: 10.1021/ja9705102. URL `https://pubs.acs.org/doi/10.1021/ja9705102`.

[28] Derek R. Handwerk, Patrick D. Shipman, Christopher B. Whitehead, Saim Özkar, and Richard G. Finke. Mechanism-Enabled Population Balance Modeling of Particle Formation en Route to Particle Average Size and Size Distribution Understanding and Control. *Journal of the American Chemical Society*, 141(40): 15827–15839, oct 2019. ISSN 0002-7863. doi: 10.1021/jacs.9b06364. URL `https://pubs.acs.org/doi/10.1021/jacs.9b06364`.

[29] Haitao Liu, Jonathan S. Owen, and A. Paul Alivisatos. Mechanistic Study of Precursor Evolution in Colloidal Group II-VI Semiconductor Nanocrystal Synthesis. *Journal of the American Chemical Society*, 129(2):305–312, jan 2007. ISSN 0002-7863. doi: 10.1021/ja0656696. URL `https://pubs.acs.org/doi/10.1021/ja0656696`.

[30] Jonathan S. Owen, Jungwon Park, Paul-Emile Trudeau, and A. Paul Alivisatos. Reaction Chemistry and Ligand Exchange at Cadmium-Selenide Nanocrystal Surfaces. *Journal of the American Chemical Society*, 130(37):12279–12281, sep 2008. ISSN 0002-7863. doi: 10.1021/ja804414f. URL `https://pubs.acs.org/doi/10.1021/ja804414f`.

[31] Mark P. Hendricks, Michael P. Campos, Gregory T. Cleveland, Ilan Jen-La Plante, and Jonathan S. Owen. A tunable library of substituted thiourea precursors to metal sulfide nanocrystals. *Science*, 348(6240):1226–1230, jun 2015. ISSN 0036-8075. doi: 10.1126/science.aaa2951. URL `https://www.science.org/doi/10.1126/science.aaa2951`.

[32] Andreas Riedinger, Florian D. Ott, Aniket Mule, Sergio Mazzotti, Philippe N. Knüsel, Stephan J.P. Kress, Ferry Prins, Steven C. Erwin, and David J. Norris. An intrinsic growth instability in isotropic materials leads to quasi-two-dimensional nanoplatelets. *Nature Materials*, 16(7):743–748, jul 2017. ISSN 14764660. doi: 10.1038/nmat4889. URL `http://www.nature.com/articles/nmat4889`.

[33] Samuel E. Lohse and Catherine J. Murphy. The Quest for Shape Control: A History of Gold Nanorod Synthesis. *Chemistry of Materials*, 25(8): 1250–1261, apr 2013. ISSN 0897-4756. doi: 10.1021/cm303708p. URL `https://pubs.acs.org/doi/10.1021/cm303708p`.

[34] Franziska Krieg, Stefan T Ochsenbein, Sergii Yakunin, Stephanie ten Brinck, Philipp Aellen, Adrian Süess, Baptiste Clerc, Dominic Guggisberg, Olga Nazarenko, Yevhen Shynkarenko, Sudhir Kumar, Chih-Jen Shih, Ivan Infante, and Maksym V Kovalenko. Colloidal CsPbX 3 (X = Cl, Br, I) Nanocrystals 2.0: Zwitterionic Capping Ligands for Improved Durability and Stability. *ACS Energy Letters*, 3(3): 641–646, mar 2018. ISSN 2380-8195. doi: 10.1021/acsenergylett.8b00035. URL `http://pubs.acs.org/doi/10.1021/acsenergylett.8b00035`.

[35] Zeke Liu, Yehonadav Bekenstein, Xingchen Ye, Son C. Nguyen, Joseph Swabeck, Dandan Zhang, Shuit Tong Lee, Peidong Yang, Wanli Ma, and A. Paul Alivisatos. Ligand Mediated Transformation of Cesium Lead Bromide Perovskite Nanocrystals to Lead Depleted Cs4PbBr6 Nanocrystals. *Journal of the American Chemical Society*, 139(15):5309–5312, apr 2017. ISSN 15205126. doi: 10.1021/jacs.7b01409. URL `http://pubs.acs.org/doi/abs/10.1021/jacs.7b01409`.

[36] Brent A. Koscher, Zachary Nett, and A. Paul Alivisatos. The Underlying Chemical Mechanism of Selective Chemical Etching in CsPbBr 3 Nanocrystals for Reliably Accessing Near-Unity Emitters. *ACS Nano*, 13(10):11825–11833, oct 2019. ISSN 1936-0851. doi: 10.1021/acsnano.9b05782. URL `https://pubs.acs.org/doi/10.1021/acsnano.9b05782`.

[37] David P. Nenon, Kimo Pressler, Jun Kang, Brent A. Koscher, Jacob H. Olshansky, Wojciech T. Osowiecki, Matthew A. Koc, Lin-Wang Wang, and A. Paul Alivisatos. Design Principles for Trap-Free CsPbX 3 Nanocrystals: Enumerating and Eliminating Surface Halide Vacancies with Softer Lewis Bases. *Journal of the American Chemical Society*, 140(50):17760–17772, dec 2018. ISSN 0002-7863. doi: 10.1021/jacs.8b11035. URL `https://pubs.acs.org/doi/10.1021/jacs.8b11035`.

[38] Kira L. Gardner, Jeffrey G. Tait, Tamara Merckx, Weiming Qiu, Ulrich W. Paetzold, Lucinda Kootstra, Manoj Jaysankar, Robert Gehlhaar, David Cheyns, Paul Heremans, and Jef Poortmans. Nonhazardous Solvent Systems for Processing Perovskite Photovoltaics. *Advanced Energy Materials*, 6(14):

1600386, jul 2016. ISSN 1614-6832. doi: 10.1002/aenm.201600386. URL `https://onlinelibrary.wiley.com/doi/10.1002/aenm.201600386`.

[39] Bekele Hailegnaw, Saar Kirmayer, Eran Edri, Gary Hodes, and David Cahen. Rain on Methylammonium Lead Iodide Based Perovskites: Possible Environmental Effects of Perovskite Solar Cells. *The Journal of Physical Chemistry Letters*, 6(9): 1543–1547, may 2015. ISSN 1948-7185. doi: 10.1021/acs.jpclett.5b00504. URL `https://pubs.acs.org/doi/10.1021/acs.jpclett.5b00504`.

[40] Brandon J. Beberwyck, Yogesh Surendranath, and A. Paul Alivisatos. Cation Exchange: A Versatile Tool for Nanomaterials Synthesis. *The Journal of Physical Chemistry C*, 117(39):19759–19770, oct 2013. ISSN 1932-7447. doi: 10.1021/jp405989z. URL `https://pubs.acs.org/doi/10.1021/jp405989z`.

[41] Brent A. Koscher, Noah D. Bronstein, Jacob H. Olshansky, Yehonadav Bekenstein, and A. Paul Alivisatos. Surface- vs Diffusion-Limited Mechanisms of Anion Exchange in CsPbBr3 Nanocrystal Cubes Revealed through Kinetic Studies. *Journal of the American Chemical Society*, 138(37):12065–12068, sep 2016. ISSN 15205126. doi: 10.1021/jacs.6b08178. URL `http://pubs.acs.org/doi/abs/10.1021/jacs.6b08178`.

[42] Georgian Nedelcu, Loredana Protesescu, Sergii Yakunin, Maryna I. Bodnarchuk, Matthias J. Grotevent, and Maksym V. Kovalenko. Fast Anion-Exchange in Highly Luminescent Nanocrystals of Cesium Lead Halide Perovskites (CsPbX 3 , X = Cl, Br, I). *Nano Letters*, 15(8):5635–5640, aug 2015. ISSN 1530-6984. doi: 10.1021/acs.nanolett.5b02404. URL `http://pubs.acs.org/doi/10.1021/acs.nanolett.5b02404` `http://pubs.acs.org/doi/abs/10.1021/acs.nanolett.5b02404`.

[43] Francisco Palazon, Carmine Urso, Luca De Trizio, Quinten Akkerman, Sergio Marras, Federico Locardi, Ilaria Nelli, Maurizio Ferretti, Mirko Prato, and Liberato Manna. Postsynthesis Transformation of Insulating Cs 4 PbBr 6 Nanocrystals into Bright Perovskite CsPbBr 3 through Physical and Chemical Extraction of CsBr. *ACS Energy Letters*, 2(10):2445–2448, oct 2017. ISSN 2380-8195. doi: 10.1021/acsenergylett.7b00842. URL `https://pubs.acs.org/doi/10.1021/acsenergylett.7b00842`.

[44] Thumu Udayabhaskararao, Lothar Houben, Hagai Cohen, Matan Menahem, Iddo Pinkas, Liat Avram, Tamar Wolf, Ayelet Teitelboim, Michal Leskes, Omer Yaffe, Dan Oron, and Miri Kazes. A Mechanistic Study of Phase Transformation in Perovskite Nanocrystals Driven by Ligand Passivation. *Chemistry of Materials*, 30(1): 84–93, jan 2018. ISSN 0897-4756. doi: 10.1021/acs.chemmater.7b02425. URL `http://pubs.acs.org/doi/10.1021/acs.chemmater.7b02425`.

[45] Jakob C. Dahl, Xingzhi Wang, Xiao Huang, Emory M. Chan, and A. Paul Alivisatos. Elucidating the Weakly Reversible Cs–Pb–Br Perovskite Nanocrystal Reaction Network with High-Throughput Maps and Transformations. *Journal of the American Chemical Society*, 142(27):11915–11926, jul 2020. ISSN 0002-7863. doi: 10.1021/jacs.0c04997. URL `https://pubs.acs.org/doi/10.1021/jacs.0c04997`.

[46] Hao Zhang, Kinjal Dasbiswas, Nicholas B. Ludwig, Gang Han, Byeongdu Lee, Suri Vaikuntanathan, and Dmitri V. Talapin. Stable colloids in molten inorganic salts. *Nature*, 542(7641):328–331, feb 2017. ISSN 0028-0836. doi: 10.1038/nature21041. URL `http://www.nature.com/articles/nature21041`.

[47] Riley E. Brandt, Jeremy R. Poindexter, Prashun Gorai, Rachel C. Kurchin, Robert L. Z. Hoye, Lea Nienhaus, Mark W. B. Wilson, J. Alexander Polizzotti, Raimundas Sereika, Raimundas Žaltauskas, Lana C. Lee, Judith L. MacManus-Driscoll, Moungi Bawendi, Vladan Stevanović, and Tonio Buonassisi. Searching for "Defect-Tolerant" Photovoltaic Materials: Combined Theoretical and Experimental Screening. *Chemistry of Materials*, 29(11): 4667–4674, jun 2017. ISSN 15205002. doi: 10.1021/acs.chemmater.6b05496. URL `http://pubs.acs.org/doi/abs/10.1021/acs.chemmater.6b05496` `http://pubs.acs.org/doi/10.1021/acs.chemmater.6b05496`.

[48] Jun Kang and Lin-Wang Wang. High Defect Tolerance in Lead Halide Perovskite CsPbBr ¡sub¿3¡/sub¿. *The Journal of Physical Chemistry Letters*, 8(2): 489–493, jan 2017. ISSN 1948-7185. doi: 10.1021/acs.jpclett.6b02800. URL `http://pubs.acs.org/doi/10.1021/acs.jpclett.6b02800`.

[49] Jonathan De Roo, Maria Ibáñez, Pieter Geiregat, Georgian Nedelcu, Willem Walravens, Jorick Maes, Jose C. Martins, Isabel Van Driessche, Maksym V. Kovalenko, and Zeger Hens. Highly Dynamic Ligand Binding and Light Absorption Coefficient of Cesium Lead Bromide Perovskite Nanocrystals. *ACS Nano*, 10 (2):2071–2081, feb 2016. ISSN 1936-0851. doi: 10.1021/acsnano.5b06295. URL `https://pubs.acs.org/doi/10.1021/acsnano.5b06295`.

[50] Yunhua Chen, Sara R. Smock, Anne H. Flintgruber, Frédéric A. Perras, Richard L. Brutchey, and Aaron J. Rossini. Surface Termination of CsPbBr 3 Perovskite Quantum Dots Determined by Solid-State NMR Spectroscopy. *Journal of the American Chemical Society*, 142(13):6117–6127, apr 2020. ISSN 0002-7863. doi: 10.1021/jacs.9b13396. URL `https://pubs.acs.org/doi/10.1021/jacs.9b13396`.

[51] Bayrammurad Saparov, Jon Paul Sun, Weiwei Meng, Zewen Xiao, Hsin Sheng Duan, Oki Gunawan, Donghyeop Shin, Ian G. Hill, Yanfa Yan, and David B. Mitzi. Thin-Film Deposition and Characterization of a Sn-Deficient Perovskite Derivative Cs2SnI6. *Chemistry of Materials*, 28(7):2315–2322, apr

2016. ISSN 15205002. doi: 10.1021/acs.chemmater.6b00433. URL `http://pubs.acs.org/doi/10.1021/acs.chemmater.6b00433`.

[52] Andrew Ng. Introduction to Machine Learning, 2018. URL `https://www.coursera.org/learn/machine-learning`.

[53] Fabian Pedregosa, Ron Weiss, Matthieu Brucher, F. et al. Pedregosa, Fabian Pedregosa, G Varoquaux, A Gramfort, V Michel, B Thirion, O Grisel, M Blondel, P Prettenhofer, Ron Weiss, V Dubourg, J Vanderplas, A Passos, D Cournapeau, Matthieu Brucher, M Perrot, and E Duchesnay. Scikit-learn: Machine Learning in Python. *Journal of Machine Learning Research*, 12:2825–2830, 2011. URL `http://jmlr.org/papers/v12/pedregosa11a.html`.

[54] Chi Chen, Weike Ye, Yunxing Zuo, Chen Zheng, and Shyue Ping Ong. Graph Networks as a Universal Machine Learning Framework for Molecules and Crystals. *Chemistry of Materials*, 31(9):3564–3572, may 2019. ISSN 0897-4756. doi: 10.1021/acs.chemmater.9b01294. URL `https://pubs.acs.org/doi/10.1021/acs.chemmater.9b01294`.

[55] Derek T. Ahneman, Jesús G. Estrada, Shishi Lin, Spencer D. Dreher, and Abigail G. Doyle. Predicting reaction performance in C–N cross-coupling using machine learning. *Science*, 360(6385):186–190, apr 2018. ISSN 0036-8075. doi: 10.1126/science.aar5169. URL `https://www.science.org/doi/10.1126/science.aar5169`.

[56] Paul Raccuglia, Katherine C. Elbert, Philip D. F. Adler, Casey Falk, Malia B. Wenny, Aurelio Mollo, Matthias Zeller, Sorelle A. Friedler, Joshua Schrier, and Alexander J. Norquist. Machine-learning-assisted materials discovery using failed experiments. *Nature*, 533(7601):73–76, may 2016. ISSN 0028-0836. doi: 10.1038/nature17439. URL `http://www.nature.com/articles/nature17439`.

[57] Miao Zhong, Kevin Tran, Yimeng Min, Chuanhao Wang, Ziyun Wang, Cao-Thang Dinh, Phil De Luna, Zongqian Yu, Armin Sedighian Rasouli, Peter Brodersen, Song Sun, Oleksandr Voznyy, Chih-Shan Tan, Mikhail Askerka, Fanglin Che, Min Liu, Ali Seifitokaldani, Yuanjie Pang, Shen-Chuan Lo, Alexander Ip, Zachary Ulissi, and Edward H. Sargent. Accelerated discovery of CO2 electrocatalysts using active machine learning. *Nature*, 581(7807):178–183, may 2020. ISSN 0028-0836. doi: 10.1038/s41586-020-2242-8. URL `http://www.nature.com/articles/s41586-020-2242-8`.

[58] Donna G. Blackmond. Reaction Progress Kinetic Analysis: A Powerful Methodology for Mechanistic Studies of Complex Catalytic Reactions. *Angewandte Chemie International Edition*, 44(28):4302–4320, jul 2005. ISSN 1433-7851. doi: 10.1002/anie.200462544. URL `https://onlinelibrary.wiley.com/doi/10.1002/anie.200462544`.

[59] Alexander Dunn, Qi Wang, Alex Ganose, Daniel Dopp, and Anubhav Jain. Benchmarking materials property prediction methods: the Matbench test set and Automatminer reference algorithm. *npj Computational Materials*, 6(1): 138, dec 2020. ISSN 2057-3960. doi: 10.1038/s41524-020-00406-3. URL `https://www.nature.com/articles/s41524-020-00406-3`.

[60] Benjamin Sanchez-Lengeling and Alán Aspuru-Guzik. Inverse molecular design using machine learning: Generative models for matter engineering. *Science*, 361 (6400):360–365, jul 2018. ISSN 0036-8075. doi: 10.1126/science.aat2663. URL `https://www.science.org/doi/10.1126/science.aat2663`.

[61] Andrew F. Zahrt, Jeremy J. Henle, Brennan T. Rose, Yang Wang, William T. Darrow, and Scott E. Denmark. Prediction of higher-selectivity catalysts by computer-driven workflow and machine learning. *Science*, 363 (6424), jan 2019. ISSN 0036-8075. doi: 10.1126/science.aau5631. URL `https://www.science.org/doi/10.1126/science.aau5631`.

[62] Jarosław M. Granda, Liva Donina, Vincenza Dragone, De-Liang Long, and Leroy Cronin. Controlling an organic synthesis robot with machine learning to search for new reactivity. *Nature*, 559(7714):377–381, jul 2018. ISSN 0028-0836. doi: 10.1038/s41586-018-0307-8. URL `http://www.nature.com/articles/s41586-018-0307-8`.

[63] Edward Kim, Kevin Huang, Adam Saunders, Andrew McCallum, Gerbrand Ceder, and Elsa Olivetti. Materials Synthesis Insights from Scientific Literature via Text Extraction and Machine Learning. *Chemistry of Materials*, 29(21):9436–9444, nov 2017. ISSN 0897-4756. doi: 10.1021/acs.chemmater.7b03500. URL `https://pubs.acs.org/doi/10.1021/acs.chemmater.7b03500`.

[64] Oleksandr Voznyy, Larissa Levina, James Z. Fan, Mikhail Askerka, Ankit Jain, Min-Jae Choi, Olivier Ouellette, Petar Todorović, Laxmi K. Sagar, and Edward H. Sargent. Machine Learning Accelerates Discovery of Optimal Colloidal Quantum Dot Synthesis. *ACS Nano*, 13(10):11122–11128, oct 2019. ISSN 1936-0851. doi: 10.1021/acsnano.9b03864. URL `https://pubs.acs.org/doi/10.1021/acsnano.9b03864`.

[65] Flore Mekki-Berrada, Zekun Ren, Tan Huang, Wai Kuan Wong, Fang Zheng, Jiaxun Xie, Isaac Parker Siyu Tian, Senthilnath Jayavelu, Zackaria Mahfoud, Daniil Bash, Kedar Hippalgaonkar, Saif Khan, Tonio Buonassisi, Qianxiao Li, and Xiaonan Wang. Two-step machine learning enables optimized nanoparticle synthesis. *npj Computational Materials*, 7(1):55, dec 2021. ISSN 2057-3960. doi: 10.1038/s41524-021-00520-w. URL `http://www.nature.com/articles/s41524-021-00520-w`.

[66] Daniel Salley, Graham Keenan, Jonathan Grizou, Abhishek Sharma, Sergio Martín, and Leroy Cronin. A nanomaterials discovery robot for the Darwinian evolution of shape programmable gold nanoparticles. *Nature Communications*, 11

(1):2771, dec 2020. ISSN 2041-1723. doi: 10.1038/s41467-020-16501-4. URL `http://www.nature.com/articles/s41467-020-16501-4`.

[67] Zhi Li, Mansoor Ani Najeeb, Liana Alves, Alyssa Z. Sherman, Venkateswaran Shekar, Peter Cruz Parrilla, Ian M. Pendleton, Wesley Wang, Philip W. Nega, Matthias Zeller, Joshua Schrier, Alexander J. Norquist, and Emory M. Chan. Robot-Accelerated Perovskite Investigation and Discovery. *Chemistry of Materials*, 32(13): 5650–5663, jul 2020. ISSN 0897-4756. doi: 10.1021/acs.chemmater.0c01153. URL `https://pubs.acs.org/doi/10.1021/acs.chemmater.0c01153`.

[68] Ian M. Pendleton, Gary Cattabriga, Zhi Li, Mansoor Ani Najeeb, Sorelle A. Friedler, Alexander J. Norquist, Emory M. Chan, and Joshua Schrier. Experiment Specification, Capture and Laboratory Automation Technology (ESCALATE): a software pipeline for automated chemical experimentation and data management. *MRS Communications*, 9(3):846–859, sep 2019. ISSN 2159-6859. doi: 10.1557/mrc.2019.72. URL `http://link.springer.com/10.1557/mrc.2019.72`.

[69] Anubhav Jain, Shyue Ping Ong, Geoffroy Hautier, Wei Chen, William Davidson Richards, Stephen Dacek, Shreyas Cholia, Dan Gunter, David Skinner, Gerbrand Ceder, and Kristin A. Persson. Commentary: The Materials Project: A materials genome approach to accelerating materials innovation. *APL Materials*, 1(1):011002, jul 2013. ISSN 2166-532X. doi: 10.1063/1.4812323. URL `http://aip.scitation.org/doi/10.1063/1.4812323`.

[70] Steven M. Kearnes, Michael R. Maser, Michael Wleklinski, Anton Kast, Abigail G. Doyle, Spencer D. Dreher, Joel M. Hawkins, Klavs F. Jensen, and Connor W. Coley. The Open Reaction Database. *Journal of the American Chemical Society*, 143 (45):18820–18826, nov 2021. ISSN 0002-7863. doi: 10.1021/jacs.1c09820. URL `https://pubs.acs.org/doi/10.1021/jacs.1c09820`.

[71] Leonard Bezinge, Richard M. Maceiczyk, Ioannis Lignos, Maksym V. Kovalenko, and Andrew J. DeMello. Pick a Color MARIA: Adaptive Sampling Enables the Rapid Identification of Complex Perovskite Nanocrystal Compositions with Defined Emission Characteristics. *ACS Applied Materials & Interfaces*, 10(22): 18869–18878, jun 2018. ISSN 1944-8244. doi: 10.1021/acsami.8b03381. URL `https://pubs.acs.org/doi/10.1021/acsami.8b03381`.

[72] Weiqi Ji, Weilun Qiu, Zhiyu Shi, Shaowu Pan, and Sili Deng. Stiff-PINN: Physics-Informed Neural Network for Stiff Chemical Kinetics. *The Journal of Physical Chemistry A*, 125(36):8098–8106, sep 2021. ISSN 1089-5639. doi: 10.1021/acs.jpca.1c05102. URL `https://pubs.acs.org/doi/10.1021/acs.jpca.1c05102`.

[73] Piotr S. Gromski, Alon B. Henson, Jarosław M. Granda, and Leroy Cronin. How to explore chemical space using algorithms and automation. *Nature Reviews Chem-*

istry, 3(2):119–128, feb 2019. ISSN 2397-3358. doi: 10.1038/s41570-018-0066-y. URL `http://www.nature.com/articles/s41570-018-0066-y`.

[74] Jonathan M. Stokes, Kevin Yang, Kyle Swanson, Wengong Jin, Andres Cubillos-Ruiz, Nina M. Donghia, Craig R. MacNair, Shawn French, Lindsey A. Carfrae, Zohar Bloom-Ackerman, Victoria M. Tran, Anush Chiappino-Pepe, Ahmed H. Badran, Ian W. Andrews, Emma J. Chory, George M. Church, Eric D. Brown, Tommi S. Jaakkola, Regina Barzilay, and James J. Collins. A Deep Learning Approach to Antibiotic Discovery. *Cell*, 180(4):688–702.e13, feb 2020. ISSN 00928674. doi: 10.1016/j.cell.2020.01.021. URL `https://linkinghub.elsevier.com/retrieve/pii/S0092867420301021`.

[75] Konstantin Troshin and John F. Hartwig. Snap deconvolution: An informatics approach to high-throughput discovery of catalytic reactions. *Science*, 357 (6347):175–181, jul 2017. ISSN 0036-8075. doi: 10.1126/science.aan1568. URL `https://www.sciencemag.org/lookup/doi/10.1126/science.aan1568`.

[76] Radislav Potyrailo, Krishna Rajan, Klaus Stoewe, Ichiro Takeuchi, Bret Chisholm, and Hubert Lam. Combinatorial and High-Throughput Screening of Materials Libraries: Review of State of the Art. *ACS Combinatorial Science*, 13 (6):579–633, nov 2011. ISSN 2156-8952. doi: 10.1021/co200007w. URL `https://pubs.acs.org/doi/10.1021/co200007w`.

[77] Younan Xia, Yujie Xiong, Byungkwon Lim, and Sara E. Skrabalak. Shape-Controlled Synthesis of Metal Nanocrystals: Simple Chemistry Meets Complex Physics? *Angewandte Chemie International Edition*, 48(1):60–103, jan 2009. ISSN 14337851. doi: 10.1002/anie.200802248. URL `http://doi.wiley.com/10.1002/anie.200802248`.

[78] Jun Cui, Yong S. Chu, Olugbenga O. Famodu, Yasubumi Furuya, Jae. Hattrick-Simpers, Richard D. James, Alfred Ludwig, Sigurd Thienhaus, Manfred Wuttig, Zhiyong Zhang, and Ichiro Takeuchi. Combinatorial search of thermoelastic shape-memory alloys with extremely small hysteresis width. *Nature Materials*, 5(4):286–290, apr 2006. ISSN 1476-1122. doi: 10.1038/nmat1593. URL `http://www.nature.com/articles/nmat1593`.

[79] Mark R. Langille, Michelle L. Personick, Jian Zhang, and Chad A. Mirkin. Defining Rules for the Shape Evolution of Gold Nanoparticles. *Journal of the American Chemical Society*, 134(35):14542–14554, sep 2012. ISSN 0002-7863. doi: 10.1021/ja305245g. URL `https://pubs.acs.org/doi/10.1021/ja305245g`.

[80] Jonathan S. Owen, Emory M. Chan, Haitao Liu, and A. Paul Alivisatos. Precursor Conversion Kinetics and the Nucleation of Cadmium Selenide Nanocrystals. *Journal of the American Chemical Society*, 132(51):18206–18213, dec 2010. ISSN 0002-7863. doi: 10.1021/ja106777j. URL `https://pubs.acs.org/doi/10.1021/ja106777j`.

[81] Emory M. Chan, Chenxu Xu, Alvin W. Mao, Gang Han, Jonathan S. Owen, Bruce E. Cohen, and Delia J. Milliron. Reproducible, High-Throughput Synthesis of Colloidal Nanocrystals for Optimization in Multidimensional Parameter Space. *Nano Letters*, 10(5):1874–1885, may 2010. ISSN 1530-6984. doi: 10.1021/nl100669s. URL `https://pubs.acs.org/doi/10.1021/nl100669s`.

[82] Joseph Berry, Tonio Buonassisi, David A. Egger, Gary Hodes, Leeor Kronik, Yueh-Lin Loo, Igor Lubomirsky, Seth R. Marder, Yitzhak Mastai, Joel S. Miller, David B. Mitzi, Yaron Paz, Andrew M. Rappe, Ilan Riess, Boris Rybtchinski, Oscar Stafsudd, Vladan Stevanovic, Michael F. Toney, David Zitoun, Antoine Kahn, David Ginley, and David Cahen. Hybrid Organic-Inorganic Perovskites (HOIPs): Opportunities and Challenges. *Advanced Materials*, 27(35):5102–5112, sep 2015. ISSN 09359648. doi: 10.1002/adma.201502294. URL `http://doi.wiley.com/10.1002/adma.201502294`.

[83] Samuel D. Stranks and Henry J. Snaith. Metal-halide perovskites for photovoltaic and light-emitting devices. *Nature Nanotechnology*, 10(5):391–402, may 2015. ISSN 1748-3387. doi: 10.1038/nnano.2015.90. URL `http://www.nature.com/articles/nnano.2015.90`.

[84] Quinten A. Akkerman, Sungwook Park, Eros Radicchi, Francesca Nunzi, Edoardo Mosconi, Filippo De Angelis, Rosaria Brescia, Prachi Rastogi, Mirko Prato, and Liberato Manna. Nearly Monodisperse Insulator Cs4PbX6 (X = Cl, Br, I) Nanocrystals, Their Mixed Halide Compositions, and Their Transformation into CsPbX3 Nanocrystals. *Nano Letters*, 17(3):1924–1930, mar 2017. ISSN 15306992. doi: 10.1021/acs.nanolett.6b05262. URL `http://pubs.acs.org/doi/abs/10.1021/acs.nanolett.6b05262`.

[85] Maksym V Kovalenko, Loredana Protesescu, and Maryna I Bodnarchuk. Properties and potential optoelectronic applications of lead halide perovskite nanocrystals. *Science*, 358(6364):745–750, nov 2017. ISSN 0036-8075. doi: 10.1126/science.aam7093. URL `http://www.ncbi.nlm.nih.gov/pubmed/29123061` `http://www.sciencemag.org/lookup/doi/10.1126/science.aam7093` `https://www.science.org/doi/10.1126/science.aam7093`.

[86] Kun-Hua Wang, Liang Wu, Lei Li, Hong-Bin Yao, Hai-Sheng Qian, and Shu-Hong Yu. Large-Scale Synthesis of Highly Luminescent Perovskite-Related CsPb 2 Br 5 Nanoplatelets and Their Fast Anion Exchange. *Angewandte Chemie International Edition*, 55(29):8328–8332, jul 2016. ISSN 14337851. doi: 10.1002/anie.201602787. URL `http://doi.wiley.com/10.1002/anie.201602787`.

[87] Subila K. Balakrishnan and Prashant V. Kamat. Ligand Assisted Transformation of Cubic CsPbBr 3 Nanocrystals into Two-Dimensional CsPb 2 Br 5 Nanosheets. *Chemistry of Materials*, 30(1):74–78, jan

2018. ISSN 0897-4756. doi: 10.1021/acs.chemmater.7b04142. URL `https://pubs.acs.org/doi/10.1021/acs.chemmater.7b04142`.

[88] Loredana Protesescu, Sergii Yakunin, Maryna I. Bodnarchuk, Franziska Krieg, Riccarda Caputo, Christopher H. Hendon, Ruo Xi Yang, Aron Walsh, and Maksym V. Kovalenko. Nanocrystals of Cesium Lead Halide Perovskites (CsPbX3, X = Cl, Br, and I): Novel Optoelectronic Materials Showing Bright Emission with Wide Color Gamut. *Nano Letters*, 15(6):3692–3696, jun 2015. ISSN 1530-6984. doi: 10.1021/nl5048779. URL `http://pubs.acs.org/doi/10.1021/nl5048779`.

[89] Yehonadav Bekenstein, Jakob C. Dahl, Jianmei Huang, Wojciech T. Osowiecki, Joseph K. Swabeck, Emory M. Chan, Peidong Yang, and A. Paul Alivisatos. The Making and Breaking of Lead-Free Double Perovskite Nanocrystals of Cesium Silver-Bismuth Halide Compositions. *Nano Letters*, 18(6):3502–3508, jun 2018. ISSN 15306992. doi: 10.1021/acs.nanolett.8b00560. URL `http://pubs.acs.org/doi/10.1021/acs.nanolett.8b00560`.

[90] Emre Yassitepe, Zhenyu Yang, Oleksandr Voznyy, Younghoon Kim, Grant Walters, Juan Andres Castañeda, Pongsakorn Kanjanaboos, Mingjian Yuan, Xiwen Gong, Fengjia Fan, Jun Pan, Sjoerd Hoogland, Riccardo Comin, Osman M. Bakr, Lazaro A. Padilha, Ana F. Nogueira, and Edward H. Sargent. Amine-Free Synthesis of Cesium Lead Halide Perovskite Quantum Dots for Efficient Light-Emitting Diodes. *Advanced Functional Materials*, 26(47):8757–8763, dec 2016. ISSN 1616301X. doi: 10.1002/adfm.201604580. URL `http://doi.wiley.com/10.1002/adfm.201604580`.

[91] Aizhao Pan, Bo He, Xiaoyun Fan, Zeke Liu, Jeffrey J. Urban, A. Paul Alivisatos, Ling He, and Yi Liu. Insight into the Ligand-Mediated Synthesis of Colloidal CsPbBr 3 Perovskite Nanocrystals: The Role of Organic Acid, Base, and Cesium Precursors. *ACS Nano*, 10(8):7943–7954, aug 2016. ISSN 1936-0851. doi: 10.1021/acsnano.6b03863. URL `http://pubs.acs.org/doi/10.1021/acsnano.6b03863`.

[92] Guilherme Almeida, Luca Goldoni, Quinten Akkerman, Zhiya Dang, Ali Hossain Khan, Sergio Marras, Iwan Moreels, and Liberato Manna. Role of Acid–Base Equilibria in the Size, Shape, and Phase Control of Cesium Lead Bromide Nanocrystals. *ACS Nano*, 12(2):1704–1711, feb 2018. ISSN 1936-0851. doi: 10.1021/acsnano.7b08357. URL `http://pubs.acs.org/doi/10.1021/acsnano.7b08357`.

[93] Muhammad Imran, Palvasha Ijaz, Dmitry Baranov, Luca Goldoni, Urko Petralanda, Quinten Akkerman, Ahmed L. Abdelhady, Mirko Prato, Paolo Bianchini, Ivan Infante, and Liberato Manna. Shape-Pure, Nearly Monodispersed CsPbBr 3 Nanocubes Prepared Using Secondary Aliphatic Amines. *Nano Letters*, 18(12): 7822–7831, dec 2018. ISSN 1530-6984. doi: 10.1021/acs.nanolett.8b03598. URL `https://pubs.acs.org/doi/10.1021/acs.nanolett.8b03598`.

[94] Shibin Sun, Dan Yuan, Yuan Xu, Aifei Wang, and Zhengtao Deng. Ligand-Mediated Synthesis of Shape-Controlled Cesium Lead Halide Perovskite Nanocrystals via Reprecipitation Process at Room Temperature. *ACS Nano*, 10(3): 3648–3657, mar 2016. ISSN 1936086X. doi: 10.1021/acsnano.5b08193. URL `http://pubs.acs.org/doi/abs/10.1021/acsnano.5b08193`.

[95] Erick J. Braham, Junsang Cho, Kristel M. Forlano, David F. Watson, Raymundo Arròyave, and Sarbajit Banerjee. Machine Learning-Directed Navigation of Synthetic Design Space: A Statistical Learning Approach to Controlling the Synthesis of Perovskite Halide Nanoplatelets in the Quantum-Confined Regime. *Chemistry of Materials*, 31(9):3281–3292, may 2019. ISSN 0897-4756. doi: 10.1021/acs.chemmater.9b00212. URL `https://pubs.acs.org/doi/10.1021/acs.chemmater.9b00212`.

[96] Qiang Jing, Yue Xu, Yucong Su, Xing Xing, and Zhenda Lu. A systematic study of the synthesis of cesium lead halide nanocrystals: does Cs 4 PbBr 6 or CsPbBr 3 form? *Nanoscale*, 11(4):1784–1789, 2019. ISSN 2040-3364. doi: 10.1039/C8NR08116F. URL `http://xlink.rsc.org/?DOI=C8NR08116F`.

[97] Jasmina A. Sichert, Yu Tong, Niklas Mutz, Mathias Vollmer, Stefan Fischer, Karolina Z. Milowska, Ramon García Cortadella, Bert Nickel, Carlos Cardenas-Daw, Jacek K. Stolarczyk, Alexander S. Urban, and Jochen Feldmann. Quantum Size Effect in Organometal Halide Perovskite Nanoplatelets. *Nano Letters*, 15(10): 6521–6527, oct 2015. ISSN 1530-6984. doi: 10.1021/acs.nanolett.5b02985. URL `https://pubs.acs.org/doi/10.1021/acs.nanolett.5b02985`.

[98] Brent A. Koscher, Joseph K. Swabeck, Noah D. Bronstein, and A. Paul Alivisatos. Essentially Trap-Free CsPbBr 3 Colloidal Nanocrystals by Postsynthetic Thiocyanate Surface Treatment. *Journal of the American Chemical Society*, 139(19):6566–6569, may 2017. ISSN 15205126. doi: 10.1021/jacs.7b02817. URL `http://pubs.acs.org/doi/abs/10.1021/jacs.7b02817` `http://pubs.acs.org/doi/10.1021/jacs.7b02817`.

[99] Je-Ruei Wen, Benjamin J. Roman, Freddy A. Rodriguez Ortiz, Noel Mireles Villegas, Nicholas Porcellino, and Matthew Sheldon. Chemical Availability of Bromide Dictates CsPbBr 3 Nanocrystal Growth. *Chemistry of Materials*, 31(20): 8551–8557, oct 2019. ISSN 0897-4756. doi: 10.1021/acs.chemmater.9b03709. URL `https://pubs.acs.org/doi/10.1021/acs.chemmater.9b03709`.

[100] Yasser Hassan, Yin Song, Ryan D. Pensack, Ahmed I. Abdelrahman, Yoichi Kobayashi, Mitchell A. Winnik, and Gregory D. Scholes. Structure-Tuned Lead Halide Perovskite Nanocrystals. *Advanced Materials*, 28(3):566–573, jan 2016. ISSN 09359648. doi: 10.1002/adma.201503461. URL `http://doi.wiley.com/10.1002/adma.201503461`.

[101] Bo Yin, John Cavin, Dong Wang, Daniel Khan, Meikun Shen, Craig Laing, Rohan Mishra, and Bryce Sadtler. Fluorescence microscopy of single lead bromide nanocrystals reveals sharp transitions during their transformation to methylammonium lead bromide. *Journal of Materials Chemistry C*, 7(12):3486–3495, 2019. ISSN 2050-7526. doi: 10.1039/C8TC06470A. URL `http://xlink.rsc.org/?DOI=C8TC06470A`.

[102] Jakob C. Dahl, Wojciech T. Osowiecki, Yao Cai, Joseph K. Swabeck, Yehonadav Bekenstein, Mark Asta, Emory M. Chan, and A. Paul Alivisatos. Probing the Stability and Band Gaps of Cs 2 AgInCl 6 and Cs 2 AgSbCl 6 Lead-Free Double Perovskite Nanocrystals. *Chemistry of Materials*, 31(9):3134–3143, may 2019. ISSN 0897-4756. doi: 10.1021/acs.chemmater.8b04202. URL `https://pubs.acs.org/doi/10.1021/acs.chemmater.8b04202`.

[103] Muhammad Imran, Vincenzo Caligiuri, Mengjiao Wang, Luca Goldoni, Mirko Prato, Roman Krahne, Luca De Trizio, and Liberato Manna. Benzoyl Halides as Alternative Precursors for the Colloidal Synthesis of Lead-Based Halide Perovskite Nanocrystals. *Journal of the American Chemical Society*, 140(7): 2656–2664, feb 2018. ISSN 0002-7863. doi: 10.1021/jacs.7b13477. URL `http://pubs.acs.org/doi/10.1021/jacs.7b13477`.

[104] Yehonadav Bekenstein, Brent A. Koscher, Samuel W. Eaton, Peidong Yang, and A. Paul Alivisatos. Highly Luminescent Colloidal Nanoplates of Perovskite Cesium Lead Halide and Their Oriented Assemblies. *Journal of the American Chemical Society*, 137(51):16008–16011, dec 2015. ISSN 15205126. doi: 10.1021/jacs.5b11199. URL `http://pubs.acs.org/doi/abs/10.1021/jacs.5b11199`.

[105] Ibrahim Dursun, Michele De Bastiani, Bekir Turedi, Badriah Alamer, Aleksander Shkurenko, Jun Yin, Ahmed M. El-Zohry, Issam Gereige, Ahmed AlSaggaf, Omar F. Mohammed, Mohamed Eddaoudi, and Osman M. Bakr. CsPb 2 Br 5 Single Crystals: Synthesis and Characterization. *ChemSusChem*, 10 (19):3746–3749, oct 2017. ISSN 18645631. doi: 10.1002/cssc.201701131. URL `http://doi.wiley.com/10.1002/cssc.201701131`.

[106] Zhaojun Qin, Shenyu Dai, Viktor G. Hadjiev, Chong Wang, Lixin Xie, Yizhou Ni, Chunzheng Wu, Guang Yang, Shuo Chen, Liangzi Deng, Qingkai Yu, Guoying Feng, Zhiming M. Wang, and Jiming Bao. Revealing the Origin of Luminescence Center in 0D Cs 4 PbBr 6 Perovskite. *Chemistry of Materials*, 31(21): 9098–9104, nov 2019. ISSN 0897-4756. doi: 10.1021/acs.chemmater.9b03426. URL `https://pubs.acs.org/doi/10.1021/acs.chemmater.9b03426`.

[107] A. J. H. Eijkelenkamp and K. Vos. Reflectance Measurements on Single Crystals of PbFCl, PbFBr, and PbBr2. *physica status solidi (b)*, 76(2): 769–778, aug 1976. ISSN 03701972. doi: 10.1002/pssb.2220760238. URL `http://doi.wiley.com/10.1002/pssb.2220760238`.

[108] Seog Joon Yoon, Kevin G. Stamplecoskie, and Prashant V. Kamat. How Lead Halide Complex Chemistry Dictates the Composition of Mixed Halide Perovskites. *Journal of Physical Chemistry Letters*, 7(7):1368–1373, apr 2016. ISSN 19487185. doi: 10.1021/acs.jpclett.6b00433. URL `http://pubs.acs.org/doi/abs/10.1021/acs.jpclett.6b00433`.

[109] Seung-Jean Kim, K. Koh, M. Lustig, Stephen Boyd, and Dimitry Gorinevsky. An Interior-Point Method for Large-Scale -Regularized Least Squares. *IEEE Journal of Selected Topics in Signal Processing*, 1(4):606–617, dec 2007. ISSN 1932-4553. doi: 10.1109/JSTSP.2007.910971. URL `http://ieeexplore.ieee.org/document/4407767/`.

[110] Jerome Friedman, Trevor Hastie, and Rob Tibshirani. Regularization Paths for Generalized Linear Models via Coordinate Descent. *Journal of statistical software*, 33(1): 1–22, 2010. ISSN 1548-7660. URL `http://www.ncbi.nlm.nih.gov/pubmed/20808728` `http://www.pubmedcentral.nih.gov/articlerender.fcgi?artid=PMC2929880`.

[111] Florian D. Ott, Andreas Riedinger, David R. Ochsenbein, Philippe N. Knüsel, Steven C. Erwin, Marco Mazzotti, and David J. Norris. Ripening of Semiconductor Nanoplatelets. *Nano Letters*, 17(11):6870–6877, nov 2017. ISSN 1530-6984. doi: 10.1021/acs.nanolett.7b03191. URL `https://pubs.acs.org/doi/10.1021/acs.nanolett.7b03191`.

[112] Philippe N. Knüsel, Andreas Riedinger, Aurelio A. Rossinelli, Florian D. Ott, Aniket S. Mule, and David J. Norris. Experimental Evidence for Two-Dimensional Ostwald Ripening in Semiconductor Nanoplatelets. *Chemistry of Materials*, 32(7): 3312–3319, apr 2020. ISSN 0897-4756. doi: 10.1021/acs.chemmater.0c01238. URL `https://pubs.acs.org/doi/10.1021/acs.chemmater.0c01238`.

[113] Juan Hui, Yingnan Jiang, Ömür Ö Gökçinar, Junbin Tang, Qiyu Yu, Meng Zhang, and Kui Yu. Unveiling the Two-Step Formation Pathway of Cs 4 PbBr 6 Nanocrystals. *Chemistry of Materials*, page acs.chemmater.0c00661, may 2020. ISSN 0897-4756. doi: 10.1021/acs.chemmater.0c00661. URL `https://pubs.acs.org/doi/10.1021/acs.chemmater.0c00661`.

[114] Martin Feinberg. Chemical reaction network structure and the stability of complex isothermal reactors—I. The deficiency zero and deficiency one theorems. *Chemical Engineering Science*, 42(10):2229–2268, 1987. ISSN 00092509. doi: 10.1016/0009-2509(87)80099-4. URL `https://linkinghub.elsevier.com/retrieve/pii/0009250987800994`.

[115] Thumu Udayabhaskararao, Miri Kazes, Lothar Houben, Hong Lin, and Dan Oron. Nucleation, Growth, and Structural Transformations of Perovskite Nanocrystals. *Chemistry of Materials*, 29(3):1302–1308, feb

2017. ISSN 0897-4756. doi: 10.1021/acs.chemmater.6b04841. URL `https://pubs.acs.org/doi/10.1021/acs.chemmater.6b04841`.

[116] Stefano Toso, Dmitry Baranov, Davide Altamura, Francesco Scattarella, Jakob Dahl, Xingzhi Wang, Sergio Marras, A. Paul Alivisatos, Andrej Singer, Cinzia Giannini, and Liberato Manna. Multilayer Diffraction Reveals That Colloidal Superlattices Approach the Structural Perfection of Single Crystals. *ACS Nano*, 15 (4):6243–6256, apr 2021. ISSN 1936-0851. doi: 10.1021/acsnano.0c08929. URL `https://pubs.acs.org/doi/10.1021/acsnano.0c08929`.

[117] Jason J. Calvin, Justin C. Ondry, Jakob C. Dahl, Adam B. Sedlak, Amy McKeown-Green, Xingzhi Wang, Michelle F. Crook, Samuel P. Gleason, Matthew R. Hauwiller, Anne M. Baranger, and A. Paul Alivisatos. Research Group-Led Undergraduate Research Program: Analyzing and Improving a Versatile Springboard for First-Year Undergraduates. *Journal of Chemical Education*, 99(2): 799–809, feb 2022. ISSN 0021-9584. doi: 10.1021/acs.jchemed.1c01065. URL `https://pubs.acs.org/doi/10.1021/acs.jchemed.1c01065`.

[118] Chang Lu, Marcus W. Wright, Xiao Ma, Hui Li, Dominique S. Itanze, Jake A. Carter, Corey A. Hewitt, George L. Donati, David L. Carroll, Pamela M. Lundin, and Scott M. Geyer. Cesium Oleate Precursor Preparation for Lead Halide Perovskite Nanocrystal Synthesis: The Influence of Excess Oleic Acid on Achieving Solubility, Conversion, and Reproducibility. *Chemistry of Materials*, 31(1): 62–67, jan 2019. ISSN 0897-4756. doi: 10.1021/acs.chemmater.8b04876. URL `https://pubs.acs.org/doi/10.1021/acs.chemmater.8b04876`.

[119] Wes McKinney. Data Structures for Statistical Computing in Python. In Stéfan van der Walt and Jarrod Millman, editors, *Proceedings of the 9th Python in Science Conference*, pages 51–56, 2010.

[120] Abraham. Savitzky and M. J. E. Golay. Smoothing and Differentiation of Data by Simplified Least Squares Procedures. *Analytical Chemistry*, 36(8): 1627–1639, jul 1964. ISSN 0003-2700. doi: 10.1021/ac60214a047. URL `https://pubs.acs.org/doi/abs/10.1021/ac60214a047`.

[121] Pauli Virtanen, Ralf Gommers, Travis E. Oliphant, Matt Haberland, Tyler Reddy, David Cournapeau, Evgeni Burovski, Pearu Peterson, Warren Weckesser, Jonathan Bright, Stéfan J. van der Walt, Matthew Brett, Joshua Wilson, K. Jarrod Millman, Nikolay Mayorov, Andrew R. J. Nelson, Eric Jones, Robert Kern, Eric Larson, C J Carey, İlhan Polat, Yu Feng, Eric W. Moore, Jake VanderPlas, Denis Laxalde, Josef Perktold, Robert Cimrman, Ian Henriksen, E. A. Quintero, Charles R. Harris, Anne M. Archibald, Antônio H. Ribeiro, Fabian Pedregosa, and Paul van Mulbregt. SciPy 1.0: fundamental algorithms for scientific computing in Python. *Nature Methods*,

17(3):261–272, mar 2020. ISSN 1548-7091. doi: 10.1038/s41592-019-0686-2. URL `http://www.nature.com/articles/s41592-019-0686-2`.

[122] Weiqi Ji and Sili Deng. Autonomous Discovery of Unknown Reaction Pathways from Data by Chemical Reaction Neural Network. *The Journal of Physical Chemistry A*, 125(4):1082–1092, feb 2021. ISSN 1089-5639. doi: 10.1021/acs.jpca.0c09316. URL `https://pubs.acs.org/doi/10.1021/acs.jpca.0c09316`.

[123] Jolene P. Reid, Rupert S. J. Proctor, Matthew S. Sigman, and Robert J. Phipps. Predictive multivariate linear regression analysis guides successful catalytic enantioselective minisci reactions of diazines. *Journal of the American Chemical Society*, 141(48):19178–19185, Dec 2019. ISSN 0002-7863. doi: 10.1021/jacs.9b11658. URL `https://doi.org/10.1021/jacs.9b11658`.

[124] Christopher Rackauckas and Qing Nie. DifferentialEquations.jl – A Performant and Feature-Rich Ecosystem for Solving Differential Equations in Julia. *Journal of Open Research Software*, 5, may 2017. ISSN 2049-9647. doi: 10.5334/jors.151. URL `http://openresearchsoftware.metajnl.com/articles/10.5334/jors.151/`.

[125] S. K. Novoselov, K. A. Geim, V. S. Morozov, D. Jiangand, Y. Zhang, V. S. Dubonos, V. I. Grigorieva, and A. A. Firsov. Electric field effect in atomically thin carbon films. *Science*, 306(5696):666–669, Oct 2004. doi: 10.1126/science.1102896. URL `https://doi.org/10.1126/science.1102896`.

[126] Mingsheng Xu, Tao Liang, Minmin Shi, and Hongzheng Chen. Graphene-like two-dimensional materials. *Chemical Reviews*, 113(5):3766–3798, May 2013. ISSN 0009-2665. doi: 10.1021/cr300263a. URL `https://doi.org/10.1021/cr300263a`.

[127] Karim Khan, Ayesha Khan Tareen, Muhammad Aslam, Renheng Wang, Yupeng Zhang, Asif Mahmood, Zhengbiao Ouyang, Han Zhang, and Zhongyi Guo. Recent developments in emerging two-dimensional materials and their applications. *Journal of Materials Chemistry C*, 8(2):387–440, 2020. ISSN 2050-7526. doi: 10.1039/C9TC04187G. URL `https://doi.org/10.1039/C9TC04187G`.

[128] Quinten A. Akkerman, Gabriele Rainò, Maksym V. Kovalenko, and Liberato Manna. Genesis, challenges and opportunities for colloidal lead halide perovskite nanocrystals. *Nature Materials*, 17(5):394–405, may 2018. ISSN 1476-1122. doi: 10.1038/s41563-018-0018-4. URL `http://www.nature.com/articles/s41563-018-0018-4`.

[129] Xinyi Chia and Martin Pumera. Characteristics and performance of two-dimensional materials for electrocatalysis. *Nature Catalysis*, 1(12):909–921, Dec 2018. ISSN 2520-1158. doi: 10.1038/s41929-018-0181-7. URL `https://doi.org/10.1038/s41929-018-0181-7`.

[130] Adam Bolotsky, Derrick Butler, Chengye Dong, Katy Gerace, Nicholas R. Glavin, Christopher Muratore, Joshua A. Robinson, and Aida Ebrahimi. Two-dimensional materials in biosensing and healthcare: From in vitro diagnostics to optogenetics and beyond. *ACS Nano*, 13(9):9781–9810, Sep 2019. ISSN 1936-0851. doi: 10.1021/acsnano.9b03632. URL `https://doi.org/10.1021/acsnano.9b03632`.

[131] Gianluca Fiori, Francesco Bonaccorso, Giuseppe Iannaccone, Tomás Palacios, Daniel Neumaier, Alan Seabaugh, Sanjay K. Banerjee, and Luigi Colombo. Electronics based on two-dimensional materials. *Nature Nanotechnology*, 9(10): 768–779, Oct 2014. ISSN 1748-3395. doi: 10.1038/nnano.2014.207. URL `https://doi.org/10.1038/nnano.2014.207`.

[132] Christos Tsakonas, Marinos Dimitropoulos, Anastasios C. Manikas, and Costas Galiotis. Growth and in situ characterization of 2D materials by chemical vapour deposition on liquid metal catalysts: a review. *Nanoscale*, 13(6):3346–3373, 2021. ISSN 2040-3364. doi: 10.1039/D0NR07330J. URL `http://xlink.rsc.org/?DOI=D0NR07330J`.

[133] Minchao Qin, Pok Fung Chan, and Xinhui Lu. A Systematic Review of Metal Halide Perovskite Crystallization and Film Formation Mechanism Unveiled by In Situ GIWAXS. *Advanced Materials*, 33(51):2105290, dec 2021. ISSN 0935-9648. doi: 10.1002/adma.202105290. URL `https://onlinelibrary.wiley.com/doi/10.1002/adma.202105290`.

[134] Justin M. Hoffman, Joseph Strzalka, Nathan C. Flanders, Ido Hadar, Shelby A. Cuthriell, Qingteng Zhang, Richard D. Schaller, William R. Dichtel, Lin X. Chen, and Mercouri G. Kanatzidis. In Situ Grazing-Incidence Wide-Angle Scattering Reveals Mechanisms for Phase Distribution and Disorientation in 2D Halide Perovskite Films. *Advanced Materials*, 32(33):2002812, aug 2020. ISSN 0935-9648. doi: 10.1002/adma.202002812. URL `https://onlinelibrary.wiley.com/doi/10.1002/adma.202002812`.

[135] James C. Sadighian and Cathy Y. Wong. Just Scratching the Surface: In Situ and Surface-Specific Characterization of Perovskite Nanocrystal Growth. *The Journal of Physical Chemistry C*, 125(38):20772–20782, sep 2021. ISSN 1932-7447. doi: 10.1021/acs.jpcc.1c06582. URL `https://pubs.acs.org/doi/10.1021/acs.jpcc.1c06582`.

[136] Narayan Pradhan. Growth of Lead Halide Perovskite Nanocrystals: Still in Mystery. *ACS Physical Chemistry Au*, page acsphyschemau.2c00001, feb 2022. ISSN 2694-2445. doi: 10.1021/acsphyschemau.2c00001. URL `https://pubs.acs.org/doi/10.1021/acsphyschemau.2c00001`.

[137] Feng Liu, Chao Ding, Yaohong Zhang, Teresa S. Ripolles, Taichi Kamisaka, Taro Toyoda, Shuzi Hayase, Takashi Minemoto, Kenji Yoshino, Songyuan Dai, Masatoshi

Yanagida, Hidenori Noguchi, and Qing Shen. Colloidal Synthesis of Air-Stable Alloyed CsSn 1– x Pb x I 3 Perovskite Nanocrystals for Use in Solar Cells. *Journal of the American Chemical Society*, 139(46):16708–16719, nov 2017. ISSN 0002-7863. doi: 10.1021/jacs.7b08628. URL `http://pubs.acs.org/doi/10.1021/jacs.7b08628`.

[138] Suman Bera, Rakesh Kumar Behera, Samrat Das Adhikari, Amit K. Guria, and Narayan Pradhan. Equilibriums in Formation of Lead Halide Perovskite Nanocrystals. *The Journal of Physical Chemistry Letters*, 12(49):11824–11833, dec 2021. ISSN 1948-7185. doi: 10.1021/acs.jpclett.1c03461. URL `https://pubs.acs.org/doi/10.1021/acs.jpclett.1c03461`.

[139] Yeongsu Cho and Timothy C. Berkelbach. Optical Properties of Layered Hybrid Organic–Inorganic Halide Perovskites: A Tight-Binding GW-BSE Study. *The Journal of Physical Chemistry Letters*, 10(20):6189–6196, oct 2019. ISSN 1948-7185. doi: 10.1021/acs.jpclett.9b02491. URL `https://pubs.acs.org/doi/10.1021/acs.jpclett.9b02491`.

[140] Soline Boyer-Richard, Claudine Katan, Boubacar Traoré, Reinhard Scholz, Jean-Marc Jancu, and Jacky Even. Symmetry-Based Tight Binding Modeling of Halide Perovskite Semiconductors. *The Journal of Physical Chemistry Letters*, 7(19): 3833–3840, oct 2016. ISSN 1948-7185. doi: 10.1021/acs.jpclett.6b01749. URL `https://pubs.acs.org/doi/10.1021/acs.jpclett.6b01749`.

[141] Hamid M. Ghaithan, Zeyad A. Alahmed, Saif M. H. Qaid, Mahmoud Hezam, and Abdullah S. Aldwayyan. Density Functional Study of Cubic, Tetragonal, and Orthorhombic CsPbBr 3 Perovskite. *ACS Omega*, 5(13):7468–7480, apr 2020. ISSN 2470-1343. doi: 10.1021/acsomega.0c00197. URL `https://pubs.acs.org/doi/10.1021/acsomega.0c00197`.

[142] John P. Perdew, Adrienn Ruzsinszky, Gábor I. Csonka, Oleg A. Vydrov, Gustavo E. Scuseria, Lucian A. Constantin, Xiaolan Zhou, and Kieron Burke. Restoring the Density-Gradient Expansion for Exchange in Solids and Surfaces. *Physical Review Letters*, 100(13):136406, apr 2008. ISSN 0031-9007. doi: 10.1103/PhysRevLett.100.136406. URL `https://link.aps.org/doi/10.1103/PhysRevLett.100.136406`.

[143] P Giannozzi, O Andreussi, T Brumme, O Bunau, M Buongiorno Nardelli, M Calandra, R Car, C Cavazzoni, D Ceresoli, M Cococcioni, N Colonna, I Carnimeo, A Dal Corso, S de Gironcoli, P Delugas, R A DiStasio, A Ferretti, A Floris, G Fratesi, G Fugallo, R Gebauer, U Gerstmann, F Giustino, T Gorni, J Jia, M Kawamura, H-Y Ko, A Kokalj, E Küçükbenli, M Lazzeri, M Marsili, N Marzari, F Mauri, N L Nguyen, H-V Nguyen, A Otero-de-la Roza, L Paulatto, S Poncé, D Rocca, R Sabatini, B Santra, M Schlipf, A P Seitsonen, A Smogunov, I Timrov, T Thonhauser, P Umari, N Vast, X Wu, and S Baroni. Advanced capabilities for materi-

als modelling with Quantum ESPRESSO. *Journal of Physics: Condensed Matter*, 29(46):465901, nov 2017. ISSN 0953-8984. doi: 10.1088/1361-648X/aa8f79. URL `https://iopscience.iop.org/article/10.1088/1361-648X/aa8f79`.

[144] Arash A. Mostofi, Jonathan R. Yates, Young-Su Lee, Ivo Souza, David Vanderbilt, and Nicola Marzari. wannier90: A tool for obtaining maximally-localised Wannier functions. *Computer Physics Communications*, 178(9):685–699, may 2008. ISSN 00104655. doi: 10.1016/j.cpc.2007.11.016. URL `https://linkinghub.elsevier.com/retrieve/pii/S0010465507004936`.

[145] Edoardo Mosconi, Paolo Umari, and Filippo De Angelis. Electronic and optical properties of MAPbX 3 perovskites (X = I, Br, Cl): a unified DFT and GW theoretical analysis. *Physical Chemistry Chemical Physics*, 18(39):27158–27164, 2016. ISSN 1463-9076. doi: 10.1039/C6CP03969C. URL `http://xlink.rsc.org/?DOI=C6CP03969C`.

[146] L. S. R. Cavalcante, A. Chaves, B. Van Duppen, F. M. Peeters, and D. R. Reichman. Electrostatics of electron-hole interactions in van der Waals heterostructures. *Physical Review B*, 97(12):125427, mar 2018. ISSN 2469-9950. doi: 10.1103/PhysRevB.97.125427. URL `https://link.aps.org/doi/10.1103/PhysRevB.97.125427`.

[147] Emilia Ridolfi, Caio H. Lewenkopf, and Vitor M. Pereira. Excitonic structure of the optical conductivity in ¡math¿ ¡msub¿ ¡mi¿MoS¡/mi¿ ¡mn¿2¡/mn¿ ¡/msub¿ ¡/math¿ monolayers. *Physical Review B*, 97(20):205409, may 2018. ISSN 2469-9950. doi: 10.1103/PhysRevB.97.205409. URL `https://link.aps.org/doi/10.1103/PhysRevB.97.205409`.

[148] Krzysztof Galkowski, Anatolie Mitioglu, Atsuhiko Miyata, Paulina Plochocka, Oliver Portugall, Giles E. Eperon, Jacob Tse-Wei Wang, Thomas Stergiopoulos, Samuel D. Stranks, Henry J. Snaith, and Robin J. Nicholas. Determination of the exciton binding energy and effective masses for methylammonium and formamidinium lead tri-halide perovskite semiconductors. *Energy and Environmental Science*, 9(3):962–970, 2016. ISSN 1754-5692. doi: 10.1039/C5EE03435C. URL `http://xlink.rsc.org/?DOI=C5EE03435C`.

[149] Teruya Ishihara, Jun Takahashi, and Takenari Goto. Optical properties due to electronic transitions in two-dimensional semiconductors (¡math display="inline"¿ ¡mrow¿ ¡msub¿ ¡mrow¿ ¡mi mathvariant="normal"¿C¡/mi¿ ¡/mrow¿ ¡mrow¿ ¡mi mathvariant="italic"¿n¡/mi¿ ¡/mrow¿ ¡/msub¿ ¡/mrow¿ ¡/math¿ ¡math display=. *Physical Review B*, 42(17):11099–11107, dec 1990. ISSN 0163-1829. doi: 10.1103/PhysRevB.42.11099. URL `https://link.aps.org/doi/10.1103/PhysRevB.42.11099`.

[150] Thenner S. Rodrigues, Ming Zhao, Tung-Han Yang, Kyle D. Gilroy, Anderson G. M. da Silva, Pedro H. C. Camargo, and Younan Xia. Synthesis of Colloidal Metal Nanocrystals: A Comprehensive Review on

the Reductants. *Chemistry – A European Journal*, 24(64):16944–16963, nov 2018. ISSN 0947-6539. doi: 10.1002/chem.201802194. URL `https://onlinelibrary.wiley.com/doi/10.1002/chem.201802194`.

[151] Alexander Sharenko, Cameron Mackeen, Leila Jewell, Frank Bridges, and Michael F. Toney. Evolution of Iodoplumbate Complexes in Methylammonium Lead Iodide Perovskite Precursor Solutions. *Chemistry of Materials*, 29(3):1315–1320, feb 2017. ISSN 0897-4756. doi: 10.1021/acs.chemmater.6b04917. URL `https://pubs.acs.org/doi/10.1021/acs.chemmater.6b04917`.

[152] Yunlong Guo, Kazutaka Shoyama, Wataru Sato, Yutaka Matsuo, Kento Inoue, Koji Harano, Chao Liu, Hideyuki Tanaka, and Eiichi Nakamura. Chemical Pathways Connecting Lead(II) Iodide and Perovskite via Polymeric Plumbate(II) Fiber. *Journal of the American Chemical Society*, 137(50):15907–15914, dec 2015. ISSN 0002-7863. doi: 10.1021/jacs.5b10599. URL `https://pubs.acs.org/doi/10.1021/jacs.5b10599`.

[153] Feng Hao, Constantinos C. Stoumpos, Zhao Liu, Robert P. H. Chang, and Mercouri G. Kanatzidis. Controllable Perovskite Crystallization at a Gas–Solid Interface for Hole Conductor-Free Solar Cells with Steady Power Conversion Efficiency over 10%. *Journal of the American Chemical Society*, 136(46):16411–16419, nov 2014. ISSN 0002-7863. doi: 10.1021/ja509245x. URL `https://pubs.acs.org/doi/10.1021/ja509245x`.

[154] Atsushi Wakamiya, Masaru Endo, Takahiro Sasamori, Norihiro Tokitoh, Yuhei Ogomi, Shuzi Hayase, and Yasujiro Murata. Reproducible Fabrication of Efficient Perovskite-based Solar Cells: X-ray Crystallographic Studies on the Formation of CH 3 NH 3 PbI 3 Layers. *Chemistry Letters*, 43(5):711–713, may 2014. ISSN 0366-7022. doi: 10.1246/cl.140074. URL `http://www.journal.csj.jp/doi/10.1246/cl.140074`.

[155] Sergey A. Fateev, Andrey A. Petrov, Victor N. Khrustalev, Pavel V. Dorovatovskii, Yan V. Zubavichus, Eugene A. Goodilin, and Alexey B. Tarasov. Solution Processing of Methylammonium Lead Iodide Perovskite from γ-Butyrolactone: Crystallization Mediated by Solvation Equilibrium. *Chemistry of Materials*, 30(15):5237–5244, aug 2018. ISSN 0897-4756. doi: 10.1021/acs.chemmater.8b01906. URL `https://pubs.acs.org/doi/10.1021/acs.chemmater.8b01906`.

[156] Karin Oldenburg and Arnd Vogler. Electronic Spectra and Photochemistry of Tin(II), Lead(II), Antimony(III), and Bismuth(III) Bromide Complexes in Solution. *Zeitschrift für Naturforschung B*, 48(11):1519–1523, nov 1993. ISSN 1865-7117. doi: 10.1515/znb-1993-1109. URL `https://www.degruyter.com/view/journals/znb/48/11/article-p1519.xml`.

[157] A. Bohun, J. Sak, and J. Dolejší. Optische und elektrische Erscheinungen in bleiaktivierten Alkalihalogeniden. *physica status solidi (b)*, 9(2): 341–350, 1965. ISSN 03701972. doi: 10.1002/pssb.19650090205. URL `http://doi.wiley.com/10.1002/pssb.19650090205`.

[158] A.R. Jones and D.A. Aikens. The nature of pb(II)-bromide complexes in propylene carbonate. *Polyhedron*, 1(2):169–174, jan 1982. ISSN 02775387. doi: 10.1016/S0277-5387(00)80980-8. URL `https://linkinghub.elsevier.com/retrieve/pii/S0277538700809808`.

[159] O. Horváth, T. Marosvölgyi, and J. Vörös. Microenvironmental effects on equilibrium and photoredox chemistry of bromo complexes in reverse micelles. In *From Colloids to Nanotechnology*, pages 17–23. Springer Berlin Heidelberg, Berlin, Heidelberg, jul 2004.

[160] Diego Ferri, Francesco Salvatore, and Ermanno Vasca. Complex Formation Between Lead(II) and Bromide Ions. *Journal of Coordination Chemistry*, 20(1): 11–20, jun 1989. ISSN 0095-8972. doi: 10.1080/00958978909408843. URL `http://www.tandfonline.com/doi/abs/10.1080/00958978909408843`.

[161] Suman Bera, Rakesh Kumar Behera, and Narayan Pradhan. alpha-Halo Ketone for Polyhedral Perovskite Nanocrystals: Evolutions, Shape Conversions, Ligand Chemistry, and Self-Assembly. *Journal of the American Chemical Society*, 142 (49):20865–20874, dec 2020. ISSN 0002-7863. doi: 10.1021/jacs.0c10688. URL `https://pubs.acs.org/doi/10.1021/jacs.0c10688`.

[162] Feiming Li, Fangyuan Lin, Yipeng Huang, Zhixiong Cai, Linhang Qiu, Yimeng Zhu, Yaqi Jiang, Yiru Wang, and Xi Chen. Bromobenzene aliphatic nucleophilic substitution guided controllable and reproducible synthesis of high quality cesium lead bromide perovskite nanocrystals. *Inorganic Chemistry Frontiers*, 6(12):3577–3582, 2019. ISSN 2052-1553. doi: 10.1039/C9QI01095E. URL `http://xlink.rsc.org/?DOI=C9QI01095E`.

[163] Leslie S. Hamachi, Haoran Yang, Ilan Jen-La Plante, Natalie Saenz, Kevin Qian, Michael P. Campos, Gregory T. Cleveland, Iva Rreza, Aisha Oza, Willem Walravens, Emory M. Chan, Zeger Hens, Andrew C. Crowther, and Jonathan S. Owen. Precursor reaction kinetics control compositional grading and size of CdSe 1-x S x nanocrystal heterostructures. *Chemical Science*, 10(26):6539–6552, 2019. ISSN 2041-6520. doi: 10.1039/C9SC00989B. URL `http://xlink.rsc.org/?DOI=C9SC00989B`.

[164] Evgeny Epifanovsky, Andrew T.B. Gilbert, Xintian Feng, Joonho Lee, Yuezhi Mao, Narbe Mardirossian, Pavel Pokhilko, Alec F. White, Marc P. Coons, Adrian L. Dempwolff, Zhengting Gan, Diptarka Hait, Paul R. Horn, Leif D. Jacobson, Ilya Kaliman, Jörg Kussmann, Adrian W. Lange, Ka Un Lao, Daniel S. Levine, Jie Liu, Simon C. McKenzie, Adrian F. Morrison, Kaushik D. Nanda, Felix Plasser, Dirk R. Rehn, Marta L. Vidal, Zhi Qiang You, Ying Zhu, Bushra Alam, Benjamin J. Albrecht, Abdulrahman Aldossary, Ethan Alguire, Josefine H. Andersen, Vishikh Athavale, Dennis Barton, Khadiza Begam, Andrew Behn, Nicole Bellonzi, Yves A. Bernard, Eric J. Berquist, Hugh G.A. Burton, Abel Carreras, Kevin Carter-Fenk, Romit Chakraborty, Alan D. Chien, Kristina D. Closser, Vale Cofer-Shabica, Saswata Dasgupta, Marc De

Wergifosse, Jia Deng, Michael Diedenhofen, Hainam Do, Sebastian Ehlert, Po Tung Fang, Shervin Fatehi, Qingguo Feng, Triet Friedhoff, James Gayvert, Qinghui Ge, Gergely Gidofalvi, Matthew Goldey, Joe Gomes, Cristina E. González-Espinoza, Sahil Gulania, Anastasia O. Gunina, Magnus W.D. Hanson-Heine, Phillip H.P. Harbach, Andreas Hauser, Michael F. Herbst, Mario Hernández Vera, Manuel Hodecker, Zachary C. Holden, Shannon Houck, Xunkun Huang, Kerwin Hui, Bang C. Huynh, Maxim Ivanov, Ádám Jász, Hyunjun Ji, Hanjie Jiang, Benjamin Kaduk, Sven Kähler, Kirill Khistyaev, Jaehoon Kim, Gergely Kis, Phil Klunzinger, Zsuzsanna Koczor-Benda, Joong Hoon Koh, Dimitri Kosenkov, Laura Koulias, Tim Kowalczyk, Caroline M. Krauter, Karl Kue, Alexander Kunitsa, Thomas Kus, István Ladjánszki, Arie Landau, Keith V. Lawler, Daniel Lefrancois, Susi Lehtola, Run R. Li, Yi Pei Li, Jiashu Liang, Marcus Liebenthal, Hung Hsuan Lin, You Sheng Lin, Fenglai Liu, Kuan Yu Liu, Matthias Loipersberger, Arne Luenser, Aaditya Manjanath, Prashant Manohar, Erum Mansoor, Sam F. Manzer, Shan Ping Mao, Aleksandr V. Marenich, Thomas Markovich, Stephen Mason, Simon A. Maurer, Peter F. McLaughlin, Maximilian F.S.J. Menger, Jan Michael Mewes, Stefanie A. Mewes, Pierpaolo Morgante, J. Wayne Mullinax, Katherine J. Oosterbaan, Garrette Paran, Alexander C. Paul, Suranjan K. Paul, Fabijan Pavošević, Zheng Pei, Stefan Prager, Emil I. Proynov, Ádám Rák, Eloy Ramos-Cordoba, Bhaskar Rana, Alan E. Rask, Adam Rettig, Ryan M. Richard, Fazle Rob, Elliot Rossomme, Tarek Scheele, Maximilian Scheurer, Matthias Schneider, Nickolai Sergueev, Shaama M. Sharada, Wojciech Skomorowski, David W. Small, Christopher J. Stein, Yu Chuan Su, Eric J. Sundstrom, Zhen Tao, Jonathan Thirman, Gábor J. Tornai, Takashi Tsuchimochi, Norm M. Tubman, Srimukh Prasad Veccham, Oleg Vydrov, Jan Wenzel, Jon Witte, Atsushi Yamada, Kun Yao, Sina Yeganeh, Shane R. Yost, Alexander Zech, Igor Ying Zhang, Xing Zhang, Yu Zhang, Dmitry Zuev, Alán Aspuru-Guzik, Alexis T. Bell, Nicholas A. Besley, Ksenia B. Bravaya, Bernard R. Brooks, David Casanova, Jeng Da Chai, Sonia Coriani, Christopher J. Cramer, György Cserey, A. Eugene Deprince, Robert A. Distasio, Andreas Dreuw, Barry D. Dunietz, Thomas R. Furlani, William A. Goddard, Sharon Hammes-Schiffer, Teresa Head-Gordon, Warren J. Hehre, Chao Ping Hsu, Thomas C. Jagau, Yousung Jung, Andreas Klamt, Jing Kong, Daniel S. Lambrecht, Wanzhen Liang, Nicholas J. Mayhall, C. William McCurdy, Jeffrey B. Neaton, Christian Ochsenfeld, John A. Parkhill, Roberto Peverati, Vitaly A. Rassolov, Yihan Shao, Lyudmila V. Slipchenko, Tim Stauch, Ryan P. Steele, Joseph E. Subotnik, Alex J.W. Thom, Alexandre Tkatchenko, Donald G. Truhlar, Troy Van Voorhis, Tomasz A. Wesolowski, K. Birgitta Whaley, H. Lee Woodcock, Paul M. Zimmerman, Shirin Faraji, Peter M.W. Gill, Martin Head-Gordon, John M. Herbert, and Anna I. Krylov. Software for the frontiers of quantum chemistry: An overview of developments in the Q-Chem 5 package. *Journal of Chemical Physics*, 155(8):084801, aug 2021. ISSN 10897690. doi: 10.1063/5.0055522. URL `https://aip.scitation.org/doi/10.1063/5.0055522`.

[165] A. D. Becke. Density-functional exchange-energy approximation with

correct asymptotic behavior. *Physical Review A*, 38(6):3098–3100, sep 1988. ISSN 0556-2791. doi: 10.1103/PhysRevA.38.3098. URL `https://link.aps.org/doi/10.1103/PhysRevA.38.3098`.

[166] Chengteh Lee, Weitao Yang, and Robert G. Parr. Development of the Colle-Salvetti correlation-energy formula into a functional of the electron density. *Physical Review B*, 37(2):785–789, jan 1988. ISSN 0163-1829. doi: 10.1103/PhysRevB.37.785. URL `https://link.aps.org/doi/10.1103/PhysRevB.37.785`.

[167] Axel D. Becke. Density-functional thermochemistry. III. The role of exact exchange. *The Journal of Chemical Physics*, 98(7):5648–5652, apr 1993. ISSN 0021-9606. doi: 10.1063/1.464913. URL `http://aip.scitation.org/doi/10.1063/1.464913`.

[168] Dmitrij Rappoport and Filipp Furche. Property-optimized Gaussian basis sets for molecular response calculations. *The Journal of Chemical Physics*, 133 (13):134105, oct 2010. ISSN 0021-9606. doi: 10.1063/1.3484283. URL `http://aip.scitation.org/doi/10.1063/1.3484283`.

[169] Florian Weigend and Reinhart Ahlrichs. Balanced basis sets of split valence, triple zeta valence and quadruple zeta valence quality for H to Rn: Design and assessment of accuracy. *Physical Chemistry Chemical Physics*, 7(18):3297, 2005. ISSN 1463-9076. doi: 10.1039/b508541a. URL `http://xlink.rsc.org/?DOI=b508541a`.

[170] D. Andrae, U. Huermann, M. Dolg, H. Stoll, and H. Preu. Energy-adjustedab initio pseudopotentials for the second and third row transition elements. *Theoretica Chimica Acta*, 77(2):123–141, 1990. ISSN 0040-5744. doi: 10.1007/BF01114537. URL `http://link.springer.com/10.1007/BF01114537`.

[171] Aleksandr V. Marenich, Christopher J. Cramer, and Donald G. Truhlar. Universal Solvation Model Based on the Generalized Born Approximation with Asymmetric Descreening. *Journal of Chemical Theory and Computation*, 5 (9):2447–2464, sep 2009. ISSN 1549-9618. doi: 10.1021/ct900312z. URL `https://pubs.acs.org/doi/10.1021/ct900312z`.

[172] Björn Dahlgren. ChemPy: A package useful for chemistry written in Python. *Journal of Open Source Software*, 3(24):565, apr 2018. ISSN 2475-9066. doi: 10.21105/joss.00565. URL `http://joss.theoj.org/papers/10.21105/joss.00565`.

[173] Quinten A. Akkerman, Silvia Genaro Motti, Ajay Ram Srimath Kandada, Edoardo Mosconi, Valerio D'Innocenzo, Giovanni Bertoni, Sergio Marras, Brett A. Kamino, Laura Miranda, Filippo De Angelis, Annamaria Petrozza, Mirko Prato, and Liberato Manna. Solution Synthesis Approach to Colloidal Cesium Lead Halide Perovskite Nanoplatelets with Monolayer-Level Thickness Control. *Journal of the American Chemical Society*, 138(3):1010–

1016, jan 2016. ISSN 15205126. doi: 10.1021/jacs.5b12124. URL `http://pubs.acs.org/doi/abs/10.1021/jacs.5b12124`.

[174] Ward van der Stam, Jaco J. Geuchies, Thomas Altantzis, Karel H. W. van den Bos, Johannes D. Meeldijk, Sandra Van Aert, Sara Bals, Daniel Vanmaekelbergh, and Celso de Mello Donega. Highly Emissive Divalent-Ion-Doped Colloidal CsPb 1– x M x Br 3 Perovskite Nanocrystals through Cation Exchange. *Journal of the American Chemical Society*, 139(11):4087–4097, mar 2017. ISSN 0002-7863. doi: 10.1021/jacs.6b13079. URL `https://pubs.acs.org/doi/10.1021/jacs.6b13079`.

[175] Loredana Protesescu, Sergii Yakunin, Sudhir Kumar, Janine Bär, Federica Bertolotti, Norberto Masciocchi, Antonietta Guagliardi, Matthias Grotevent, Ivan Shorubalko, Maryna I. Bodnarchuk, Chih Jen Shih, and Maksym V. Kovalenko. Dismantling the ”red Wall” of Colloidal Perovskites: Highly Luminescent Formamidinium and Formamidinium-Cesium Lead Iodide Nanocrystals. *ACS Nano*, 11(3): 3119–3134, mar 2017. ISSN 1936086X. doi: 10.1021/acsnano.7b00116. URL `http://pubs.acs.org/doi/abs/10.1021/acsnano.7b00116`.

[176] Quinten A. Akkerman, Valerio D'Innocenzo, Sara Accornero, Alice Scarpellini, Annamaria Petrozza, Mirko Prato, and Liberato Manna. Tuning the optical properties of cesium lead halide perovskite nanocrystals by anion exchange reactions. *Journal of the American Chemical Society*, 137(32):10276–10281, aug 2015. ISSN 15205126. doi: 10.1021/jacs.5b05602. URL `http://pubs.acs.org/doi/abs/10.1021/jacs.5b05602`.

[177] Samuel W. Eaton, Minliang Lai, Natalie A. Gibson, Andrew B. Wong, Letian Dou, Jie Ma, Lin-Wang Wang, Stephen R. Leone, and Peidong Yang. Lasing in robust cesium lead halide perovskite nanowires. *Proceedings of the National Academy of Sciences*, 113(8):1993–1998, feb 2016. ISSN 0027-8424. doi: 10.1073/pnas.1600789113. URL `http://www.pnas.org/lookup/doi/10.1073/pnas.1600789113`.

[178] Letian Dou, Yang (Micheal) Yang, Jingbi You, Ziruo Hong, Wei-Hsuan Chang, Gang Li, and Yang Yang. Solution-processed hybrid perovskite photodetectors with high detectivity. *Nature Communications*, 5(1):5404, dec 2014. ISSN 2041-1723. doi: 10.1038/ncomms6404. URL `http://www.nature.com/articles/ncomms6404`.

[179] Zhi-Kuang Tan, Reza Saberi Moghaddam, May Ling Lai, Pablo Docampo, Ruben Higler, Felix Deschler, Michael Price, Aditya Sadhanala, Luis M. Pazos, Dan Credgington, Fabian Hanusch, Thomas Bein, Henry J. Snaith, and Richard H. Friend. Bright light-emitting diodes based on organometal halide perovskite. *Nature Nanotechnology*, 9(9):687–692, sep 2014. ISSN 1748-3387. doi: 10.1038/nnano.2014.149. URL `http://www.nature.com/articles/nnano.2014.149`.

[180] G P Nagabhushana, Radha Shivaramaiah, and Alexandra Navrotsky. Direct calorimetric verification of thermodynamic instability of lead halide hybrid perovskites. *Proceedings of the National Academy of Sciences of the United States of America*, 113(28):7717–21, jul 2016. ISSN 1091-6490. doi: 10.1073/pnas.1607850113. URL `http://www.ncbi.nlm.nih.gov/pubmed/27357677` `http://www.pubmedcentral.nih.gov/articlerender.fcgi?artid=PMC4948354`.

[181] Sidney E. Creutz, Evan N. Crites, Michael C. De Siena, and Daniel R. Gamelin. Colloidal Nanocrystals of Lead-Free Double-Perovskite (Elpasolite) Semiconductors: Synthesis and Anion Exchange to Access New Materials. *Nano Letters*, 18(2): 1118–1123, feb 2018. ISSN 15306992. doi: 10.1021/acs.nanolett.7b04659. URL `http://pubs.acs.org/doi/10.1021/acs.nanolett.7b04659`.

[182] Federico Locardi, Matilde Cirignano, Dmitry Baranov, Zhiya Dang, Mirko Prato, Filippo Drago, Maurizio Ferretti, Valerio Pinchetti, Marco Fanciulli, Sergio Brovelli, Luca De Trizio, and Liberato Manna. Colloidal Synthesis of Double Perovskite Cs 2 AgInCl 6 and Mn-Doped Cs 2 AgInCl 6 Nanocrystals. *Journal of the American Chemical Society*, 140(40):12989–12995, oct 2018. ISSN 0002-7863. doi: 10.1021/jacs.8b07983. URL `http://pubs.acs.org/doi/10.1021/jacs.8b07983`.

[183] Taame Abraha Berhe, Wei-Nien Su, Ching-Hsiang Chen, Chun-Jern Pan, Ju-Hsiang Cheng, Hung-Ming Chen, Meng-Che Tsai, Liang-Yih Chen, Amare Aregahegn Dubale, and Bing-Joe Hwang. Organometal halide perovskite solar cells: degradation and stability. *Energy and Environmental Science*, 9(2):323–356, feb 2016. ISSN 1754-5692. doi: 10.1039/C5EE02733K. URL `http://xlink.rsc.org/?DOI=C5EE02733K`.

[184] Aslihan Babayigit, Dinh Duy Thanh, Anitha Ethirajan, Jean Manca, Marc Muller, Hans-Gerd Boyen, and Bert Conings. Assessing the toxicity of Pb- and Sn-based perovskite solar cells in model organism Danio rerio. *Scientific Reports*, 6(1):18721, may 2016. ISSN 2045-2322. doi: 10.1038/srep18721. URL `http://www.nature.com/articles/srep18721`.

[185] Christopher N. Savory, Aron Walsh, and David O. Scanlon. Can Pb-Free Halide Double Perovskites Support High-Efficiency Solar Cells? *ACS Energy Letters*, 1 (5):949–955, nov 2016. ISSN 2380-8195. doi: 10.1021/acsenergylett.6b00471. URL `http://pubs.acs.org/doi/abs/10.1021/acsenergylett.6b00471`.

[186] Adam H. Slavney, Te Hu, Aaron M. Lindenberg, and Hemamala I. Karunadasa. A Bismuth-Halide Double Perovskite with Long Carrier Recombination Lifetime for Photovoltaic Applications. *Journal of the American Chemical Society*, 138 (7):2138–2141, feb 2016. ISSN 15205126. doi: 10.1021/jacs.5b13294. URL `http://pubs.acs.org/doi/abs/10.1021/jacs.5b13294`.

[187] George Volonakis, Marina R. Filip, Amir Abbas Haghighirad, Nobuya Sakai, Bernard Wenger, Henry J. Snaith, and Feliciano Giustino. Lead-Free Halide Double Perovskites

via Heterovalent Substitution of Noble Metals. *Journal of Physical Chemistry Letters*, 7(7):1254–1259, apr 2016. ISSN 19487185. doi: 10.1021/acs.jpclett.6b00376. URL `http://pubs.acs.org/doi/abs/10.1021/acs.jpclett.6b00376`.

[188] Sudip Chakraborty, Wei Xie, Nripan Mathews, Matthew Sherburne, Rajeev Ahuja, Mark Asta, and Subodh G. Mhaisalkar. Rational Design: A High-Throughput Computational Screening and Experimental Validation Methodology for Lead-Free and Emergent Hybrid Perovskites. *ACS Energy Letters*, 2(4):837–845, apr 2017. ISSN 2380-8195. doi: 10.1021/acsenergylett.7b00035. URL `http://pubs.acs.org/doi/abs/10.1021/acsenergylett.7b00035`.

[189] Alex M Ganose, Christopher N Savory, and David O Scanlon. Beyond methylammonium lead iodide: prospects for the emergent field of ns2containing solar absorbers. *Chemical Communications*, 53(1):20–44, 2017. ISSN 1364548X. doi: 10.1039/c6cc06475b. URL `www.rsc.org/chemcomm`.

[190] Tom C. Jellicoe, Johannes M. Richter, Hugh F. J. Glass, Maxim Tabachnyk, Ryan Brady, Siân E. Dutton, Akshay Rao, Richard H. Friend, Dan Credgington, Neil C. Greenham, and Marcus L. Böhm. Synthesis and Optical Properties of Lead-Free Cesium Tin Halide Perovskite Nanocrystals. *Journal of the American Chemical Society*, 138(9):2941–2944, mar 2016. ISSN 0002-7863. doi: 10.1021/jacs.5b13470. URL `http://pubs.acs.org/doi/abs/10.1021/jacs.5b13470`.

[191] Andrew Barnabas Wong, Yehonadav Bekenstein, Jun Kang, Christopher S. Kley, Dohyung Kim, Natalie A. Gibson, Dandan Zhang, Yi Yu, Stephen R. Leone, Lin Wang Wang, A. Paul Alivisatos, and Peidong Yang. Strongly Quantum Confined Colloidal Cesium Tin Iodide Perovskite Nanoplates: Lessons for Reducing Defect Density and Improving Stability. *Nano Letters*, 18(3):2060–2066, mar 2018. ISSN 15306992. doi: 10.1021/acs.nanolett.8b00077. URL `http://pubs.acs.org/doi/10.1021/acs.nanolett.8b00077`.

[192] Lin Jer Chen. Synthesis and optical properties of lead-free cesium germanium halide perovskite quantum rods. *RSC Advances*, 8(33):18396–18399, 2018. ISSN 2046-2069. doi: 10.1039/C8RA01150H. URL `http://pubs.rsc.org/en/content/articlepdf/2018/RA/C8RA01150H` `http://xlink.rsc.org/?DOI=C8RA01150H`.

[193] Yao Cai, Wei Xie, Hong Ding, Yan Chen, Krishnamoorthy Thirumal, Lydia H. Wong, Nripan Mathews, Subodh G. Mhaisalkar, Matthew Sherburne, and Mark Asta. Computational Study of Halide Perovskite-Derived A 2 BX 6 Inorganic Compounds: Chemical Trends in Electronic Structure and Structural Stability. *Chemistry of Materials*, 29(18):7740–7749, sep 2017. ISSN 0897-4756. doi: 10.1021/acs.chemmater.7b02013. URL `http://pubs.acs.org/doi/10.1021/acs.chemmater.7b02013`.

[194] Aifei Wang, Xingxu Yan, Mian Zhang, Shibin Sun, Ming Yang, Wei Shen, Xiaoqing Pan, Peng Wang, and Zhengtao Deng. Controlled synthesis of lead-free and stable perovskite derivative Cs2SnI6 nanocrystals via a facile hot-injection process. *Chemistry of Materials*, 28(22):8132–8140, 2016. ISSN 15205002. doi: 10.1021/acs.chemmater.6b01329.

[195] Byunghong Lee, Constantinos C. Stoumpos, Nanjia Zhou, Feng Hao, Christos Malliakas, Chen Yu Yeh, Tobin J. Marks, Mercouri G. Kanatzidis, and Robert P.H. Chang. Air-stable molecular semiconducting iodosalts for solar cell applications: Cs2SnI6 as a hole conductor. *Journal of the American Chemical Society*, 136 (43):15379–15385, oct 2014. ISSN 15205126. doi: 10.1021/ja508464w. URL `http://pubs.acs.org/doi/10.1021/ja508464w`.

[196] Yuhai Zhang, Jun Yin, Manas R. Parida, Ghada H. Ahmed, Jun Pan, Osman M. Bakr, Jean-Luc Brédas, and Omar F. Mohammed. Direct-Indirect Nature of the Bandgap in Lead-Free Perovskite Nanocrystals. *The Journal of Physical Chemistry Letters*, 8 (14):3173–3177, jul 2017. ISSN 1948-7185. doi: 10.1021/acs.jpclett.7b01381. URL `http://pubs.acs.org/doi/abs/10.1021/acs.jpclett.7b01381`.

[197] Kyle M. McCall, Constantinos C. Stoumpos, Svetlana S. Kostina, Mercouri G. Kanatzidis, and Bruce W. Wessels. Strong Electron–Phonon Coupling and Self-Trapped Excitons in the Defect Halide Perovskites A 3 M 2 I 9 (A = Cs, Rb; M = Bi, Sb). *Chemistry of Materials*, 29(9):4129–4145, may 2017. ISSN 15205002. doi: 10.1021/acs.chemmater.7b01184. URL `http://pubs.acs.org/doi/abs/10.1021/acs.chemmater.7b01184` `http://pubs.acs.org/doi/10.1021/acs.chemmater.7b01184`.

[198] Jaya Pal, Suman Manna, Anirban Mondal, Shyamashis Das, K. V. Adarsh, and Angshuman Nag. Colloidal Synthesis and Photophysics of M 3 Sb 2 I 9 (M=Cs and Rb) Nanocrystals: Lead-Free Perovskites. *Angewandte Chemie International Edition*, 56 (45):14187–14191, nov 2017. ISSN 14337851. doi: 10.1002/anie.201709040. URL `http://doi.wiley.com/10.1002/anie.201709040`.

[199] Jun Zhou, Zhiguo Xia, Maxim S. Molokeev, Xiuwen Zhang, Dongsheng Peng, and QuanLin Liu. Composition design, optical gap and stability investigations of lead-free halide double perovskite Cs2AgInCl6. *Journal of Materials Chemistry A*, 5(29):15031–15037, 2017. ISSN 20507496. doi: 10.1039/c7ta04690a. URL `http://pubs.rsc.org/en/content/articlepdf/2017/ta/c7ta04690a` `http://pubs.rsc.org/en/Content/ArticleLanding/2017/TA/C7TA04690A`.

[200] George Volonakis, Amir Abbas Haghighirad, Rebecca L. Milot, Weng H. Sio, Marina R. Filip, Bernard Wenger, Michael B. Johnston, Laura M. Herz, Henry J. Snaith, and Feliciano Giustino. Cs2InAgCl6: A New Lead-Free Halide Double Perovskite with Direct Band Gap. *Journal of Physical Chemistry Letters*,

8(4):772–778, feb 2017. ISSN 19487185. doi: 10.1021/acs.jpclett.6b02682. URL `https://arxiv.org/ftp/arxiv/papers/1611/1611.05426.pdf` `http://arxiv.org/abs/1611.05426` `http://pubs.acs.org/doi/abs/10.1021/acs.jpclett.6b0`

[201] T. Thao Tran, Jessica R. Panella, Juan R. Chamorro, Jennifer R. Morey, and Tyrel M. McQueen. Designing indirect–direct bandgap transitions in double perovskites. *Mater. Horiz.*, 4(4):688–693, jul 2017. ISSN 2051-6347. doi: 10.1039/C7MH00239D. URL `http://xlink.rsc.org/?DOI=C7MH00239D`.

[202] Jiajun Luo, Xiaoming Wang, Shunran Li, Jing Liu, Yueming Guo, Guangda Niu, Li Yao, Yuhao Fu, Liang Gao, Qingshun Dong, Chunyi Zhao, Meiying Leng, Fusheng Ma, Wenxi Liang, Liduo Wang, Shengye Jin, Junbo Han, Lijun Zhang, Joanne Etheridge, Jianbo Wang, Yanfa Yan, Edward H. Sargent, and Jiang Tang. Efficient and stable emission of warm-white light from lead-free halide double perovskites. *Nature*, 563(7732):541–545, nov 2018. ISSN 0028-0836. doi: 10.1038/s41586-018-0691-0. URL `http://www.nature.com/articles/s41586-018-0691-0`.

[203] V. M. Goldschmidt. Die Gesetze der Krystallochemie. *Die Naturwissenschaften*, 14(21):477–485, may 1926. ISSN 00281042. doi: 10.1007/BF01507527. URL `http://link.springer.com/10.1007/BF01507527`.

[204] Qingde Sun and Wan Jian Yin. Thermodynamic Stability Trend of Cubic Perovskites. *Journal of the American Chemical Society*, 139(42):14905–14908, 2017. ISSN 15205126. doi: 10.1021/jacs.7b09379. URL `https://pubs.acs.org/sharingguidelines`.

[205] W. Travis, E. N.K. Glover, H. Bronstein, D. O. Scanlon, and R. G. Palgrave. On the application of the tolerance factor to inorganic and hybrid halide perovskites: A revised system. *Chemical Science*, 7(7):4548–4556, jun 2016. ISSN 20416539. doi: 10.1039/c5sc04845a. URL `http://xlink.rsc.org/?DOI=C5SC04845A`.

[206] He Huang, Maryna I Bodnarchuk, Stephen V Kershaw, Maksym V Kovalenko, and Andrey L Rogach. Lead Halide Perovskite Nanocrystals in the Research Spotlight: Stability and Defect Tolerance. *ACS Energy Letters*, 2(9):2071–2083, sep 2017. ISSN 2380-8195. doi: 10.1021/acsenergylett.7b00547. URL `http://pubs.acs.org/journal/aelccp` `http://pubs.acs.org/doi/10.1021/acsenergylett.7b00547`.

[207] Peter M Scop. Band structure of Silver Cloride and Silver bromide. *Physical Review*, 139(49):934–940, 1965.

[208] M. T. Bennebroek, A. Arnold, O. G. Poluektov, P. G. Baranov, and J. Schmidt. Spatial distribution of the wave function of the self-trapped exciton in AgCl. *Physical Review B*, 53(23):15607–15616, jun 1996. ISSN 0163-1829. doi: 10.1103/PhysRevB.53.15607. URL `https://link.aps.org/doi/10.1103/PhysRevB.53.15607`.

[209] J. Tauc. Optical properties and electronic structure of amorphous Ge and Si. *Materials Research Bulletin*, 3(1):37–46, jan 1968. ISSN 0025-5408. doi: 10.1016/0025-5408(68)90023-8.

[210] Shunran Li, Jiajun Luo, Jing Liu, and Jiang Tang. Self-Trapped Excitons in All-Inorganic Halide Perovskites: Fundamentals, Status, and Potential Applications. *The Journal of Physical Chemistry Letters*, 10(8):1999–2007, apr 2019. ISSN 1948-7185. doi: 10.1021/acs.jpclett.8b03604. URL `https://pubs.acs.org/doi/10.1021/acs.jpclett.8b03604`.

[211] Bridget A. Connor, Linn Leppert, Matthew D. Smith, Jeffrey B. Neaton, and Hemamala I. Karunadasa. Layered halide double perovskites: Dimensional reduction of Cs2AgBiBr6. *Journal of the American Chemical Society*, 140(15): 5235–5240, apr 2018. ISSN 15205126. doi: 10.1021/jacs.8b01543. URL `http://pubs.acs.org/doi/10.1021/jacs.8b01543`.

[212] Gary L. Miessler, Paul J. Fischer, and Donald A. Tarr. *Inorganic Chemistry*. Pearson, fifth edition, 2014. ISBN 9780321811059.

[213] R. W. Gurney and N. F. Mott. The Theory of the Photolysis of Silver Bromide and the Photographic Latent Image. *Proceedings of the Royal Society of London. Series A - Mathematical and Physical Sciences*, 164(917): 151–167, jan 1938. ISSN 0080-4630. doi: 10.1098/rspa.1938.0011. URL `https://royalsocietypublishing.org/doi/10.1098/rspa.1938.0011`.

[214] Keyan Li and Dongfeng Xue. Estimation of Electronegativity Values of Elements in Different Valence States. *The Journal of Physical Chemistry A*, 110 (39):11332–11337, oct 2006. ISSN 1089-5639. doi: 10.1021/jp062886k. URL `https://pubs.acs.org/doi/10.1021/jp062886k`.

[215] Robert G. Parr and Ralph G. Pearson. Absolute hardness: companion parameter to absolute electronegativity. *Journal of the American Chemical Society*, 105 (26):7512–7516, dec 1983. ISSN 0002-7863. doi: 10.1021/ja00364a005. URL `http://pubs.acs.org/doi/abs/10.1021/ja00364a005`.

[216] John R. Rumble. "Physical Constants of Inorganic Compounds," in CRC Handbook of Chemistry and Physics. In John R. Rumble, editor, *CRC Handbook of Chemistry and Physics*, chapter Physical C. CRC Press/Taylor & Francis, Boca Raton, FL, 99 edition, 2018.

[217] John P. Perdew, Kieron Burke, and Matthias Ernzerhof. Generalized gradient approximation made simple. *Physical Review Letters*, 77(18):3865–3868, oct 1996. ISSN 10797114. doi: 10.1103/PhysRevLett.77.3865.

[218] G. Kresse and J. Furthmüller. Efficient iterative schemes for ab initio total-energy calculations using a plane-wave basis set. *Physical Review B - Condensed Matter and Materials Physics*, 54(16):11169–11186, 1996. ISSN 1550235X. doi: 10.1103/PhysRevB.54.11169.

[219] Gregory H. Wannier. The structure of electronic excitation levels in insulating crystals. *Physical Review*, 52(3):191–197, 1937. ISSN 0031899X. doi: 10.1103/PhysRev.52.191.

[220] Georg K.H. Madsen and David J. Singh. BoltzTraP. A code for calculating band-structure dependent quantities. *Computer Physics Communications*, 175(1):67–71, 2006. ISSN 00104655. doi: 10.1016/j.cpc.2006.03.007.

Appendix A

Supplementary Figures

A.1 Chapter 2 Supplementary Figures

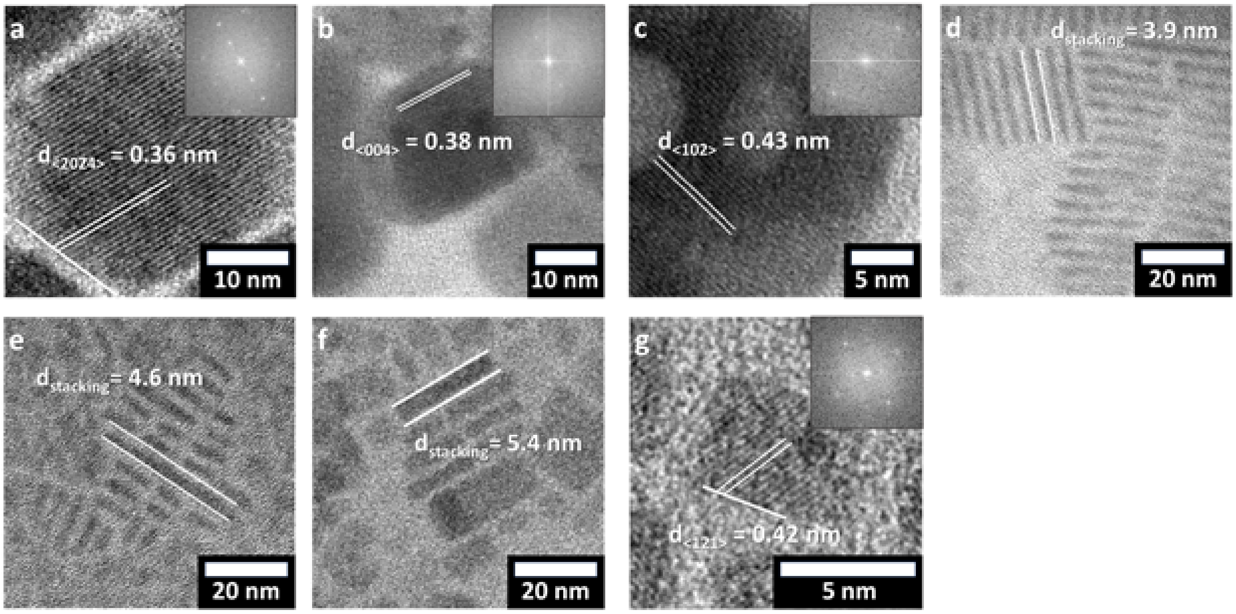

Figure A.1.1: High-Resolution TEM of $Cs_xPb_yBr_z$ species, with measured d-spacings. For the nanoplatelets, stacking distances were measured instead of lattice d-spacings. Lattice planes hkl indices and Fourier transform pattern included when applicable. a) Cs_4PbBr_6, b) $CsPb_2Br_5$, c) $PbBr_2$, d) 2 ML nanoplatelets, e) 3 ML nanoplatelets, f) 4 ML nanoplatelets, g) $CsPbBr_3$ nanocubes.

Each panel shows 16 experiments with varying Cs and Pb levels. Generally, at low Cs and Pb levels, there are small plates (1 ML or 2 ML), which increase to thicker species at higher concentrations of reagents. This increase is much sharper and shifted towards the

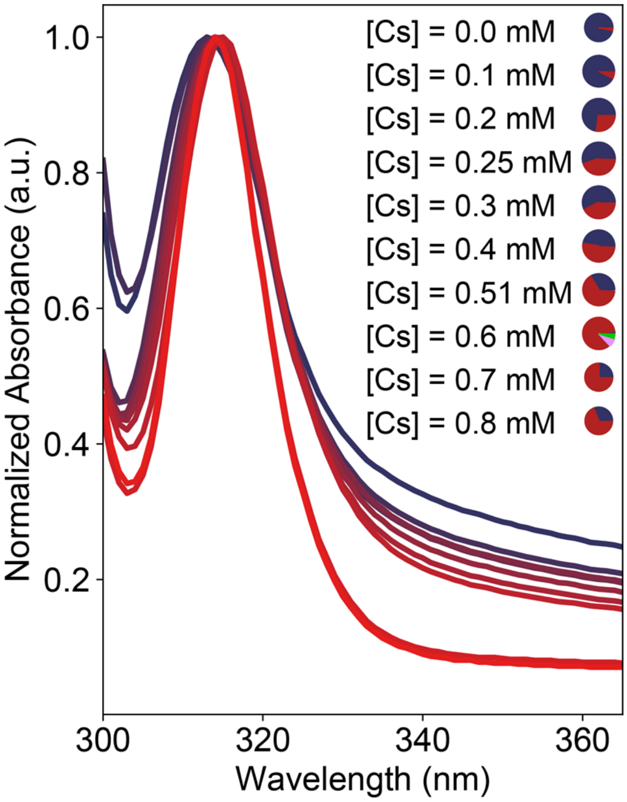

Figure A.1.2: Series of synthesis conducted at varying Cs concentrations with Pb = 0.26 mM, OLA = 4.9 mM, Br = 12.72 mM, OA = 4.8 mM at 30 C. This series shows a transition from $[PbBr_x]$ to Cs_4PbBr_6 with increased Cs concentration, as detailed by the pie charts showing the analysis estimate (red is Cs_4PbBr_6, dark purple is $[PbBr_x]$). The deconvolution between these two species is successful because of the change in absorption onset and decrease in peak width.

lower right with decreasing OLA (as in Figure 2.5 in the main text), or with increasing temperatures. There is some Cs4PbBr6 at low Pb and high Cs levels, particularly at lower temperatures and high OLA concentrations. CsPb2Br5 is prevalent mainly at very low OLA concentrations and increases somewhat with Temperature. At higher temperatures, low OLA concentrations and high Cs and Pb levels, visible products eventually vanish entirely – we attribute this to formation of ever larger nanocrystals which will eventually aggregate. The decrease in plate thicknesses between T = 40 and T = 50 is likely due to an experimental batch error at T=40.

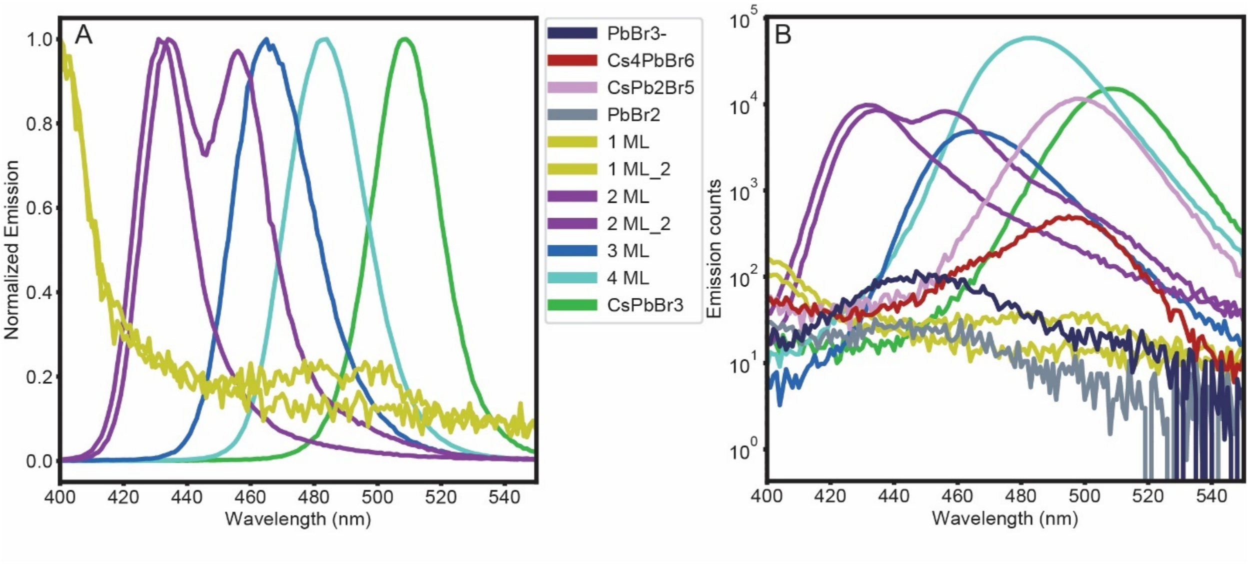

Figure A.1.3: Photoluminescence Spectra of Samples chosen as Reference Spectra

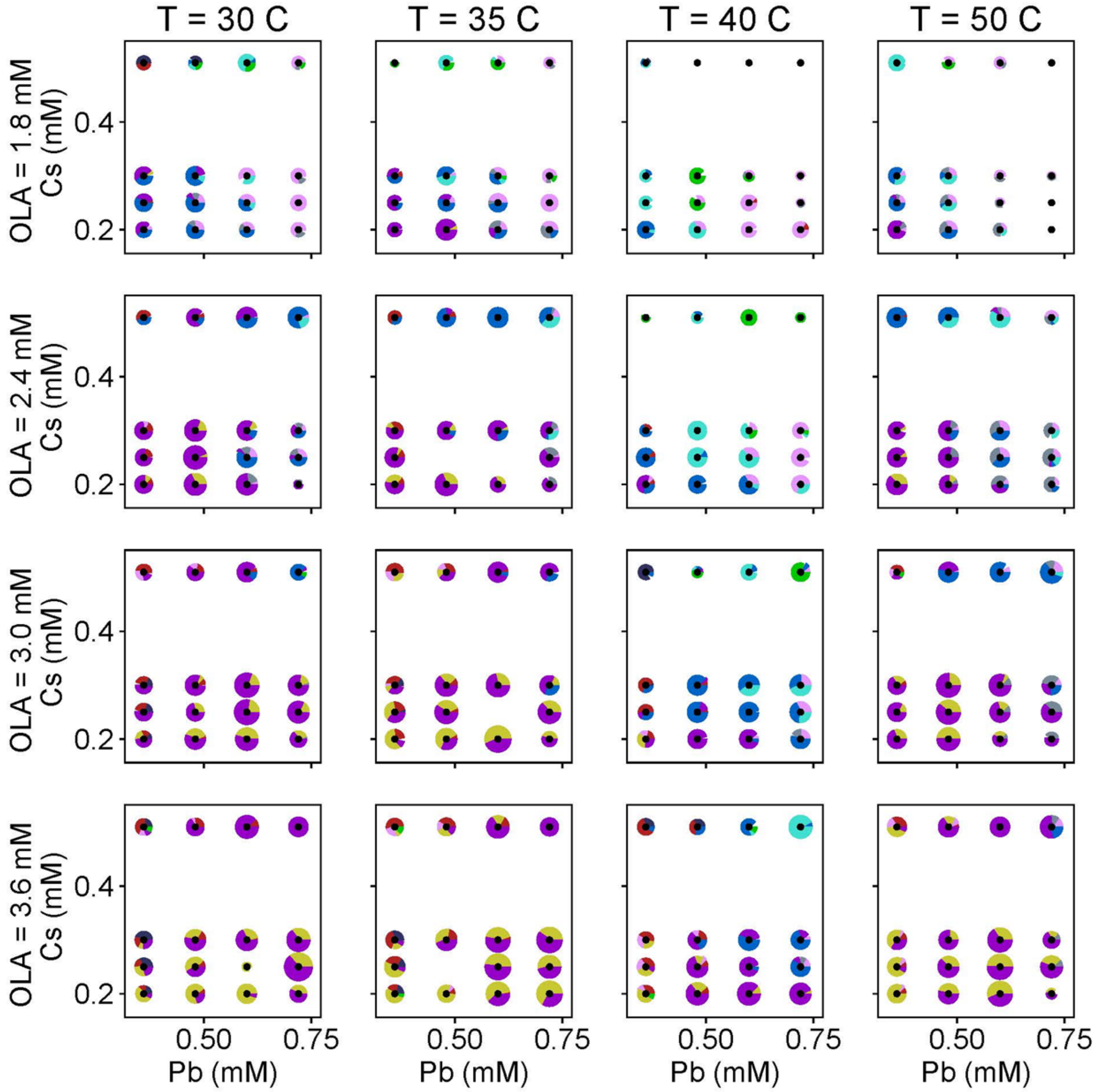

Figure A.1.4: *Pie Chart Array varied in Temperature, and OLA, Pb and Cs* Arrays of pie charts showing a factorial experiment in T, OLA, Cs and Pb. Br = 12.72 mM, OA = 4.8 mM + adjustments for solubility of Cs and Pb precursors

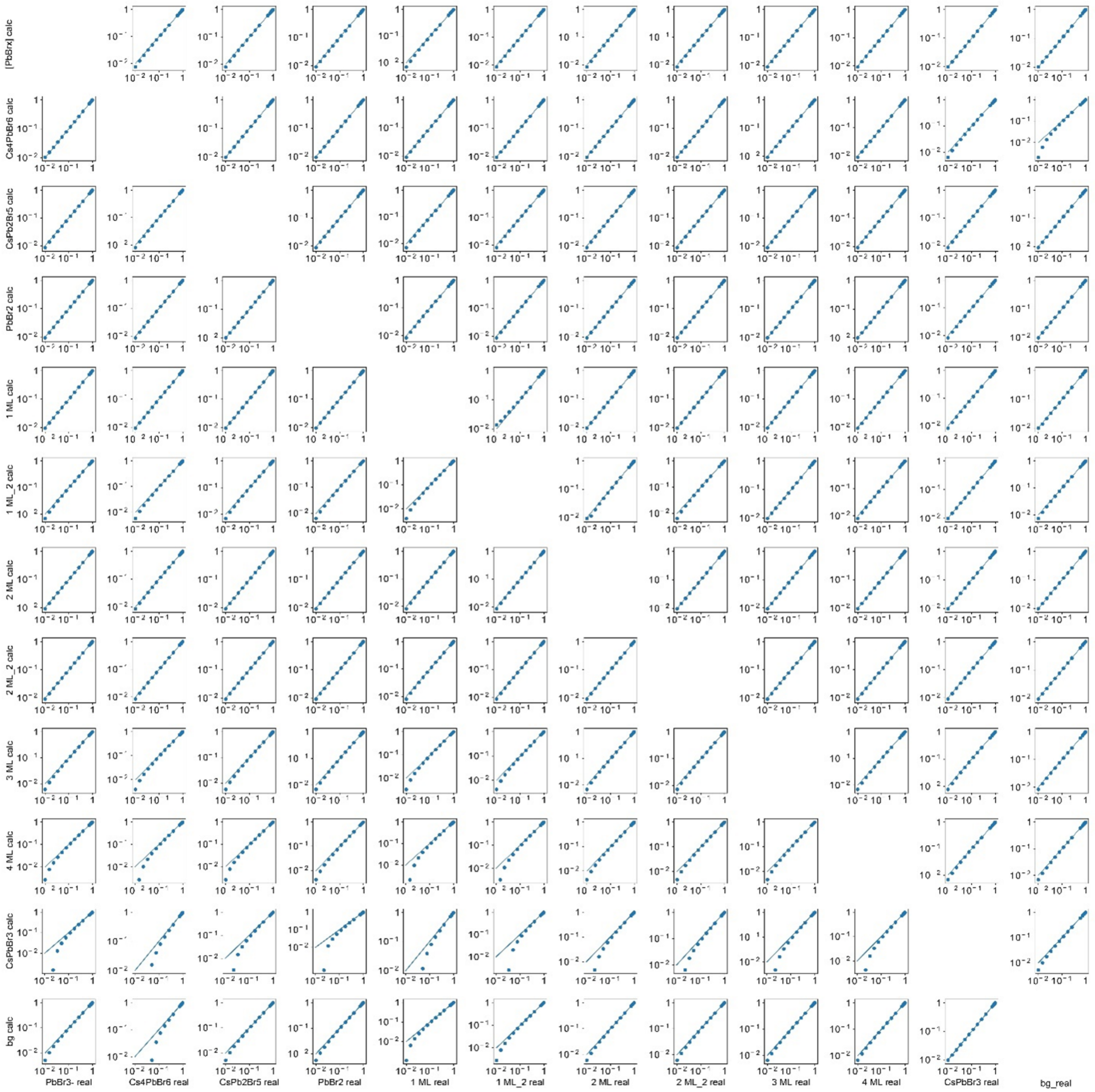

Figure A.1.5: Simulated binary mixtures of reference spectra. Position in matrix: Mixture between species in x column and species in y column. X-axis: true value of species in y column. Y-axis: calculated value of species in y column. Dots: simulated reference spectra, 19 per subplot, 2584 overall. Line: idealized perfect correspondence between simulated and calculated spectra. Dots in the space above the line correspond to overestimations, dots under the line correspond to underestimations.

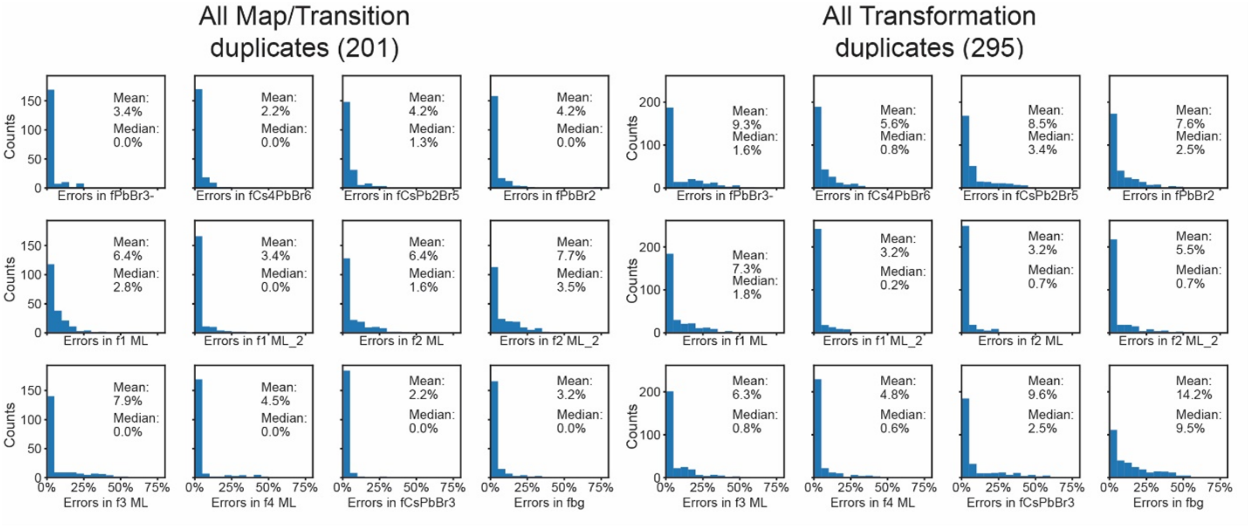
All Map/Transition duplicates (201)

All Transformation duplicates (295)

Figure A.1.6: Histograms of measured standard deviations in the fraction of species assigned (spectral purity) of all duplicates in Map type and Transformation type experiments. Bin width is 5 %

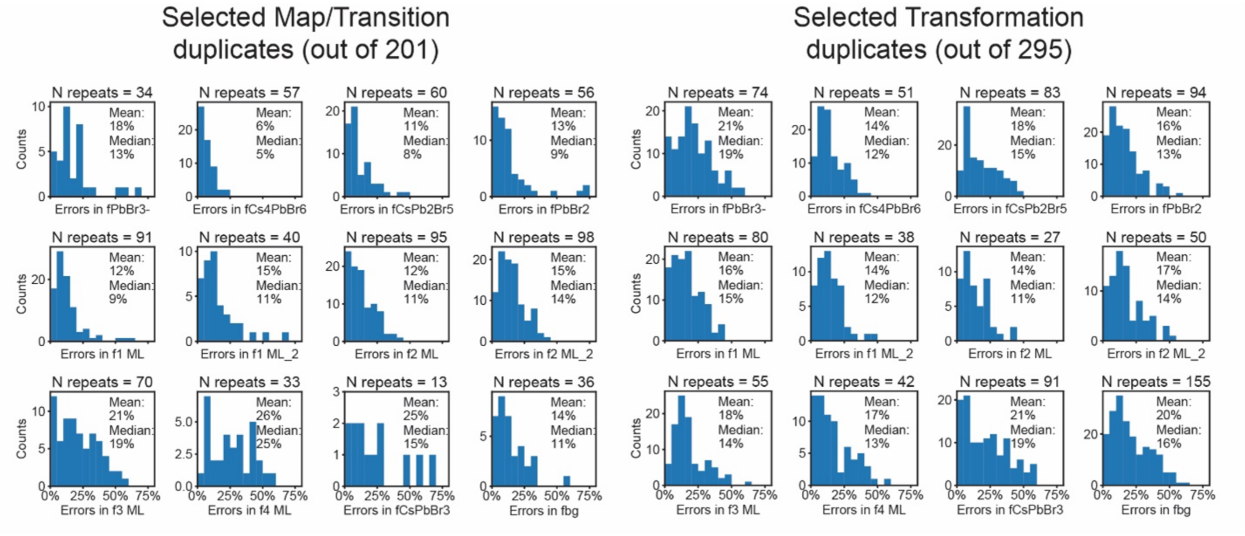
Selected Map/Transition duplicates (out of 201)

Selected Transformation duplicates (out of 295)

Figure A.1.7: Histograms of measured standard deviations in the fraction of species assigned (spectral purity) in duplicates containing more than 5% of the species in question for Map and Transformation type experiments. Bin width is 5 %

A.2 Chapter 3 Supplementary Figures

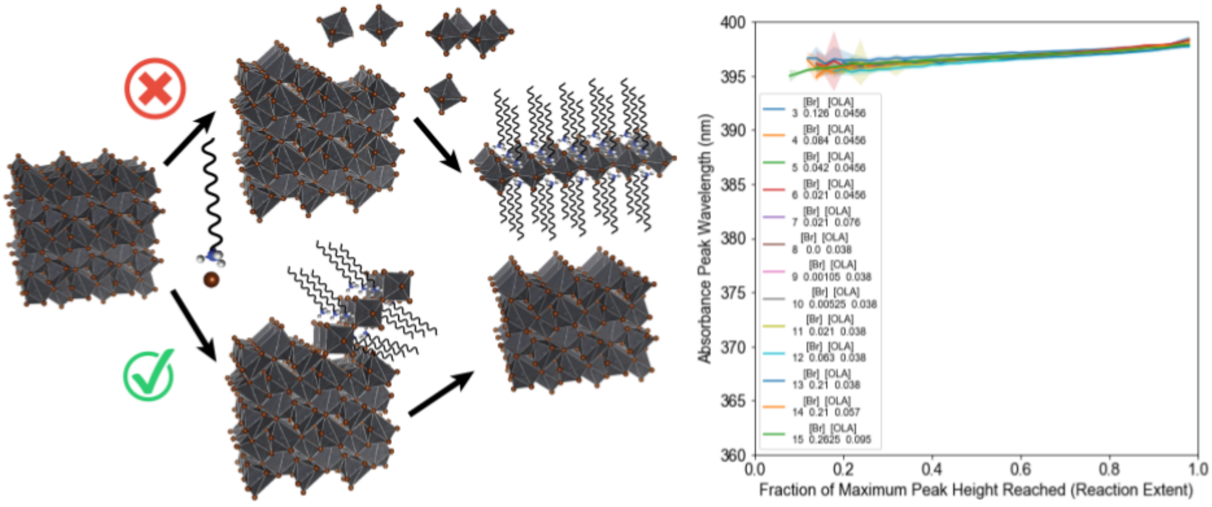

Figure A.2.1: *Variation of Transformations from* $PbBr_2$ A) Cartoon of the transformation process from $PbBr_2$ B) Plots of extracted peak Wavelength as a function of a reaction coordinate, the maximum fraction of peak absorbance reached, to remove confounding kinetic factors. The reaction coordinate is defined separately for each reaction as $\frac{Abs_{Peak}}{Abs_{Peak,max}}$, and is averaged in 20 steps. Concentrations of benzoyl bromide and oleylamine in the legend are reported in mM, and the same concentration of lead bromide nanocrystals was used throughout$\sim 0.5 O.D. @ 330 nm$.

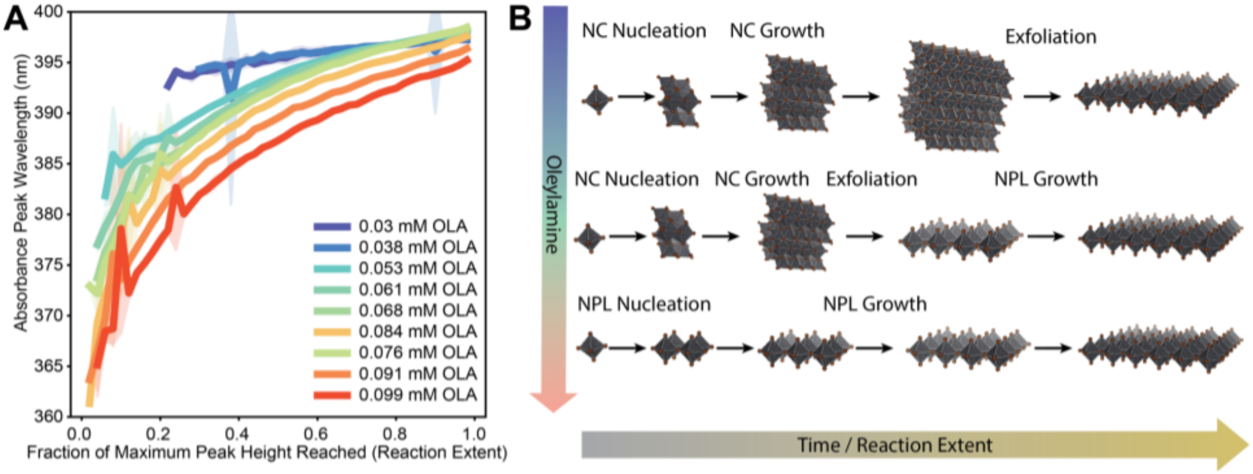

Figure A.2.2: *2D Perovskite formation with variation of OLA* A) Plots of extracted peak Wavelength as a function of a reaction coordinate, the maximum fraction of peak absorbance reached, to remove confounding kinetic factors. The reaction coordinate is defined separately for each reaction as $\frac{Abs_{Peak}}{Abs_{Peak,max}}$

, and is averaged in 20 steps. B) Cartoon of formation process at variable concentrations of oleylamine

A.3 Chapter 4 Supplementary Figures

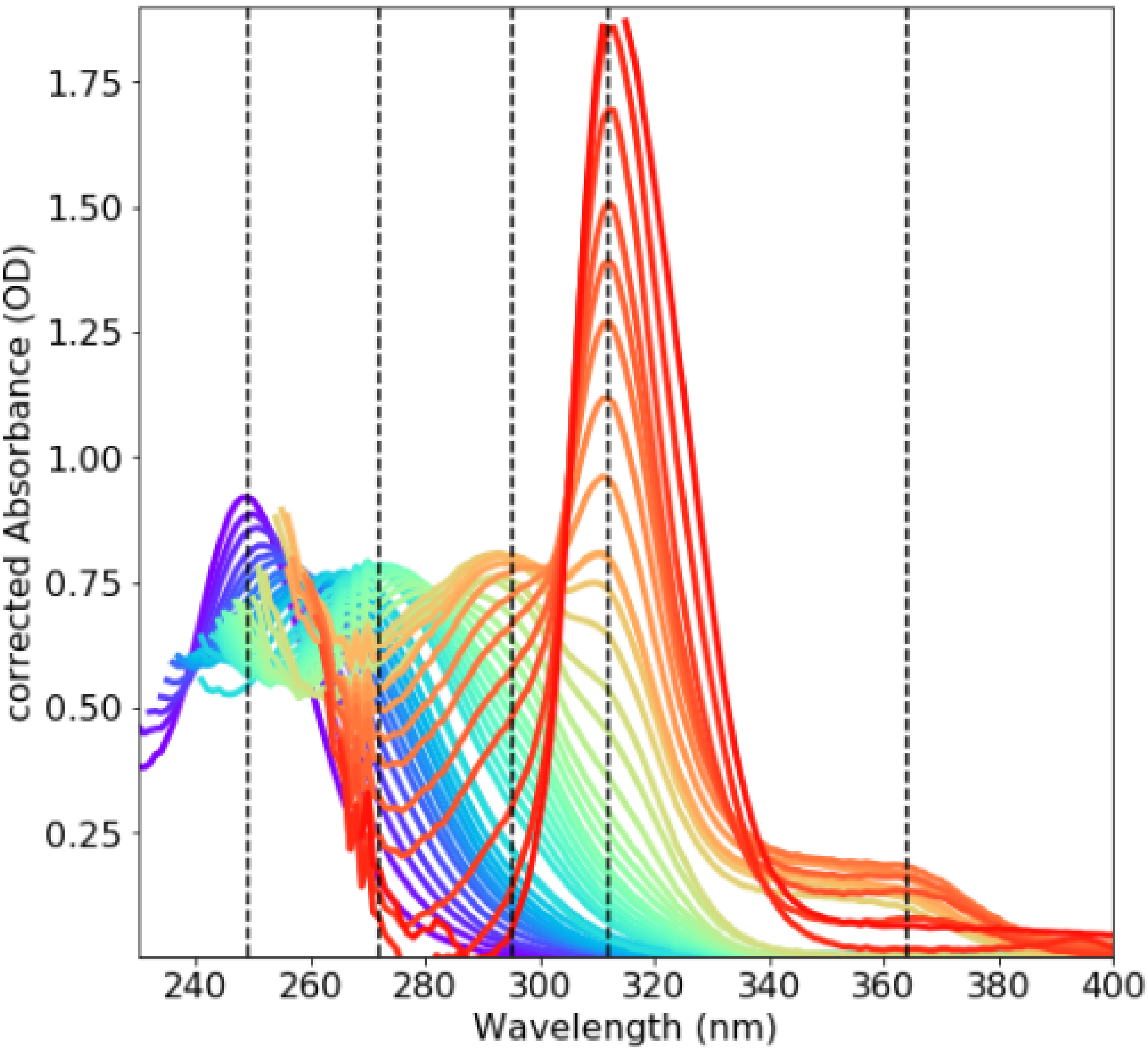

Figure A.3.1: Titration at higher Pb:OLA ratio

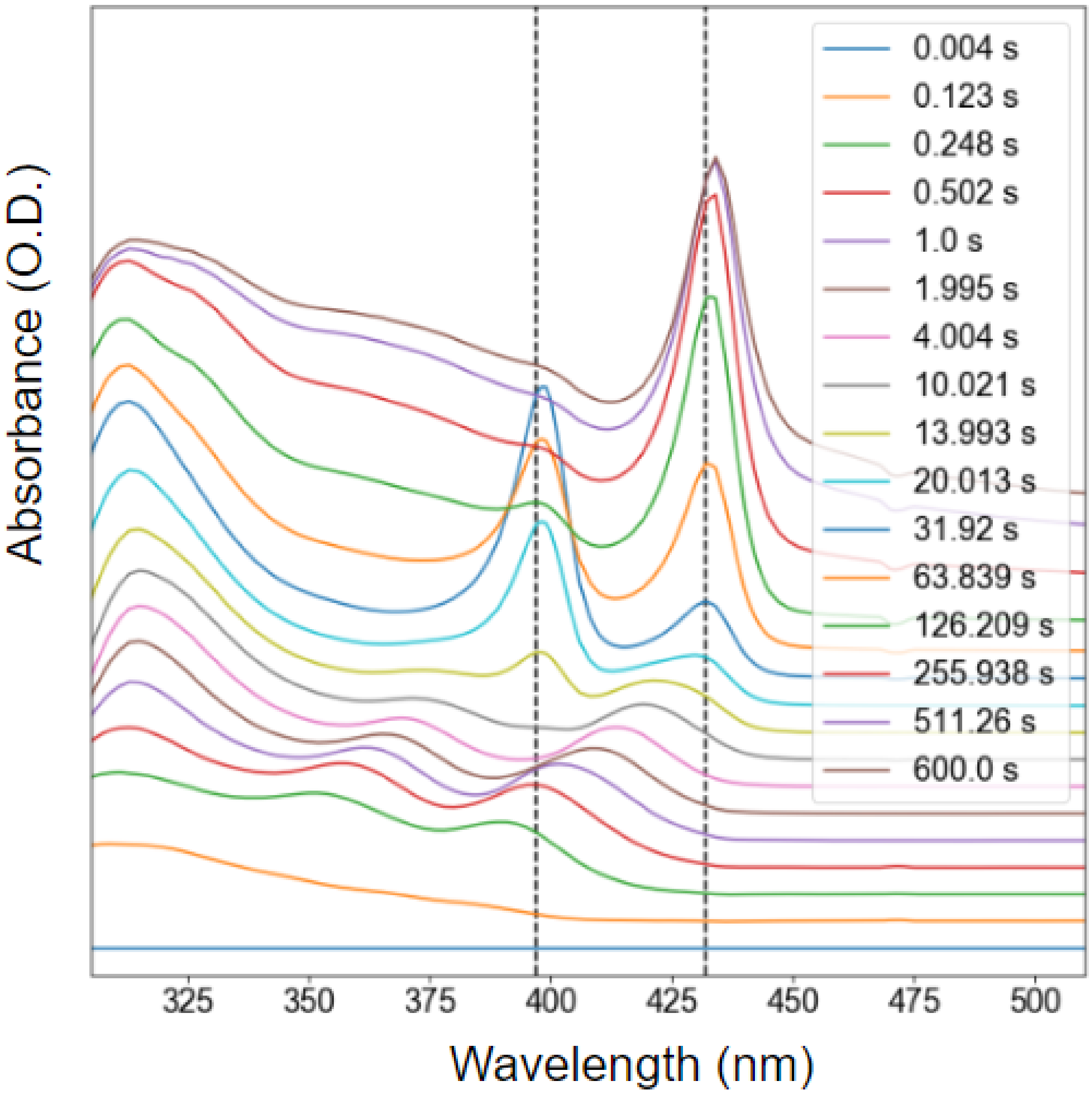

Figure A.3.2: *1 ML to 2 ML Ostwald ripening* Observation of Stopped flow synthesis showing Ostwald ripening as proposed by Riedinger et al. We have not observed this type of synthesis frequently.

A.4 Chapter 5 Supplementary Figures

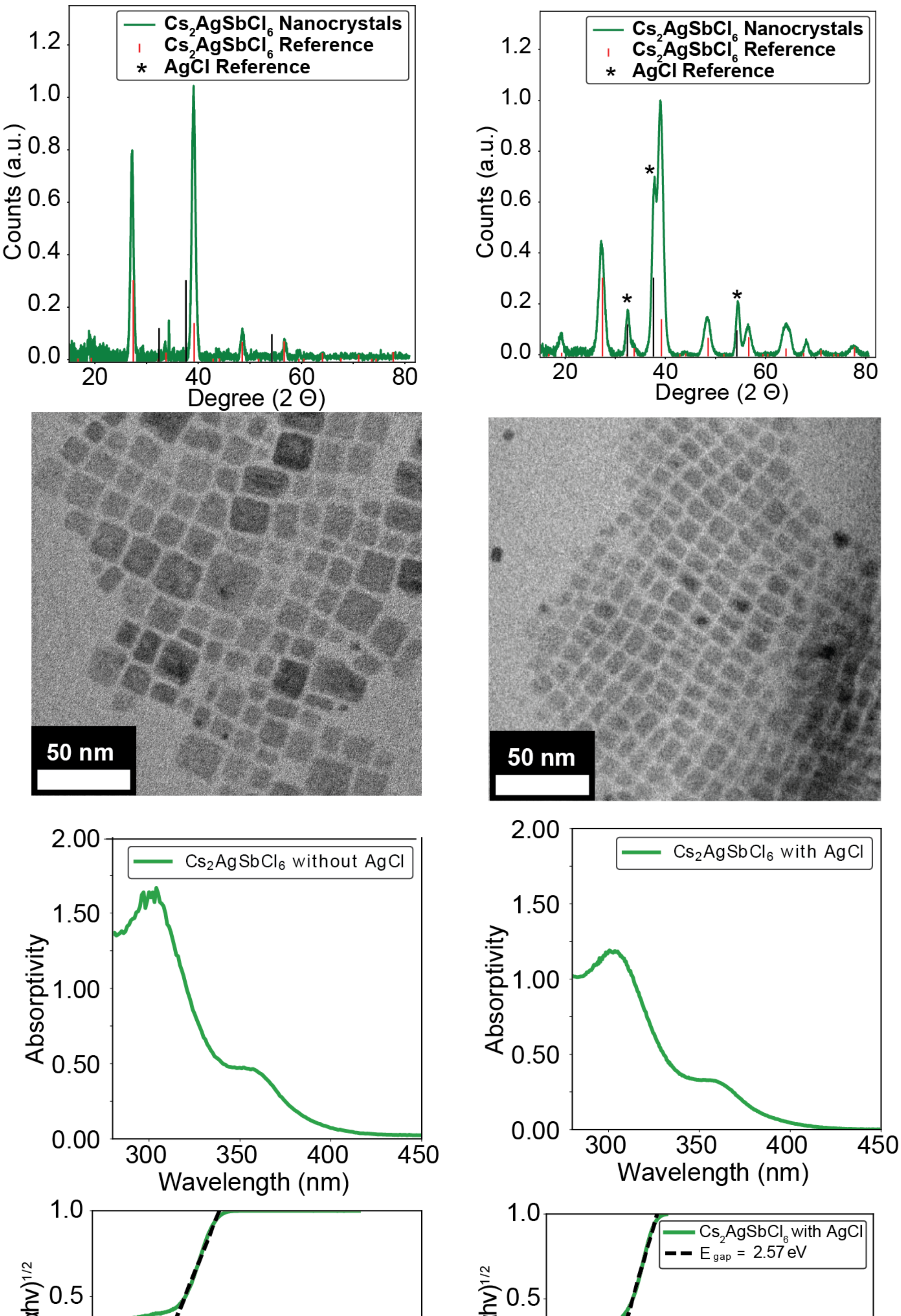
Cs$_2$AgSbCl$_6$ Nanocrystals
Cs$_2$AgSbCl$_6$ Reference
AgCl Reference
Counts (a.u.)
0.0
0.2
0.4
0.6
0.8
1.0
1.2
20
40
60
80
Degree (2 Θ)
*
50 nm
Cs$_2$AgSbCl$_6$ without AgCl
Cs$_2$AgSbCl$_6$ with AgCl
Absorptivity
0.00
0.50
1.00
1.50
2.00
300
350
400
450
Wavelength (nm)
1.0
0.5
hν)$^{1/2}$
Cs$_2$AgSbCl$_6$ with AgCl
E$_{gap}$ = 2.57 eV

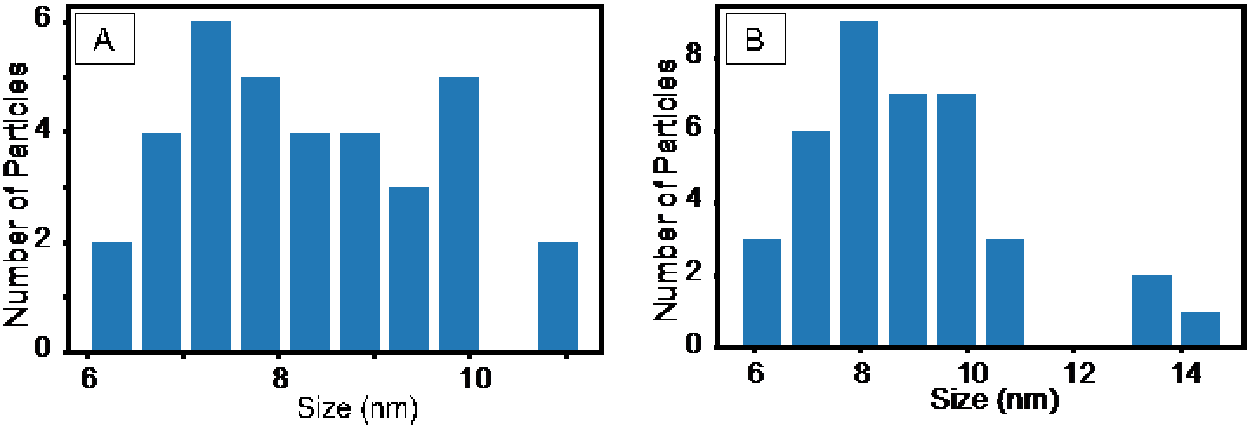

Figure A.4.2: *Sizing Histograms of Double Perovskite Nanocrystals* Size Analysis of TEM image of (A) Figure A.4.1 B ($Cs_2AgSbCl_6$ 8.3 ± 1.3 nm) and (B) Figure 5.2 F ($Cs_2AgInCl_6$, 8.9 ± 1.9 nm)

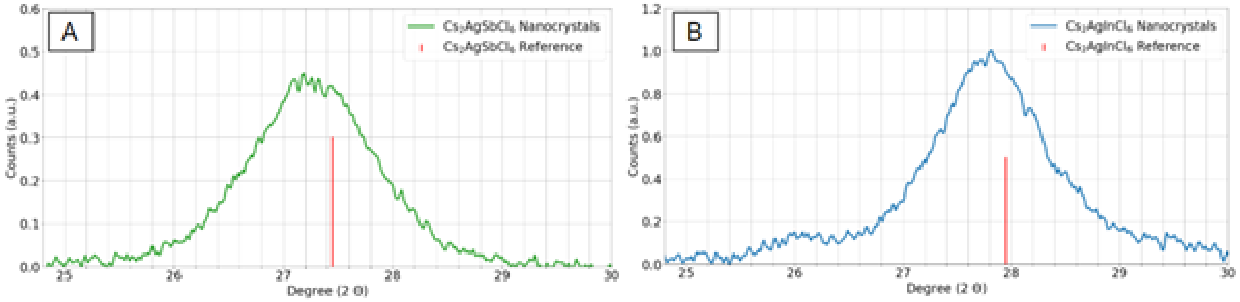

Figure A.4.3: *XRD Peak Widths of Double Perovskite Nanocrystals*

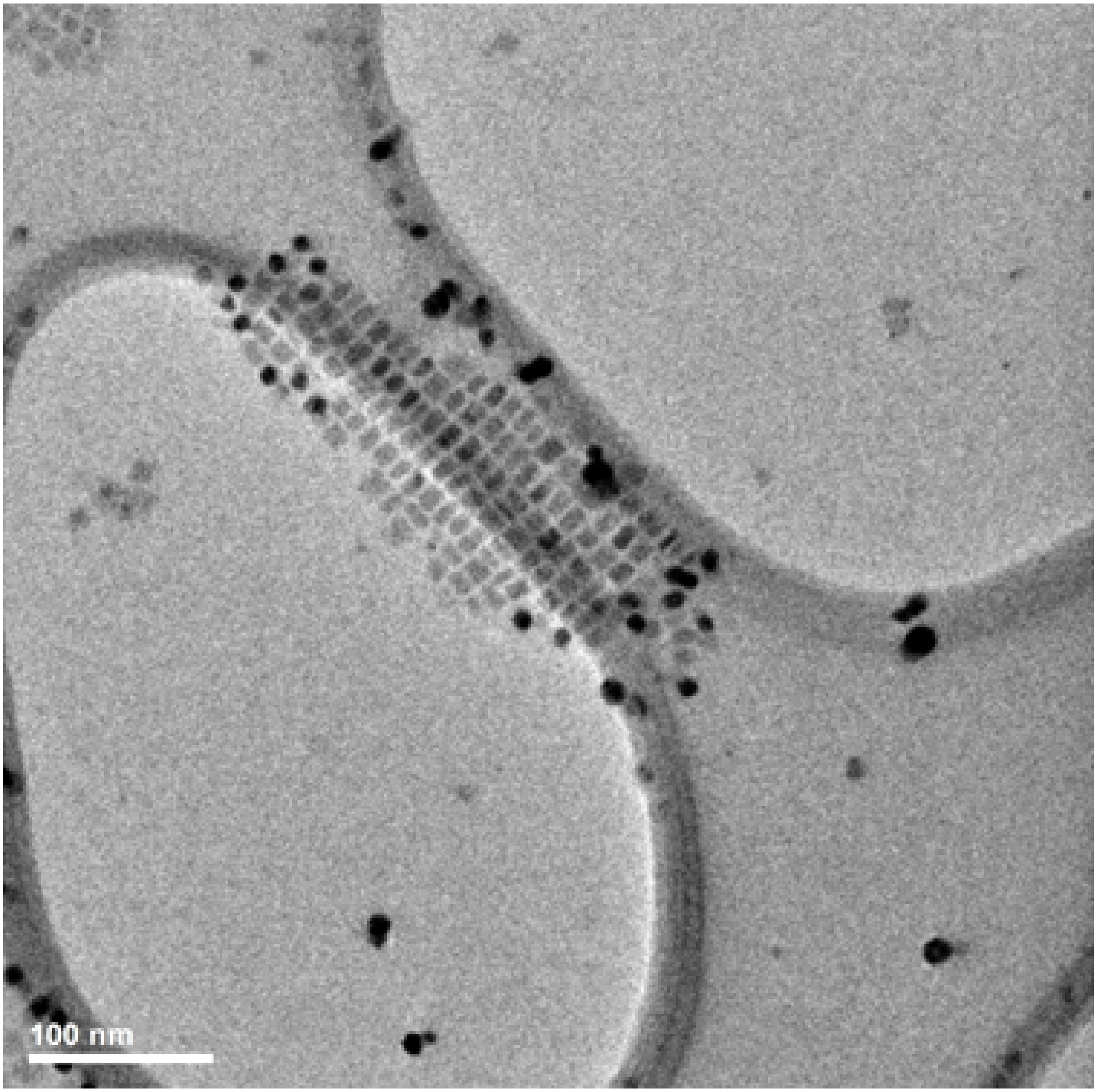

Figure A.4.4: *TEM of AgCl Contamination* $Cs_2AgSbCl_6$ nanocrystals (square shapes with lower contrast) along with AgCl nanocrystals (round shapes, higher contrast)

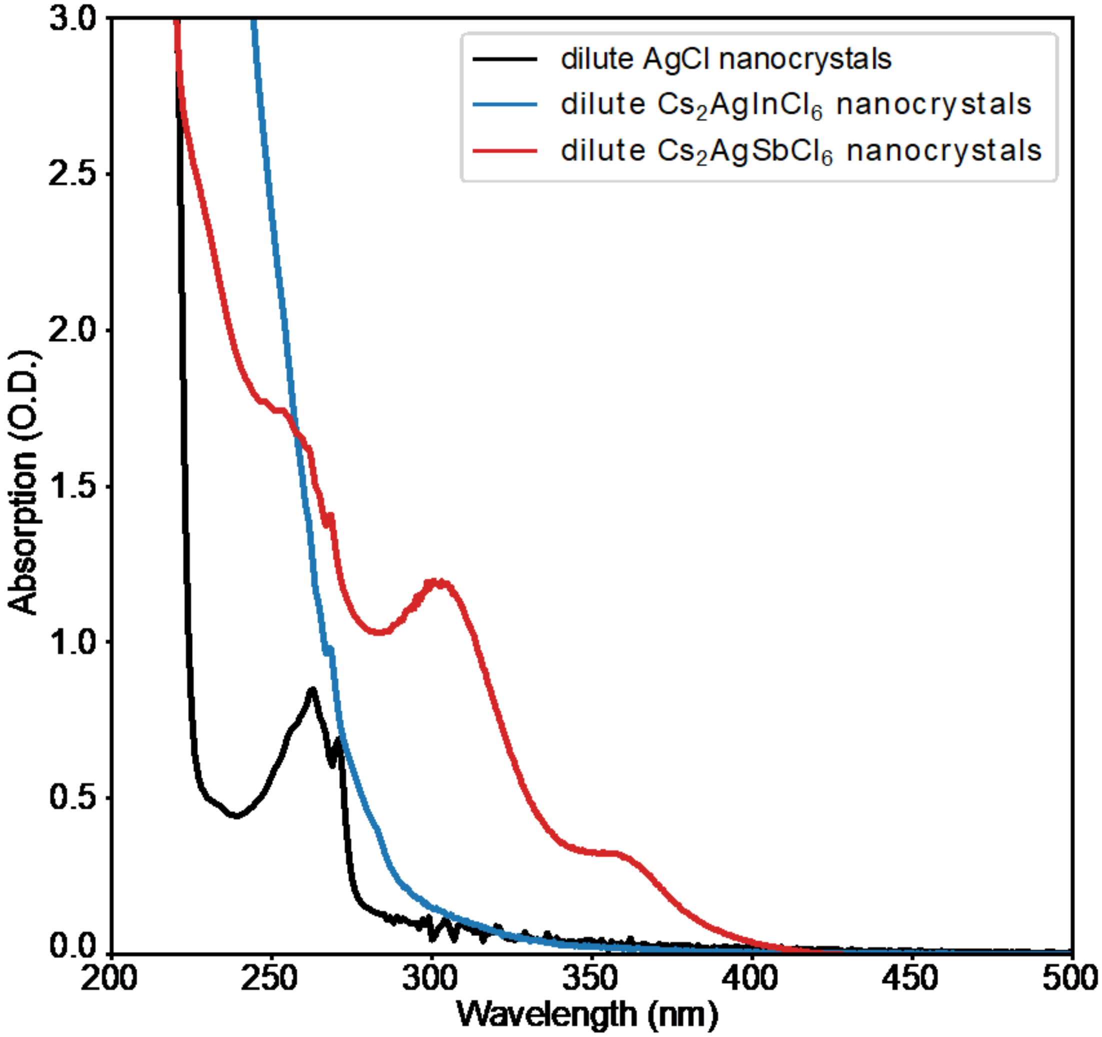

Figure A.4.5: *Absorption of AgCl Nanocrystals* Absorption spectroscopy of dilute solutions (100 µL of as-synthesized nanocrystals dissolved in 3 mL of hexanes) of $Cs_2AgInCl_6$, $Cs_2AgSbCl_6$ and AgCl. AgCl nanocrystals do not appear to have much absorption of their own, as most of the absorption in this sample can be attributed to organic impurities (see Figure A.4.8)

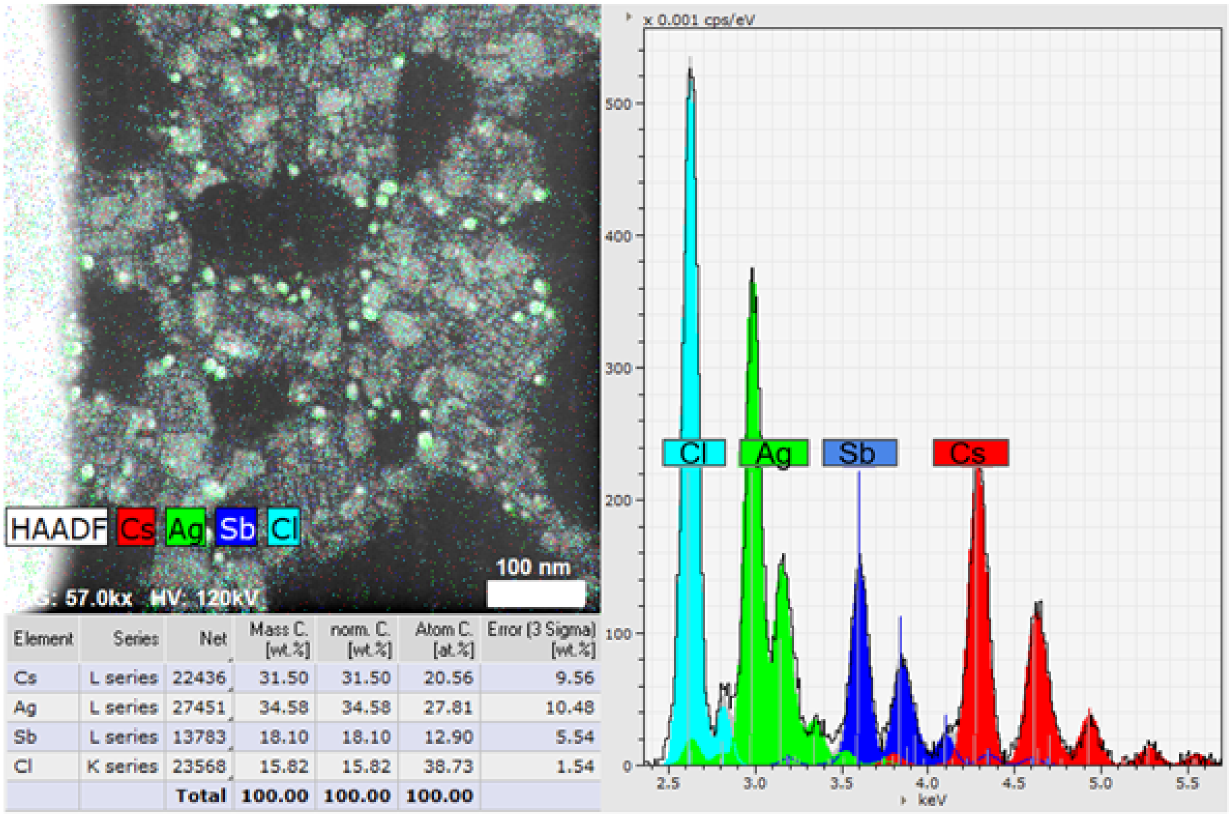

Element	Series	Net	Mass C. [wt.%]	norm. C. [wt.%]	Atom C. [at.%]	Error (3 Sigma) [wt.%]
Cs	L series	22436	31.50	31.50	20.56	9.56
Ag	L series	27451	34.58	34.58	27.81	10.48
Sb	L series	13783	18.10	18.10	12.90	5.54
Cl	K series	23568	15.82	15.82	38.73	1.54
		Total	**100.00**	**100.00**	**100.00**	

Figure A.4.6: *EDS analysis of AgCl Contamination* Large scale $Cs_2AgSbCl_6$ nanocrystal image, including areas of silver accumulation. The excess of Ag over Sb in this image in atomic percent is 14.9 %, which leads to a molar ratio of $Cs_2AgSbCl_6$ to AgCl of 1:1

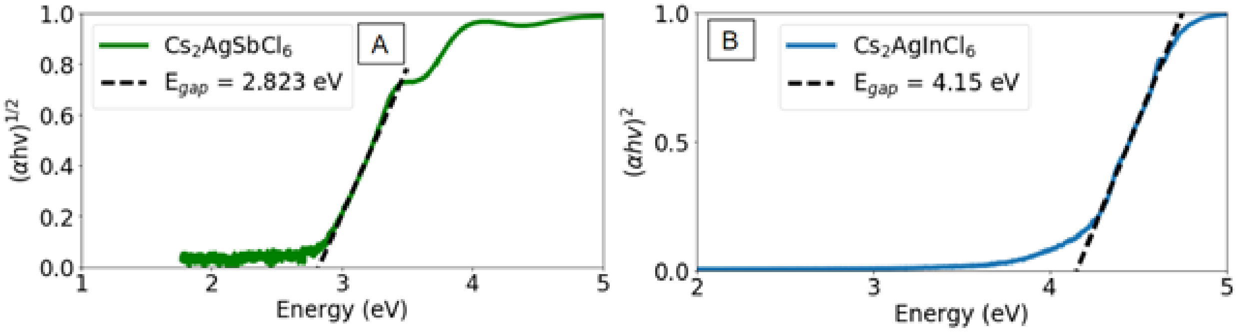

Figure A.4.7: *Tauc plots of dilute nanocrystal solutions* Tauc plots of dilute nanocrystal solutions (A) $Cs_2AgSbCl_6$ and of (B) $Cs_2AgInCl_6$. Tauc analysis on dilute solutions ignores weakly absorbing parts of the absorption spectrum of materials close to the band edge, which is especially problematic if the band edge is forbidden or indirect, as it is in this case. Using Tauc analysis on dilute nanocrystal in this way is incorrect, and the procedure used for Figure 3C and 3D should be used instead.

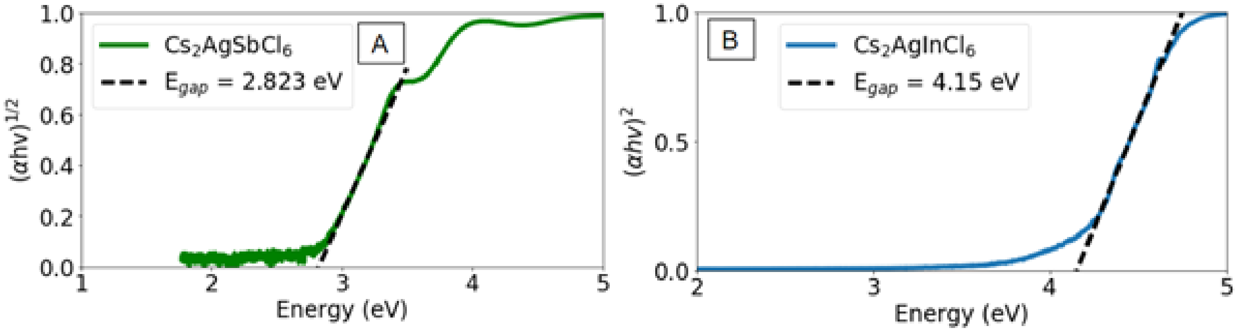

Figure A.4.8: *Absorption Spectra of Organic Contaminants* Absorption spectra of xylene (5 µL in 3 mL of hexane), oleylamine (2 µ L in 3 mL of hexane) and a dilute sample of $Cs_2AgInCl_6$ nanocrystals. Absorption past 290 nm is most likely dominated by a small amount of organic impurities. As some of those impurities appear associated with the ligands, we have not been able to remove them through cleaning.

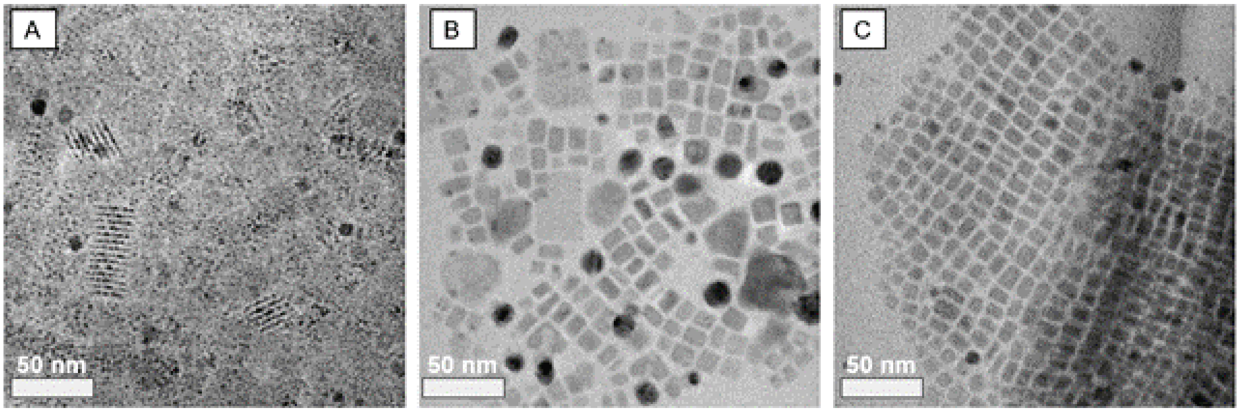

Figure A.4.9: TEM images of $Cs_2AgSbCl_6$ nanocrystals synthesized with: (A) molar ratio of 1:6 antimony (III) acetate:benzoyl chloride; (B) molar ratio of 1:12 antimony (III) acetate:benzoyl chloride (C) molar ratio of 1:6 antimony (III) acetate:2-ethylhexanoyl chloride

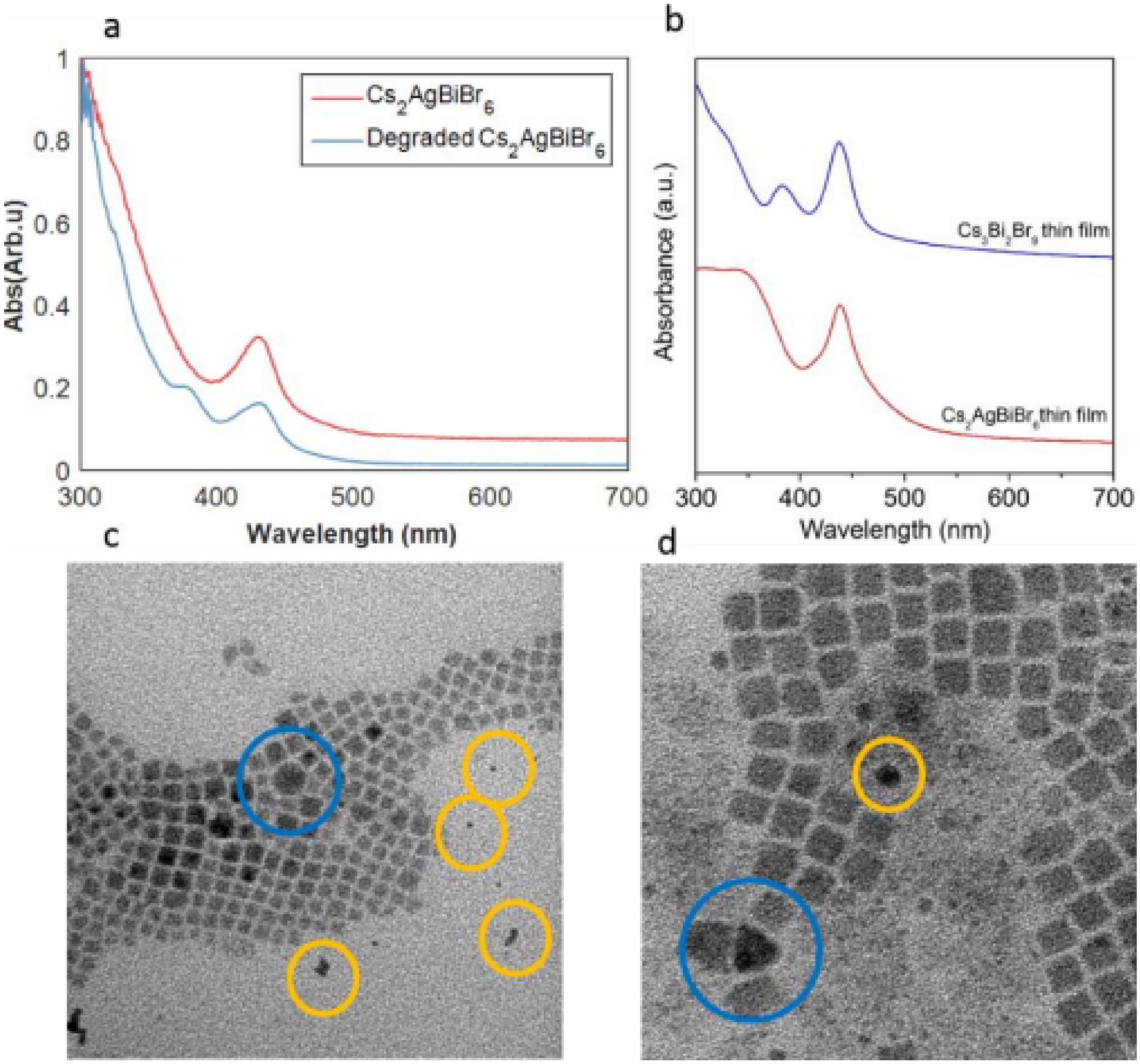

Figure A.4.10: *Degradation of $Cs_2AgBiBr_6$ NCs* (a) UV/vis Absorption measurements of fresh $Cs_2AgBiBr_6$ NCs (red) and a degraded sample (blue);the 380 nm peak indicates the presence of Cs3Bi2Br9 NCs. To further confirm this we directly made (b) Cs3Bi2Br9 films (blue) these were measured and compared to thin films of $Cs_2AgBiBr_6$ (red) using an integrating sphere, depicting similar absorption features. (c and d) TEM characterization of the degraded samples reveals NCs with shapes that deviate from the cubic shape we observed for the $Cs_2AgBiBr_6$ NCs These shapes include (c) circular NCs and (d) triangular prisms (blue) that we assign to the hexagonal Cs3Bi2Br9 composition and smaller, higher contrast circular silver NCs (yellow) discussed in the main text.

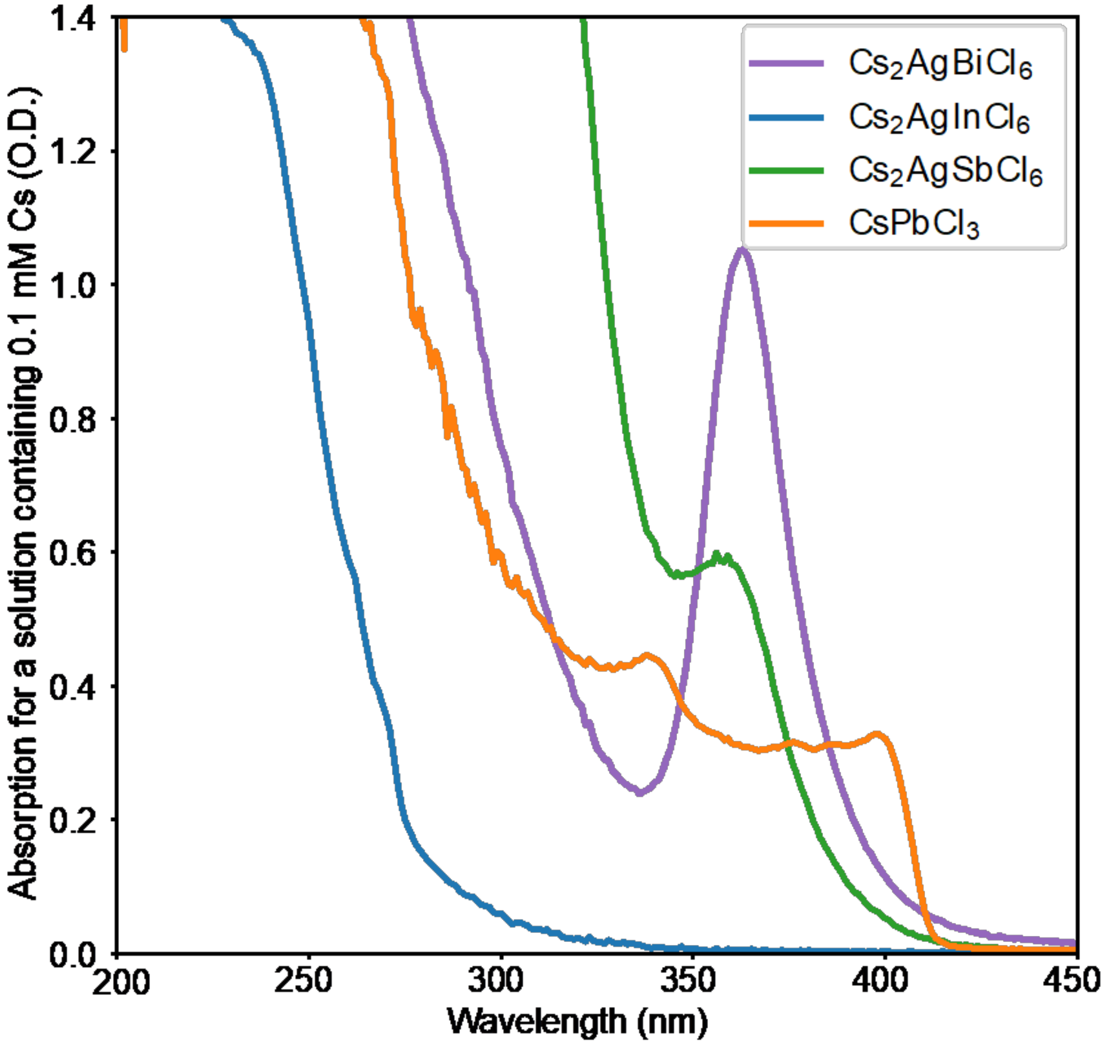

Figure A.4.11: *Calculated Extinction Spectra* Calculated 0.1 mM Cs equivalent absorption curves based on Cs GF-AAS. $Cs_2AgSbCl_6$ has a molar absorption coefficient per formula unit of $1.2 \times 10^4 M^{-1}$ at a peak wavelength of 356 nm, $Cs_2AgBiCl_6$ of $2.1 \times 10^4 M^{-1}$ at a peak wavelength of 363 nm.

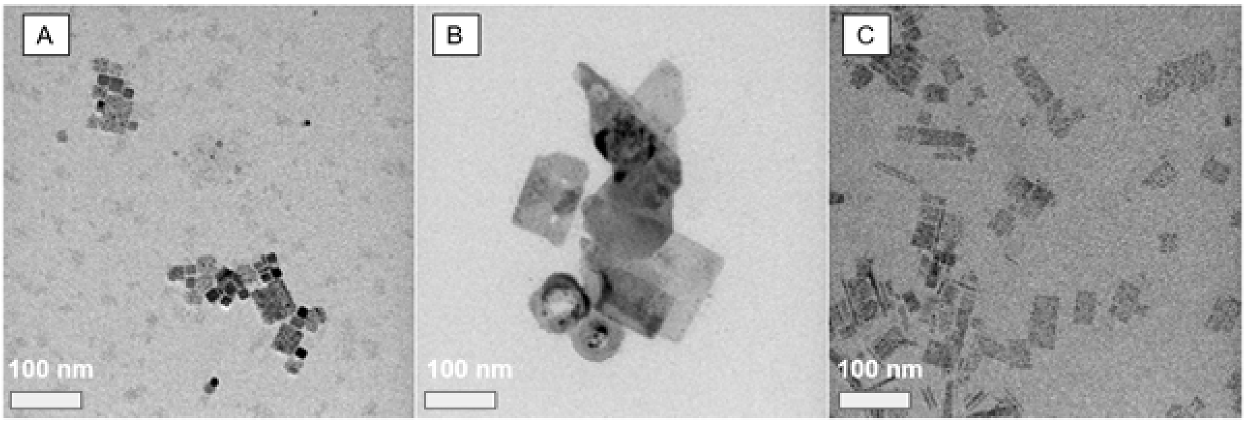

Figure A.4.12: *TEM images of Amine Degraded Nancrystals* (A) $Cs_2AgBiCl_6$ (B) $Cs_2AgInCl_6$ and (C) $CsPbCl_3$

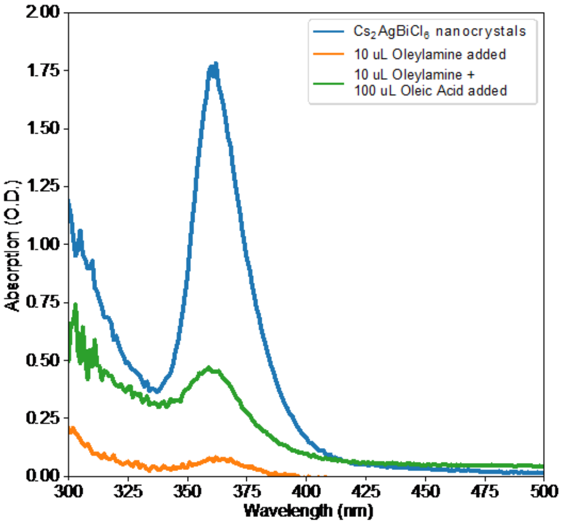

Figure A.4.13: *Reversibility of $Cs_2AgBiCl_6$ degradation* While an addition of primary amines decreases the characteristic absorption of $Cs_2AgBiCl_6$, a subsequent addition of a large excess of oleic acid reverses the trend and increases the characteristic absorption again

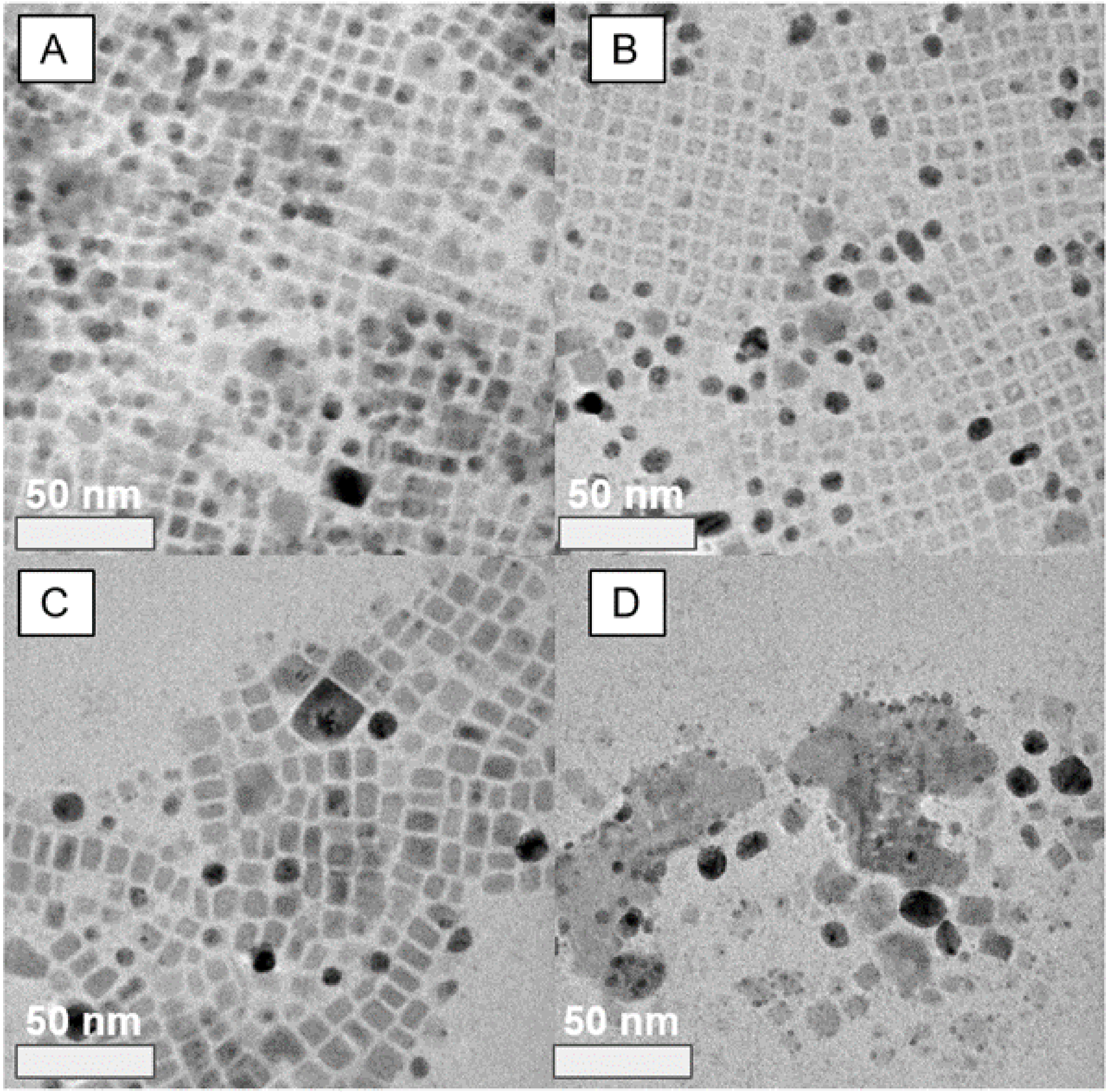

Figure A.4.14: *Atmospheric Stability of Double Perovskites on a TEM Grid* (A) $Cs_2AgInCl_6$ sample 1 hour after preparation. (B) $Cs_2AgInCl_6$ sample after 1 week. (C) $Cs_2AgSbCl_6$ sample 1 hour after preparation. (D) $Cs_2AgSbCl_6$ sample after 2 days

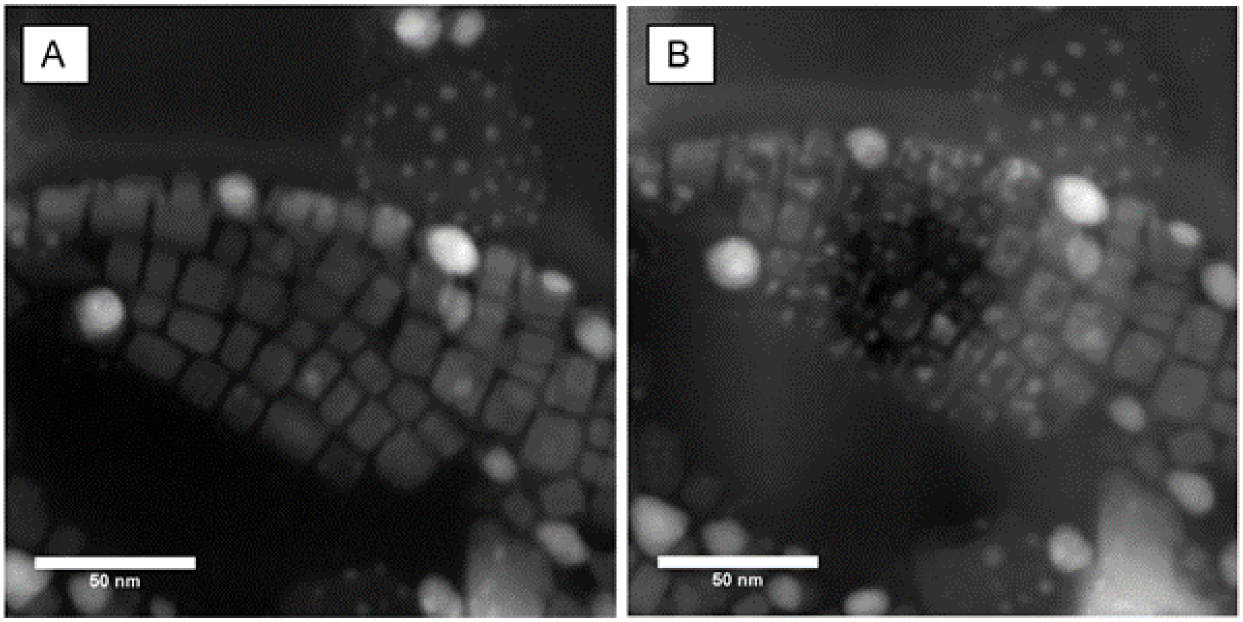

Figure A.4.15: *Degradation of $Cs_2AgSbCl_6$ under STEM Beam* TEM images of $Cs_2AgSbCl_6$ (A) before and (B) after a 300 pA electron beam dose over 5 minutes, showing extensive beam damage. Comparable beam damage in $Cs_2AgInCl_6$ nanocrystals was not observed

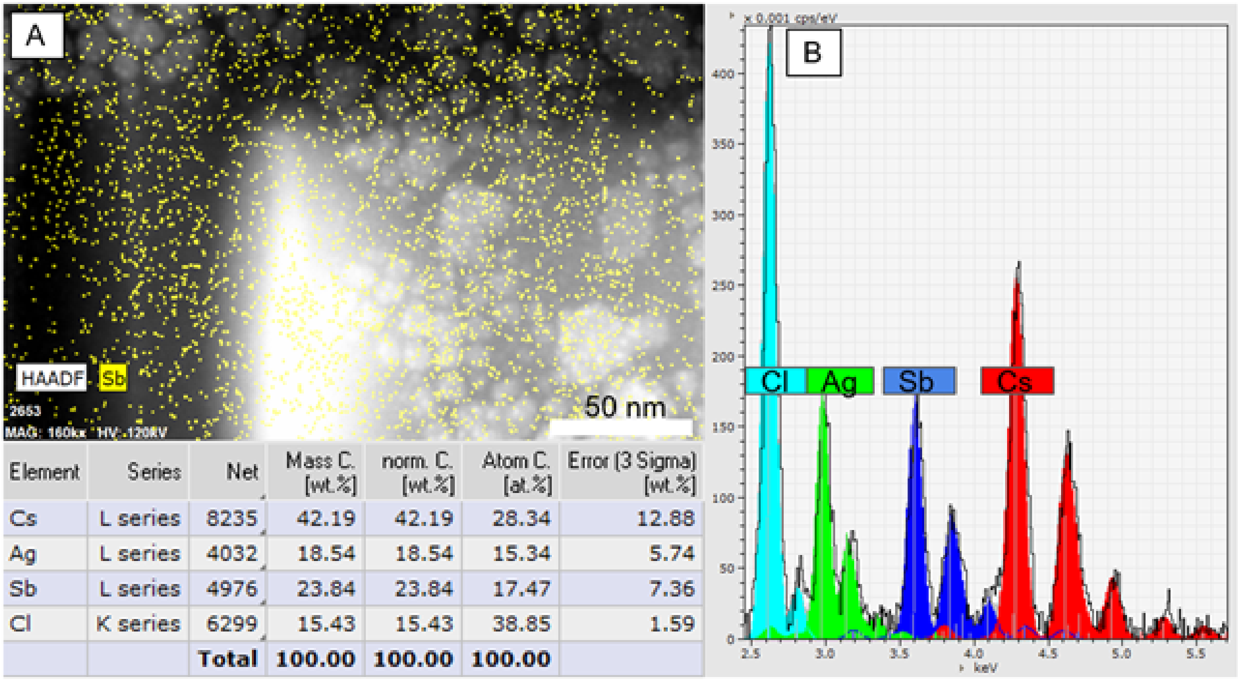

Element	Series	Net	Mass C. [wt.%]	norm. C. [wt.%]	Atom C. [at.%]	Error (3 Sigma) [wt.%]
Cs	L series	8235	42.19	42.19	28.34	12.88
Ag	L series	4032	18.54	18.54	15.34	5.74
Sb	L series	4976	23.84	23.84	17.47	7.36
Cl	K series	6299	15.43	15.43	38.85	1.59
		Total	**100.00**	**100.00**	**100.00**	

Figure A.4.16: *STEM-EDS of $Cs_2AgSbCl_6$ degradation products* T(A) STEM-EDS map and composition analysis showing Sb dispersed across the entire sample area in a sample degraded by humidity, not localized in the crystals. (B) STEM-EDS Spectrum, showing significant signal of Sb.